UNIVERSITY OF LONDON

IMPERIAL COLLEGE OF SCIENCE AND TECHNOLOGY

DEPARTMENT OF ELECTRICAL ENGINEERING

DIGITAL GENERATOR PROTECTION

by

Kheldun Rauf Khan

Thesis submitted for the Degree of **Doctor of Philosophy** and the **Diploma of Imperial College** in the Faculty of Engineering

February, 1985

To my wife, **Sohela Parween**, for her constant encouragement and guidance.

ABSTRACT

This research investigates digital algorithms for the 100% protection of the stator windings of large turbo-alternators against earth faults.

The approach chosen was to use digital fourier transform based spectral estimation methods to study the spectral nature of this fault condition on a small micro-machine based model of a typical 500 MW CEGB turbo-alternator system. The digital spectral estimation was implemented on a mini-computer using both weighted and frequency interpolated FFT algorithms. Analogue input to the mini-computer was provided by a bit-slice based data aquisition system. Theoretical backup was provided a computer simulation of the stator windings under earth fault conditions.

Two algorithms based on the third harmonic components of the generator terminal and neutral emfs are proposed as a result of this study. One algorithm achieves the protection by measuring an undervoltage of the neutral third harmonic while the other measures unbalance between the terminal and neutral third harmonic emfs.

A detailed laboratory study shows both algorithms to offer superior performance to present third harmonic electro-magnetic schemes. The two main features of the algorithms are their very high protection stability against heavy current faults and their insensitivity to the generator load setting. Both algorithms are also very fast with a maximum operating time of one and a half cycles.

An algorithm for the location of stator earth faults is also proposed. Experimental results show it to be accurate to within 2% across the entire winding. Furthur work is however needed to evaluate its performance to high resistance earth faults.

ACKNOWLEDGEMENTS

The work in this thesis was carried out under the supervision of **Dr. B. J. Cory**, B.Sc. (Eng.), D.Sc., ACGI, C. Eng., Sen. MIEEE, FIEE, Reader in Electrical Engineering, Imperial College of Science and Technology, London. I wish to thank Dr. Cory for his helpful guidance, constant encouragement and keen interest during the preparation and completion of this research.

I would also like to thank the following:

Dr. D. C. Macdonald for his help and guidance on machine theory.

GEC-Measurements Ltd and SERC for sponsoring this research.

All my colleagues in the **Power Systems Group** for the comradeship which made my stay so enjoyable.

All my colleagues at GEC-Measurements, especially **Peter Crossley, Robin Millar** and **Ted Walker**, for their support and guidance.

'Wally' Brown of the electrical engineering workshop for his help in modifications to the micro-machine.

Ned for the typing and immaculate layout of the thesis.

Finally, a special thanks is due to my wife for her understanding in the face of numerous late nights in the laboratory.

TABLE OF CONTENTS

Appendix

LIST OF ILLUSTRATIONS

LIST OF TABLES

LIST OF FLOWCHARTS

LIST OF SYMBOLS

The following conventions have been observed in this thesis:

(i) Vector quantities are shown printed in bold type.

(ii) Matrix quantities are shown enclosed by square brackets.

(iii) This list refers only to symbols used within the main body of the thesis. Symbols used in the appendices are not listed.

Main symbols

A	- complex fourier series coefficient
a	- filter or fourier series coefficient
b	- filter or fourier series coefficient
c	- stator coil number from the neutral
E	- steady-state emf
f	- frequency
I	- steady-state current
K	- gain factor
k	- sensitivity factor
N	- window length
N(subscripted)	- number of ...
p	- pole pairs
Q	- total number of slots in a machine winding
R	- resistance
r	- stator coil number from the terminals
s	- slot number
	- s-plane operator
S	- relaying signal
T	- discrete time interval
t	- time

W	- frequency domain weighting function
	- FFT twiddle factor
w	- time domain weighting function
X	- frequency domain function
	- reactance
x	- time domain input function
y	- time domain output function
Z	- impedence

Greek symbols

α	- slot angle for the fundamental
μ	- averaging function
δ	- central difference function
ϕ	- phase
Ω	- discrete frequency interval
ω	- angular frequency
θ	- slot angle
Δ	- trip threshold
	- convergence criterion
Υ	- reference signal
δ	- start threshold
λ	- 120 deg. phase shift operator

Subscripts

a	- armature
A	- stator A-phase
B	- stator B-phase
c	- cutoff
C	- stator C-phase
c	- stator coil number from the neutral
d	- differential leakage
e	- end winding
	- external

G	- ground
H	- half cycle
i	- integer variable
k	- discrete frequency operator
l	- leakage
m	- integer variable
	- magnetizing
n	- discrete time operator
N	- neutral
o	- operate signal descriptor
p	- parallel arm
	- periodic
P	- potential transformer
R	- restrain signal descriptor
r	- stator coil number from the terminals
s	- sample
	- series arm
	- series arm
	- slot number
t	- time
W	- weighted

Abbreviations

A.D.C	- analogue to digital convertor
AC	- alternating current
ARMA	- auto-regression moving average
AVR	- automatic voltage regulator
C.T.	- current transformer
CEGB	- Central Electricity Generating Board, UK.
CFT	- continuous fourier transform
D.A.C	- digital to analogue convertor
D.A.S	- data acquisition system
DC	- direct current
DFT	- Discrete Fourier Transform
d.w.r	- divided winding rotor

emf	- electro-motive force
FFT	- Fast Fourier Transform
FIFO	- first in first out
FIR	- finite impulse response
G.T.	- generator transformer
H.V	- high voltage
I.D.M.T.	- inverse definite minimum time
IIR	- infinite impulse response
L.V.	- low voltage
MVAR	- megavolt ampere reactive
mmf	- magneto-motive force
n.p.s	- negative-phase-sequence
PFA	- prime factor algorithm
P.L.L	- phase lock loop
P.O.W	- point on wave
p.p.s	- positive-phase-sequence
P.T.	- potential transformer
PHD	- Pisarenko Harmonic Decomposition
p.u.	- per unit
rms	- root mean square
s/c	- samples per cycle of the fundamental
TCR	- time constant regulator
UAT	- unit-auxiliary transformer
VA	- volt ampere
VCVS	- voltage controlled voltage source
V.T.	- voltage transformer
z.p.s	- zero-phase-sequence
WFT	- Winograd Fourier Transform

CHAPTER ONE

Introduction

An introduction to the field of digital generator protection is presented. The advantages and disadvantages of digital methods of protection are discussed and the present state of research into generator protection reviewed. A brief overview of the protection requirements, tripping philosophies, and protection methods for large generators is also presented.

This chapter also reviews the short comings in present generator protection and defines the area of research, to be described in later chapters. The objectives of the research and the organisation of the thesis is described.

1.1 The Advantages of Digital Protection

Since Last and Stalewski [42] first proposed the use of digital computers in power system protection, there has been considerable research [82] in this field. The advantages of using digital methods are many, among which are:

(i) The manufacture of digital relays can be highly automated, and inevitably a time will come when the manufacture of analogue relays becomes uneconomic [82].

(ii) A high reliability can be achieved as a digital device can inherently monitor itself, but the indications are that even without self-monitoring digital methods are not intrinsically any less reliable than conventional methods [25].

(iii) Performance consistency is better or as good, in general, as the best solid-state analogue designs.

(iv) Certain features such as memory action and complex signal processing techniques are more easily realizable in digital relays.

(v) There is no performance change with age.

(vi) Different types of relays can share a common hardware structure within limits dictated by input and output requirements for a particular protection [40].

(vii) Revisions or modifications can be very easily carried out by modifying the software.

(viii) Different operational options and relaying characteristics can be easily integrated in one relay [92], giving the user greater flexibility and decreasing manufacturing costs by reducing the number of inventories needed for a particular product.

(ix) Supervisory and auxiliary functions which do not compromise the main protection function of the relay can be easily included. Some of the possible auxiliary functions are error logging for postfault analysis, fault location (where applicable) and condition monitoring.

(x) Digital relays can be integrated into a communications system enabling system interaction [40]. This is of particular importance as it provides for system, interaction between critical protection functions without compromising their security. Centralizing protection functions within one computer, on the other hand, would seriously compromise the integrity of the protection system [82].

The main disadvantages of digital methods are:

(i) Software development costs, both in terms of manpower and hardware support, can be very high and will, in fact, probably constitute the major part of the development cost for any digital relay. This makes the use of digital methods uneconomic for small production runs.

(ii) Digital systems are not well suited to the noisy and harsh power systems environment and considerable ingenuity needs to be excercised to obtain acceptable levels [79] of noise immunity.

Initially, research into digital relaying was mainly concentrated in deriving digital imitations of analogue protective relays [82]. The results of this research effort can be seen in the present commercial availability of purely digital equivalents of certain analogue relays [90,92]. In recent years with the advent of more powerful micro-computers, the emphasis of research has shifted. Present thinking is that digital relays need not be imitations of analogue equivalents, but should instead offer a purely digital solution to the same problem.

Recent proposals for the use of probabalistic tripping criteria [70], Fourier transform based spectral analysis [5,22,38,58,74], and Kalman filtering [19,22-24,51]; methods which do not possess analogue counterparts, are all indicative of this trend.

Research into digital protection with particular reference to large alternators is described in section 1.3. First an overview of the protection philosophy for large generators is presented.

1.2 An Overview of Generator Protection

In a broad sense, the field of generator protection [18,54,78,85,88,91] encompasses not only the protection of the generator itself, but the protection of the generation system as a whole. The generation system - henceforth with specific reference to large turbo-alternators - is a complex electro-mechanical system comprising the prime mover and its steam source, the alternator, the unit-auxiliary transformers (UAT) and the unit transformer (G.T.) as illustrated in figure 1.1.

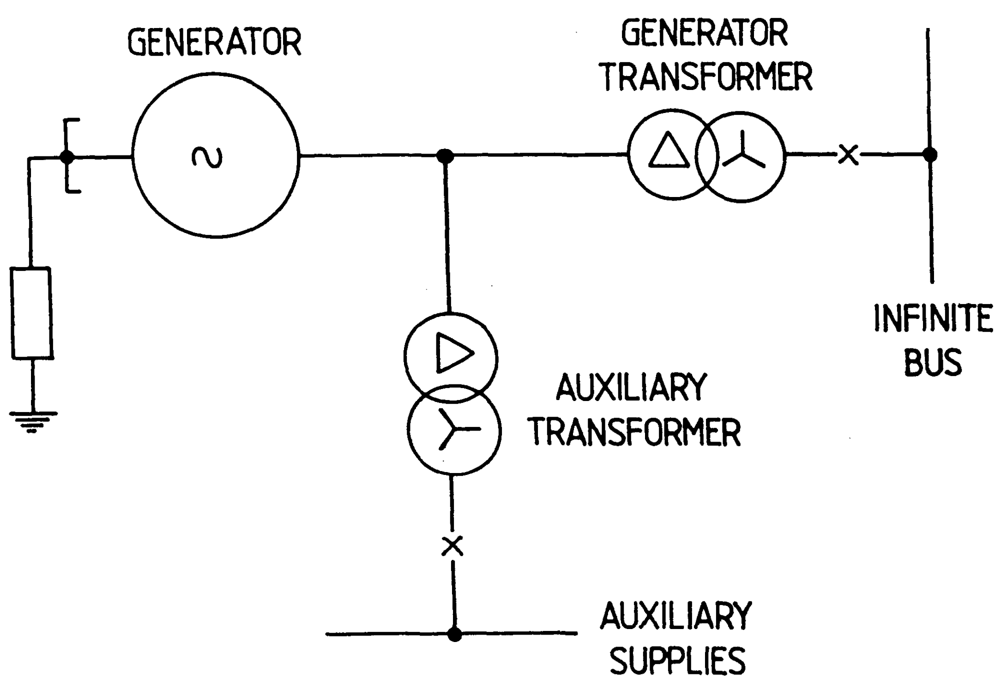

Figure 1.1: The generator system.

Mechanically, the prime mover and the generator are one system, while electrically the generator and the equipment connected to it upto and including the unit transformer is another. As a result the protection philosophy for the complete system is quite complex. However, the alternator protection can be considered separately provided the mechanical and electrical constraints imposed by the rest of the generating system are taken into account. The two main constraints are:

(i) A trip of the electrical side must be appropriately coordinated with a shutdown of the prime mover.

(ii) The interaction of the alternator protection with that of the rest of the electrical system must be considered.

The first constraint results in generator faults being classified into two types according to the tripping action initiated by the protection. The two types are:

(i) Class 1 faults which require a coincidental trip of both sides of the generating set.

(ii) Class 2 faults for which the electrical side trip is delayed until steam input to the prime mover has reduced to a safe level.

This tripping practice is a compromise between two safety criteria:

(i) If the tripping is effected coincidentally and the steam stop valves do not close fully, the generator will overspeed dangerously as it is no longer on load.

(ii) On the other hand, if the alternator is tripped only when steam input has ceased, severe fault damage within the electrical generator system may result from the fault initiating the trip.

The tripping classification is achieved in practice by interlocking all trips to be classified as class 2 with a relay measuring the electrical power output of the generator. This relay is called the ´low power interlock´ relay [54,88] and is usually duplicated to ensure the security of the generator protection.

The electrical fault conditions an alternator must be protected from fall into two categories which will be described separately:

(i) Winding faults within the alternator.

(ii) Unstable or dangerous operating conditions.

The generator also needs to be protected against mechanincal failure to itself or its maintenance systems - bearing wear, lubrication of the bearing and hydrogen seals, hydrogen cooling system etc. Their study [18,54,87] is not within the scope of this research.

1.2.1 Alternator Winding Faults

Internal winding faults are the most serious and common of all faults encountered on large turbo-alternators and can result in serious damage to the machine, especially if a large fault current is produced. The most serious consequences are:

(i) Severe overheating and stressing of the windings.

(ii) Burning of the core metal.

(iii) Stressing of the bearings and shaft due to torque pulsations and asymmetric magnetic forces.

In addition such faults may also cause disturbances in the power system. Very severe winding faults could cause the distance relays closest to the faulted generating set to maloperate causing disruption to the system [78].

The main winding faults are:

(i) Inter-phase faults clear of earth on the stator windings.

(ii) Earth faults on stator.

(iii) Inter-turn faults on the stator.

(iv) Rotor winding faults.

Experience has shown that the greater majority (about 80%) of winding faults are to earth [18,54,78,88,93,94]. Inter-phase faults clear of earth are much less common as they can only usually persist in the end windings. In the rest of the winding, localized burning will inevitably cause core and conductor to contact. Inter-turn faults clear of earth are uncommon for similar reasons, but have been known to occur because of vibration induced abrasion in the end windings.

1.2.1.1 Inter-phase Fault Protection

Biased differential protection is universal for detecting inter-phase faults, and is also the main generator winding protection. Figure 1.2 illustrates a typical scheme.

The protection is based on the Merz-Price [88] circulating current technique. A circulating current loop is formed by connecting the secondaries of two current transformers (C.T.) placed at either end of each phase of the generator winding as illustrated in figure 1.2. A through current across the generator produces circulating currents in the loop without producing a current in the relay. For internal winding faults, however, the secondary current loop becomes unbalanced and the relay operates. A biased relay is used to minimize the sensitivity of the protection to mismatches between the two C.T.s.

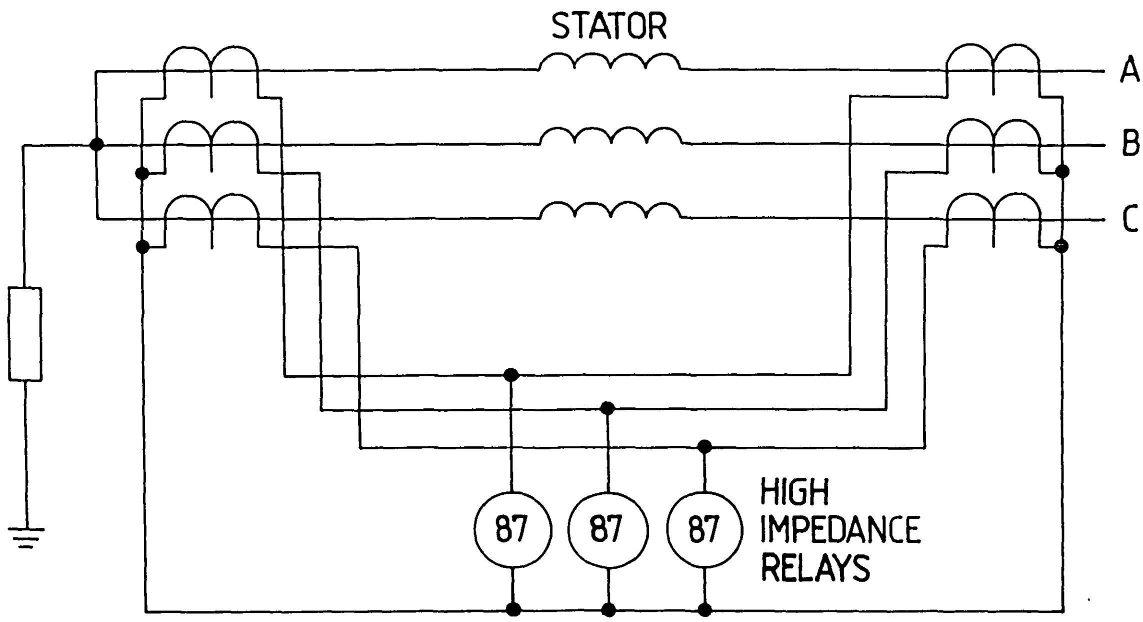

Figure 1.2: Biased differential protection for generators.

The mode of application of differential protection varies. The three methods are:

(i) Across the generator and unit transformer to protect both as one unit.

(ii) Dual differential protection with one protection directly across the alternator and the other as in (i).

(iii) Directly across the alternator only, with seperate differential protection for the unit and unit-auxiliary transformers, if a generator isolating switch to facilitate starting is present.

As very high currents can be expected, the tripping action initiated is always a class 1 trip. Backup protection is provided by the following methods:

(i) Impedence relay looking into the generator from the low voltage (L.V.) side of the unit transformer.

(ii) Overcurrent I.D.M.T. (inverse definite minimum time) relays connected at the alternator terminals and operating for an infeed of fault current from the infinite-bus.

1.2.1.2 Stator Earth Faults

Stator earth faults are much less serious than inter-phase faults because of high resistance neutral grounding techniques used in all large generators [78,84,87,88]. The fault current is limited to typically less than 0.1% of rated current, well below the sensitivity of the main differential protection. Consequently a seperate earth fault protection is needed.

All earth fault protection is based on the common principle of sensing an overvoltage (or overcurrent) of the fundamental at the neutral of the alternator. Figure 1.3 illustrates, schematically, the protection.

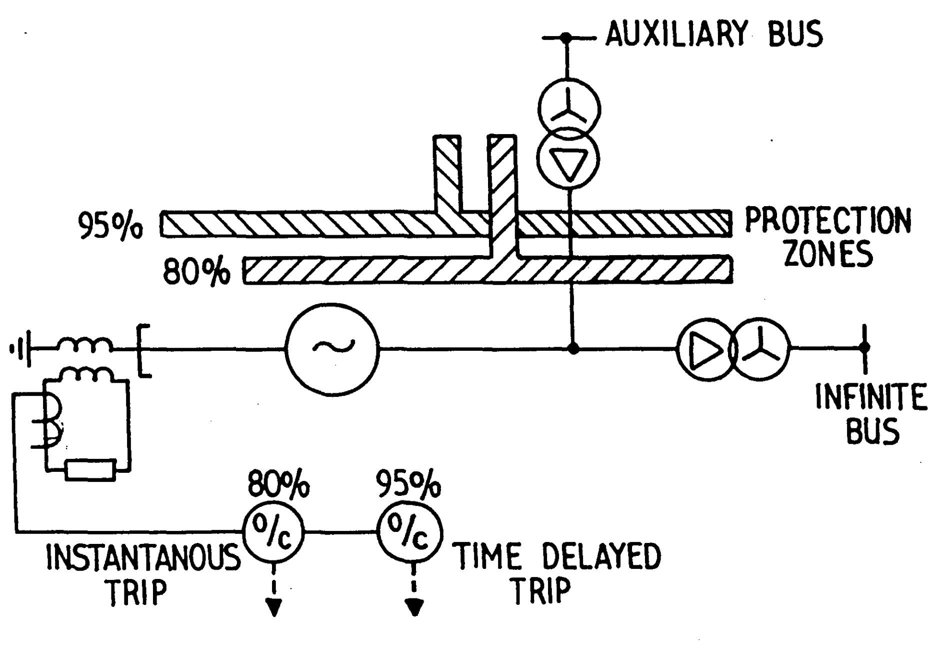

Figure 1.3: Stator earth fault protection.

Typically, it is possible to obtain instantaneous detection covering upto 80% of the winding from the line end and a time delayed detection covering 95%. Earth fault protection is also effective at covering against earth faults the whole of the electrical side of the generation system, upto and including the L.V. sides of the unit and unit-auxiliary transformers.

The only limitation to present methods, is the lack of coverage for the remaining 5% of the winding near the neutral. This blind spot is potentially very serious, as an occurrence of earth leakage within it will effectively bypass the high resistance grounding of the neutral. Any subsequent earth fault could cause serious damage, especially if the main differential protection is rendered inoperative by both fault points being within its zone of protection.

Tripping action is usually of the class 2 type as the fault currents are low and fault damage minimal. Some utilities arrange only for an alarm, but this is not good practice because:

(i) The likelihood of the fault deteriorating to an inter-phase short circuit is high.

(ii) The current limiting characteristic of the high resistance generator neutral grounding is rendered inoperative.

1.2.1.3 Stator Inter-turn Protection

Present methods to detect inter-turn faults are:

(i) Zero sequence inter-turn protection.

(ii) Transverse differential protection for generators with parallel windings per phase (double wound generators).

The first type of protection measures the zero-sequence current at the terminals of a generator which occurs when an inter-turn short circuit unbalances the symmetry of the three-phase stator windings. Transverse differential protection is a form of differential protection applied between the line ends of the two parallel windings constituting each phase as illustrated in figure 1.4.

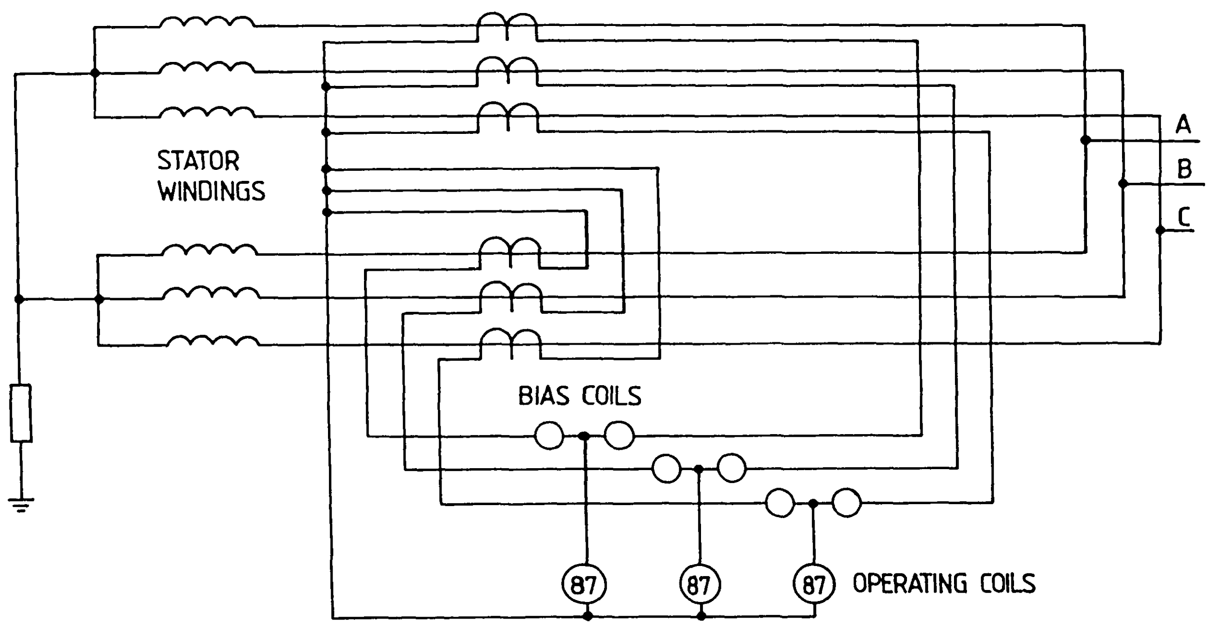

Figure 1.4: Transverse differential protection.

The application of inter-turn protection is by no means universal as both methods have inadequate sensitivity. Inter-turn faults involving only a fraction of a turn can pose a hazard to the machine but produce no discernable effect at its terminals. The result of such faults is to produce localized burning due to circulating currents within the shorted turn, with the inherent danger of the fault deteriorating further into an inter-phase or earth fault.

Some utilities, because of these sensitivity problems, do not provide for specific inter-turn protection, relying instead on the earth fault and differential protection tripping when the fault worsens to include another phase or earth. This is an unsatisfactory state of affairs as,

(i) it can take considerable time for this to occur especially if the fault is at the end windings,

(ii) fault damage will inevitably be greater.

1.2.1.4 Rotor Winding Faults

The field winding must be protected against two types of faults:

(i) Earth faults.

(ii) Inter-turn winding faults.

Rotor earth fault protection is usually achieved by applying an external voltage between the normally floating rotor circuit and ground (or the rotor shaft via brushes), and basing the ´fault´ decision on an increase in the injection current to ground. Both AC and DC emfs can be used as injection sources, though the use of AC sources has the disadvantage that some current will always flow to earth via the capacitance of the field winding. This can lead to a possible erosion of the rotor bearing [83]. Figure 1.5 illustrates the two injection methods.

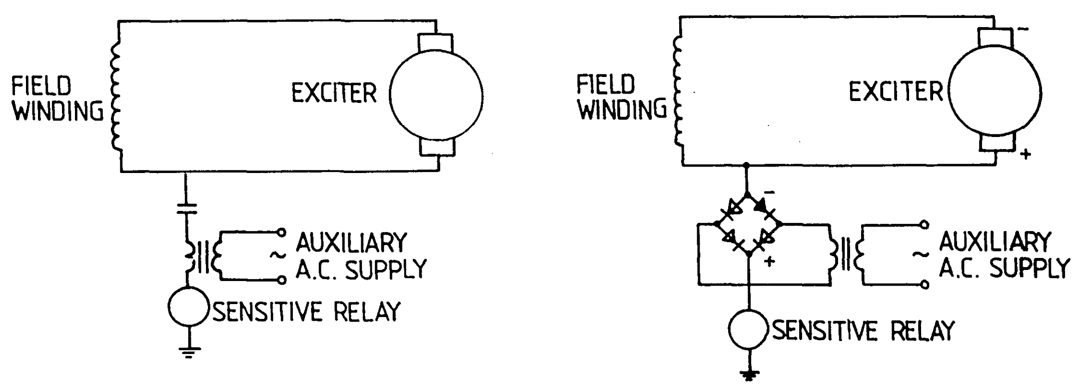

Figure 1.5: Rotor earth fault protection using (a) AC injection and (b) using DC injection.

A third method is the potentiometer method, in which a centre tapped resistor is connected across the field winding. An earth fault produces a voltage across a voltage sensitive relay connected at the centre tap, its maximum occurring for faults at the ends of the winding. This method has the disadvantage that a null point exists at the centre of the winding and therefore operator supervision is required. The null point is checked by changing the tapping point.

Rotor earth faults are classified as class 2 faults for the first earth fault, as it does not present an immediate hazard to the normally floating field circuit but, as for the stator, a second earth fault is extremely serious. For brushless generators monitoring earth leakage is not possible.

Inter-turn faults are detected by the measurement of an overcurrent in the exciter field (or pilot exciter field if the generator is a brushless design). This method, however, is inadequately sensitive based as it is on a secondary effect; and therefore some utilities do not bother installing rotor inter-turn protection, relying instead on the bearing vibration relay [87,88] to trip for serious rotor winding faults. This is unsatisfactory protection practice as then rotor winding faults will almost certainly only be detected once serious damage has ocurred.

Clearly rotor winding protection is one of the most inadequate areas within generator protection.

1.2.2 Abnormal Operating Conditions

The main abnormal operating conditions an alternator must be protected against are,

(i) unbalanced loading,

(ii) loss of synchronism,

(iii) and motoring.

None of these conditions, unlike heavy current winding faults, are immediately damaging to the alternator. The ability of large modern alternators to withstand sustained abnormal operation is, however, small due to their very high specific loadings - a matter of seconds rather than minutes - and prompt action is necessary to prevent the occurrence of damage. All these conditions are universally classed as class 2 faults.

1.2.2.1 Unbalanced Loading

Unbalanced loading of the alternator gives rise to negative-phase-sequence (n.p.s.) currents in the stator windings which, in turn, produce second harmonic eddy currents in the rotor. These can be quite large and cause the rotor to overheat severely, with a consequent softening of the rotor teeth. The n.p.s current rating for large alternators varies according to manufacturer, but is typically less than 10% [54,88] of the continuous positive-sequence (p.p.s.) rating. This very low rating is a consequence, as mentioned previously, of the very high specific loading obtained on large alternators by means of intensive cooling techniques.

Present practice is to detect this condition using a relay measuring the n.p.s. current at the neutral. Tripping action is arranged to be automatic on the n.p.s. rating of the generator being exceeded.

1.2.2.2 Generator Loss of Synchronism

Generator loss of synchronism can take two specific forms,

(i) asynchronous operation (field failure),

(ii) pole slipping.

Asynchronous operation takes place for a failure of the excitation. As a consequence the alternator will act as an induction generator, generating power at the load setting of the governor. This mode of operation is in itself not unstable, but as an alternator is not designed to run as an induction machine the following consequences are possible:

(i) Severe voltage depression due to the MVAR consumption.

(ii) Overheating of the damper cage.

(iii) Field overvoltage, if the field is on open circuit.

(iv) Overheating of the stator windings due to increased currents.

The methods of protection are:

(i) Measurement of abnormal power flow from the exciter to the field winding using DC underpower relays.

(ii) Offset mho relay based on the machine impedance in asynchronous mode as illustrated in figure 1.6. This is also known as a capacitance minimum reactance relay.

(iii) Detection of MVAR's absorbed by the system.

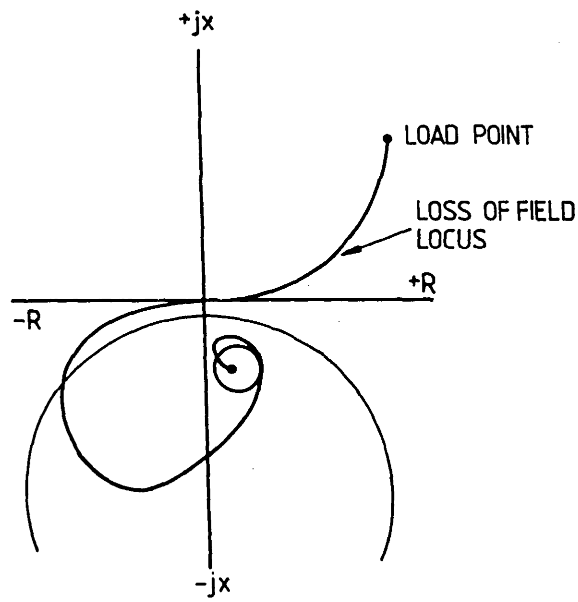

Figure 1.6: Field failure protection based on offset mho relay.

Protection (ii) is sometimes used in conjunction with a directional, undervoltage relay to detect the exceeding of the under excitation limit. Undercurrent relays in the field or exciter field circuits cannot be used, as large alternators may deliberately be run with very low excitation under certain conditions. A short time delay of a few seconds is sometimes incorporated prior to tripping to allow for possible self-correction of the excitation by the automatic voltage regulator (AVR) and control system.

Pole slipping is a condition distinct from asynchronous operation and occurs when faults or instability in the connected power system cause the alternator to lose synchronism or, if it is overloaded, when operating with a leading power factor. Unlike asynchronous operation, this is not a stable condition and the alternator is subject to violent torque and power oscillations. The consequences are:

(i) Disturbance to the external power system due to power oscillations.

(ii) Mechanical and thermal stressing of the stator windings.

(iii) Shaft fatigue due to torque pulsations.

Protection practice for this condition varies. Some utilities rely on the field failure protection to detect this condition as well, while others have seperate pole slipping protection. There are two reasons for this:

(i) Tripping arrangements may differ.

(ii) Field failure protection is not ideally suited to this application as the power swing impedance loci are not well defined.

If seperate protection is used, it is usually based on the crossing by the apparent generator impedance vector variation of two typical impedance loci in sequence. Practical examples are double ohm, circle, and lenticular characteristics amongst others. Figure 1.7 illustrates the use of the double ohm characteristic for pole slipping protection.

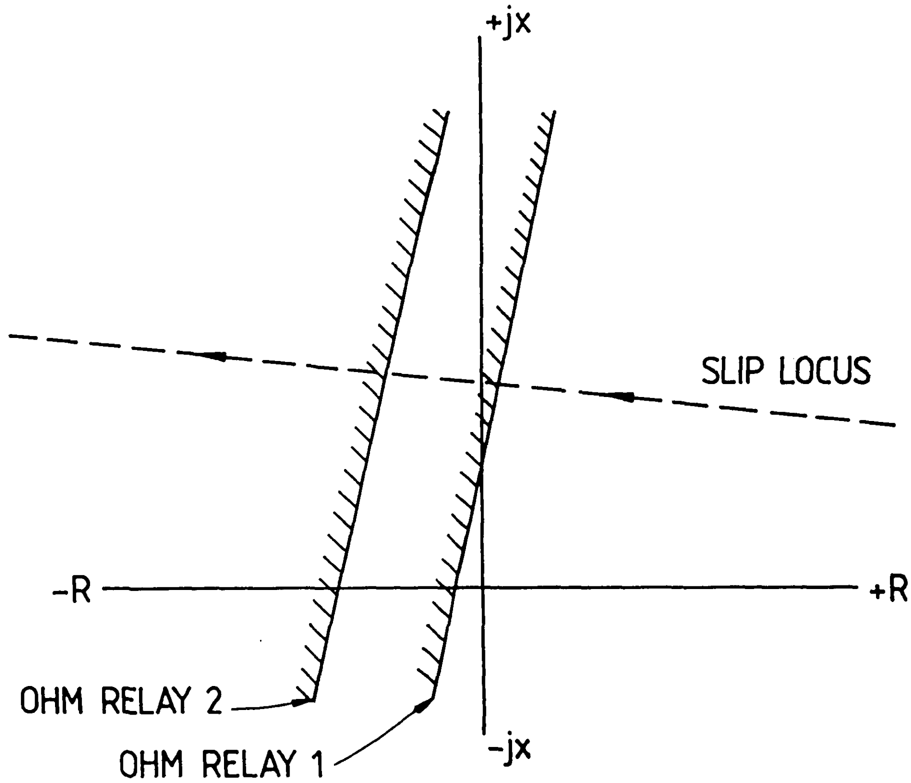

Figure 1.7: Pole slipping protection based on a double ohm characteristic.

Tripping policies vary, though all are class 2:

(i) Delayed tripping to allow for possible re-synchronisation.

(ii) Reduction of pole slipping condition to that of asynchronous operation to remove torque and power pulsations, and subsequent re-synchronisation at a low power setting.

(iii) Immediate trip.

1.2.2.3 Motoring

Short term motoring is a common occurrence, it will occur everytime the low power interlock relay delays the alternator trip. Sustained motoring, on the other hand, though not harmful to the alternator can cause serious problems to the turbine and must never be allowed to persist. Sustained motoring can occur for two possible reasons:

(i) Failure of the low power interlock relay to operate, though this is unlikely as it is usually duplicated.

(ii) Inadvertant closure of the high voltage (H.V.) circuit breaker (or generator isolating switch) while the alternator is at standstill. The alternator will then try to start as an induction machine.

The possible consequences are:

(i) After a turbine trip due to mechanical failure, sustained motoring may aggravate the turbine fault condition.

(ii) Sustained motoring, in any case, will cause overheating of the turbine blades.

(iii) Serious shaft damage could occur if the alternator tries to start as an induction motor.

Many utilities do not provide specific protection for this condition [54,85] as it is very unlikely. This approach does not compromise the safety of the generating set significantly as large generating stations are always manned. If automatic tripping is required, it can be provided by a wattmetric relay [88] similar in type to the low power interlock relay. Tripping policy differs from others in this section:

(i) An attempted start as an induction motor is always treated as a class 1 fault.

(ii) Sustained motoring after a turbine trip is, however, a class 2 fault.

1.2.3 Summary

A brief overview of generator protection has been presented. Figure 1.8 summarizes the protection requirements and tripping philosophy of a typical generator protection system.

The description has illustrated three areas within generator protection where present methods are inadequate. These are:

(i) Stator earth fault protection. Present methods do not provide a 100% coverage of the stator windings.

(ii) Inter-turn protection. Present methods lack sensitivity.

(iii) Rotor winding protection. Both rotor earth fault and inter-turn protection are inadequate with the latter especially so. For a brushless design, rotor earth fault protection is not possible and inter-turn protection very insensitive.

1.3 Present State of Research into Generator Protection

1.3.1 Digital Inter-phase Fault Protection

The earliest work on digital generator protection was reported by Sachdev and Wind [68] in 1973 into differential winding protection. Because of limitations in micro-computers available at the time, the approach chosen was a hybrid analogue-digital implementation. The operate and restraint signals were filtered and formulated by solid-state analogue hardware with the tripping criterion determined in software, and based on their instantaneous values. Though not very practical, the research was

Figure 1.8 : Protection requirements for a typical large turbo-alternator.

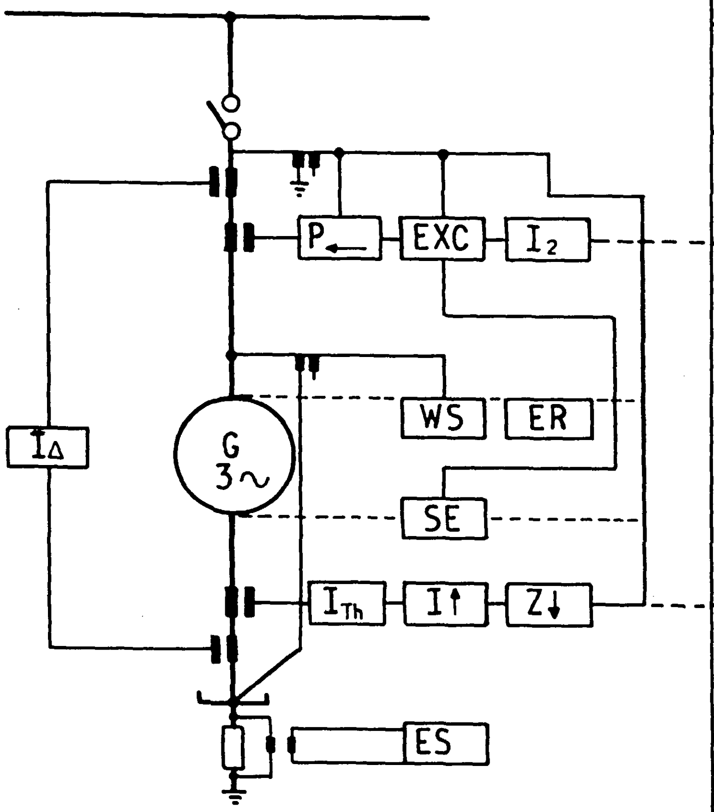

Symbol	Function	Short circuits	Interturn faults	Stator earth-faults	Self-excitation	Reverse power flow	Unbalance	Rotor earth-fault	Open circuit in excitation	Emergency trip (Class 1)	Circuit breaker (Class 2)	Tripping time in s
I↑	overcurrent-time protection	X								X	X	0,5-10
P←	reverse power protection Step 1 / Step 2					X X				X	X	1-2 / 5-15
IΔ	differential protection	X								X	X	0
ER	rotor earth-fault protection							X				1-5
ES	stator earth fault prot. (unit) 95%			X							X	0,1-0,5
WS	interturn fault protection		X								X	0,1-0,5
SE	self-excitation				X						X	0-0,5
I_2	asymmetry (negative sequence) Step 1 / Step 2						X X				X	1-5 / 5-15
Z↓	minimum ipedance protection	X								X	X	0,1-0,5
EXC	protection against loss of excitation								X		X	2-5

amongst the first to show that digital relays were feasible.

The first practical proposal was reported by Hope, et al. [33] in 1977. Basing their design on research into signal processing techniques adapted from communications for distance relaying [82], they formulated the line and neutral side currents as phasors using auto-correlation (section 2.1.2). This was a more robust and practical approach than the earlier work by Sachdev and Wind [68], and still forms the basis of most digital differential relays designs.

Dash, et al. [14] have also proposed a novel alternate method for detecting high current stator winding faults based on the measurement of the second harmonic induced in the field circuit as a result of stator winding asymmetry. This research, however, has limited application since:

(i) It offers little advantage over standard differential protection.

(ii) Sensitivity to inter-turn faults is no better than that of zero-sequence inter-turn protection.

(iii) Many modern large alternators are self-excited and the field circuit inaccessible.

More recently a new type of differential relay has been reported by McCleer and Mir [49] which they call "the delta differential relay". An increase in sensitivity, of an order of magnitude, and coverage over standard percentage differential relaying is achieved by the use of micro-computer cancellation of prefault through currents.

A number of other researchers [15,41,72-74] have also reported work on digital differential protection but with particular reference to its application for transformers. Most of the algorithms are in principle similar to that of Hope et al. [33] but with enhancements particular to transformer protection, e.g. inrush currents. Though not directly applicable to generator protection, particular mention must be made of work reported by Thorpe and Phadke [74] on a discrete fourier transform

(DFT) based algorithm (section 2.1.2). They were the first researchers to implement a real-time DFT based algorithm to characterise and discriminate the spectral nature of current transformer saturation and the inrush phenomena.

1.3.2 100% Stator Earth Fault Protection

In recent years, another area of generator protection which has received extensive attention is a 100% stator earth fault protection. All the methods presently being researched, are based on the common principle of enclosing the neutral end of the generator with a signal source, not necessarily at the fundamental frequency.

Fiorentzis and Pencinger [17] have reported a novel neutral injection method, using a signal at fundamental frequency but switched on and off at a quarter of that frequency. The spectral nature of this signal, despite its derivation from the mains supply, is such that it does not contain the fundamental or any of its harmonics. Consequently, it does not suffer from either of the two drawbacks usually associated with continuous sine wave injection systems. These are:

(i) If the injection signal is at the fundamental frequency, its amplitude must be greater than the maximum residual neutral fundamental frequency voltage expected under normal operating conditions. Consequently, a large and expensive injection transformer is needed.

(ii) On the other hand, if the injection signal frequency differs from the system frequency, usually subharmonic to minimize the influence of stray capacitive impedences, a relatively expensive signal generator is needed.

Pope [63] has reported on a novel subharmonic injection method, the injection signal consisting of a 2Hz periodic burst of three cycles of 15Hz square wave. As square waves are easy to generate, this scheme does not require an expensive signal generator. On the other hand, the very low period frequency of 2Hz dictates a slow operating speed.

Another approach to the same problem is to use the natural third harmonic voltage of the generator, produced as a result of the finite distribution of the rotor winding (appendix E), as it effectively encloses the neutral being a zero-sequence component. This approach has very significant advantages over injection schemes because,

(i) there is minimal disruption to the generator grounding scheme [80,84,88],

(ii) comparatively expensive signal generation and injection equipment is unnecessary.

Griffin and Pope [28,63] have reported on a number of such 100% stator earth fault protection schemes using conventional electromagnetic undervoltage and overvoltage relays. Figure 1.9 illustrates one of their schemes based on the neutral voltage. The lower 15% of the stator winding

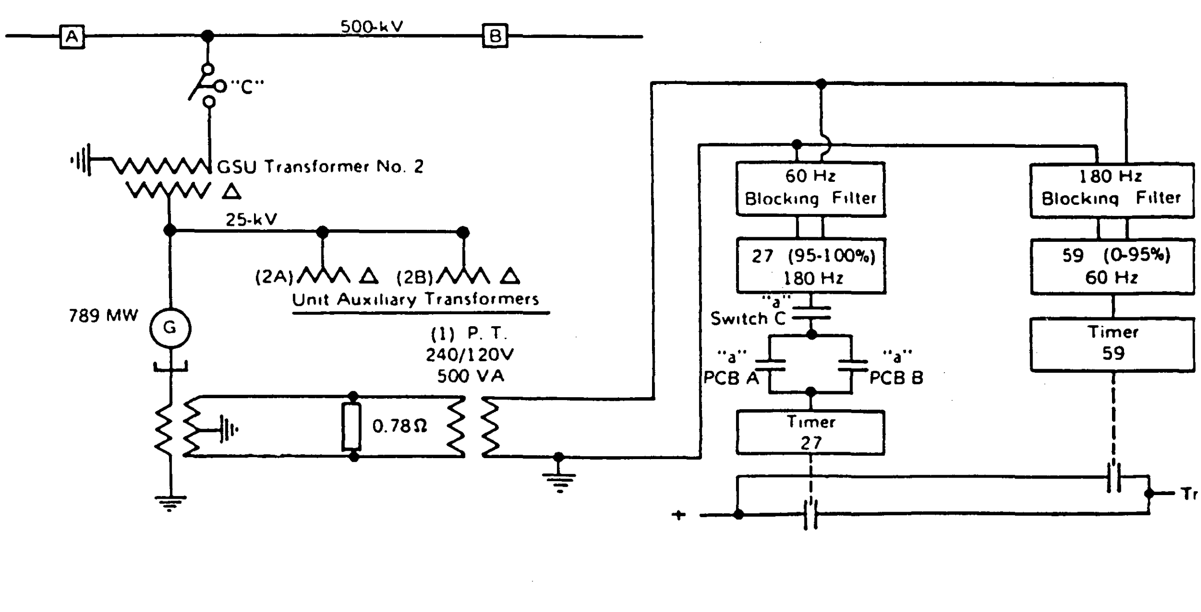

Figure 1.9: 100% stator earth fault protection based on the neutral emf.

near the neutral is covered by an undervoltage relay tuned to the third harmonic while the rest of the winding is protected by an overvoltage relay tuned to the fundamental

However, the technique has one very serious drawback. The third harmonic voltages at the neutral and terminals of a machine, though well defined, are not consistent between different generating sets, even if of the same type thus requiring the protection to be customized to the generator being protected. The following factors influence their magnitude:

(i) The stray capacitance to ground of the alternator and all associated electrical equipment connected to it.

(ii) The effective impedence of the neutral grounding method.

(iii) The frequency response of the neutral grounding transformer.

(iv) The effective impedance of any voltage transformer connections to ground at the terminals of the machine (section 3.1.1).

(v) The load setting.

Schlake et al. [71] have reported on a computer model to investigate the influence of some of these factors on the residual third harmonic neutral voltage, but conclude that such models are not sufficently accurate for relay calibration.

1.3.3 Inter-turn Protection

A number of researchers have reported work on inter-turn fault protection for machine windings. Most of the methods reported are essentially based on the principle of detecting the axial flux asymmetry of the airgap mmf (magneto-motive force) due to either rotor or stator inter-turn faults.

The earliest work was reported by Albright [2] in 1971. He proposed the installation of a small search coil in the periphery of the airgap to detect the rotor slot harmonics. For a normal rotor, the positive and negative half cycles of the induced voltage waveform due to the two halves of the rotor winding are exactly equivalent but for a rotor with an inter-turn fault they are not. However, the visual comparison he proposed was impractical.

Byars [8] in a later study proposed a more practical technique using analogue delay lines to generate a null signal by the subtraction of the positive and negative half cycles of the induced voltage waveform. This study highlighted some of the problems associated with such methods. These are:

(i) Small variations in the apparent rotor angular speed will cause an imperfect cancellation of the negative and positive half cycles of the induced voltage waveform.

(ii) Magnetic inhomegeneties (e.g. magnetic slot wedges) may give an erroneous comparison.

(iii) Installing the search coil may require an extended outage with the removal of the rotor.

Lodge, Mulhaus and Ward [45] have proposed an alternative method which is easier to apply. They report that for generators with parallel windings per stator phase, rotor inter-turn faults can be detected by measuring the second harmonic current circulating between the parallel windings which is induced by even space harmonics produced by the asymmetric rotor mmf [6]. Their scheme, as proposed, is not applicable to generators with single windings on each stator phase.

Penman and others [58-60] have proposed a stator inter-turn protection based on the measurement of the fundamental component of the induced voltage in an external coil wound axially on the main shaft of a machine to sense the axial flux. They report a dramatic increase in the fundamental component for stator inter-turn faults.

1.4 Objectives of the Research

In section 1.2.3 three areas of generator protection have been defined where present methods provide inadequate protection. These are stator earth fault, stator inter-turn and rotor winding fault protection. This research will be concentrated in the first area.

Mention has also been made in section 1.3.2 of work by Griffin and Pope [28,63] on 100% stator earth fault protection utilizing the natural third harmonic emf of the generator. These schemes have a number of drawbacks which are:

(i) Application requires extensive prior measurement of third harmonic voltage components at the neutral and terminals of the machine. In effect, the protection has to be customized to the generator.

(ii) They are not inherently stable to other generator faults or external power system disturbances.

(iii) Consequently, to prevent maloperation the speed of response is slow, typically one second.

(iv) They are sensitive to power variations and this must be taken into account. If the third harmonic variation with power is very wide, it may be necessary to suppress the protection at low governor settings, thereby compromising the safety of the machine.

(v) The discrimination of the third harmonic voltage with conventional tuned relays is poor.

This research investigates a new type of digital 100% stator earth fault protection which does not suffer from the above drawbacks, concentrating in particular on:

(i) The possibility of using harmonic information in addition to the third harmonic to give a robust characterisation of the fault condition.

(ii) The influence of the generator system parameters on the harmonic content of the generator voltages and currents.

(iii) The use of digital real-time spectral estimation methods in obtaining a very accurate discrimination of the harmonic content of the protection measurands.

A subsidiary objective of the research is the development of a stator earth fault location algorithm to complement the 100% stator earth fault protection. There is a very real need [93,94] for an earth fault location process because of the practical difficulty of locating such faults, which is a manifestation of the very low fault current levels associated with this fault condition. Because of the low fault current level, very little visual evidence is usually present.

1.5 Organization of the Thesis

Chapter two reviews previous research into digital signal processing methods for power system protection, and assesses the use of discrete fourier transform spectral estimation methods for the harmonic analysis of the generator voltages and currents. Its performance, limitations and error correction methods are evaluated and discussed. Its choice over other spectral estimation methods is also assessed. A brief theoretical background to the DFT is given in appendix A and details of the correction methods in appendices B and C.

Chapter three describes the design and implementation of a micro-machine based model of a typical large alternator system, and a mini-computer based spectral analysis and data aquisition system. The experimental system is used to study the nature of the harmonic content of the neutral and terminal emfs of the alternator model for various stator winding faults. Details of the micro-machine and its modifications are in appendix D.

Chapter four describes the computer simulation of the harmonic content of the neutral and terminal emfs of the laboratory generator for stator earth faults. Calculated and experimental results, obtained from the spectral analysis system, are compared and the significance of the alternator system parameters on the spectral content of the generator neutral and terminal voltages assessed. The chapter concludes with an assessment of the harmonics most suitable for use as protection measurands for 100% stator earth fault protection.

A brief theoretical background to the presence of harmonic distortion in a machine is given in appendix E, and appendix F illustrates the calculation of the micro-machine reactances needed for the simulation program. Appendix G describes a proposal for a general computer simulation applicable to all types of stator winding faults.

In chapter five the design and test of two digital algorithms for 100% stator earth fault protection, based on the theoretical and experimental study of chapter four, is illustrated. DFT spectral estimation methods, examined in chapter two, are used to filter the harmonic measurands. A detailed evaluation, using off-line simulations on the mini-computer, of the performance and protection stability of both algorithms is presented.

Chapter six evaluates the performance and design of a fault location algorithm for stator earth faults to complement the protection algorithms. The thesis concludes with a review of the research, contributions and recommendations for future work in chapter seven.

CHAPTER TWO

DFT Spectral Estimation for Protection

Research into digital signal processing techniques applied to protective relaying has almost exclusively been devoted to the improved discrimination of the fundamental component from the power system measurands. The processing requirements for spectral analysis are very different - the vector response of a number of frequency components need to be estimated at the same instant instead of just the fundamental component. The previous work needs to be reconsidered in this new context.

This chapter reviews previous research into digital signal processing methods and assesses the use of discrete fourier transform (DFT) methods for spectral estimation. Performance, limitations, and correction methods and corrections are evaluated and discussed. Its choice over other spectral estimation methods is also assessed.

2.1 Review of Digital Filtering Methods for Protection

From a modern perspective, previous research into digital filters for power systems can be classified into two broad types [4,9,64]. They are:

(i) Infinite impulse response (IIR) filters. The response of this class of filters depends not only on the filter transfer function but on the past response as well, e.g.

$$y_n = \sum_{i=0}^{N} a_i x_{n-i} - \sum_{i=1}^{N} b_i y_{n-i} \tag{2.1}$$

where a_i, b_i : filter coefficients.
y_n : discrete output sequence.
x_n : discrete input sequence.
N : order of filter.

(ii) Finite impulse response (FIR) filters. The response of this type of filter depends only on the transfer function.

$$y_n = \sum_{i=0}^{N} a_i x_{n-i} \tag{2.2}$$

Note that these two categories of filters are also referred to as ´recursive´ and ´nonrecursive´ respectively because of their time domain structures.

The main differences between the two classes of filters are:

(i) FIR filters have a constant group delay and linear phase response.

(ii) FIR are inherently stable as there is no feedback of the input.

(iii) Because of this nonrecursive structure in FIR filters, computational round-off errors can be minimized.

(iv) IIR filters, on the other hand, can achieve a higher selectivity for a given order of filter.

(v) They can be used to realize digital equivalents for conventional analogue filters, though this is not necessarily their only use.

From a protection point of view the linear phase and constant group delay properties of FIR filters are extremely important, and is in fact one of the strengths of a digital solution in protection as this class of filters is not easily realizable in analogue form. Previously researchers were always limited by the need to balance any increase in selectivity to a deterioration in step response and resultant increase in operating time. Consequently the bulk of the research has been concentrated in this class of filters, though some IIR designs have also been applied.

Sykes and Morrison [72] proposed the use of second order IIR band-pass filters in a percentage differential current protection for transformers. Filters given by equation 2.3a and b were used to filter the fundamental and second harmonic, for the harmonic restraint function, respectively.

$$y_n = 0.096x_n - 0.096x_{n-1} + 1.81y_{n-1} - 0.905y_{n-2} \tag{2.3a}$$

$$yn = 0.045x_n - 0.045x_{n-1} + 1.580y_{n-1} - 0.953y_{n-2} \tag{2.3b}$$

More recently, Girgis [22-24] has reported work on the application of optimal Kalman filters [19]. This is not, however, a deterministic IIR technique and not within the scope of this research.

Research into FIR filter realizations has been concentrated in the following areas:

(i) Numerical analysis methods.

(ii) Fourier methods.

(iii) Least squares fitting of a discrete measurand to an assumed signal model.

These methods will now be discussed in turn.

2.1.1 Numerical Analysis Methods

Mann and Morrison [47] first reported the use of FIR filters based on numerical analysis methods. Their technique was based on the principle that the peak value of a sinusoid can be predicted at any point on the waveform from its discrete value at that instant and its derivative. To calculate the derivative, use was made of the Sterling Central Difference formula [4]:

$$x_n' = 1/T_s[\mu\delta - \delta^2/6 + \delta^3/30 - \ldots]\ x_n \tag{2.4}$$

where μ : averaging function.

δ : central difference function.

T_s : discrete time interval between samples.

A very simple approximation is obtained by neglecting all but the first term to give

$$x_{n-1}' = -1/2T_s\ (x_{n-2} - x_n) \tag{2.5}$$

The authors, however, did not appear to fully appreciate the frequency response aspects of their algorithm, choosing a high sampling rate with no prefiltering in an attempt to minimize numerical errors and increase speed. Ranjbar [66], in a later study demonstrated the frequency response of the Mann-Morrison algorithm to be a function of the sampling frequency as shown in figure 2.1, the optimum sampling rate being 4 s/c (samples per cycle of fundamental).

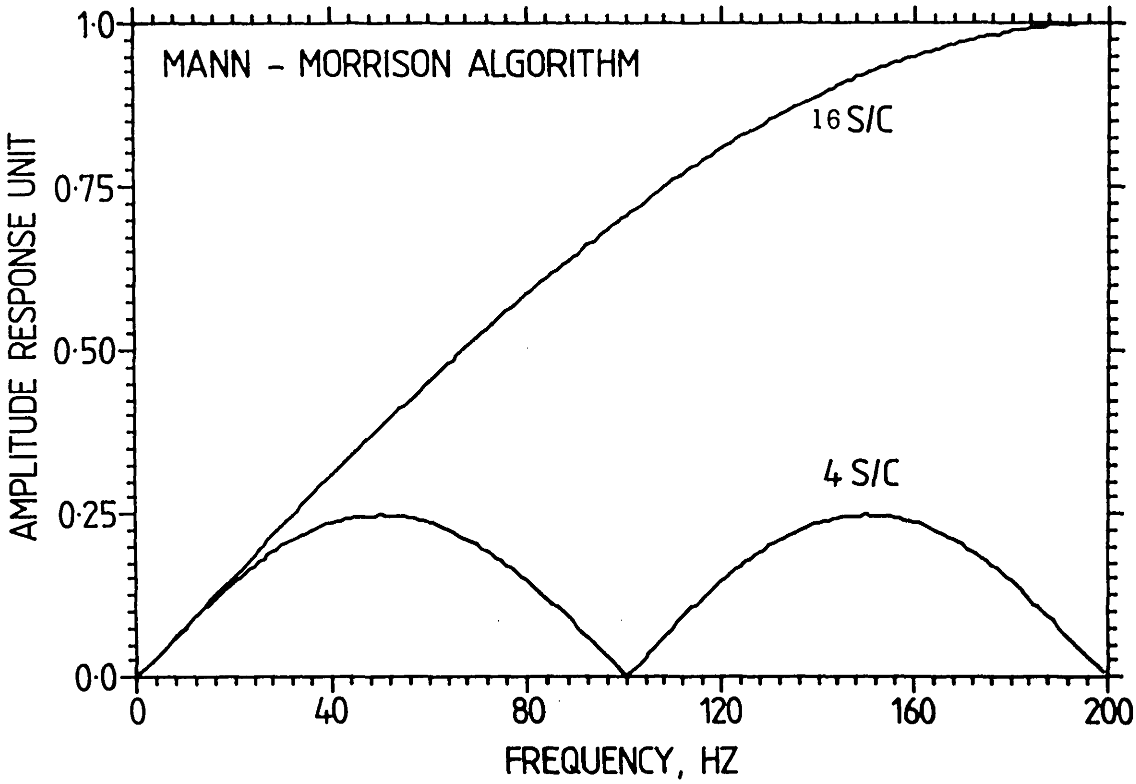

Figure 2.1: Frequency response of the Mann-Morrison algorithm.

Clearly, the design is a compromise between two conflicting criteria:

(i) A high sampling rate is essential in minimizing numerical errors.

(ii) However, a high sampling rate will also accentuate the high frequency response of the algorithm.

Because of this the algorithm, as proposed, lacked robustness. Its main disadvantages are:

(i) Very poor noise rejection.

(ii) Unpredictable response when the data window includes the fault instant, henceforth called ´the fault transition period´.

The main advantages are a very short group delay, three samples only, and simplicity.

Gilcrest, Rockefeller and Udren [21] attempted to improve the Mann-Morrison algorithm by including a second term in the Sterling formula for the derivative, and additional numerical integration procedures to control the poor noise rejection. However, Ranjbar [66] later demonstrated that the primary effect of including additional terms in the Sterling formula, despite decreasing numerical errors and improving the low frequency response, was to cause a further deterioration in the high frequency noise rejection response of the filter.

Phadke, Hilbka and Ibrahim [62], recognising the deficiencies of Mann-Morrison type algorithms, proposed prefiltering the discrete measurand using least squares polynomial filters to remove high frequency noise at source. Applied with a high sampling rate and narrow window the algorithm demonstrated a marked improvement in performance. A number of other researchers have also reported the use of sample and derivative filter algorithms for various relaying applications. The reader is referred to reference [82] for specific application.

A second approach to the use of numerical analysis methods in FIR filter design is to solve the power system differential equations [66,82]. These filters can achieve a very good performance as they inherently account for low frequency transients but have a restricted application to transmission line impedence measurement. A similar approach for generator winding protection is not realizable because of the mathematical complexity of the solution (appendix G).

2.1.2 Fourier Methods

Since Ramamoorty [65] first suggested in 1968 the use of fourier based FIR filtering for protective relaying, it has developed into a widely used and robust technique. The mathematical basis of the method is the continuous fourier transform (CFT) [47] given by the expression

$$X(\omega) = \int_{-\infty}^{\infty} x(t)\, e^{-j\omega t}\, dt \tag{2.6a}$$

$$= X(\omega)\, e^{\,j\phi(\omega)} \tag{2.6b}$$

where $X(\omega) = |X(\omega)|$

$\phi(\omega) = \arg X(\omega)$

and $x(t)$: any continuous time signal.

The CFT is a mathematical transformation from the time to the frequency domain, and if this can be accomplished practically then the desired frequency components - usually just the fundamental - are immediately available as vectors. Note that the CFT is also known simply as the 'fourier transform' in many texts.

The discrete equivalent of the CFT is the discrete fourier tranform (DFT) given by the expression,

$$\mathbf{X}_p(k\Omega) = \sum_{n=0}^{N-1} x_p(nT_s)\, e^{-j2\pi nk/N} \qquad k = 0,1, \ldots, N-1 \tag{2.7a}$$

$$= X(k\Omega)\, e^{j\phi(k\Omega)} \tag{2.7b}$$

where $X_p(k\Omega) = |\mathbf{X}_p(k\Omega)|$

$\phi(k\Omega) = \arg \mathbf{X}_p(k\Omega)$

$x_p(nT_s)$: periodic band-limited discrete time sequence.

$\Omega = \omega_s/N$: discrete frequency interval.

$\omega_s = 1/T_s$: sampling frequency.

N : window length.

n : discrete time operator.

k : discrete frequency operator.

p : periodic descriptor.

The mistake often made is to treat the DFT as the exact discrete equivalent of the CFT which it most certainly is not. The discretization process fundamentally modifies the behaviour of the fourier transform as is shown in appendix A. While the CFT is applicable to all signals, the DFT is specifically defined for periodic signals only.

For periodic waveforms, the discrete frequency amplitude spectral components given by the DFT are but for a scaling factor, equal to the fourier series coefficients, A_k (equation A.5). The relationship is given by the expression,

$$A_k = X_p(k\Omega)/N \qquad k = 0, 1, \ldots, N-1 \qquad (2.8)$$

and this defines the fourier filter.

The frequency response for k=1 and a sampling rate of 32 s/c, which for power system protection applications gives a 'band-pass' filter centred at 50Hz, is illustrated in figure 2.2. Consistent with the definition of the DFT, the frequency response indicates a perfect rejection of all periodic harmonic components upto the foldover frequency (section A.2), but not of nonharmonic frequency components.

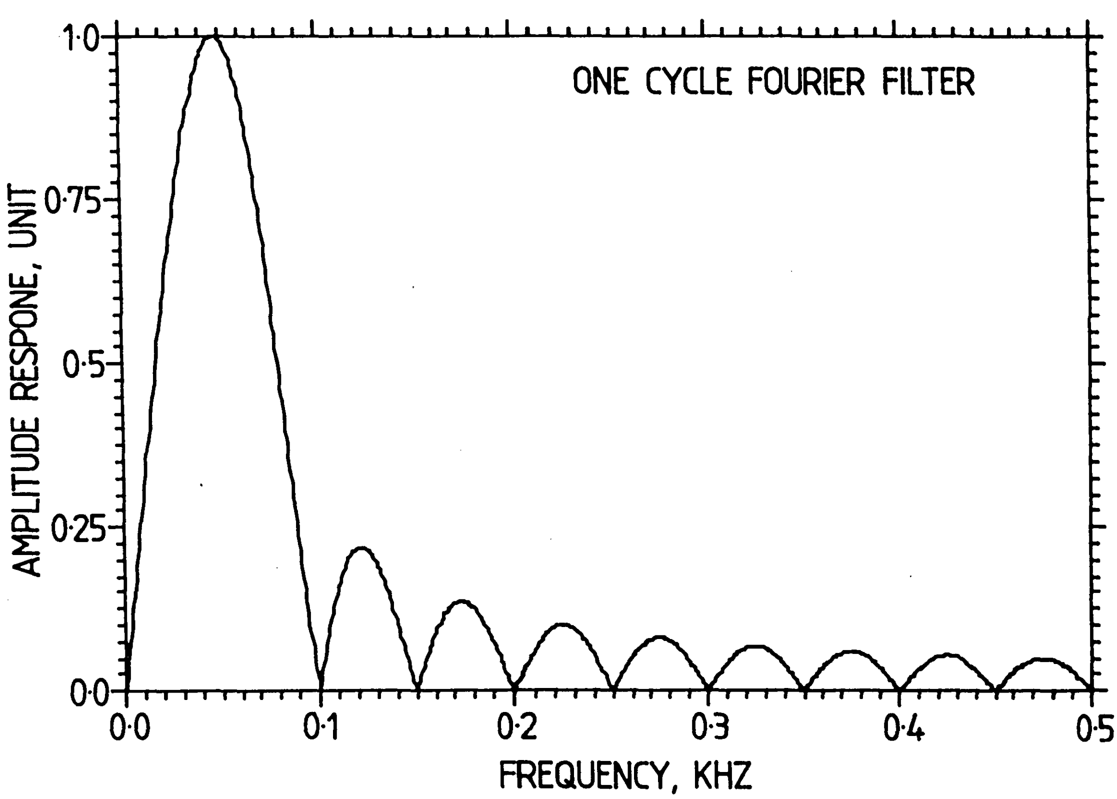

Figure 2.2: Frequency response of the one cycle 50Hz fourier filter

Before proceeding further, the nomenclature associated with fourier methods will be clarified. Fourier filters have been described as orthogonal notch filters, sine-cosine correlators, fourier series filters and DFT filters. All these terms essentially refer to the same process of filtering via a discrete frequency transformation based on the DFT. Consequently, they could be used interchangeably to describe the fourier filter in general. In this thesis, the names ´fourier filter´ and ´DFT filter´ will be used.

Carr and Jackson [10] were the first researchers to report a quantitative analysis of the one cycle fourier filter (i.e., N and $_s$ are chosen to enclose one cycle of the waveform). Using recorded data and an effective sampling rate of 4 s/c, they reported a very well damped response with high noise rejection.

Soon afterwards Maclaren and Redfern [50] also evaluated the fourier filter using an off-line computer program and simulated data, and a high sampling rate of 128 s/c. Though the simulated data used was unrealistic in that it contained constant amplitude postfault noise signals, useful insight was obtained into the noise rejection properties of the filter. However, derivation of the filter characteristics in ref. [50] appear to have been carried out without a rigorous study of the effects of discretization on the CFT.

Hope and Umamaheswaran [34] proposed a simplified alternative to the one cycle fourier filter, replacing the sine-cosine orthogonal functions with even and odd square waves. Later investigations by Ranjbar [66] showed it to be less robust than the fourier filter with a poorer rejection of noise and subharmonic transients.

A novel variation to the one cycle fourier filter using Walsh functions - a pair of odd and even square waves plus a set of harmonically related square waves whose transitions occur according to a binary counting sequence - was reported by Horton [36]. This approach was an attempt to amalgamate the computational simplicity of square wave correlation and the robustness of fourier methods. Promising results were obtained though not quite as good as for the fourier filter.

One of the drawbacks to the use of fourier filters is their comparatively large group delay of one cycle of fundamental, defined by the window length N, compared to sample and derivative algorithms. Phadke et al. [62] first proposed the use of the half cycle fourier filter which is given by the expression,

$$X_H(k\Omega) = 2/N \sum_{n=0}^{N/2-1} x_p(nT_s)\, e^{-j2\pi nk/N} \qquad k=1,3,\ldots,N-1 \tag{2.9}$$

where $x_p(nT_s)$ is periodic over the range 0 - (N-1).

Note that equation 2.9 is only defined for odd harmonics compromising the integrity of the fourier filter particularly at the fault instant. The half cycle fourier filter was found to have the following deficiencies compared to the one cycle filter:

(i) Accentuated response to subharmonics.

(ii) Degraded rejection of nonharmonic noise.

(iii) The response at the fault instant is less stable.

(iv) Very poor response in the presence of even harmonics.

The frequency response is shown plotted in figure 2.3 and reflects these deficiencies.

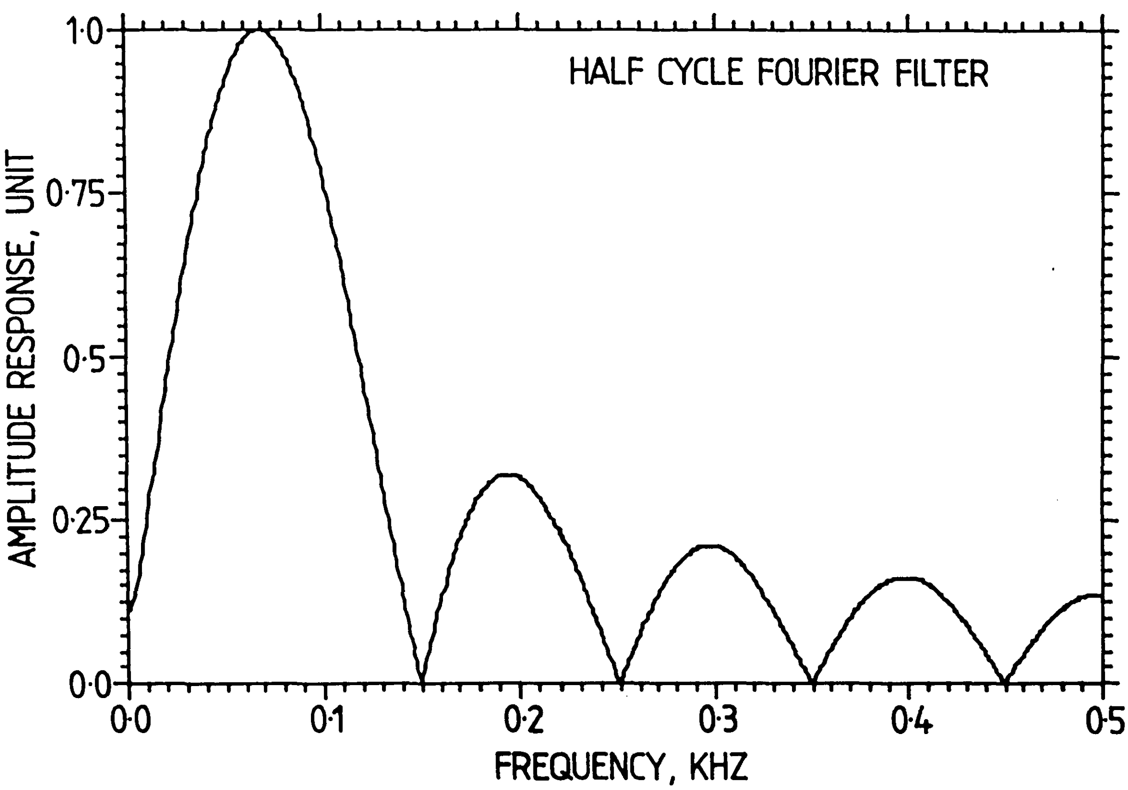

Figure 2.3: Frequency response of the half cycle 50Hz fourier filter.

Thorpe et al. [75] in a very complete study concluded that the performance of the half cycle fourier filter was within acceptable limits for impedance relaying provided a mimic circuit was used to compensate for its accentuated low frequency response.

Fakhro [16] approached the problem from the different viewpoint of waveform prediction of a complete periodic cycle of data from half and quarter cycles of data. He showed that from half a cycle of data, a full cycle of a periodic sequence can be formed by either repetition or replication as illustrated in figure 2.4. Negative repetition was shown to be exactly equivalent to the half cycle fourier filter as proposed by Phadke et al. [62] and was chosen as the only viable predictive method for practical application (figure 2.4a,b).

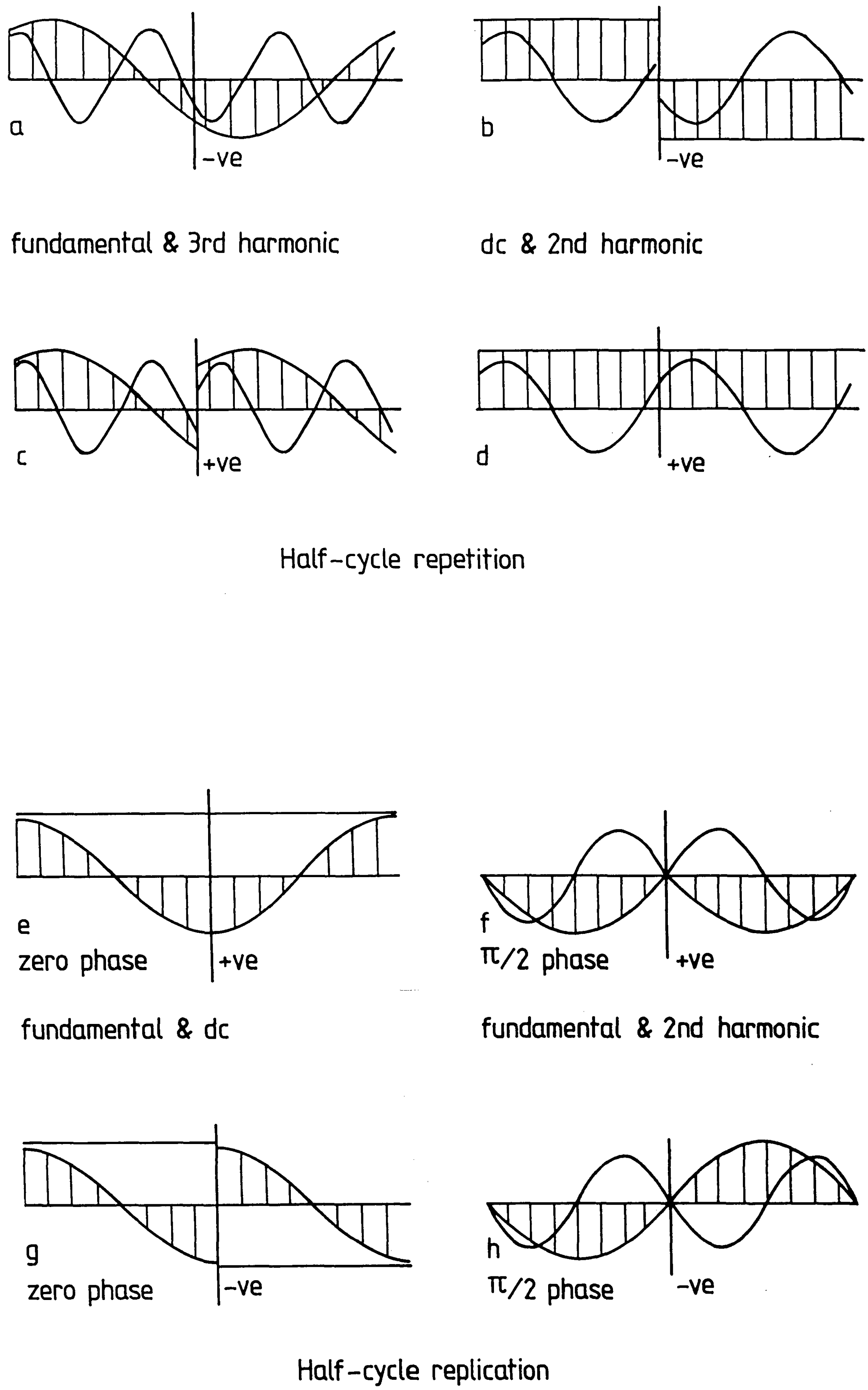

Figure 2.4: Waveform prediction methods.

Positive repetition was also found to be unsuitable as it only predicts even harmonics correctly (figure 2.4c,d) while replication requires synchronised sampling (figures 2.4e-h). Synchronised sampling was also found to be essential for quarter cycle methods making these unsuitable as well.

Wiszniewski [76] adopted a radically different approach to the problem of the accentuated low frequency response of the half cycle fourier filter. He proposed that the sine-cosine functions in the correlation process of the DFT be chosen to have time periods equal to the window length rather than the time period of the fundamental. The resultant expression for this DFT is

$$X_H(2k\Omega) = 2/N \sum_{n=0}^{N/2-1} x_p(nT_s)\, e^{-j2\pi n.2k/N} \quad k = 0,1,2,\ldots,N/2-1 \qquad (2.10)$$

where $x_p(nT_s)$ is periodic in the range 0 - (N-1).

Equation 2.10 illustrates a fourier filter centred, for k=1, not at the fundamental but at the second harmonic. Therefore, effectively, the proposal is to use the output of such a filter due to 'spill over' from the fundamental, as a measure of the fundamental itself. A greater rejection of low frequency transients was reported, but only at the expense of an increased ripple component.

Johns and Martin [38,39] have reported on a novel analogue transversal filter implementation of the fourier filter using a high sampling rate of 4kHz and a half cycle data window. They report that this approach gives superior results compared to other types of half cycle fourier filters because a closer approximation to the CFT is achieved.

A large number of applications of fourier filters have been reported. Some of these have already been mentioned in connection with digital generator protection [14,33] and differential protection [15,41,49,73,74]. Application has been particularly intensive in the field of distance relaying [10,16,34,38,50,66,75,76]. The reader is especially referred to ref. [82] for a complete bibliography. Recently, fourier filters have also been applied for the measurement of frequency and rate of change of frequency [22,61].

2.1.3 Least Squares Signal Modelling

Despite their general robustness, the main deficiency of fourier filters is in their low frequency response. One approach, in realizing filters with a better low frequency rejection, is to use a least squares minimization procedure for the identification of a signal containing low frequency transients as well as periodic components. In this context the one cycle fourier filter itself can be shown [64] to be a least squares minimization to a periodic signal with harmonically related sinusoids. This approach was first proposed by Luckett et al. [46] in 1978 but Sachdev and Baribeau [69] presented a more complete study later. Their assumed signal model consisted only of a subharmonic transient, the fundamental, and the third harmonic; but the method was shown to be general and easily extendable to other harmonics. The method of solution, based on the solution of a set of simultaneous linear equations, is very similar to the unified matrix DFT solution [64].

2.2 Methods for Spectral Analysis

In a physical sense, digital spectral estimation can be imagined to be a parallel filtering process at various frequencies selected using a prior knowledge of the signal, or some identification procedure. Despite this it would be simplistic to assume that the spectral estimation process is based on this physical model, and much of the previous work into digital filtering for power system protection and control is not directly applicable. However, some of the existing techniques, principally the one cycle fourier filter and the Sachdev and Baribeau [69] least squares fit algorithm, borrow heavily from spectral estimation concepts.

The unifying concept in relating the various spectral estimation methods is to view the process as one of matching a discrete input process to an assumed or identified signal model. The classical method is DFT spectral estimation based on a model of harmonically related sinusoids. The one cycle fourier filter is in fact a single frequency DFT spectral estimator, i.e. all calculations pertaining to frequencies other than the fundamental are discarded as redundant. The Sachdev and Baribeau [69] least squares fit algorithm bears a strong resemblance to the matrix representation of the DFT [64], the only difference being the inclusion of subharmonic transient terms in the DFT coefficient matrix. A number of newer methods assume different signal models. These are:

(i) Auto-regression moving average (ARMA) spectral [9,48] estimation. This is actually a class of methods based on a model that assumes the output sequence to be a linear regression on itself plus a weighted average of past inputs, as given by the expression

$$x_n = \sum_{i=0}^{q} b_i y_{n-1} - \sum_{m=1}^{p} a_m x_{n-m} \qquad (2.11)$$

where b_i : auto-regression weighting coefficients.
a_m : moving-average weighting coefficients.

(ii) Pisarenko Harmonic Decomposition (PHD) [9,48] based on a model of nonharmonically related undamped sinusoids on white noise.

(iii) Prony´s method [48], a spectral estimation procedure which asssumes a model of nonharmonically related damped exponentials.

(iv) Prony´s spectral line decomposition [48] based on a model of nonharmonically related sinusoids.

The newer spectral estimation procedures have been developed in an attempt to overcome the two main drawbacks of DFT spectral estimation; a course frequency resolution for short data lengths, and truncation errors. These drawbacks will be discussed in section 2.3. However, there is no arbitrary figure of merit between the various methods. Marple and Kay [48] in a comparative study of the various methods, have highlighted the main criteria in the selection process. Their main conclusions are:

(i) The most accurate spectral estimate for a discrete waveform is given by the procedure which is based on the signal model which most closely approximates to the waveform. However, if the waveform consists of more than one process, for example sinusoids and broad-band processes together, then the choice must be a compromise. Alternatively, more than one method must be used to build the spectral estimate.

(ii) The intrinsically most accurate method may not be the most computationally efficient procedure in achieving a set specification. At one extreme, the DFT method is the most efficient of all, especially if fast fourier transforms (FFT) algorithms (see section 3.2.1) are used. At the other, PHD spectral estimation is complex and unsuited to real-time application. The newer methods are partly more complex because, compared to the DFT, additional identification procedures are needed. For example, in Prony spectral line decomposition a polynomial rooting must be formed and solved to identify the position of the spectral components prior to their actual estimation. In the classical DFT approach, the position of the spectral components is assumed fixed and set by selecting the DFT window length as will be illustrated in section 2.3.1.

In general, protective relaying measurands can be expected to approximate to either of two signal models:

(i) Harmonically related sinusoids during steady-state power system conditions.

(ii) In addition to (i) low frequency nonharmonically related sinusoids during the power system fault instant.

The ideal spectral estimation methods would appear to be PHD or Prony spectral line decomposition, as the signal models they are based upon will be accurate for either of the expected conditions in contrast to the DFT model. However, the spectral estimation method chosen is the classical DFT method, for the following reasons:

(i) The spectral estimation specification (section 3.1.2) can almost entirely be achieved using DFT spectral estimation in conjunction with additional auxiliary correction procedures (section 2.3.3).

(ii) The DFT approach is the most computationally efficient.

(iii) PHD and Prony spectral estimation do not provide, in their present form, any phase information.

(iv) PHD spectral estimation is computationally complex.

(v) Being a recent method, very little error analysis exists for Prony spectral line decomposition.

2.3 DFT Spectral Estimation

It is often a source of considerable confusion that the DFT is a result of two distinct sampling processes. The first process is the well known discretization of the continuous time signal governed by the time domain sampling theorem. This states that if the spectrum of a function, x(t), is zero for all frequencies greater than a certain frequency (this is called the foldover or Nyquist frequency), then x(t) can be uniquely determined from its sampling values, sampled at twice that frequency.

However, the spectrum of a discrete time signal is not necessarily itself discrete. The process of discretization merely periodically extends the spectrum (section A.2). Consequently the second discretization process is the decimation of the frequency spectrum. Equivalently, it is made possible by the frequency domain sampling theorem which states that; if a function is time-limited (i.e., $x(t)=0$) after a certain time, then its continuous fourier transform, $X(\omega)$ can be uniquely determined from equidistant samples of $X(\omega)$. Effectively, this implies that the waveform must be band-limited and periodic. These concepts are examined in detail in appendix A.

In practice, the frequency domain sampling theorem can only be guaranteed for steady-state power system conditions. For postfault conditions, the power system voltage and current waveforms may contain aperiodic components and it is violated. There are two reasons for this:

(i) The need to deal with finite data sequences causes truncation errors.

(ii) The spectrum (the CFT) of the postfault transient waveform will be continuous and therefore the DFT spectral estimates will not uniquely determine the spectrum.

The nature of these errors is mathematically examined in appendix A, but a more useful perception can be had by using the concept, introduced in section 2.2, of the DFT being a parallel band-pass filtering process as shown in figure 2.5. The actual frequency response of each filter is as illustrated in figure 2.2.

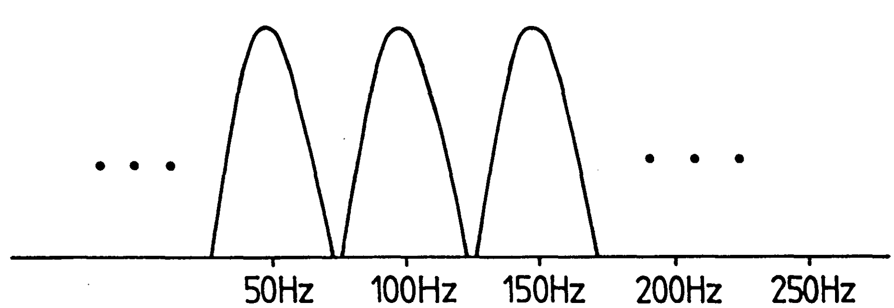

Figure 2.5: The DFT as a parallel band-pass filtering process.

The errors associated with the DFT can now be explained in an alternate fashion:

(i) Assuming the time sampling theorem holds, for a discrete process with periodic harmonically related components, the spectral components will be exactly resolved by the band-pass filters and the correct spectral estimate obtained.

(ii) On the other hand, for transient signals, additional nonharmonic spectral components will fall between the band-pass filters. The spectral energy of these spurious components will leak - hence the terms ´leakage errors´ and ´spillover´ - across the spectrum because of the overlapping side lobe responses of the band-pass filters (figure 2.2), causing a degradation in the spectral estimate.

In the following sections both the mathematical and band-pass filter representations of the DFT will be used interchangeably to gain insight into the accuracy of the DFT spectral estimate under various conditions.

2.3.1 Synchronised Sampling

The choice of optimum sampling rate and anti-aliasing filter is dependent on the specific application and accuracy required and will be discussed later in section 3.3. However, at this stage consideration must be given as to whether the sampling process should be synchronised to the fundamental power system frequency or not.

The DFT in the classical sense of requiring a zero crossing to initiate measurement [82], does not require synchronised sampling, but it can benefit from it in terms of accuracy under certain conditions. The nature of the errors is best visualized by considering the band-pass filter bank model of the DFT. The centre frequencies of the filters in the filter bank are fixed by the sampling process nominally at the fundamental and its harmonics upto the foldover frequency. If the power system waveform consists of periodic spectral components at exact multiplies of the fundamental frequency, then the filters will exactly discriminate them and the spectral estimate will be accurate. If, however, there is a relative frequency deviation between the sampling and power system frequencies, then the spectral components will fall to either side of the filters and will not be fully discriminated.

The practical effects on accuracy of this frequency mismatch between the sampling rate and the fundamental frequency of the measured waveform are:

(i) Errors in the amplitude spectral estimates caused by spectral energy leaking between the DFT filters. They are commonly referred to as leakage errors.

(ii) Ripple error components in the amplitude spectral estimates from a scanning DFT. This term refers to the derivation of the vector variation of the spectral estimates of a waveform with time, by the successive calculation of its DFT at every sample as the data window is swept across the waveform. Figures 2.6a and b illustrate the magnitudes of errors (i) and (ii) respectively in the 50Hz estimate of a 32 point DFT with a spectral resolution of 50Hz for a frequency variation of 4Hz in a nominally 50Hz pure tone of amplitude 1.0 unit.

(iii) Deterioration of dynamic range due to spectral energy leakage across the DFT filters. With reference to the frequency response of the fourier filter (figure 2.2), it can be seen that the spectral energy leakage that occurs is not just between the two filters enclosing the mismatched spectral component but across all the filters; the spillover being greatest at the filters closest to the mismatched component. This has the effect of increasing the noise and reducing dynamic range of the spectral estimates. Figure 2.6c illustrates the reduction in dynamic range of the spectral estimate for the same conditions as in (i) and (ii).

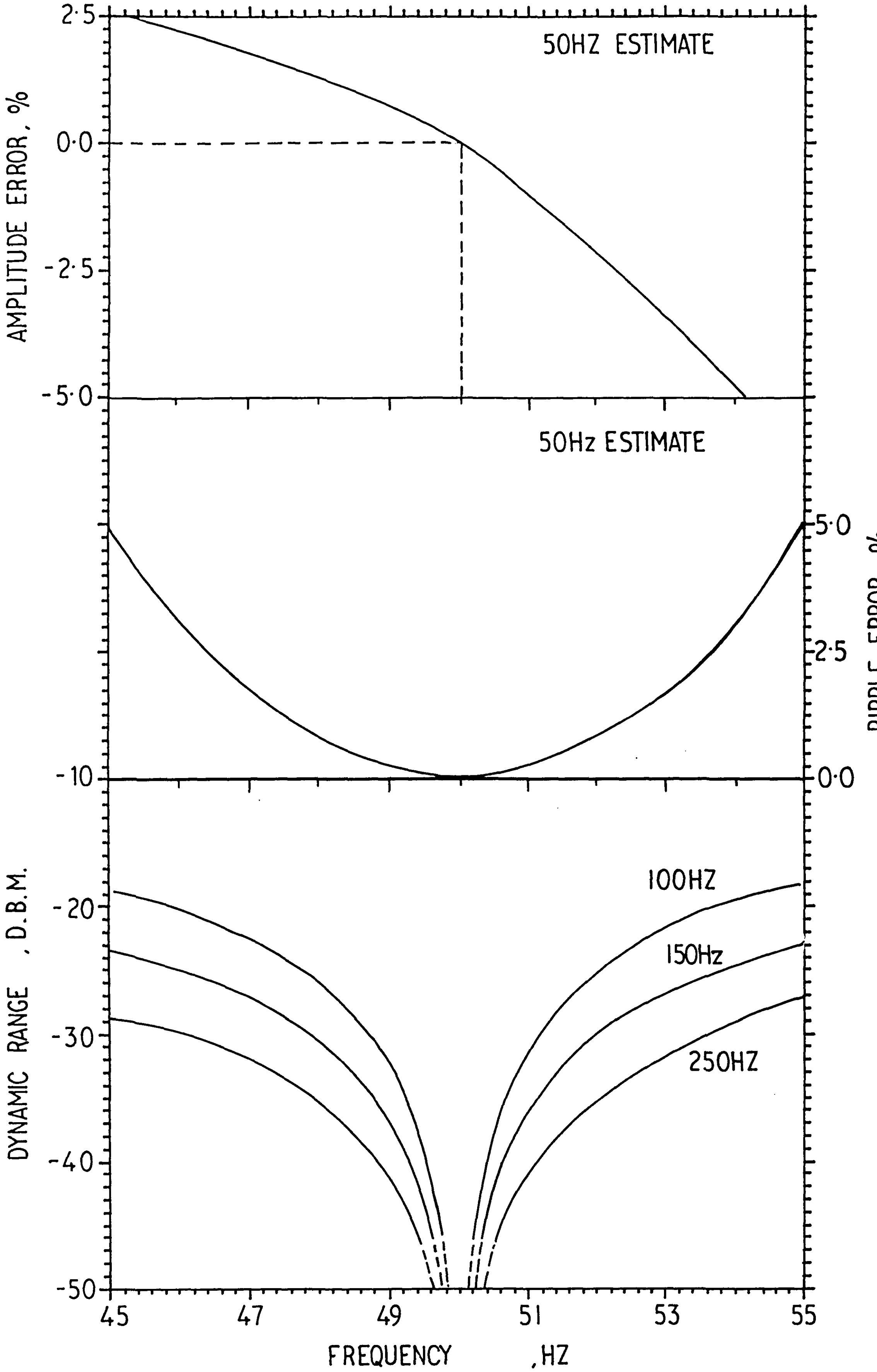

Figure 2.6: Response of the DFT to frequency deviations in a nominally 50Hz tone, (a) 50Hz estimate, (b) ripple error, (c) dynamic range.

Table 2.1 summarizes the error limits for the errors discussed in (i), (ii) and (iii) versus the frequency deviation in the nominally fundamental frequency pure tone. Note that the results would equally apply if the frequency deviation had been in the sampling frequency and the test tone frequency remained constant.

Freq. dev. (±Hz)	50Hz error (%)	Ripple (%)	Dynamic range (dbm)			
			100Hz	150Hz	250Hz	350Hz
0.5	0.5	0.4	-37.6	-42.5	-47.3	-50.1
1.0	-1.1 to 0.9	1.0	-31.6	-36.5	-41.4	-44.1
1.5	-1.1 to 1.3	1.5	-28.2	-33.1	-37.9	-40.7
2.0	-2.2 to 1.6	1.9	-25.8	-30.6	-35.5	-38.2
3.0	-3.5 to 2.0	2.8	-22.5	-27.3	-32.1	-34.9
4.0	-4.8 to 2.2	3.8	-19.5	-25.0	-29.8	-32.8

Table 2.1: Error limits in the response of the DFT to frequency deviations in a nominally 50Hz tone.

These examples are not fully representative of reality as in practice pure tones are never present and exactly the same spectral leakage will occur at every other filter in the DFT filter bank. The resultant errors will be due to a complex interleakage (appendix C) between all the filters. However, as the fundamental is usually the dominant spectral component in a power system waveform, it will dominate the performance of the DFT and these examples, therefore, do give a very good approximation to reality.

It has been shown that a relative frequency deviation between the sampling and fundamental frequencies of a discrete waveform will produce errors in the discrete spectral estimate as given by the DFT. However, the case for synchronised sampling is not as clear cut as these results would imply, because practical considerations need to be taken into account.

Under steady-state power system conditions, the power system frequency will be very stable (certainly within 0.5% and probably better for the CEGB system) and therefore if a stable quartz sampling clock is used, an accuracy of ±1% across the spectral estimate can readily be achieved (table 2.1). Even if a higher accuracy is required, a case for synchronised sampling cannot be made because the correction techniques to be described in section 2.3.3 are easier to apply and very effective.

During fault conditions it is impossible to prevent leakage errors whether synchronised sampling is used or not. The reasons for this are:

(i) Postfault aperiodic subharmonic transients will cause leakage errors in the spectral estimate which will be largely unaffected by the mode of sampling.

(ii) Synchronising the sampling to the infinite-bus is really no different to having a stable quartz reference (within the error limits of ±1%) and certainly less secure.

(iii) Synchronising the sampling to the faulted waveform itself is unacceptable protection practice. However, even if it were not, such a procedure would require a phase locked sampling clock with a high transient response to prevent leakage errors being compounded because of inadequate tracking speed.

In summary, synchronised sampling can give a high accuracy but only under steady-state conditions. For real-time application it is not recommended.

2.3.2 The Optimum Window Length

For spectral analysis, the principal condition of equation 2.7a, that the discrete sequence must be periodic within the DFT window, is inviolate. While for a fundamental frequency fourier filter the use of windows shorter than one cycle can be used to obtain an optimum compromise between group delay and accuracy, for spectral estimation they cannot as the estimation process must give equal weighting to all the harmonics within its pass band. Hence the minimum window size possible is one cycle of fundamental as defined by equation 2.7a.

The optimum maximum size depends on a number of factors which are:

(i) For real-time application, the maximum acceptable group delay.

(ii) The required frequency resolution.

(iii) The dynamic range and accuracy required.

For real-time application (i.e. a scanning DFT as described earlier), the minimum possible group delay is of prime importance. The minimum window length of one cycle of the fundamental frequency will resolve the fundamental and all its harmonics upto the foldover frequency selected by the sampling rate. For most protection applications this is sufficient and the one cycle window is the optimum choice.

Sampling considerations apart, a scanning DFT will only give a high accuracy and wide dynamic range if the energy content of subharmonic and nonharmonic components in the measurands is low. Under steady-state or slowly changing conditions, this is largely true. However, at the fault instant two factors will contribute to errors in the spectral estimates. These are:

(i) As the scanning DFT sweeps across the fault discontinuity - the fault transition period - it will generate spurious spectral components until the DFT window encloses one complete period of the postfault waveform.

(ii) Any aperiodic postfault low frequency transients in the power system measurands cannot be discriminated by a one cycle DFT and will instead contribute to the errors.

Figures 2.7 and 2.8 illustrate both these problems using computer generated tones whose spectra are accurately known.

Figure 2.7 shows the main harmonic spectral estimates from a scanning DFT for both one and two cycle window lengths, as it sweeps along a discrete sequence consisting of a burst of 1.0 unit fundamental and 0.1 unit third harmonic sampled at 32 s/c. Apart from the expected increase in group delay, two other features are of note:

(i) An increase in window size dampens the amplitude of the spurious spectral components produced by the fault discontinuity during the fault transition period. This is because an increase in window size effectively increases the number of filters in the DFT filter bank - the frequency resolution increases from 50Hz to 25Hz - and consequently the spectral energy produced by the fault discontinuity will be distributed over a larger number of filters.

(ii) The fundamental frequency spectral estimate, being the dominant component, smoothly increases to its steady-state value during the fault transition period, and consequently its vector variation can be put to use well before it stabilizes. On the other hand, the third harmonic estimate is very unstable during this interval as the fundamental component, possessing the greatest spectral energy, will tend to contribute large errors until the DFT sees an integer number of cycles of the waveform within its window. If the third harmonic was the dominant spectral component, the reverse would be observed.

Figure 2.8 demonstrates the variation of the spectral estimates from a scanning DFT for a simulated waveform of identical spectral content to that used in figure 2.7, but with a discontinuity at zero point-on-wave consisting of a reduction in the fundamental to 0.5 unit and a 2Hz 0.25 unit subharmonic transient. The main feature of note is the ripple superimposed on the spectral estimates due to the low frequency postfault transient after the fault transition period. The ripple error is greatest

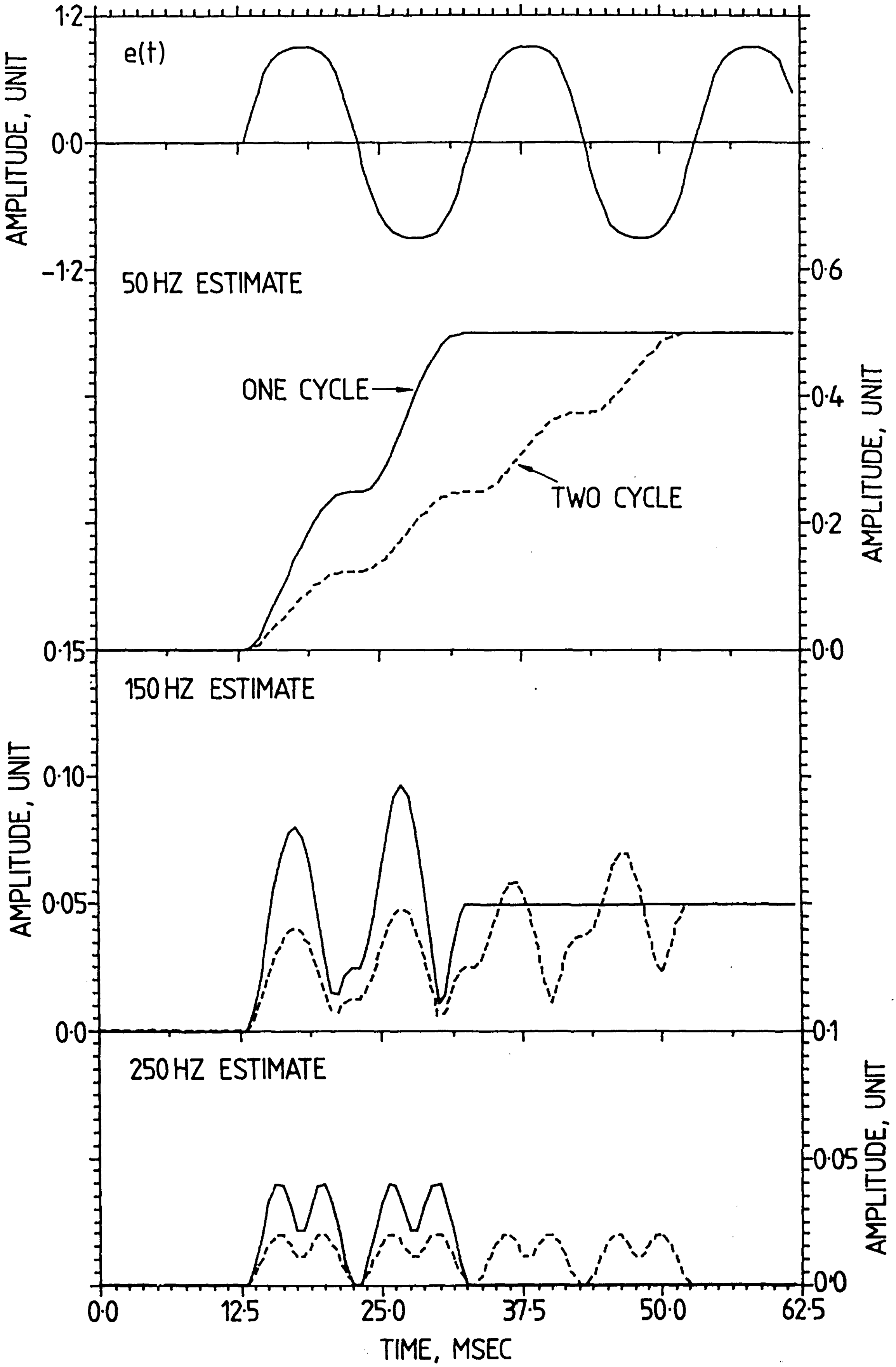

Figure 2.7: Response of the DFT during the fault transition period.

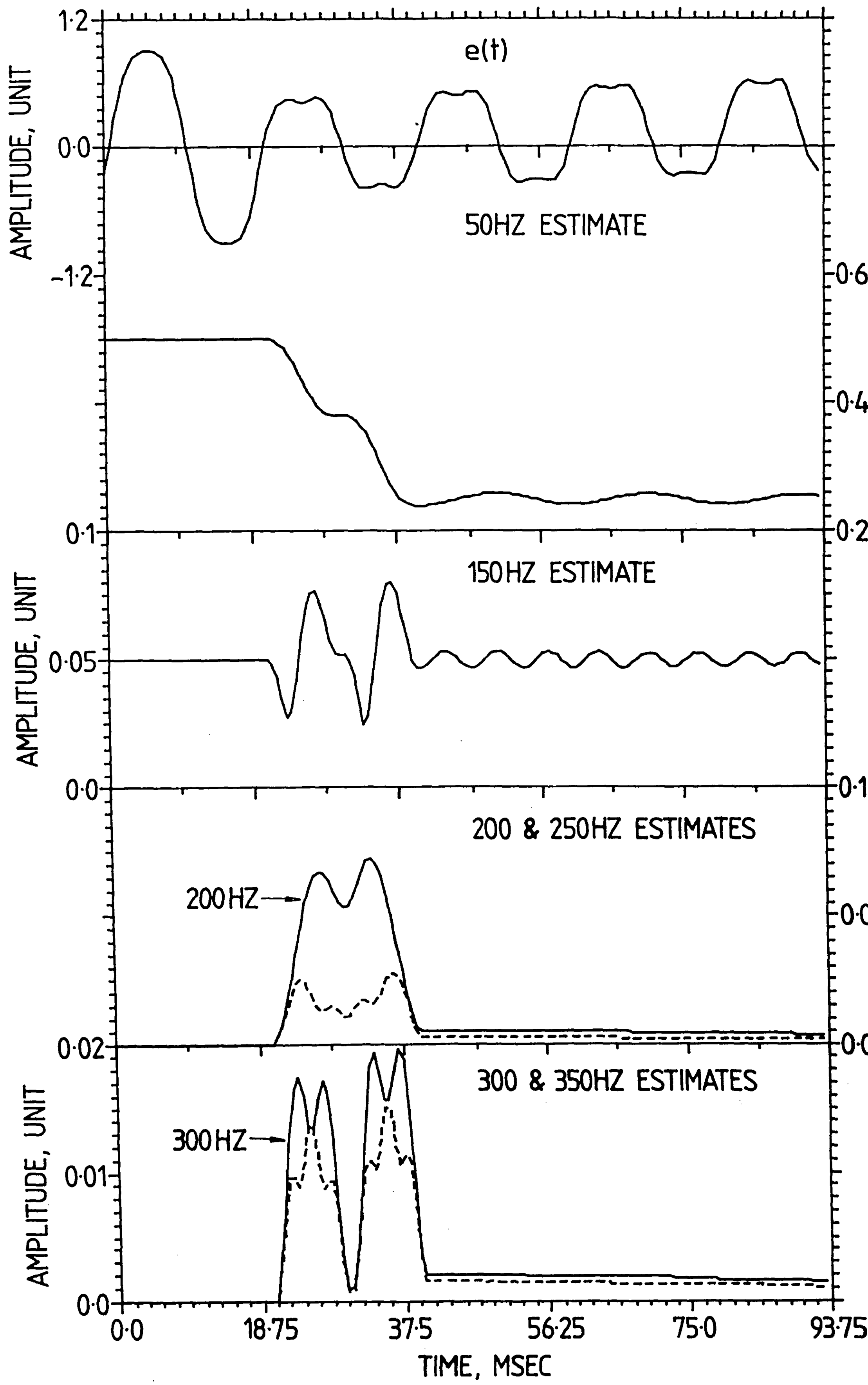

Figure 2.8: Response of the DFT to subharmonic transients.

for the fundamental frequency estimate as its filter in the DFT filter model is closest to the source of the error, and decreases for the higher harmonics.

Of the two errors, the more serious are those due to aperiodic postfault low frequency transients. The errors during the fault transition period are a manifestation of the group delay inherent in the DFT and, though not desirable, are predictable and consistent. This poor rejection of low frequency transients is the main limitation in the use of the DFT as a real-time spectral estimator (or for that matter as a fourier filter) in power systems.

For off-line applications, the group delay is of no consequence and the main criteria in the choice of the maximum window length are the frequency resolution, accuracy, and dynamic range requirements. If a high accuracy is not required (see table 2.1), the optimum window size can be selected solely on the criterion of frequency resolution. For a frequency resolution of 50Hz it will be one cycle. If a high accuracy is required then the optimum window size must be based on the criterion that every spectral component in the discrete input sequence of amplitude within the required dynamic range, must be resolved otherwise it will contribute to errors. To achieve this condition, the optimum window size may very well need to be much greater than that required by the basic frequency resolution.

In summary, for real-time application the window length must be chosen to minimize group delay and, therefore, for a 50Hz resolution the optimum length is one cycle. An increase in window length does improve the response of the DFT during the fault transition period but only at the expense of an increase in group delay. For off-line application, the window length may need to be much larger than the minimum required for a desired frequency resolution depending on the spectral nature of the waveform.

2.3.3 Leakage Error Reduction Methods

There are two methods for correcting errors in the spectral estimates due to discontinuities in the discrete time sequence. These are:

(i) The use of window functions.

(ii) Frequency domain interpolation methods.

The applicability and limitations of these methods for both real-time and off-line applications are examined.

2.3.3.1 Window Functions

An easy to apply technique for the reduction of truncation (or leakage) errors is to precondition the discrete time waveform by multiplicatively applying a class of time domain weightings known as window functions, as shown below.

If x(nT) is a discrete time sequence such that

$$x(nT) = \sum_{m=0}^{N-1} x(mT)$$

$$\text{then} \quad x_W(nT) = \sum_{m=0}^{N-1} x(mT)w(mT) \tag{2.12}$$

$$\text{and} \quad X_W(\omega) = X(\omega) * W(\omega) \tag{2.13}$$

A window function reduces errors in the DFT spectral estimate by reducing the side lobe response of the fourier filters (see figure 2.2) constituting it. The lower the side lobe response, the less will be the leakage from one filter to the next. Equivalently it can be considered to smoothen the truncation boundaries of the finite data window. A detailed study of the action of window functions is presented in appendix B. Appendix B also includes a comparative assessment of the characteristics of four window functions; the Hamming, Hann, Blackman, and Kaiser-Bessel windows, which were chosen as offering the best performance out of the very large number of available types [4,31,64].

Though window functions can be extremely effective in controlling leakage errors in the DFT spectral estimate when properly applied, their blind application can very often lead to worse results. Two characteristics general to all window functions must be considered:

(i) They will introduce a constant scale change called the insertion loss in all the amplitude spectral estimates. This will occur because the signal energy of x(nT) will be modified by that of w(nT).

(ii) Window functions reduce the spectral resolution of the DFT.

The first characteristic does not present a drawback to the application of window function, unless the discrete waveform has a poor signal-to-noise, as the insertion loss (also sometimes referred to as the coherent gain [31]) can be calculated and compensated for. The insertion loss is given by the expression

$$G_c = 1/N \sum_{n=0}^{N-1} W(nT) \tag{2.14}$$

Table B.1 lists the insertion losses, relative to that of the default rectangular window, of the four windows considered.

The second characteristic presents a more serious problem because if the minimum possible window size has been chosen to fulfil a certain frequency resolution criterion, the application of a windowing function will introduce extremely serious errors. The only recourse possible is to increase the data window size until the loss in resolution is compensated for. This may be unacceptable in many real-time applications.

Table 2.2 illustrates the effect on the one, two and three cycle DFT spectral estimates of a pure fundamental frequency tone of amplitude 1.0 unit and sampled at 32 s/c. The unweighted spectral estimate of this tone is a spectral component at 50Hz. As shown, the Blackman weighting severely distorts the spectrum, but this distortion can be dramatically reduced by increasing the window size to compensate for the reduction in frequency resolution.

f (Hz) \ N	32	64	128
0	0.06105	-0.01091	-0.00012
50	0.43763	0.49874	0.49985
100	0.30646	0.05512	0.00057
150	0.06121	0.00099	0.00011
200	0.00393	0.00036	0.00004
250	0.00157	0.00018	0.00002
300	0.00067	0.00010	0.00010
350	0.00054	0.00006	0.00000
400	0.00025	0.00004	0.00000
450	0.00026	0.00003	0.00000

Table 2.2: The effect of window functions on the accuracy of the DFT spectral estimate.

Figure 2.9 illustrates schematically using the band-pass filter model of the DFT the nature of this distortion. The reduction in resolution due to the windowing function causes the main lobe width of the fourier filters to triple (table B.1) resulting in severe frequency aliasing (figure 2.9b). The aliasing between the main lobes of the filters centred at the fundamental and its harmonics can be prevented completely by increasing to three times the seperation between them (figure 2.9c), i.e. an increase of three times in the window size. However, increasing the window size also generates additional fourier filters at intermediate frequencies between the harmonics and a small amount of frequency aliasing

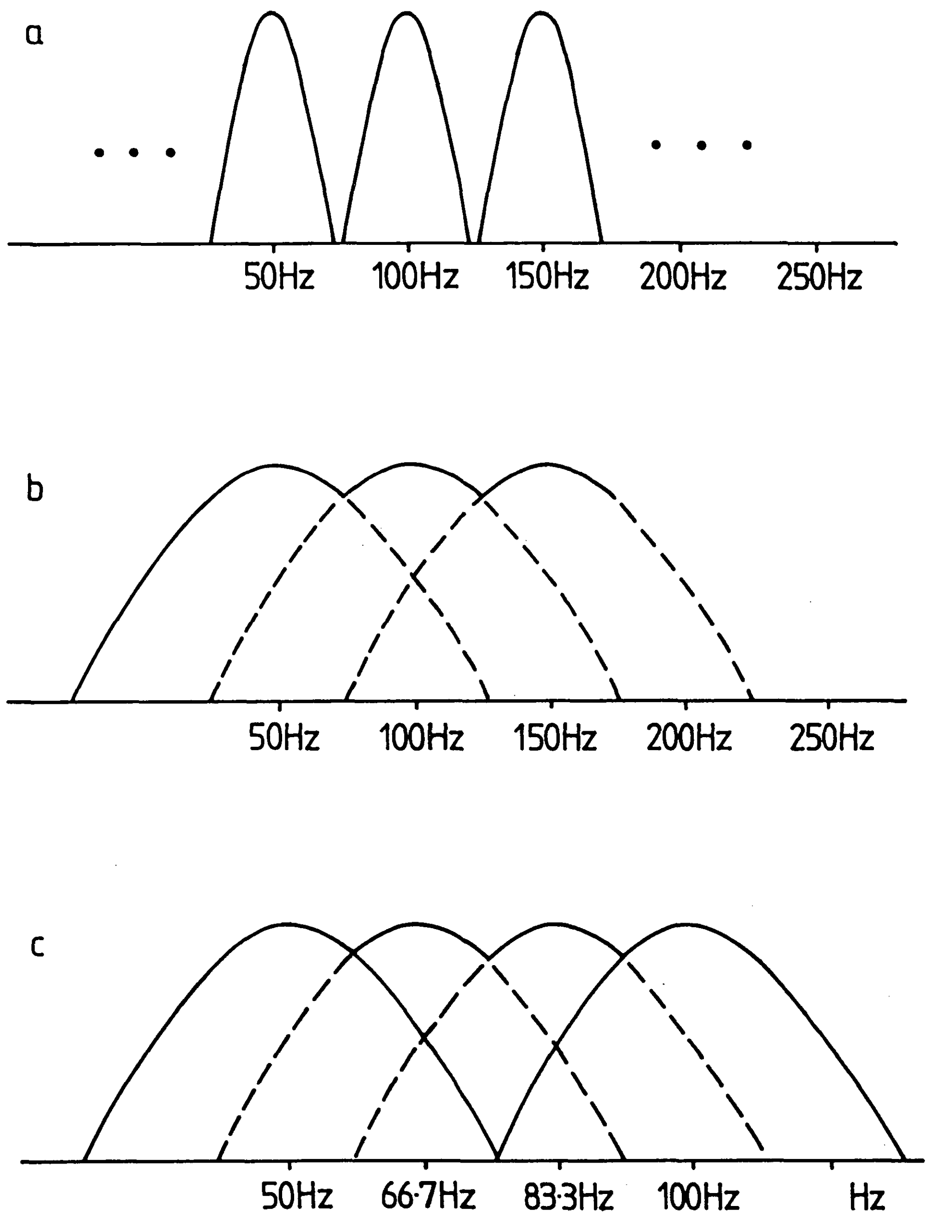

Figure 2.9: The effect of window functions in reducing the frequency resolution of the DFT.

will still take place indirectly via them and the side lobe responses of all the filters. This is illustrated by the results for N=128 (an increase of four times in the window size) in table 2.2.

A criterion for the minimum possible increase in resolution for any given window can be formulated from a knowledge of the bandwidth of the main lobes of their frequency responses and is given by the expression,

$$N_W = N.2^{R-1} \tag{2.15}$$

where N : unweighted DFT size.

N_W : minimum possible weighted DFT size.

R : ratio of the 6db bandwidth of the window to that of the default rectangular window.

The usual criterion for specifying bandwidth is the 3db frequency interval, but Harris [31] suggests the use of the 6db interval as better suited to the DFT. Table B.1 lists the values of R for the windows considered. For example R is 1.76 for the Blackman window giving N_W=54. In practice window lengths longer than the minimum may be essential to minimize the effects of 'indirect aliasing' especially if a discontinuity is present within the data window.

For real-time spectral estimation, the need for an increased frequency resolution implies a greater group delay effectively precluding the use of weighting functions unless a slower response is acceptable. This is a disappointing conclusion as a weighted scanning DFT spectral estimator has a much improved performance during the fault transition period, as shown by a Hamming weighted two cycle DFT in figure 2.10 for the waveform of figure 2.7. Compared to figure 2.7 the fundamental frequency estimate is better damped and the spurious spectral estimates are lower.

For off-line spectral estimation, weighting functions can be used most effectively to achieve a very high accuracy as an increased group

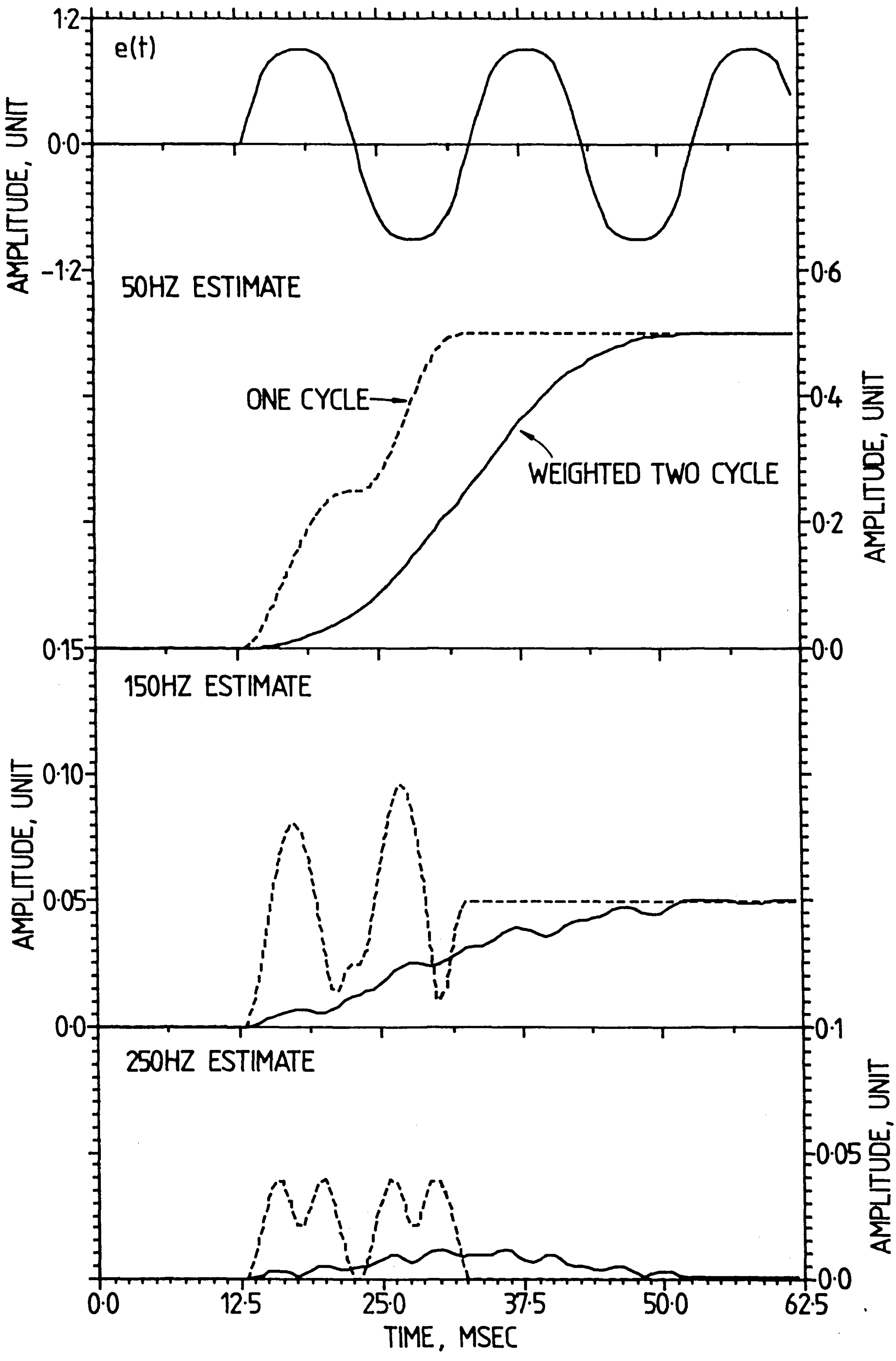

Figure 2.10: Response of a Hamming weighted DFT during the fault transition period.

delay is irrelevant. Figure 2.11 illustrates the effect of Hamming and Blackman windows in reducing leakage errors in the spectral estimate (N=1024) of a nominally 50Hz waveform with substantial levels of odd harmonics, for a frequency mismatch of 0.7 Hz.

2.3.3.2 Frequency Domain Interpolation

The second leakage reduction method is to mathematically interpolate between the DFT filters and theoretically calculate the extent of the spectral energy leakage, so as to compensate for it. Appendix C illustrates the theory of the method.

The solution is computationally complex as spectral energy leakage will occur between each and every filter in the DFT filter bank (figure 2.2) and is, therefore, not suited to real-time application. Approximations can be made, as shown in appendix C, to obtain a simpler solution but these are only valid for a large N, and therefore the approximate correction method is not suited to real-time application either as illustrated by table 2.3.

N	fund. freq. (Hz)	fund estimate	Error (%)
32	47.33	0.5134	2.68
64	46.29	0.5052	1.04
128	45.77	0.4989	-0.22
256	45.95	0.5015	0.30
512	45.99	0.4996	-0.08
1024	46.00	0.5000	0.00

Table 2.3: Accuracy of the approximate frequency domain interpolation method for various values of N.

Table 2.3 illustrates the effect of using frequency domain interpolation to correct the DFT estimate of a 46Hz pure tone sampled at 32 s/c.

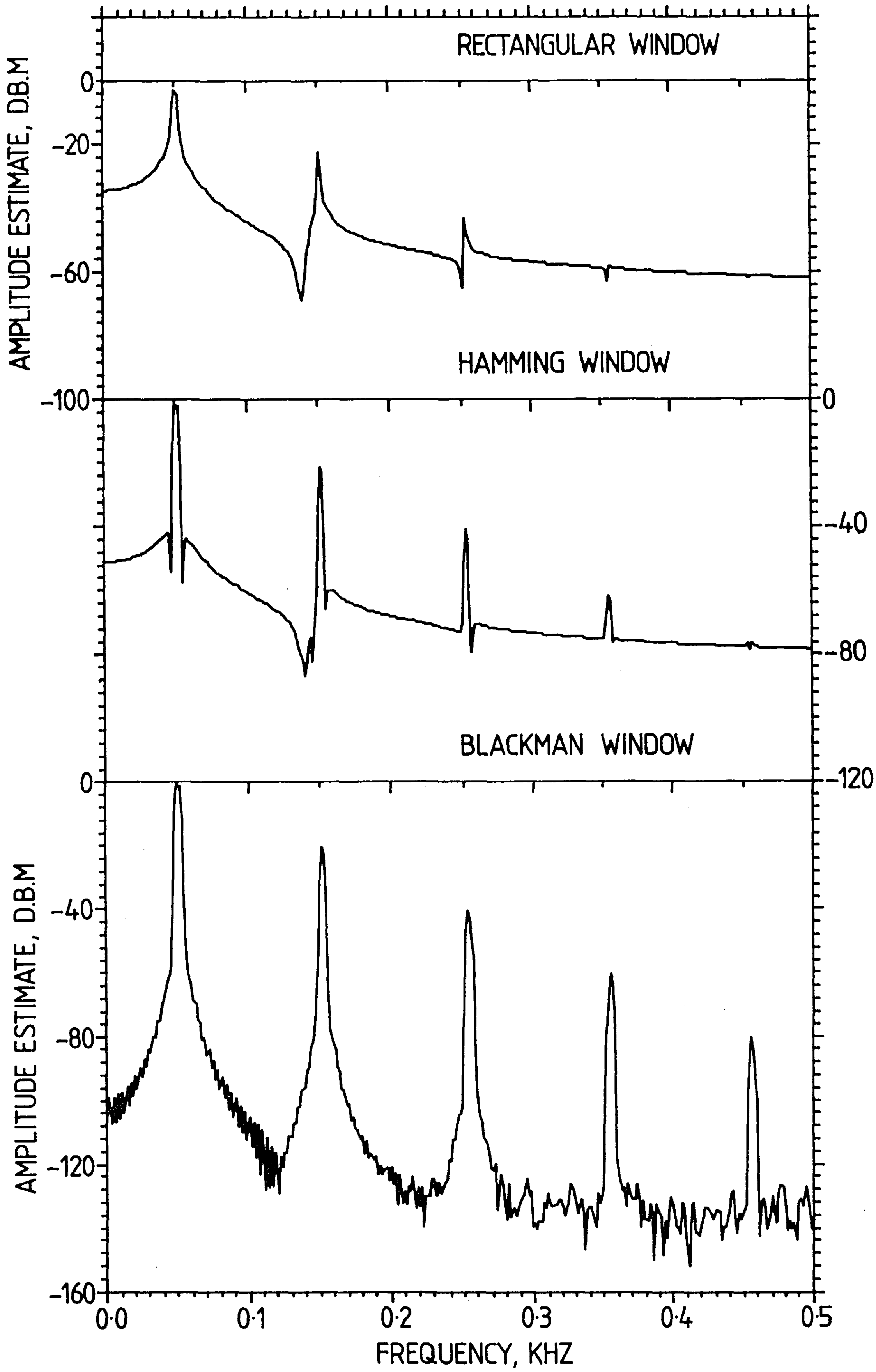

Figure 2.11: Spectral leakage reduction using window functions.

For large N, the correction is almost perfect but the effectiveness of the method is reduced for small N. In fact, for a one cycle DFT, frequency domain interpolation actually worsens the amplitude estimate of the fundamental (compare with table 2.1).

In summary, frequency domain interpolation is not suited in present form for real-time application. For off-line harmonic analysis, however, it enables very accurate spectral estimates to be obtained. The method also enables the calculation of the exact frquencies of the DFT spectral estimates and this may be an advantage, compared to windowing methods, for certain applications. Note, however, that windowing and the frequency interpolation method described here, cannot be used simultaneously. An alternate method due to Grandke [27] makes this possible (the Hamming window is used) but it was felt the additional accuracy to be unnecessary.

2.4 Conclusions

The application of DFT spectral estimation methods for the harmonic analysis of power system waveforms has been examined. The conclusions are:

(i) Synchronised sampling is not recommended for either real-time or off-line spectral analysis. For off-line application its use is possible but the windowing and frequency interpolation correction methods are simpler to apply.

(ii) For real-time spectral analysis the optimum window size is one cycle of the fundamental frequency.

(iii) The use of windowing to improve the response of the DFT is only acceptable for real-time application if an increased group delay is tolerable.

(iv) Frequency domain interpolation cannot be used for real-time application. The exact method is mathematically too complex while the approximate method is only valid for large N (> 4 cycles).

(v) For off-line spectral analysis the optimum window size is a function of the frequency resolution, accuracy, and dynamic range requirements. As the group delay is of no importance, considerable flexibility is possible in the choice of N.

(vi) Both correction methods can be used, though not simultaneously, very effectively to obtain accurate off-line spectral estimates.

In the next chapter, the design and implementation of a DFT based harmonic analysis system is described. Two requirements are met:

(i) A high accuracy spectrum analyser for the study of the spectra of steady-state waveforms.

(ii) A scanning spectrum analyser to study the spectra of rapidly changing waveforms.

CHAPTER THREE

The Experimental System

This chapter describes the design and implementation of the laboratory experimental system. This essentially consists of a suitably modified micro-alternator coupled to a mini-computer based data acquisition and spectral analysis system.

Modifications to the micro-alternator are described and justified, and an overview of the computer system is presented. A description of the spectral analysis software, based on DFT techniques described in chapter 2 is then presented. The chapter concludes with a calculation of the optimum discretization parameters for the measurands.

3.1 Description of the Experimental System

The three major requirements of the experimental laboratory system were:

(i) A micro-alternator suitably modified to reflect the triplen harmonic response of large alternators with high resistance neutral grounding, and with access to the stator windings for the application of internal winding faults.

(ii) A spectral analysis system to study the spectral nature of the micro-alternator voltages and currents under various faulted and unfaulted conditions.

(iii) A means of proving the 100% stator earth fault protection algorithms to be developed as a result of this study.

Figure 3.1 illustrates in schematic form the complete experimental system.

3.1.1 The Micro-alternator

The micro-alternator used was a three-phase 3kW machine manufactured by Mawdsley's Ltd, with a divided winding rotor (d.w.r.) and two series windings, phase displaced at an angle of 30 degrees to each other, per stator phase. A description of the machine is given in appendix D. Drive to the alternator was provided by a 5.5kW DC motor [83] driven by a variable speed thyristor drive [83]. An accurate and realistic control of the thyristor drive was achieved using a solid-state governor and turbine simulator to designs by Noble [55]. Field excitation to the micro-alternator was provided by an Amcron DC 100A [55] 1kW DC amplifier controlled by a solid-state AVR [55]. A time constant regulator (TCR) was used to decrease the effective resistance of the field winding to a realistic level [83].

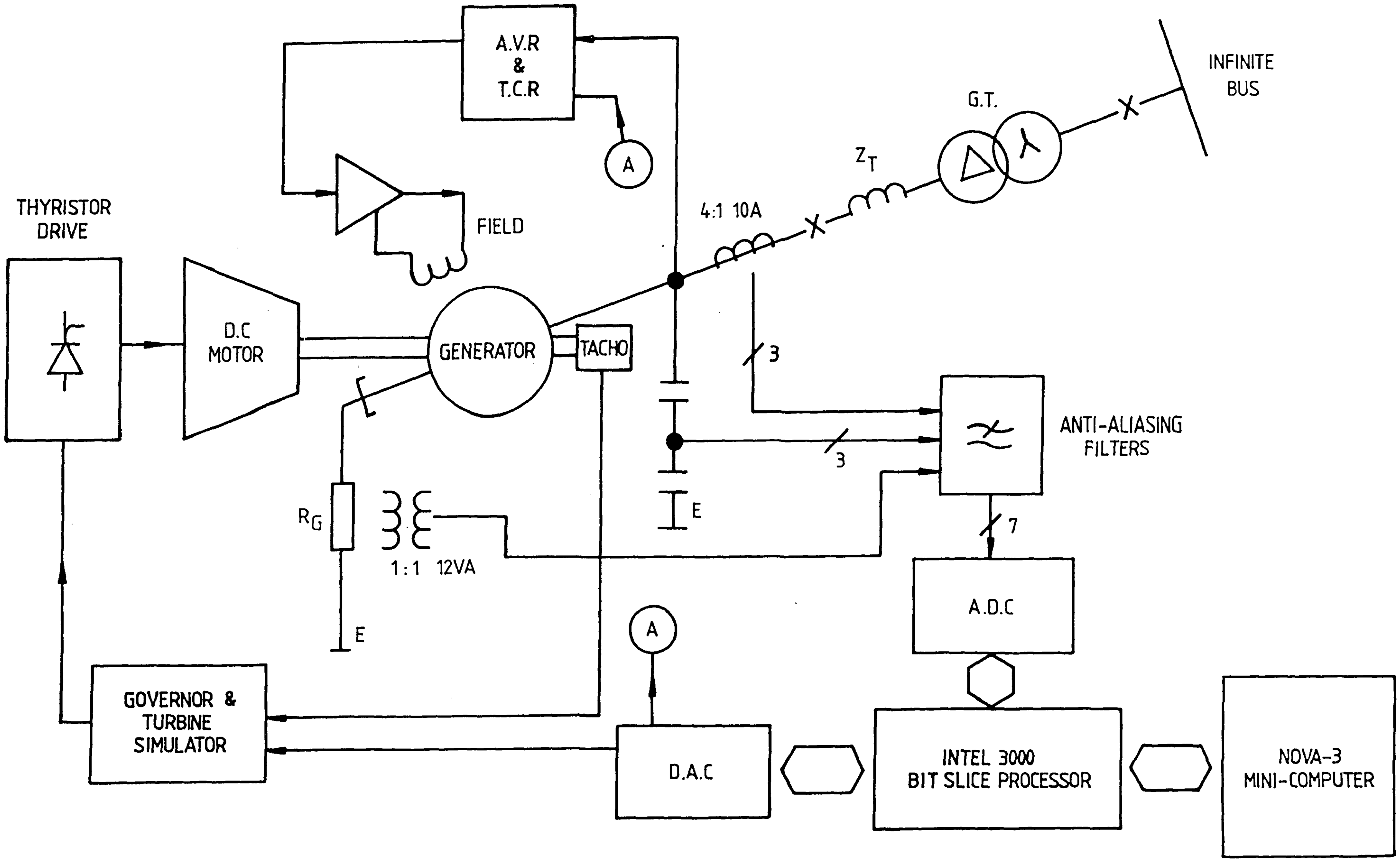

Figure 3.1 : The experimental system.

The neutral grounding impedence was simulated by a resistance connected directly at the neutral, in contrast to a real system where a very low value metallic grid type resistor is referred across the windings of a 22kv distribution transformer with its primary winding connected to the alternator neutral [84,88]. This was done for two reasons which are:

(i) The actual scheme enables the use of a resistance with a realizable power rating and possesses the additional advantage of keeping the neutral DC potential at earth, minimizing the possibility of arcing between the armature and ground. Both of these constraints are not applicable to a machine of the size and rating of the micro-alternator.

(ii) The reactive component of the effective grounding impedence is due to the transformer leakage and magnetizing reactances, and therefore will represent a negligible proportion of the total (the resistive component is typically of the order of 10^3 ohms [28,71,84,88]).

For alternators with a separate generator isolation switch (this is used to isolate the alternator from the generator system), an additional ground is always established, exactly equivalent to that at the neutral, after the isolation switch. This is done to prevent the UAT and G.T. low voltage winding earth fault protection from losing its ground reference when the alternator is switched out for maintainance, but with the station auxiliary supply continuing to be supplied from the infinite-bus.

The additional ground is established in a similar manner to the neutral ground using a three-phase star-delta distribution transformer with its star winding towards the alternator. This distribution transformer is sometimes called a potential transformer (P.T.). In the laboratory its effect was simulated by connecting similar resistances, equal in value to the neutral grounding resistance, from the machine terminals to ground.

Figure 3.1 illustrates the integration of these constituent components to form the complete micro-alternator system.

The modifications to the micro-alternator windings consist of tappings to a central patch board from each of the sixteen coils of each of the three phases of the stator winding. The modifications are illustrated in appendix D. Equal high voltage capacitors of value 0.0147 μF were introduced from the coil ends to ground to simulate the stray capacitance to ground of the stator windings of large alternators, typically 0.24μF/phase for 500-600 MW machines [28,71,84,88,93].

This modification is necessary because the stray capacitance to ground is the primary path for circulating triplen harmonic currents in the stator windings which are essential in third harmonic 100% stator earth fault protection schemes [28,63,71]. The stray capacitance to ground is proportional to the lengths of the slots in the stator and, consequently, for small machines it will be almost negligible in comparison to a large alternator. The stray capacitance at the end windings is negligible as they are not closely enclosed by the earthed stator core metal [44,71].

Tapping of the rotor winding for fault application purposes could, unfortunately, not be achieved because of the very tightly packed winding structure. The only possible way to do this effectively would have involved rebuilding the rotor.

3.1.2 The Spectral Analysis System

In fulfilling the second requirement for the experimental system commercial spectrum and transfer function analysers were found to be unsuitable, because at the low frequency range of interest (below 0.5 kHz) they are slow and require a large amount of data for accurate results. The slow speed, though not a drawback for the spectral measurement of prefault steady-state measurands, severely limits their usefulness for the measurement of postfault voltage and current harmonics during high current faults, which could cause severe damage to the micro-alternator if allowed to persist. These drawbacks also preclude the use of spectrum analysers for the analysis of rapidly changing phenomena such as power swings or at a fault instant. Consequently, it was decided to design a software based spectral analysis system customized to the requirements of this research using DFT spectral estimation, methods described in section 2.3.

The spectral estimation programs were implemented on a 16-bit Data General Nova-3 mini-computer with a Tektronix 4014 graphics display terminal for I/O, and front ended by an INTEL-3000 bit slice processor and digital acquisition system (D.A.S.) designed by Pavlides [57] but essentially based on an earlier design by Horne [35]. A detailed description of the D.A.S. can be found in Pavlide's report [57] but the essential features are summarized below. They are:

(i) A phase locked (P.L.L.) sampling clock with sampling rate selectable from 2 s/c upto 192 s/c. The P.L.L. reference can be chosen as either the infinite-bus or the micro-alternator A-phase line end voltage.

(ii) A 12-bit, multiplexed 16 channel analogue to digital converter (A.D.C).

(iii) A 16 channel 10-bit digital to analogue converter (D.A.C.).

The prefiltered three-phase line voltages relative to earth, line currents, the field current and neutral voltage were discretized by the D.A.S. to enable a comprehensive spectral analysis of the micro-alternator to be carried out. A sampling rate of 32 s/c and six-pole Butterworth anti-aliasing prefilters with cutoffs at 450 Hz were used (see section 3.3).

The line current transducers used were class X, 4:1 C.T.s with 0.02 ohm shunts across the secondary windings and a knee voltage of 62 V rms. The continuous ratings were 40 A rms and 10 A rms for the primary and secondary windings respectively.

Capacitor voltage divider networks were used as the line voltage transducers (see figure 3.1). The total effective capacitance of each of the networks was arranged to be equivalent to the simulated stray capacitance to ground of the last coil (i.e. the phase coils closest to the machine terminals) of the respective phases so as to ensure the correct simulation of the stator winding stray capacitance. Voltage transformers (V.T.) are not suitable as their connection from the line terminals of the micro-alternator to ground effectively provides an additional relatively low impedance path to ground, compared to the impedance of the stray capacitance, for the third harmonic current to circulate. An accurate simulation of the neutral third harmonic voltage is then impossible.

The field current was measured directly using an 0.01 ohm shunt while the neutral voltage was measured using a 1:1 12 VA interposing transformer, for isolation purposes only, across the grounding resistor. The loading of the interposing transformer was arranged to be very low so as to minimize any high frequency attenuation.

Using this system, three distinct software requirements were met which are discussed in detail in section 3.2 but are summarized below. They are:

(i) A fine resolution, high accuracy spectral estimator, called 'SPECTRUM', for the measurement of steady-state prefault or postfault amplitude and phase spectra.

(ii) A scanning DFT spectral estimator, called 'SWEEP', for the measurement of the amplitude spectrum versus time; especially useful for the measurement of rapidly changing waveforms.

(iii) Graphics software based on the Tektronix Plot-10 [86] graphics package, for the concise and rapid display of the spectral estimates.

The specification achieved by the spectral analysis software is summarized in table 3.2, but is discussed in detail in section 3.3

PARAMETER	SPECTRUM	SWEEP
Frequency resolution	better than 0.5 Hz (2048 point FFT)	50 Hz
Bandwidth	DC - 450 Hz	DC - 450 Hz
Accuracy	±1%	±5%
Step delay	-	1.37 ms
Dynamic range	better than 60dB	-

Table 3.1: Specification for the spectral analysis software.

At the outset of the research program it was decided not to attempt a real-time implementation of the proposed harmonic 100% stator earth fault protection, but to use off-line digital simulation on the Nova mini-computer with data recorded from the micro-machine via the D.A.S. interface, and stored on a suitable mass storage device. This approach was adopted for the following reasons:

(i) It frees the algorithm from real-time constraints and therefore it can be developed in a high level language - FORTRAN in this case - thus greatly speeding up the research program.

(ii) Both the spectral analysis system and relaying algorithms can share common hardware.

(iii) The graphics package originally developed for the spectral analysis system can be equally used to display and collate results from the relaying algorithm simulations.

(iv) The commercial withdrawal of the only suitable real-time DFT integrated circuit device [77] because of reliability problems. It was found impossible to easily duplicate the quoted specification of this device (1 msec for a 32 point complex DFT) with the alternative micro-computers available.

The validity of using off-line simulation using recorded data rather than a real-time implementation is fairly well established, with a considerable number of researchers having adopted this approach in the past [82]. Provided the recorded data is accurate both implementations should give identical results upto the trip signal being given. The only drawback is that possible secondary effects due to fault clearance cannot be studied, but these are most unlikely to be so severe as to compromise the applicability of the protection. In any case, the tripping arrangements for large alternators are complex because of the turbine and boiler constraints (section 1.2) and it is doubtful whether their accurate laboratory simulation would be worth the effort.

3.2 The Spectral Analysis Software

The routine central to the spectral analysis software is the solution of the DFT using a fast fourier transform (FFT) algorithm. Consequently, before describing the software in general a description of the FFT structure is presented.

3.2.1 The Fast Fourier Transform Algorithm

FFT algorithms are a class of algorithms for the fast and efficient computation of the DFT. From the equation of the DFT (equation 2.7a) it can be seen that the number of complex multiplications for the direct solution is proportional to N^2 and hence for large window lengths the computation is most inefficient. FFT algorithms derive their computational efficiency by replacing the computation of one DFT with that of several small DFTs as will be shown below.

First let the equation of the DFT (equation 2.7a) be rewritten in simpler form.

$$X(k) = \sum_{n=0}^{N-1} x(n).W^{nk} \qquad k = 0, 1, \ldots, N-1 \tag{3.1}$$

where, in comparison to equation 2.7a, $X_p(jk\Omega) \equiv X(k)$, $x(n) \equiv x_p(nT_s)$, and $W = e^{-j2\pi/N}$. In other words the periodic nature of $x_p(nT_s)$ and $X_p(jk\Omega)$ will be assumed instead of being explicitly stated.

If N is the product of two factors such that $N = N_1N_2$ then the indices n and k in equation 3.1 can be redefined as

$$n = N_1n_2 + n_1 \qquad n_1,\ k_1 = 0, 1, \ldots, N-1 \tag{3.2a}$$

$$k = N_2k_1 + k_2 \qquad n_2,\ k_2 = 0, 1, \ldots, N-2 \tag{3.2b}$$

Substituting equations 3.2a and b into equation 3.1 yields

$$X(N_2k_1 + k_2) = \sum_{n_1=0}^{N_1-1} W^{N_2n_1k_1}.W^{n_1k_2} . \sum_{n_2=0}^{N_2-1} X(N_1n_2 + n_1).W^{N_1n_2k_2}$$

$$= \sum_{n_1=0}^{N_1-1} W_1^{n_1k_1}.W^{n_1k_1}.Y(n_1,k_2) \tag{3.3a}$$

$$\text{where} \quad Y(n_1,k_2) = \sum_{n_2=0}^{N_2-1} X(N_1n_2 + n_1).W_2^{n_2k_2} \tag{3.3b}$$

and $W^{N_2} = e^{-j2\pi/N_1} = W_1$, $W^{N_1} = e^{-j2\pi/N_2} = W_2$.

Equations 3.3 demonstrate that the DFT of length N can be viewed as a DFT of size $N_1 \times N_2$ except for the introduction of the factors $W^{n_1k_2}$ which are known as ´twiddle factors´ [4,56,64].

Thus the computation of X(k) is done in three stages which are:

(i) The evaluation of the N_1 DFTs of length N_2, corresponding to the N_1 distinct values of n_1 as given by equation 3.3b.

(ii) The multiplication of $Y(n_1,k_2)$ by the twiddle factors.

(iii) The evaluation of X(k) by calculating N_2 DFTs of N_1 points on the N_2 input sequences $Y(n_1,k_2)\ W^{n_1k_2}$ as given in equation 3.3a.

The number of complex multiplications using this procedure is $N_1N_2(N_1+N_2+1)$ [56,64] which is obviously less than N^2 for the direct solution. In practice if N is highly composite (i.e. highly factorizable) the same procedure can be used iteratively to compute the DFTs of N_1 and N_2.

The most common FFT structure, and the one originally proposed by Cooley and Tuckey [12] in 1965, is obtained when N is chosen to be a power of 2 (i.e. $N = 2^m$). Such algorithms are known as radix-2 FFT algorithms, the term ´radix´ referring to the factorization of N. However, this does not imply that a constant radix is necessary (mixed radix FFT structures are equally valid) and for a particular value of N many FFT structures will be possible.

An investigation of the optimum FFT structure for protection is, however, not within the scope of this research, especially as more recent fundamentally different algorithms based on polynomial transforms [56] have broadened the field of study - prime-factor algorithms (PFA), the Winograd fourier transform (WFT). Furthermore, it was not judged necessary to highly optimize the computational efficiency of the FFT for the proposed off-line protection algorithm simulations and spectral analysis system. Consequently, a tried and tested, efficient algorithm by Monro [52,53] was used.

Monro´s algorithm uses a radix-4 structure. N is chosen such

$$N_1 = 4, \quad N_2 = 2^{t-2} \qquad \text{where } t = 2, \ldots, N \tag{3.4}$$

This is equivalent to splitting the input sequence of N points into four sequences of N/4 points. For this partition equation 3.3a becomes

$$X(k) = \sum_{n_1=0}^{3} W^{n_1 k} \sum_{n_2=0}^{N/4-1} x(4n_2 + n_1)\, W^{4n_2 k} \tag{3.5}$$

Nussbaumer [56] has shown that the radix-4 structure reduces the computational complexity by 25% compared to the more common radix-2 structure. Specifically, for a 32 point transform the radix-4 structure requires 94 real multiplications and 456 additions (assuming one complex multiplication to be equivalent to three real multiplications and two additions) compared to the 120 real multiplications and 482 additions for the radix-2 structure.

An additional saving in computation is achieved in the algorithm by making use of the fact that for a real discrete time sequence the DFT is symmetrical about the DC component [64], i.e. components above X(k/2) are redundant (see figures A.2 and A.3). Formally this can be stated as

$$X(N-k) = X^*(k)\ , \quad k = 0, \ldots, N-1 \tag{3.6}$$

where '*' is the complex conjugate descriptor. The procedure for the computation of the N/2 unique DFT components of an N point real sequence is after Cooley et al. [13].

A complex transform, Z(k), of length N/2 is calculated using the even numbered members of the input sequence as a real part and odd numbered ones as an imaginary part.

$$Z(k) = \sum_{n=0}^{N/2-1} x(2n)\, W^{2kn} + j \sum_{n=0}^{N/2-1} x(2n+1)\, W^{2kn} \tag{3.7}$$

$$k = 0, 1, \ldots N/2 - 1$$

The required transform X(k) is related to Z(k) by the following equation

$$X(k) = 0.5 \{ [Z(k) + Z^*(-k)] - jW^{kn} [Z(k) - Z^*(k)] \} \quad (3.8)$$

Summarizing, the algorithm solves equations 3.7 and 3.6, Z(k) being solved by the radix-4 procedure described by equation 3.4.

3.2.2 Description of the Software

Two separate programs called 'SPECTRUM' and 'SWEEP' were implemented in FORTRAN on the Nova mini-computer to constitute the software spectrum analysis system. The application of the two programs is quite different.

'SPECTRUM' provides a high accuracy vector spectral estimate for the measurement of steady-state spectra very much as a conventional spectrum analyser might do but with greater versatility and accuracy. The program 'SWEEP' on the other hand measures the amplitude spectrum variation with time and, as such, can be used to examine the variation in amplitude spectra of the micro-alternator outputs during transient conditions.

The structures of both programs are, however, similar. The similarities are:

(i) Both programs are designed to be user interactive with comprehensive error reporting.

(ii) The software is highly modular with many common routines.

Flowcharts 3.1 to 3.3 demonstrate both these similarities. Flowchart 3.1 summarizes the common initialization procedures for both programs while flowcharts 3.2 and 3.3 refer specifically to 'SPECTRUM' and 'SWEEP' respectively.

Routine 'INPUT' reads the spectrum analysis parameters provided by the user and initializes the two programs. Instead of prompting the user for input, a slow and repetitive process, requiring the physical presence of the user at the input terminal, ´INPUT´ is designed to accept parameters as arguments to the execution command, thus enabling the programs to be called from within keyboard monitor procedures for unattended data processing [89].

Both programs allow the preweighting of the discrete time data by either Hann, Hamming, Blackman, or the general Kaiser-Bessel window functions using routines ´HAMM´ (this routine calculates both the Hann and Hamming windows), ´BLACK´, or ´KAISER´. The routines implement equations B.5 to B.7 respectively. The weighting routines also return their respective coherent gains calculated using equation 2.14 which is used by both programs to compensate for the insertion loss of the windows.

With proper application, as described in section 2.3.3.1, preweighting of the discrete time sequence can be used to enhance the accuracy of the spectral estimates from ´SPECTRUM´ (figure 2.11). For the amplitude spectral variation with time given by ´SWEEP´, preweighting can be used to dampen errors during the fault transition period (figure 2.10).

´SPECTRUM´ also offers an alternative correction procedure to the use of window functions based on the frequency interpolation method described in appendix C and section 2.3.3.2. The routine ´FDI´, called after the FFT routine ´FFT1´ (see flowchart 3.2), implements equations C.19-C.24. Both window functions and frequency domain interpolation cannot be used simultaneously and an error message results if this is attempted.

Monro´s radix-4 FFT algorithm was used essentially unchanged in the program ´SPECTRUM´. However, for ´SWEEP´ some modifications were necessary to make its recursive execution more efficient. They are:

(i) A transfer of the twiddle factor calculations and data shuffling procedures from the FFT routine to a seperate routine called ´INITL´ outside the scanning DFT loop (see flowchart 3.3). As they are functions of the window size only, there is no point in unnecessarily recalculating them

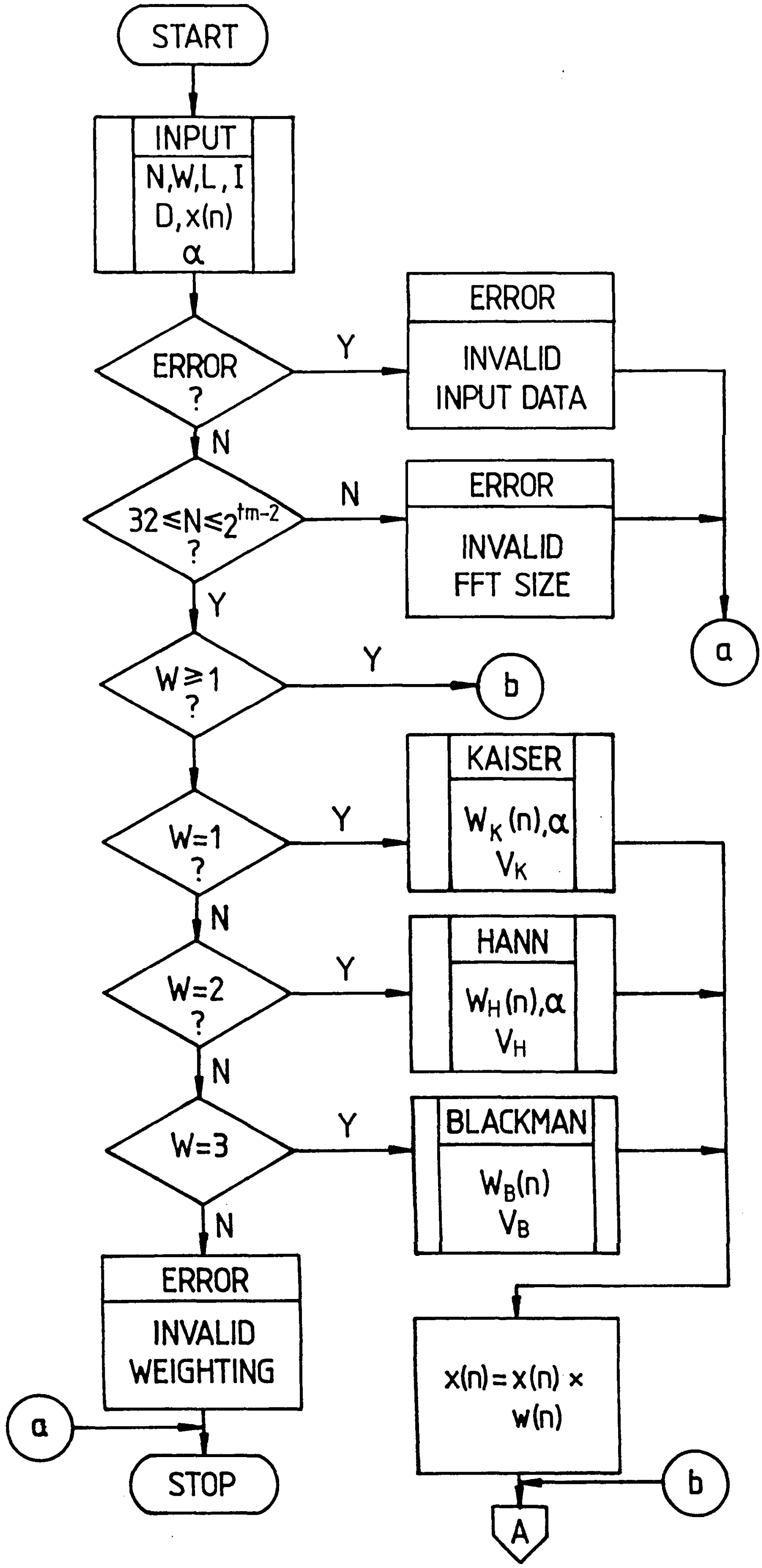

Flowchart 3.1: Initialization procedures for programs 'SPECTRUM' and 'SWEEP'.

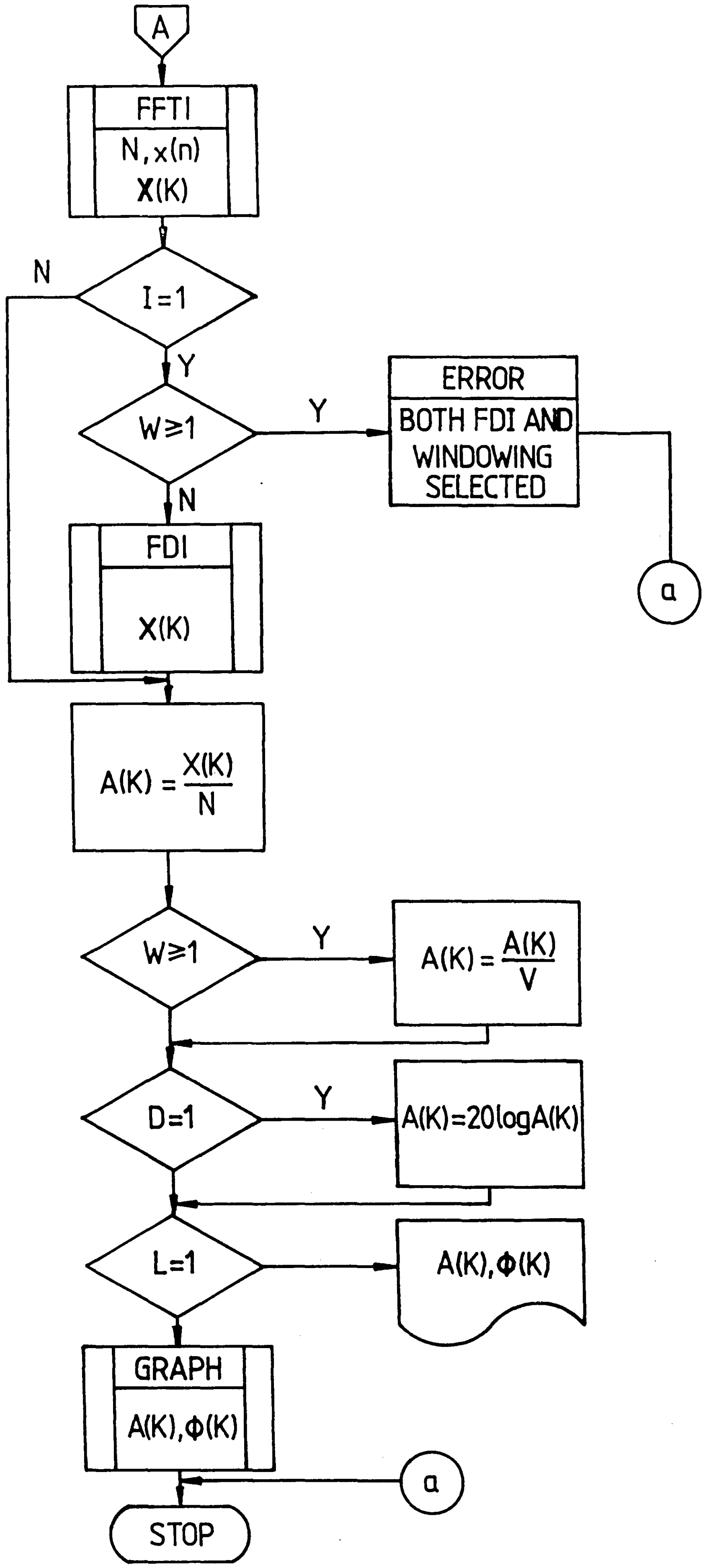

Flowchart 3.2: Structure of program 'SPECTRUM'.

at every cycle of the loop. The modified FFT algorithm is called 'FFT2' in flowchart 3.3 to distinguish it from the unmodified version.

(ii) A very efficient recursive procedure due to Halberstein [29] to accelerate the computation after the first cycle of the DFT loop.

Halberstein's procedure is based on a recursive formula which can be simply derived from the basic definition of the DFT (equation 2.7a). The formula is

$$X_{t+1}(k) = W^{-k} \{ X_t(k) \pm 1/N \, [x(N+1)t \mp x(1-N)t] \} \tag{3.9}$$

the upper and lower signs applying for even and odd values of k respectively. In other words, the spectral component X(k) at time t+1 can be calculated from its previous value at time t and the difference between the sample lost and sample gained by the scanning DFT window. The procedure is implemented in routine 'RECUR'.

Hence after the initial FFT using the radix-4 algorithm, the spectral estimate can be updated at every time step of the scan using a total of one complex multiplication and two additions per spectral point. This represents a computational saving of over 50% compared to the direct successive use of FFT1. Strictly speaking the initial FFT is not necessary as equation 3.9 will on startup stabilize to the correct spectral estimates after one cycle, but is used to obtain a more efficient initialization of the recursive procedure.

Unfortunately, Halberstein's procedure cannot be used for weighted data as the tapered time characteristic of the window functions (figure B.2) will drastically reduce the magnitudes of the samples x(N+1)t and x(1-N)t resulting in accentuated numerical errors in the calculation of their difference. Therefore, 'SWEEP' selects the routine 'RECUR' only if a window function is not selected, and consequently executes much faster for unweighted data.

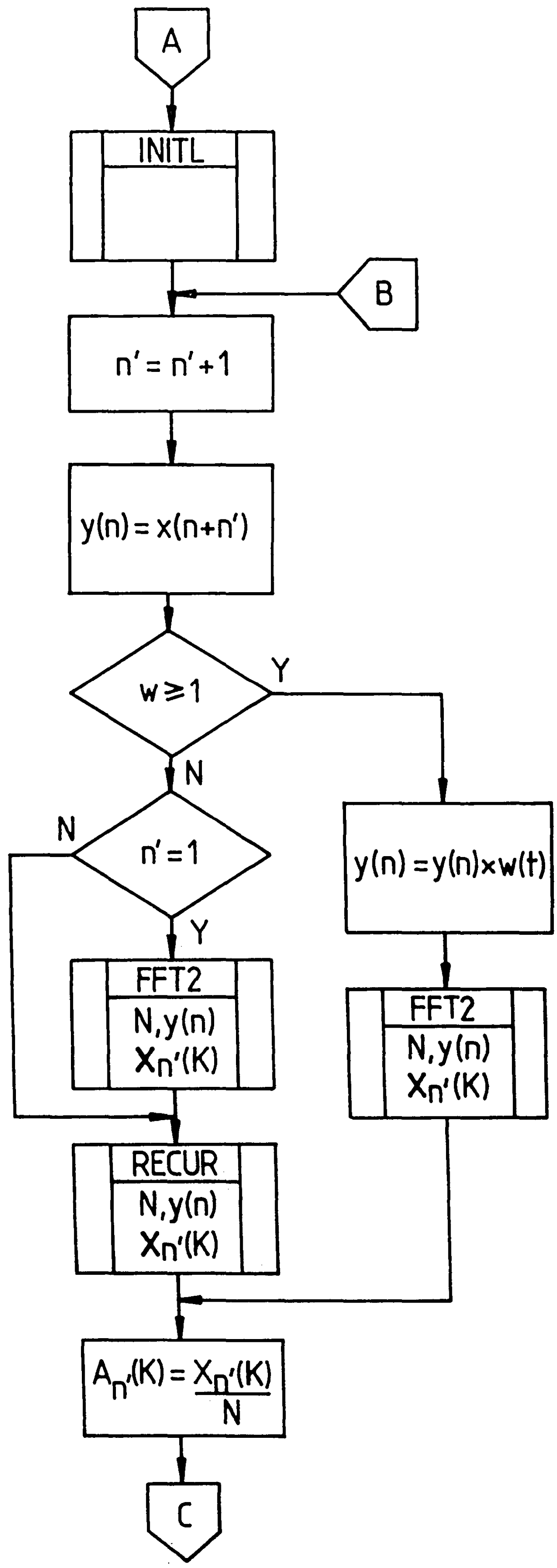

Flowchart 3.3: Structure of program 'SWEEP'.

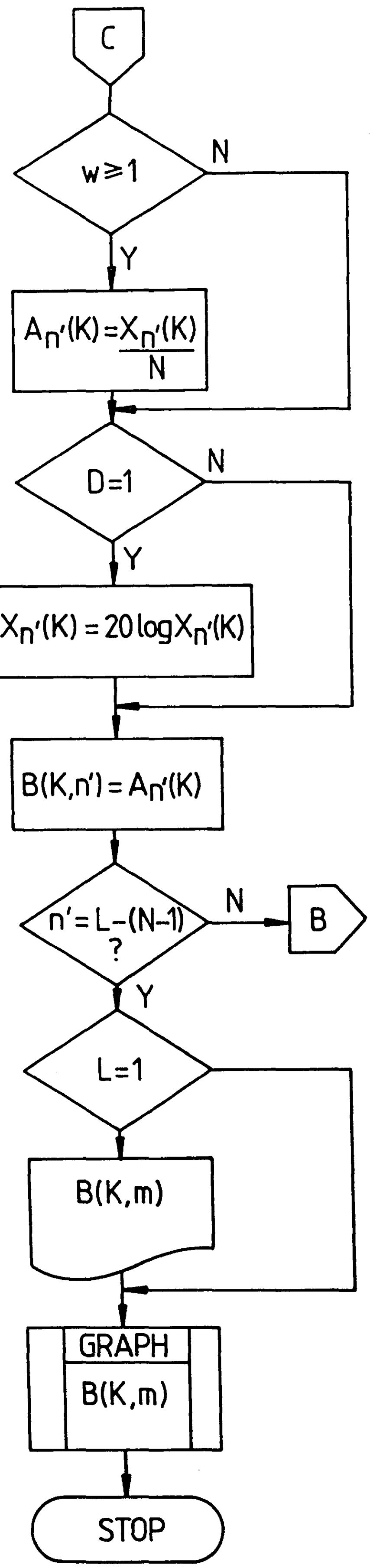

Flowchart 3.3: Continued.

3.3 The Optimum Sampling Rate and Anti-aliasing Filter

The accuracy and resolution of the digital spectral estimation programs, as for all digital processes based on discretized analogue data, is ultimately dependent on the integrity of the discretization process. The integrity can be assured if the band-limiting criterion of the sampling theorem is fulfilled. This can be done either by selecting a sampling rate high enough to resolve all possible frequency components in the measurands, or by prefiltering to reject frequency components above the pass band of interest prior to discretization. Before either of these options can be selected, a detailed examination of the spectral nature of the measurands must be made.

3.3.1 The Spectral Nature of the Measureands

Figures 3.2a-d illustrate the amplitude spectra of the neutral voltage (upto 4.8 kHz), the A-phase line voltage (relative to earth) and current, and the field current (all three upto 2.8 kHz) respectively. The spectra were measured at the full rated power and unity power factor of the micro-alternator with an effective grounding resistance at the alternator neutral of 760 ohm. Apart from the field current, which shows as it should very little harmonic distortion, three features are of note:

(i) The high level and extent of the triplen harmonics in the neutral emf.

(ii) The low frequency of the slot ripple harmonics in the line currents, with the first slot harmonic being the 11th (they are the 11th, 13th, 23rd, 25th etc).

(iii) The almost negligible level of harmonic information above the 9th harmonic in the terminal emfs of the machine which is due to the damping effect of the infinite-bus.

The neutral voltage is rich in harmonics compared to the other measurands for two reasons:

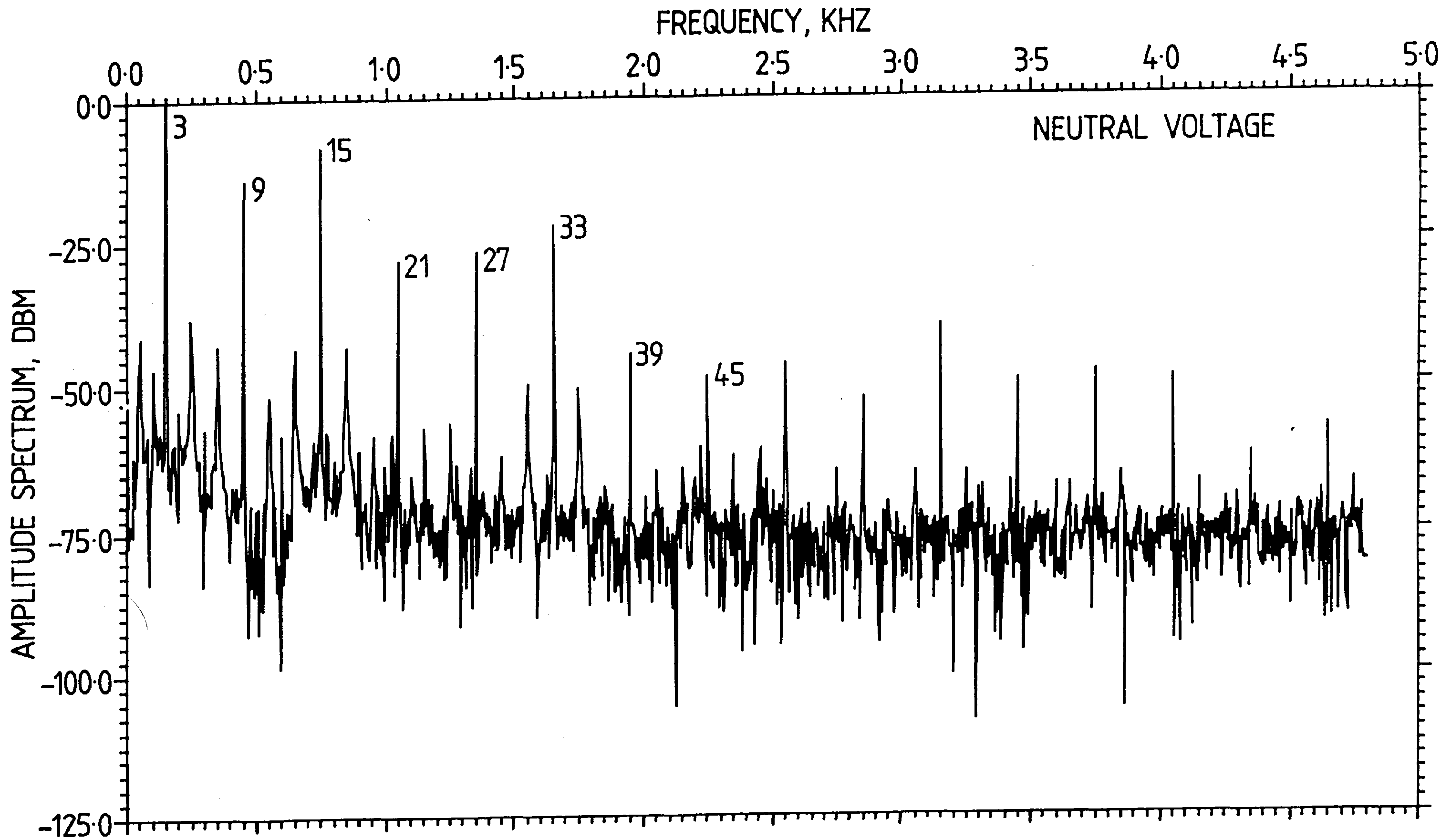

Figure 3.2a : Steady-state amplitude spectrum of the neutral emf relative to earth.

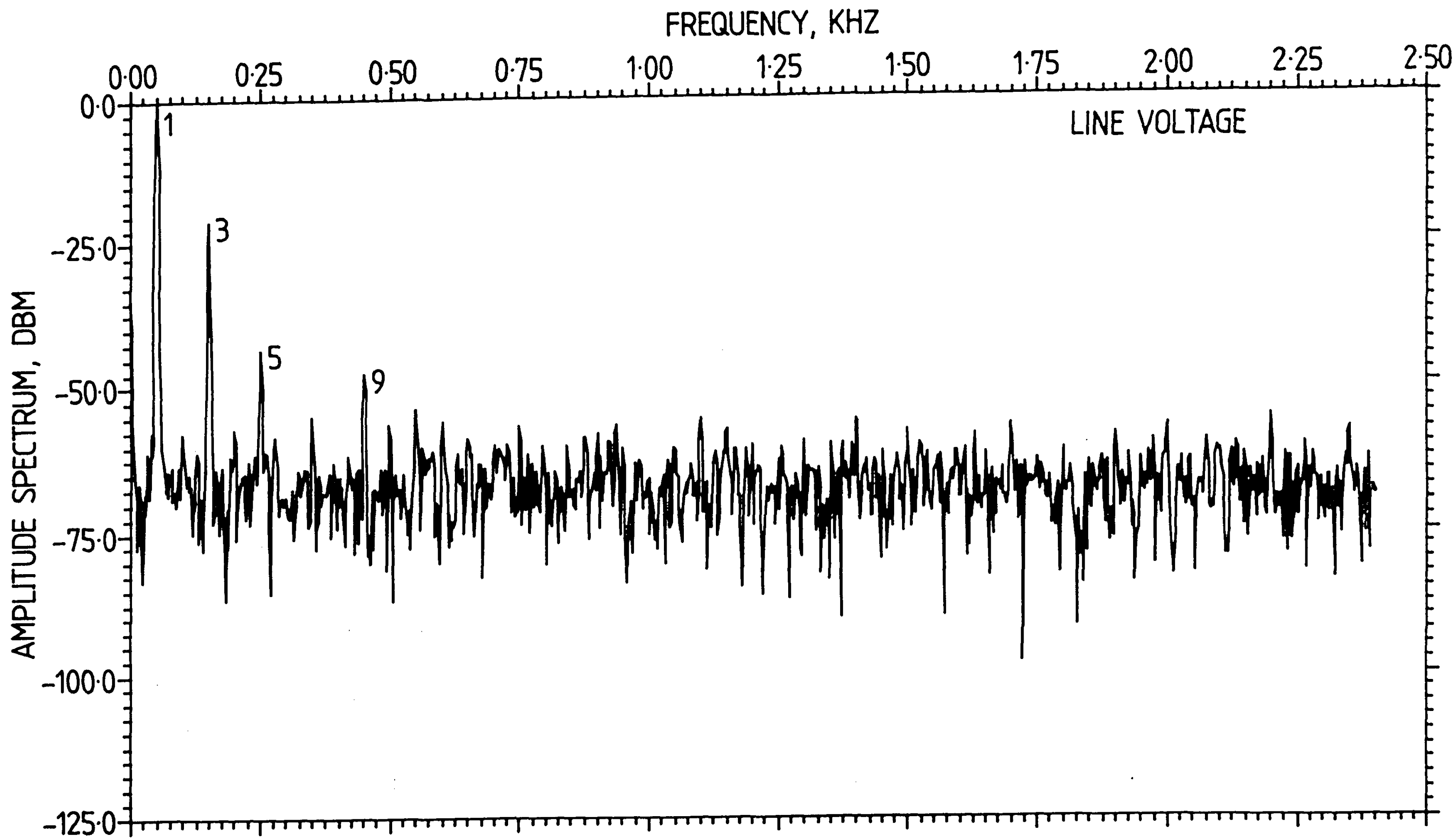

Figure 3.2b : Steady-state amplitude spectrum of the A-phase line emf relative to earth.

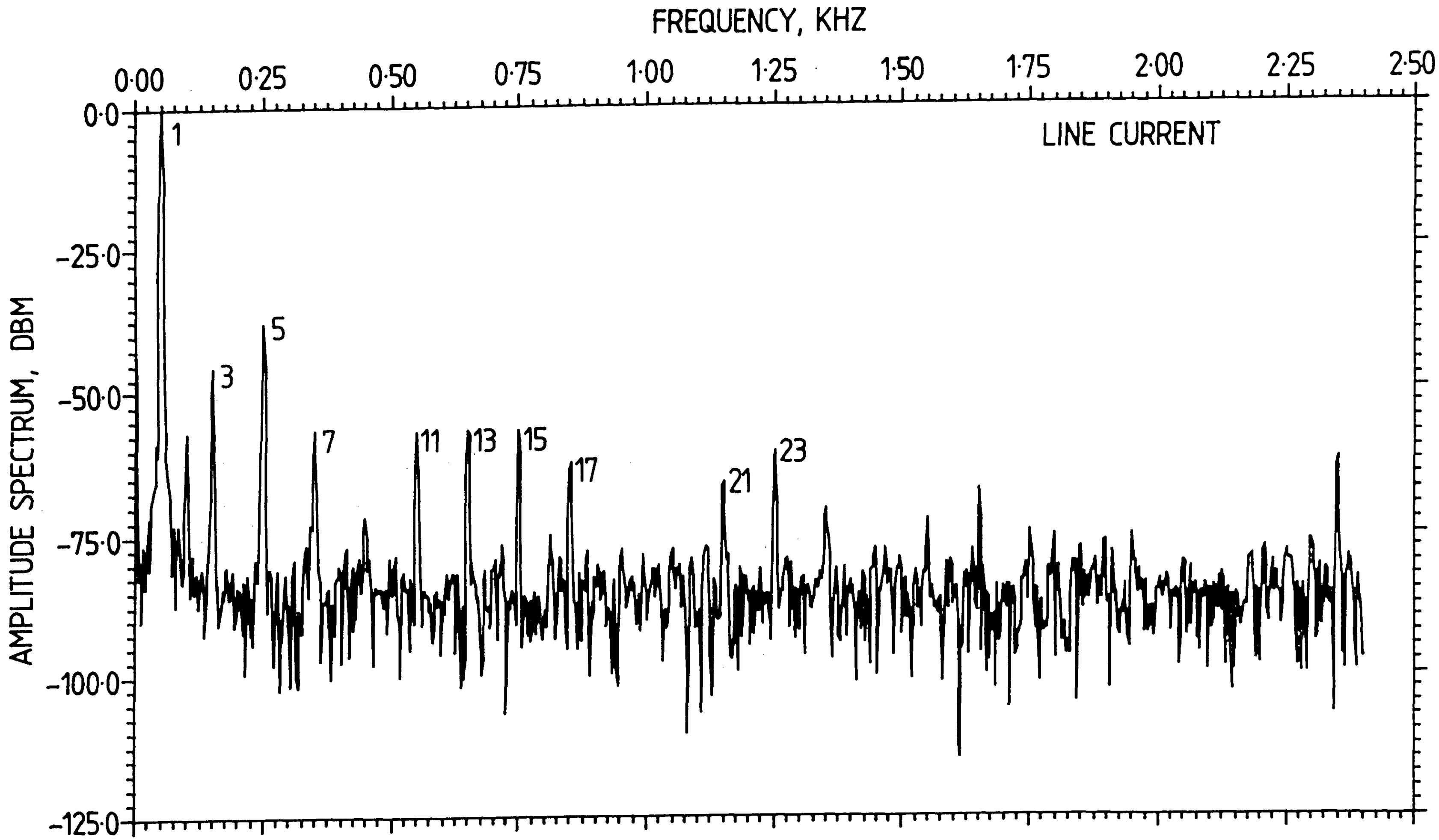

Figure 3.2c : Steady-state amplitude spectrum of the A-phase line current.

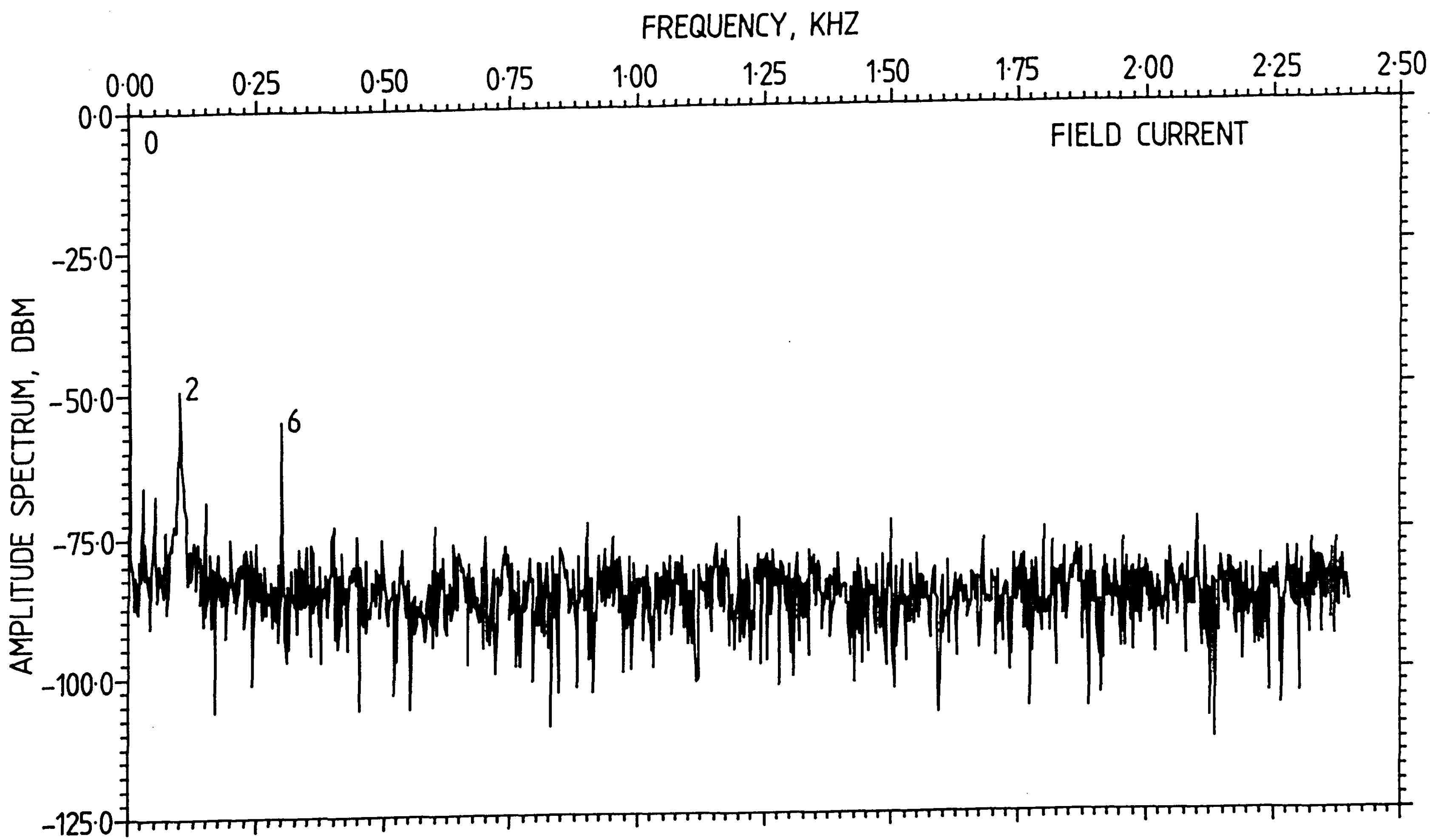

Figure 3.2d : Steady-state amplitude spectrum of the field current.

(i) The neutral is the summing point for capacitive ground currents from each phase of the micro-alternator; harmonics, especially zero-sequence triplen harmonics, are accentuated there.

(ii) The limiting impedance of the stator capacitance to ground being inversely proportional to frequency, higher frequency components are maximized relative to the lower frequency components.

The comparatively low order of the slot harmonics is a characteristic of the physically small size of the micro-alternator as the order of the main slot ripple component is proportional to the rotor slots per stator pole [3,32,44]. In a large alternator, the main slot ripple component will be, typically, at a frequency four to five times greater than for the laboratory micro-alternator.

Four conclusions can be drawn regarding the discretization and digital spectral analysis of these signals. They are:

(i) As the slot harmonics are of no interest there is no point in extending the bandwidth of the spectral analysis above the 11th harmonic. In fact, as the triplen harmonics are likely to be the most useful spectral components [23, 43-44] for the proposed protection scheme, it was decided to limit the bandwidth to the 9th harmonic.

(ii) Due to the extent of the neutral voltage amplitude spectrum, achieving the band-limiting criterion by using a high sampling rate is unrealistic.

(iii) For a bandwidth upto the 9th harmonic, the antialiasing filter will need to have a very sharp cutoff to prevent foldover distortion from the high level and low frequency of the slot harmonics in the neutral (see section 3.3.3).

(iv) For the field current, and the line end current and voltage signals a milder cutoff will suffice. However, in the interest of maintaining an equivalent step and group delay in all the measurement channels, identical filters designed with reference to the 'worst' channel (i.e. the neutral voltage) were used.

The choice of optimum anti-aliasing filters and sampling rate to achieve a bandwidth of DC-450Hz are now examined.

3.3.2 The Filter Approximation

Research [66] has shown that the maximally flat Butterworth filter approximation offers, for protective relaying, the ideal compromise between step delay and stop band attenuation. The low-pass Butterworth filter, frequency normalized to the cutoff frequency $\omega_c = 1$ rad/s, is given by:

$$H_{lp}(s) = k \, / \, B_n(s) \tag{3.10a}$$

where k is a gain constant, and $B_n(s)$ the Butterworth polynomial [4,20] given by:

$$B_n(s) = s^n + a_{n-1}s^{n-1} + \ldots + a_2 s^2 + a_1 s + 1 \tag{3.10b}$$

where a_n : Butterworth coefficients [4,20]

For spectral analysis the relevance of two characteristics of the Butterworth filter, not normally of consequence for the filtering of a single frequency component, must be examined. They are:

(i) The maximally flat frequency response.

(ii) Its nonlinear phase response.

The maximally flat frequency response of the Butterworth filter is ideal for spectral analysis as it will maintain the accuracy of the amplitude spectrum estimate given by the DFT. Equiripple [4,20] filter approximations - Chebyshev, Elliptic (Cauer) - apart from upsetting the optimum balance between step delay and stop band attenuation introduce a ripple component into the amplitude spectrum degrading the accuracy of the estimate.

The nonlinear phase response of the Butterworth filter is unimportant though it might appear to be at first sight. It will, of course, introduce phase errors in the spectral estimate. However, for protection these errors are unimportant because as the DFT window scans the data, the relative phases of the spectral vectors will not be constant in any case. For example the third harmonic spectral estimate will be a vector revolving, in the complex plane, at an angular frequency three times that of the fundamental and hence their relative phase will change from sample to sample. What is important is that the phase response of the filter approximation is consistent on all measurement channels so that relative phase measurements at a particular frequency between channels be accurate.

In summary the Butterworth filter is the optimum choice of anti-aliasing filter for the purposes of this research.

3.3.3 The Filter Step Delay

The step delay for any low-pass filter is defined as [20]

$$\tau_s = 0.5 \mid e_{1p}(t) \mid_{t \to \infty} \tag{3.11}$$

where $e_{1p}(t)$ is its step response and derived as:

$$e_{1p}(t) = {}^{-1} [H_{1p}(s) / s] \tag{3.12}$$

The exact solution of equation 3.11 requires numerical integration as the step response of a Butterworth low-pass filter consists of exponentially decaying sinusoids [20].

A simpler definition of delay time is due to Elmore [20]. He defines the step delay as the centroid of the impulse response given by

$$\tau_s = \int_0^\infty t.h_{1p}(t)\, dt \tag{3.13a}$$

and shows that it is equal to

$$\tau_s = b_1 - a_1 \tag{3.13b}$$

for filters with monotonic step responses (i.e. optimally damped). The terms b_1 and a_1 are coefficients appearing in $H_{1p}(s)$ expanded in the form

$$H_{1p}(s) = \frac{1 + a_1 s + \ldots + a_n s^n}{1 + b_1 s + \ldots + b_n s^n} \tag{3.14}$$

Butterworth filters have approximately monotonic step responses and delay times calculated using Elmore's method are reported to agree well [20] with the exact method.

Table 3.2 lists the calculated delay times obtained for filters upto the tenth order and cutoff frequencies ranging from the 9th to the 16th harmonics. All the delay times are in milliseconds obtained by dividing equation 3.13b by ω_c.

f(Hz) / n	450	550	650	750
2	0.50	0.41	0.35	0.30
3	0.71	0.58	0.49	0.42
4	0.92	0.76	0.64	0.55
5	1.14	0 94	0.79	0.69
6	1.37	1.12	0.95	0.82
7	1.59	1.30	1.10	0.95
8	1.81	1.48	1.26	1.09
9	2.04	1.67	1.41	1.22
10	2.26	1.85	1.57	1.36

Table 3.2: Calculated delay times (in msec) versus the cutoff frequency for various orders (n) of filter.

3.3.4 The Stop Band Attenuation

The stop band attenuation for the Butterworth filter approximation is given [4,20], in dbm, by the equation

$$| M |_{db} = -20 \log [1 + (\omega/\omega_c)^{2n}]^{0.5} \tag{3.15}$$

where n is the order of the filter.

For various orders of filters, the amplitudes of the filtered neutral voltage frequency components within the stop band can be calculated by the addition, to the unfiltered stop band components, of the filter attenuation at those frequencies as given by equation 3.15. Table 3.3 lists the resultant amplitudes of the four most dominant triplen harmonics within the stop band for various values of n. The unfiltered levels, derived from the amplitude spectrum of figure 3.2a, are also listed for comparison.

f \ n	15th	21st	27th	33rd
0	-8.50	-27.67	-26.34	-21.82
2	-17.90	-42.53	-45.48	-44.41
3	-22.01	-49.78	-54.97	-55.68
4	-26.32	-57.11	-64.51	-66.96
5	-30.71	-64.47	-74.05	-78.25
6	-35.13	-71.83	-83.59	-89.54
7	-39.56	-79.19	-93.14	-100.82
8	-44.00	-86.55	-102.68	-
9	-48.43	-93.91	-	-
10	-52.87	-101.27	-	-

Table 3.3: Calculated amplitudes (in dbm, referenced to the pass band gain) of the four dominant triplen harmonics within the filter stop band for various values of n. The entry for n=0 corresponds to the unfiltered components.

3.3.5 Conclusions

To achieve the accuracy specification of 1% from 0 to 450Hz for the program 'SPECTRUM' (see table 3.1), the foldover errors due to the discretization of the measurands must be reduced to a level at least an order of magnitude lower. This is essential so as to keep the total error in the spectral analysis process - DFT leakage errors (section 2.3) as well as foldover errors - within specification.

From table 3.3 it can be seen that a reduction of foldover distortion to less than 0.1% cannot be achieved even with a 10th order filter and sampling rate of 18 s/c, i.e. the minimum possible sampling rate to give a bandwidth upto the 9th harmonic. In any case, for filter orders greater than six, it becomes increasingly difficult to ensure the linearity of the filter pass band [26] within a close tolerance.

Increasing the sampling rate to 32 s/c (i.e. increasing the foldover frequency to the 16th harmonic) but retaining the filter cutoff at the 9th harmonic, places the dominant 15th harmonic component within the foldover frequency so that a 5th order filter now satisfies the band-limiting criterion to the required accuracy. However, a 6th order filter was chosen, to give a better error margin and because the complexity of its hardware realization is no greater than for a 5th order filter [26], at the expense of a slight degradation in step response. The resultant step response is, from table 3.2, 1.37 ms.

Note that a sampling rate of 30 s/c would have also sufficed in achieving the same specification but was not chosen because of incompatability with Monro's radix-4 FFT algorithm. Recapping, equation 3.4 gives the acceptable window lengths, and hence the sampling rates (section 2.3), as 4,8,16,32 s/c etc.

The anti-aliasing filters were implemented in hardware using a three stage Voltage Controlled Voltage Source (VCVS) realization [26] as shown in figure 3.3. Figure 3.4 illustrates the input buffer circuits for the various current and voltage channels. The VCVS realization was chosen for three reasons which are:

(i) VCVS circuits are easier to tune than other realizations as they can be adjusted over a wide range without the interaction of network parameters.

(ii) Less passive components are necessary per stage than either multiple-feedback, state-variable, or negative impedance convertor [26] circuits.

(iii) The overall temperature sensitivity of the circuit due to capacitor drift (they are the components which have the largest temperature coefficients) can be minimized easily.

Using ±5% tolerance components, a linearity within 0.25 db (±3%) across the pass band was achieved for all the filters. Unfortunately, this is greater than the 1% accuracy required of the spectral analysis system. Rather than optimizing the design with high tolerance components, a simpler and more accurate alternative was chosen. The measured amplitude

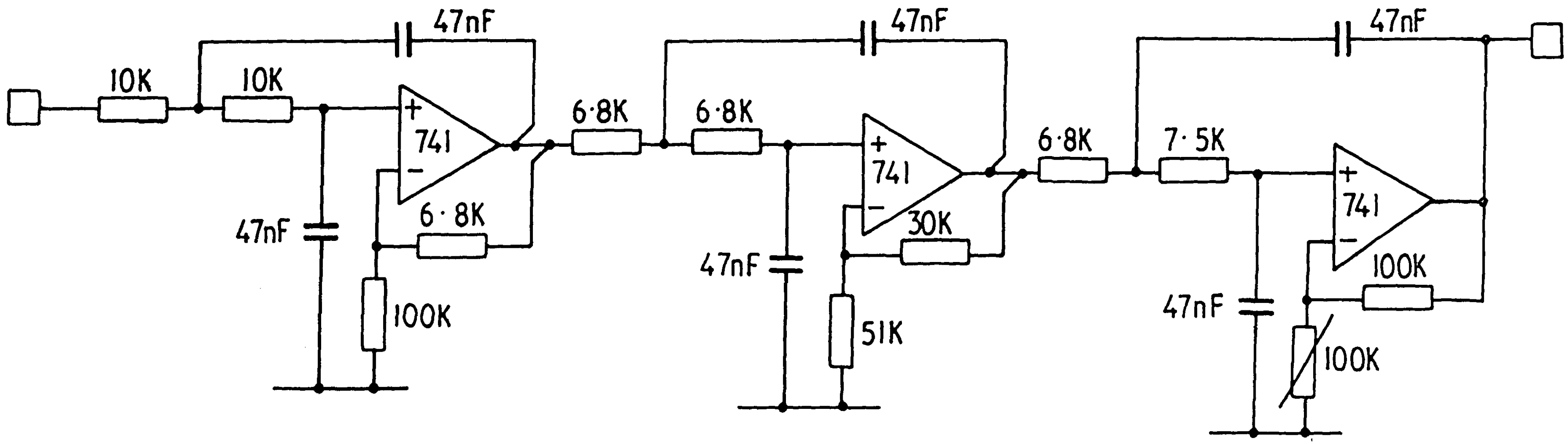

Figure 3.3 : The anti-aliasing filter.

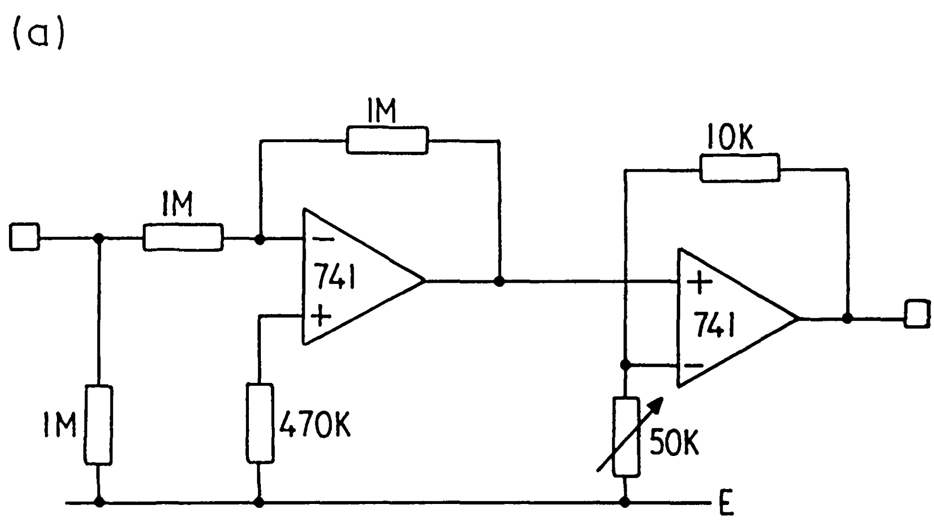

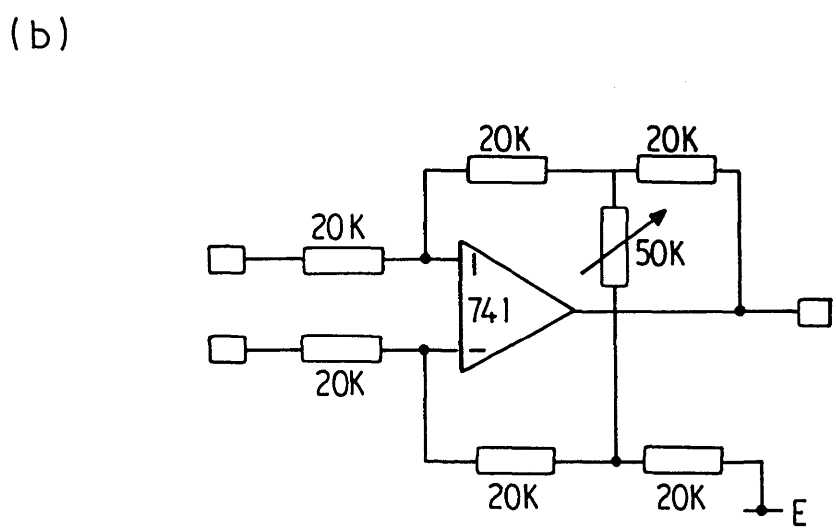

Figure 3.4 : Input buffer circuits for (a) the voltage channels and (b) the current channels.

responses of each of the eight filters were stored in the mini-computer and used to compensate the amplitude spectral estimates directly. A linearity of better than 0.1% was then achieved.

In summary, a sampling rate of 32 s/c and a sixth order Butterworth filter with cutoff at 450Hz were judged optimum for the spectral analysis system. A reduction in amplitude of the first triplen harmonic after the foldover frequency (the 21st) to -71.83 dbm was achieved at the expense of a 1.37ms delay.

For the off-line simulation used, the increase in sampling rate from 18 s/c, the minimum possible for a bandwidth upto 450Hz, to 32 s/c in order to achieve the accuracy specification is perfectly valid. In practice, it will be unlikely because of hardware limitations. However, for a real alternator a sampling frequency of 18 s/c and lower order filters will most probably suffice. There are two reasons for this

(i) In a real alternator the slot harmonics will be at a much higher frequency.

(ii) The high resistance distribution transformer grounding used in all large generators will tend to attenuate high frequency components.

CHAPTER FOUR

The Simulation of Circulating Harmonic Ground Currents in the Armature

This chapter describes the computer simulation of circulating harmonic currents from the armature winding of all large alternators to ground via the stray capacitance to ground of the windings. These harmonic currents are of importance because they effectively represent harmonic emfs enclosing the neutral end of the alternator and as such can be used to protect the complete armature windings against earth faults.

The computer model, its validity, and calculation of its parameters are presented and discussed. In conjuction with experimental results from the laboratory micro-alternator system, the applicability of using these harmonic emfs as protection measurands is examined.

The chapter answers two very important questions which are:

(i) Which of the harmonics are most suitable for deriving a 100% stator earth fault protection.

(ii) How robust these measurands are for variations in system parameters between different generator systems.

4.1 The Simulation Model

The computer simulation is based on a mesh lattice representation of the generator stator windings. In this model each coil, or a group of coils for a coarser model, is simulated by a mesh as illustrated in figure 4.1.

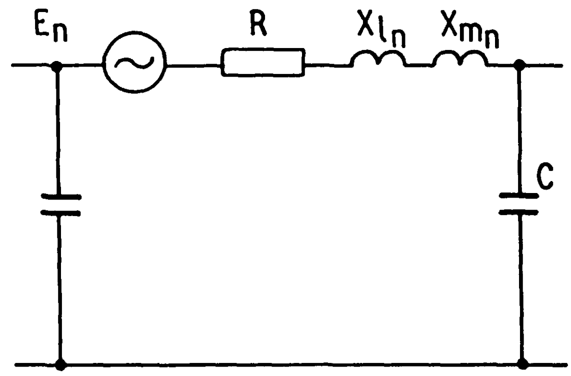

Figure 4.1 Model of a coil or group of coils of the armature windings of a machine.

Each mesh comprises the nth harmonic coil emf, E_n; the coil magnetizing and leakage reactances, X_{m_n} and X_{l_n} respectively, associated with this time harmonic; the coil resistance and its capacitance to ground. Using this basic building block a mesh lattice model can be built up to describe the complete armature windings for any harmonic. Figure 4.1 is essentially a linear decimation of the synchronous machine equivalent circuit extended to account for harmonics as shown in appendices E and F. A multi-harmonic simulation can be obtained by the linear superposition of a number of equivalent circuits, one each for the harmonics to be considered.

Other components of the alternator system - the high impedance neutral grounding resistance, generator transformer, the additional ground at the terminals (the potential transformer) - can be included in the model as additional networks. An earth fault can be simulated by the inclusion of a fault resistance term in parallel with the capacitance to ground of the appropriate coil.

A detailed description of the general nth harmonic mesh lattice model of the armature windings of an alternator connected to the infinite-bus is presented in the next section. Simplifications to the general model for zero-sequence triplen harmonics (e.g. n = 3,9,15 etc.) are presented in section 4.1.2.

4.1.1 The General Model

The general nth harmonic model is illustrated in figure 4.2. It consists of three lattice networks, representing the three phases of the armature winding, with 16 meshes per lattice representing the 16 coils (appendix D) of each phase. The parameters of the model are:

$E_{A_{cn}}, E_{B_{cn}}, E_{C_{cn}}$: nth harmonic coil emfs for the three phases
where c : coil number such that c = 1-16
n : order of time harmonic.

R_G : neutral grounding resistance.

R_P : potential transformer resistance.

$Z_{s_n} = R + j(X_{m_n} + X_{l_n})$: series arm impedance
where R : coil resistance.

X_{m_n} : nth harmonic coil magnetizing reactance.

X_{l_n} : nth harmonic coil leakage reactance.

$Z_{p_n} = -j / \omega_n C$: parallel arm impedance
where C : stray capacitance to ground per coil.

$Z_{e_n} = R_e + jX_{e_n}$: external impedance to the infinite bus.

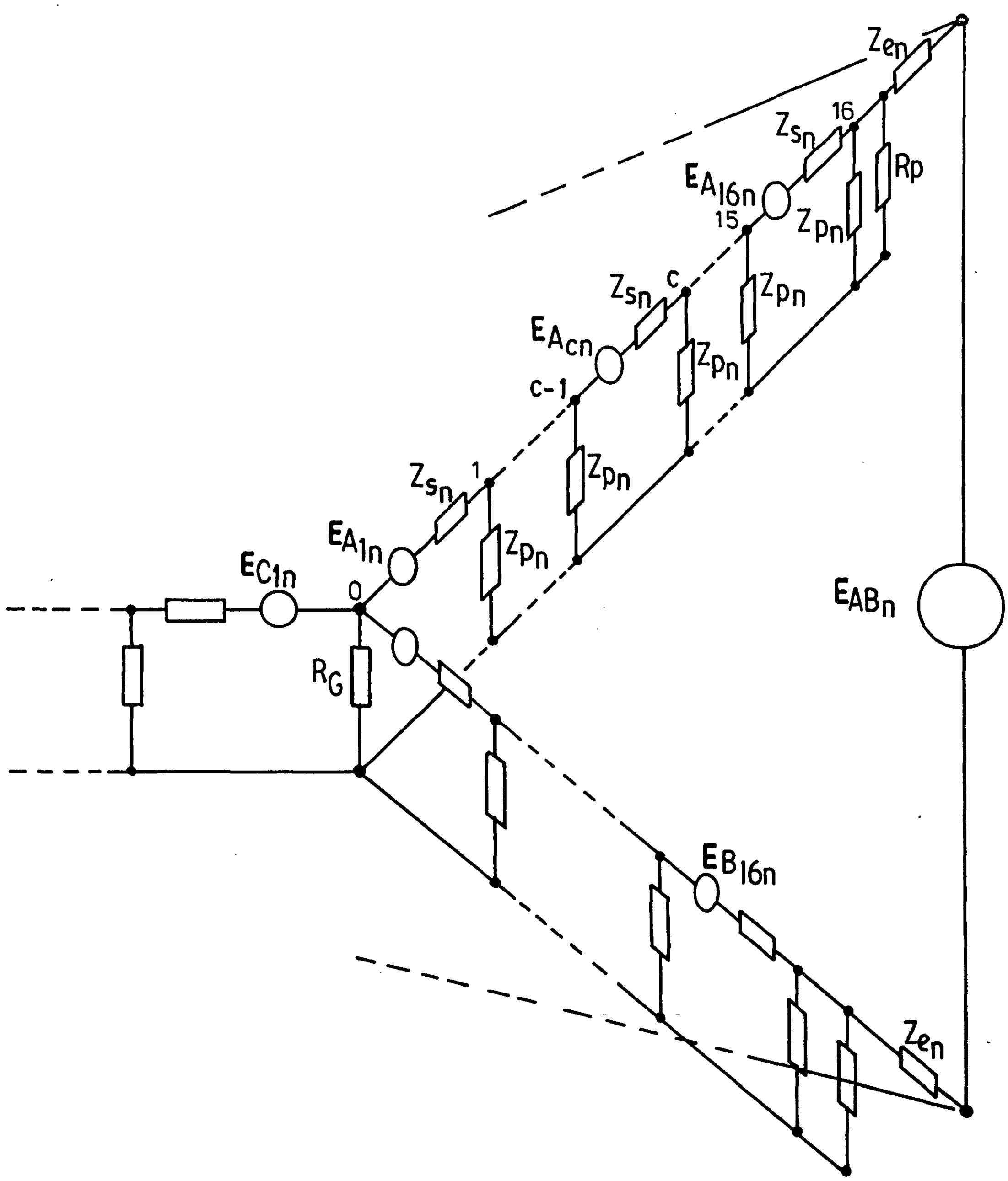

Figure 4.2: The general nth harmonic mesh lattice of the armature windings of the micro-alternator.

The coil impedances are shown to be equal for all the coils in the model which assumes the machine to be a balanced three-phase system. This assumption is largely true for earth faults on alternators with high resistance neutral grounding. The coil capacitance components are also taken as equal which is true in this case as the capacitance has been artificially introduced (see section 3.1.1). The validity of this assumption for real alternators assumes a linear distribution of the stray capacitance to ground along the armature windings and will be examined in more detail, together with other assumptions, in section 4.1.3.

All the externally connected components of the system are represented by simple parallel or series impedances, their capacitive components being neglected. These are neglected for two reasons which are:

(i) Because of the physically small size of the system, the stray capacitance to ground of the generator transformer and the external impedance are negligible in comparison to the artificially boosted capacitance of the alternator stator windings.

(ii) To simplify the model by reducing the number of meshes.

The infinite-bus is represented by the phase-to-phase nth harmonic voltage sources E_{AB_n}, E_{BC_n}, E_{CA_n} as the generator transformer has delta windings on its low voltage side (see section 3.1.1).

Earth faults can be simulated by introducing a fault resistance term in parallel with a suitable parallel arm of the mesh lattice model, as dictated by the fault position. This does of course restrict the possible fault locations to increments of one coil (i.e. at nodes 0,1,..., c-1, c, c+1,..., 15, 16) along the armature, but for the laboratory micro-alternator with 16 coils per phase this is not a significant restriction. A more general method which removes this restriction is to simulate an earth fault as causing a coil mesh to split into two meshes as described by Schlake et al. [71].

4.1.2 The Model for Triplen Harmonics

For zero-sequence triplen harmonics (i.e. 3rd, 9th etc) the general model of figure 4.2 can be simplified in two ways. These are:

(i) As the delta-star generator transformer will represent an open circuit to the triplen harmonics generated by the micro-alternator, the external impedance, Z_{e_n}, and the infinite-bus emfs E_{AB_n}, E_{BC_n}, E_{CA_n} can be neglected.

(ii) For a steady-state simulation, as the triplen harmonic voltage distributions will be identical in each phase (i.e $E_{A_{cn}} = E_{B_{cn}} = E_{C_{cn}}$, where c = 1-16 and n = 3, 9, 15 etc) identical ground currents will flow. Therefore by increasing R_G and R_P to three times their actual value, the three lattice model can be reduced to a one lattice model as shown in figure 4.3.

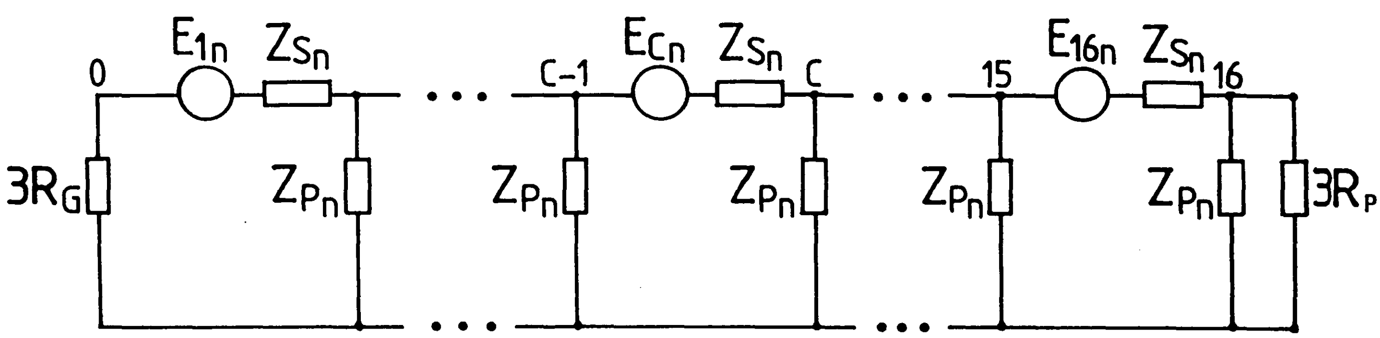

$$E_{cn} = E_{A_{cn}} = E_{B_{cn}} = E_{C_{cn}} \qquad c = 1\text{-}16$$

Figure 4.3 Steady-state triplen harmonic mesh lattice model of the micro-alternator.

For other harmonics, and indeed the fundamental, the general model must be used for the simulation of both the steady-state as well as the earth fault condition. However, for the simulation of the micro-alternator on open circuit, the external impedances and the infinite-bus emfs can be neglected as for the case of triplen harmonics.

4.1.3 The Validity of the Simulation Model

The integrity of the simulation ultimately depends on the validity of the mathematical representation of an armature coil by the mesh of figure 4.1. The validity of this representation is dependent on three assumptions which are:

(i) Negligible magnetic imbalance must exist within the machine.

(ii) The stray capacitance to ground of the windings is assumed to be linearly distributed along it.

(iii) Inter-phase and inter-turn capacitance is assumed negligible.

4.1.3.1 The Assumption of Negligible Magnetic Imbalance

This assumption is of fundamental importance to the simulation because only then can the mesh reactances and coil emf magnitudes be taken as equal and constant with time in all the meshes of the model, as shown mathematically in appendix E.

For the simulation of stator earth faults on alternators with high resistance neutral grounding, and of course under balanced steady-state operation, this assumption is valid. The high resistance neutral grounding typically reduces the maximum possible earth fault current to less than 0.1% of rated current, probably resulting in less imbalance than under normal steady-state operation.

However, for high current armature winding faults, inter-turn and inter-phase faults, the mesh model of figure 4.1 is not applicable and a time variant, transient solution based on the general differential equations [11] of the three-phase synchronous machine must be used. Such time variant solutions have been successfully applied to the computer-aided numerical analysis of short circuits at the terminals of a synchronous machine [67] but not, as far as is known, to the transient analysis of alternators with internal rotor or stator winding faults.

Preliminary research into a computer-aided transient analysis of the circulating armature ground currents in an alternator, based on the general differential equations [11], has been done and is described in appendix G. Essentially, the mesh emf and reactances are replaced by a coil inductance and the time invariant mesh current by a time variant equivalent. The coupling between the various windings, including the damper windings, is included as mutual inductance terms. However, a completion and verification of this study is not within the scope of this research, but is suggested for future work.

4.1.3.2 The Capacitive Distribution of the Armature Windings

For the laboratory micro-alternator, the simulation model is valid because the distribution of the artificially introduced capacitance exactly mirrors that of the model. However, as the micro-alternator is itself a model of the actual machine, the validity of assuming a linear distribution of the capacitance to ground of the armature windings of a true alternator must still be examined.

The assumption of a linear distribution of the capacitance to ground implies a uniform and consistent geometry for the armature windings within the stator body. Clearly within the slots this is true but not at the end-winding regions. In a large alternator the slots will contribute the dominant component of capacitance to ground of the armature because:

(i) As the ratio of the axial length to diameter of the stator of a large alternator is typically of the order of 10:1 [44], the greater proportion of the winding will be within the slots.

(ii) The end windings are not closely enclosed by the stator core metal and hence their small capacitive contribution will be further reduced.

Inter-turn capacitances can be neglected for the following reasons:

(i) The electrical shielding properties of the core metal will minimize inter-turn capacitances between conductors in adjacent slots.

(ii) Inter-turn capacitance between conductors in the same slot is outweighed by their capacitance to ground components, for a typical conductor height to width ratio of 3:1, by a factor of 26:1 [71].

(iii) Because the third harmonic voltage distribution will be identical for all three phases of the machine, there will not be much emf to drive current through the small inter-phase capacitances.

4.2 The Method of Solution

Representing the alternator armature windings by a mesh lattice model reduces the calculation of the circulating harmonic ground currents and, subsequently the neutral and line end harmonic voltages, to the solution of a set of simultaneous complex linear equations.

4.2.1 The Solution for the General Case

The A-phase equations of the general model, shown in figure 4.2, are now derived. The matrix equation for the complete model can then be written by symmetry.

Let the nth harmonic mesh currents for the three phases be

$I_{A_{cn}}$, $I_{B_{cn}}$, $I_{C_{cn}}$ where c = 1-16

and for the meshes relating the infinite-bus phase-to-phase emfs and the phase lattices, I_{AB_n}, I_{BC_n}, I_{CA_n}.

Then for the first mesh in the A-phase lattice the mesh equation is

$$(R_G + Z_{s_n} + Z_{p_n})I_{A_{1n}} - Z_{p_n}I_{A_{2n}} - R_G(I_{B_{1n}} + I_{C_{1n}}) - Z_{s_n}(I_{AB_n} - I_{BC_n}) = E_{A_{1n}} \tag{4.1}$$

For meshes 2 to 15 the mesh equations are given by

$$(2Z_{p_n} + Z_{s_n})I_{A_{cn}} - Z_{p_n}[I_{A_{(c-1)n}} + I_{A_{(c+1)n}}] - Z_{s_n}(I_{AB_n} - I_{BC_n}) = E_{A_{cn}} \tag{4.2}$$

where c = 2-14

The mesh equation for mesh 16 is

$$[Z_{p_n} + Z_{s_n} + Z_{p_n}R_P/(Z_{p_n}+R_P)]I_{A_{16n}} - Z_{p_n}I_{A_{15n}} - Z_{s_n}(I_{AB_n} - I_{BC_n}) = E_{A_{16n}} \tag{4.3}$$

Finally, the mesh equation for the mesh relating phases A and B and the infinite-bus emf E_{AB_n}, is

$$(32Z_{s_n} + 2Z_{e_n})I_{AB_n} + Z_{s_n}\sum_c I_{A_{cn}} - Z_{s_n}\sum_c I_{B_{cn}} - 16Z_{s_n}(I_{BC_n} + I_{CA_n}) = \sum_c E_{A_{cn}} - \sum_c E_{B_{cn}} + E_{AB_n}$$

or

$$2(Z_{a_n} + Z_{e_n})I_{AB_n} + Z_{s_n}\sum_c I_{A_{cn}} - Z_{s_n}\sum_c I_{B_{cn}} - Z_{a_n}(I_{BC_n} + I_{CA_n}) = E_{A_n} - E_{B_n} + E_{AB_n} \qquad c = 1, \ldots, 16 \tag{4.4}$$

where Z_{a_n} : nth harmonic armature impedance

E_{A_n}, E_{B_n} : nth harmonic A and B phase terminal voltages.

The matrix equation for the complete model can then be formulated by symmetry as

$$[I][Z] = [E] \tag{4.5}$$

where [Z] is the system impedance matrix of dimension 51 x 51 and [I] and [E] are the 51 element current and voltage vectors repectively.

The form of [I] and [E] are such that

$$[I]^T = [I_{A_{1n}}, \ldots, I_{A_{16n}}, I_{B_{1n}}, \ldots, I_{B_{16n}}, I_{C_{1n}}, \ldots, I_{C_{16n}}, I_{AB_n}, I_{BC_n}, I_{CA_n}] \tag{4.6}$$

and

$$[E]^T = [E_{A_{1n}}, \ldots, E_{A_{16n}}, E_{B_{1n}}, \ldots, E_{B_{16n}}, E_{C_{1n}}, \ldots, E_{AB_n}', E_{BC_n}', E_{CA_n}'] \tag{4.7}$$

where $E_{XY_n}' = E_{X_n} - E_{Y_n} + E_{XY_n}$ (4.8)

for X = A,B,C and Y = B,C,A respectively.

The impedance matrix is of the form :

$$[Z] = \quad \begin{array}{r}
 \\ 1 \\ 2 \\ \vdots \\ 15 \\ 16 \\ 17 \\ 18 \\ \vdots \\ 31 \\ 32 \\ 33 \\ 34 \\ \vdots \\ 47 \\ 48 \\ 49 \\ 50 \\ 51
\end{array}
\begin{array}{l}
1 \qquad\qquad\qquad\qquad 17 \qquad\qquad\qquad\qquad 33 \qquad\qquad\qquad\qquad 51 \\
\left[\begin{array}{llllllllllll}
A & I & & & & E & & & & E & & \\
I & B & I & & & & & & & & & \\
 & \ddots & \ddots & \ddots & & & & & & & & \\
 & & I & B & I & & & & & & & \\
 & & & I & C & & & & & & & \\
E & & & & & A & I & & & E & & \\
 & & & & & I & B & I & & & & \\
 & & & & & & \ddots & \ddots & \ddots & & & \\
 & & & & & & I & B & I & & & \\
 & & & & & & & I & C & & & \\
E & & & & & E & & & & A & I & \\
 & & & & & & & & & I & B & I \\
 & & & & & & & & & & \ddots & \ddots \\
 & & & & & & & & & & I\;B\;I & \\
 & & & & & & & & & & I\;C & \\
F \cdots F & G \cdots G & & & & & & & & & & D\;H\;H \\
 & F \cdots F & G \cdots G & & & & & & & & & H\;D\;H \\
G \cdots G & & F \cdots F & & & & & & & & & H\;H\;D
\end{array}\right]
\end{array} \tag{4.9}$$

where

$$A = R_G + Z_{s_n} + Z_{p_n} \tag{4.10a}$$

$$B = 2Z_{p_n} + Z_{s_n} \tag{4.10b}$$

$$C = Z_{p_n} + Z_{s_n} + Z_{p_n} R_P / (Z_{p_n} + R_P) \tag{4.10c}$$

$$D = 2(Z_{a_n} + Z_{e_n}) \tag{4.10d}$$

$$E = -R_G \tag{4.10e}$$

$$F = -G = Z_{s_n} \tag{4.10f}$$

$$H = -Z_{a_n} \tag{4.10g}$$

$$I = -Z_{p_n} \tag{4.10h}$$

4.2.2 The Solution for Triplen Harmonics

For the particular case of zero-sequence triplen harmonics or for the alternator on open circuit, equation 4.5 can be simplified by deleting elements 49-51, and rows and columns 49-51 from the voltage, current vectors (equations 4.6, 4.7) and the impedance matrix (equation 4.9) respectively.

For steady-state conditions an even greater simplification results as indicated by figure 4.3. Equation 4.5 reduces to a system of 16 linear complex simultaneous equations. The voltage and current vectors will be such that

$$[I]^T = [I_{1n}, \ldots, I_{16n}] \tag{4.11}$$

$$[E]^T = [E_{1n}, \ldots, E_{16n}] \tag{4.12}$$

The impedance matrix reduces to

$$[Z] = \begin{array}{cc} & \begin{array}{ccccc} 1 & & \cdots & & 16 \end{array} \\ \begin{array}{c} 1 \\ \\ \vdots \\ \\ 16 \end{array} & \begin{bmatrix} J & & & & \\ I & B & I & & \\ & \ddots & \ddots & \ddots & \\ & & I & B & I \\ & & & I & K \end{bmatrix} \end{array} \tag{4.13}$$

where $J = A + 2R_G$ (4.14a)

$$K = Z_{p_n} + Z_{s_n} + Z_{p_n} 3R_P / (Z_{p_n} + 3R_P) \tag{4.14b}$$

4.2.3 The Simulation of an Earth Fault

An earth fault anywhere along the armature winding can be simulated by modifying, to include the fault resistance term R_f, the appropriate elements in [Z] affected by the faulted coil. Three distinct cases need to be considered. They are:

(i) An earth fault at the neutral.

(ii) An earth fault on one phase at the terminals of the machine.

(iii) An earth fault between these two extremeties.

For an earth fault at the neutral the self-impedances, **A**, and the neutral impedances, **E**, of the meshes involving the neutral must be modified. If A_f and E_f are the faulted equivalent terms then

$$A_f = R_G R_f/(R_G + R_f) + Z_{s_n} + Z_{p_n} \tag{4.15}$$

and $$E_f = -R_G R_f \; / \; (R_G + R_f) \tag{4.16}$$

For small values of R_f, however, R_G can be replaced by R_f with minimal loss of accuracy and

$$A_f = R_f + Z_{s_n} + Z_{p_n} \tag{4.15a}$$

$$E_f = -R_f \tag{4.16a}$$

At the other extreme, for an earth fault at the terminals of the machine, the self-impedance of the last mesh in the lattice representing the faulted phase must be changed to

$$C_f = Z[m,m] = Z_{p_n} + Z_{s_n} + Z_{p_n} R_P R_f/(Z_{p_n} R_P + Z_{p_n} R_f + R_P R_f) \tag{4.17}$$

where m = 16, 32 or 48 for a fault on either the A, B or C phases respectively.

As for the previous case, for small values of R_f, equation 4.17 can be simplfied to

$$C_f = Z_{p_n} + Z_{s_n} + R_f = A_f \tag{4.17a}$$

For the third case, four elements in the impedance matrix need to be modified. These will be the two self-impedances of the meshes including the faulted node, and the two mutual terms which refer to it.

The faulted self-impedance terms are

$$Z[i+1,i+1] = Z[i,i] = B_f \tag{4.18}$$

$$= Z_{p_n} + Z_{s_n} + Z_{p_n}R_f/(Z_{p_n}+R_f)$$

where $i = 16k + m$ for $2 < m < 15$ and $k = 0$, 1 or 2 for a fault on the A, B or C phase respectively.

The faulted mutual-impedance terms are

$$Z[i,i+1] = Z[i+1,m] = I_f = -Z_{p_n}R_f / (Z_{p_n}+R_f) \tag{4.19}$$

Again for small values of R_f, equations 4.18 and 4.19 can be simplified to give

$$B_f = Z_{p_n} + Z_{s_n} + R_f = A_f = C_f \tag{4.18a}$$

and $$I_f = -R_f = E_f \tag{4.19a}$$

4.2.4 Calculation of the Mesh Parameters

Referring to figure 4.1, the main mesh parameters that need to be determined for each coil are E_n, X_{m_n} and X_{1_n}. The coil resistance can be readily determined as 0.0022 ohm by dividing the total phase resistance given in appendix D by the total number of coils per phase. The capacitance to ground per coil is, of course, known to be 0.0147μF.

4.2.4.1 The Mesh Emf Magnitude

For a symmetrical three-phase winding and assuming a uniform airgap permeance, the magnitudes of all the coil emfs are identical as shown by equation E.22. Therefore, the calculation of the mesh emf vectors involves the derivation of the coil emf magnitude and its phase distribution along the armature.

The magnitude of the mesh emf vectors can be derived in two ways. They are:

(i) From the measured value of the nth harmonic terminal emf and a knowledge of the nth harmonic distribution factor (see appendix E) of the armature winding.

(ii) By calculation from a knowledge of the machine parameters as given by equation E.22 and E.23.

The distribution factor for a distributed winding is by definition (appendix E) the ratio of the vector to the arithmetic sum of the emfs of the coils constituting it. Therefore if both the distribution factor and the measured nth harmonic terminal emf (i.e. the vector sum) are known, the arithmetic sum and consequently the coil emf can be calculated as

$$E_n = E_{a_n}'(K_{d_n})_a \;/\; N_{c_a} \tag{4.20}$$

where E_{a_n}' : measured nth harmonic terminal emf

$(K_{d_n})_a$: nth harmonic distribution factor of the armature winding

N_{c_a} = total number of armature coils per phase and $E_n = |E_{A_{cn}}| = |E_{B_{cn}}| = |E_{C_{cn}}| \quad c = 1, \ldots, 16.$

Table 4.1 lists measured and calculated (equation E.22) values of major harmonic components of the open-circuit terminal emfs of the alternator, which can be used to derive the coil emf magnitude.

n	Open-circuit values (p.u.)	
	E_{a_n}	E_{a_n}'
3	.0237	.0445
5	.0103	.0012
7	.0011	.0029
9	.0036	.0056

Table 4.1: Calculated and measured values of the main harmonic components of the open-circuit terminal emf

Note that measured and calculated results do not correlate accurately, this also being noted by Hanna [30]. For the purposes of this simulation, therefore, coil emfs calculated from measured terminal emf values will be used so as to obtain better correlation with experimental results.

Figure 4.4 illustrates the variation in the third harmonic component of the terminal emf with power, and is used to calculate the mesh emfs for correlation with experimental results taken on load.

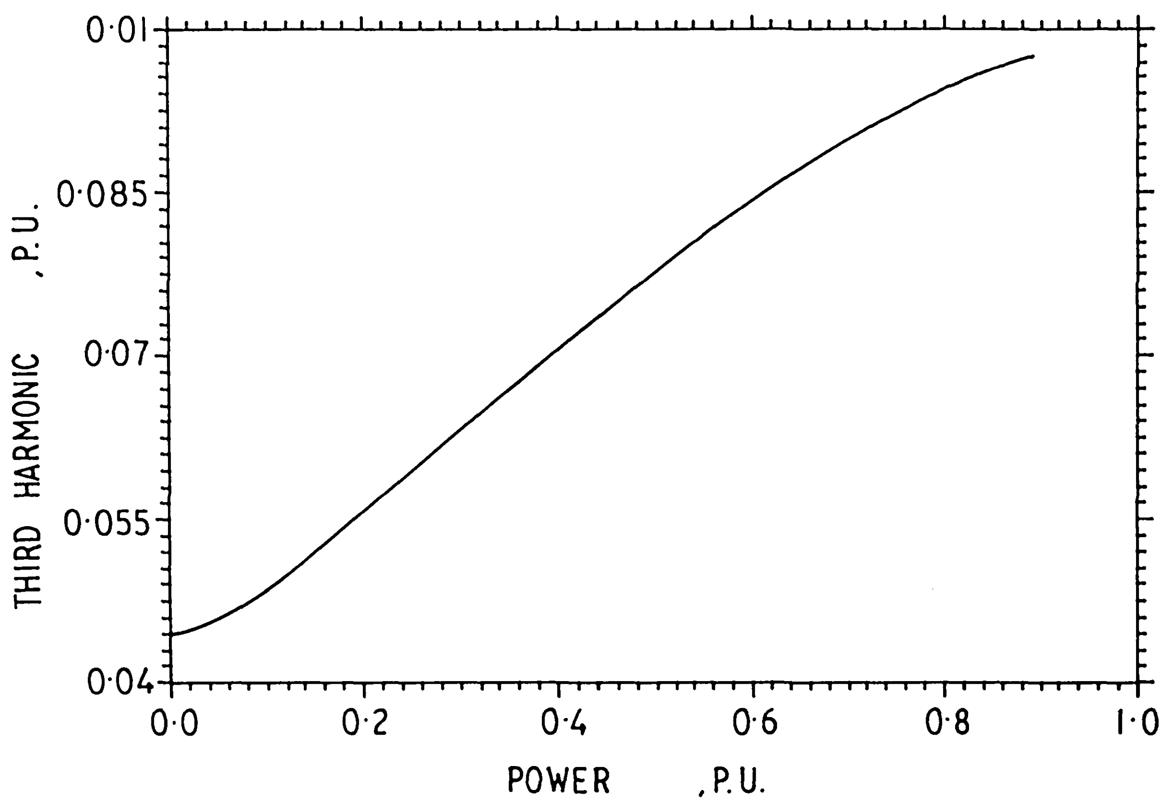

Figure 4.4: Variation of the third harmonic component of the terminal emf with power at unity power factor.

4.2.4.2 The Phase Distribution of the Mesh Emfs

The phase distribution of the coil voltages is a function of the distribution of the armature windings in the stator slots and the slot angle in electrical degrees (360 electrical degrees refers to one pole pitch while mechanical degrees refer to the machine bore). The slot angle for any slot is given as

$$\theta_{s_n} = (s-1)n\ \alpha_a \tag{4.21}$$

where s : slot number..

α_a : slot angle for the fundamental
$= 2\pi p/Q_a$ electrical degrees.

p : number of pole pairs.

Q_a : total number of slots in the armature.

The distribution of the armature windings is illustrated in figure D.1. It can be seen that each phase-belt consists of four coil groups, one coil group per pole, each consisting of two consecutive coils with a coil pitch of 10/12 arranged as a double-layer lap winding [3,44]. Therefore for the fundamental, the slot angles, as given by equation 4.21, for the first four coils are 0, 15, 195 and 180 degrees respectively. As coils three and four are connected in reverse order to coils one and two, the voltage phase distribution will be 0, 15, 15 and 0 degrees for the first four coils respectively.

This result can be stated formally for the general case as

$$\theta_{A_{cn}} = (s-1)n\,\alpha_a \qquad c = 1,2,5,6 \qquad (4.22a)$$

$$= (s-1)n\,\alpha_a - 180n \qquad c = 3,4,7,8 \qquad (4.22b)$$

$$= 30n + (s-1)n\,\alpha_a \qquad c = 9,10,13,14 \qquad (4.22c)$$

$$= 30n + (s-1)n\,\alpha_a - 180n \qquad c = 11,12,15,16 \qquad (4.22d)$$

$$\theta_{B_{cn}} = \theta_{A_{cn}} - 120n \qquad (4.22e)$$

$$\theta_{C_{cn}} = \theta_{A_{cn}} - 240n \qquad (4.22f)$$

where $\theta_{A_{cn}}$, $\theta_{B_{cn}}$, $\theta_{C_{cn}}$ are the coil emf phase distributions of the three phases such that

$$E_{X_{cn}} = E_{X_{cn}} e^{j\theta_{X_{cn}}} \quad \text{for } X = A,B,C$$

The factor 30n in equations 4.22c and d takes into account the relative angular displacement of the two phase-belts comprising each phase winding.

The phase distribution of the fundamental, third, fifth and ninth harmonic components of the coil emfs are illustrated in figures 4.5a-d respectively.

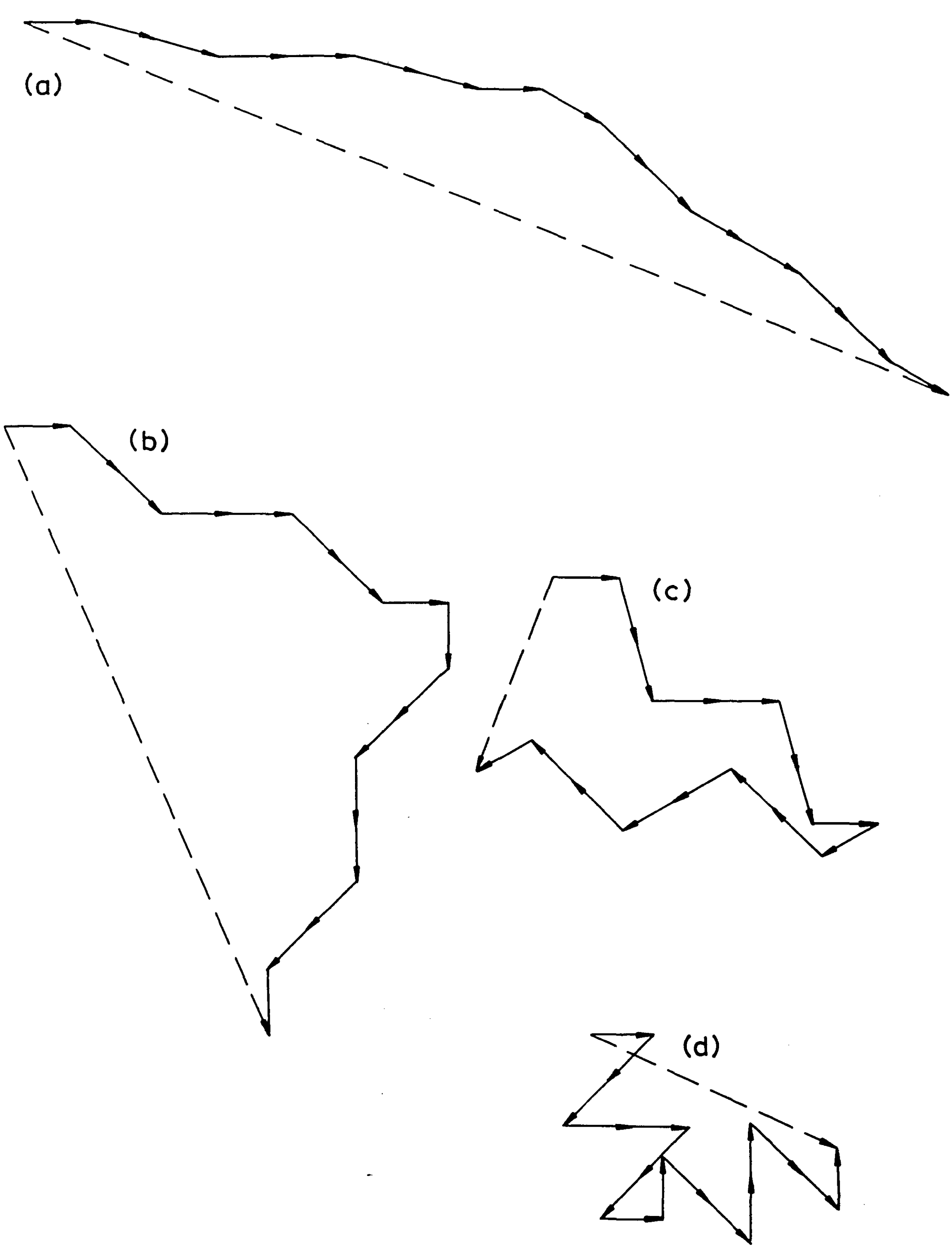

Figure 4.5: The phase distributions of the (a) fundamental, (b) third, (c) fifth, and (d) ninth harmonic components of the coil emfs.

4.2.4.3 The nth Harmonic Mesh Magnetizing and Leakage Reactance

The nth harmonic mesh magnetizing reactance can be derived from equation F.3 (the equivalent reactance of the complete winding) as

$$X_{m_{cn}} = X_{m_n} / N_{c_a}$$

$$= 3\mu_o f \tau l (T_{w_v})_a^2 / (4\pi\delta_e v^2) \tag{4.23}$$

The nth harmonic leakage reactance consists of three components such that

$$X_{1_n} = X_{slot_n} + X_{e_n} + X_{d_n} \tag{4.24}$$

where X_{slot_n} : slot leakage reactance component.

X_{e_n} : end-winding leakage reactance component.

X_{d_n} : differential leakage reactance component.

However, for the purposes of the simulation program, the components X_{e_n} and X_{d_n} are ignored and the leakage reactance is assumed to consist only of the slot leakage reactance component. The validity of this assumption is apparent with reference to table F.1 which lists the calculated values of all the reactance components upto the 13th harmonic. It can be seen that X_{e_n} and X_{d_n} represent under one percent of the total leakage reactance for all the harmonics.

Therefore, from equation F.15, the leakage reactance component for each individual coil can be written as

$$X_{1_{cn}} = X_{slot_n} / N_{c_a}$$

$$= \pi f n \mu_o l N_a^2 (1.48 + 38.7k_{s_n}) / (8S_a) \tag{4.25}$$

4.3 The Simulation Results

The computer simulation in conjunction with experimental verification from the spectrum analysis described in section 3.2 was used to examine the behaviour of the harmonic components of the terminal and neutral emfs of the micro-alternator under various conditions. The two objectives of the study are:

(i) To ascertain which harmonic components can be used as the primary measurands for a 100% stator earth fault protection.

(ii) To examine the effect of the alternator system parameters on the robustness of the measurands.

4.3.1 The Steady-state Condition

The influence of the following system parameters on the terminal and neutral harmonic emf components were investigated.

(i) The grounding resistance.

(ii) A possible additional ground reference (section 3.1.1) at the terminals of the machine.

(iii) The capacitance to ground of the armature windings.

4.3.1.1 The Influence of the Neutral Grounding Resistance

Figures 4.6a and b illustrate the variation of the open-circuit third and ninth harmonic components, respectively, of the terminal and neutral emfs versus the neutral grounding resistance. The calculated results were all obtained with the value of the respective coil emfs derived from measured open-circuit triplen harmonic terminal emfs (see table 4.1) averaged over the three phases, as given by equation 4.20.

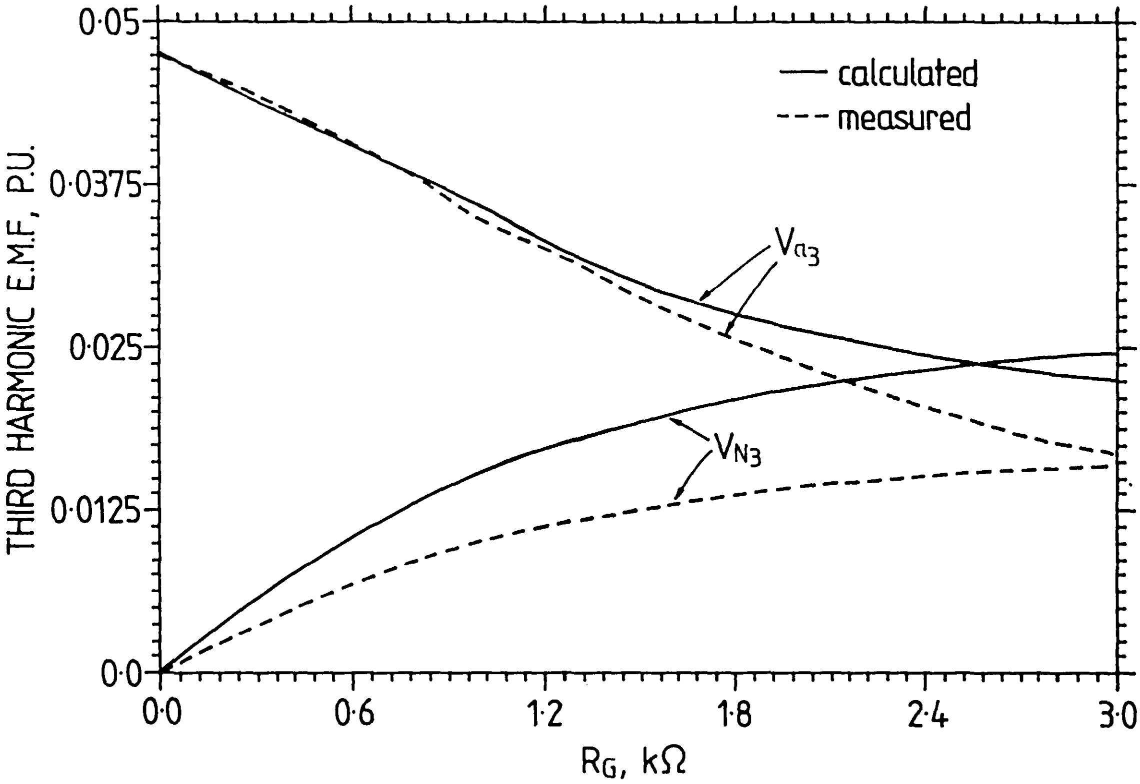

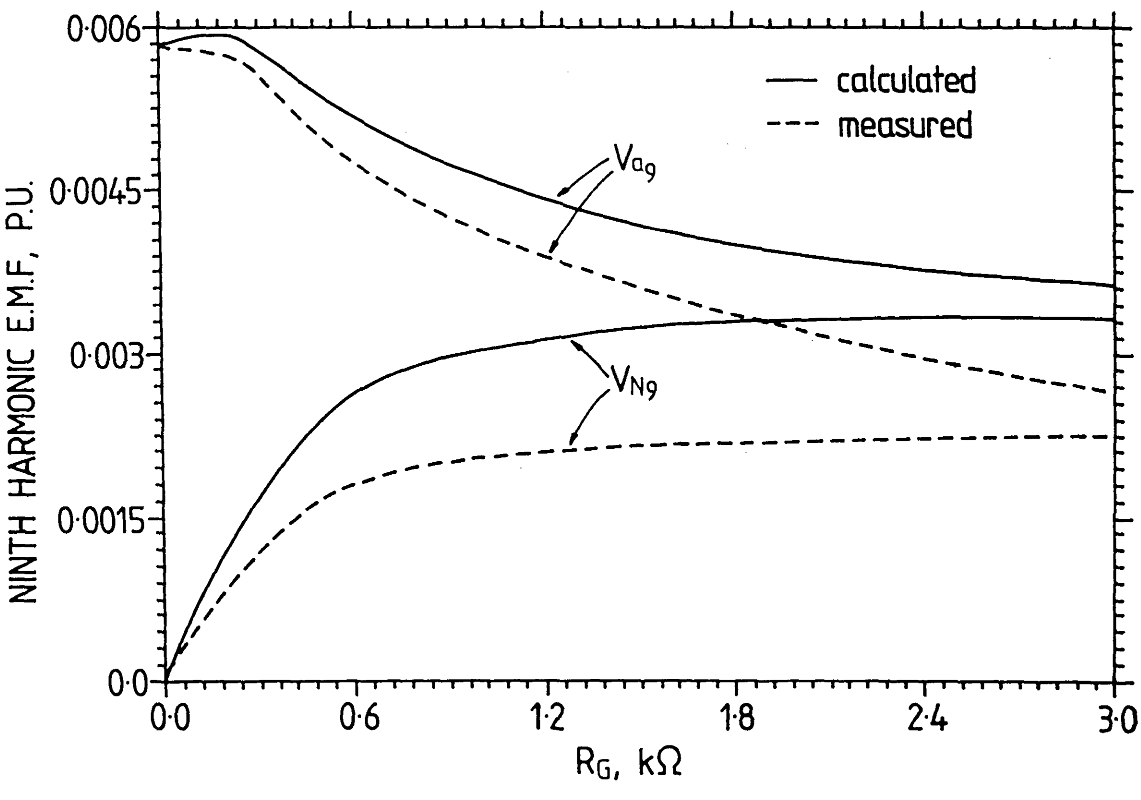

Figure 4.6: Variation of the (a) third and (b) ninth harmonic components of the terminal and neutral emfs versus the neutral grounding resistance.

The curves illustrate two very important features. They are:

(i) An increase in the value of the neutral grounding resistance results in an increase at the neutral and a decrease at the terminals of the third and ninth harmonic emf components, so as to keep their signal energy constant.

(ii) The magnitude of these harmonic components at the neutral is not significantly affected by the value of R_G provided it is of the order of 10^3 ohm.

The fifth and seventh harmonics, not being zero-sequence components, sum to zero at the neutral and hence their values at the terminals of the machine remain constant irrespective of the value of R_G. However, with the alternator synchronised to the infinite-bus their levels were found to be very unpredictable and strongly influenced by the level of harmonic distortion in the supply.

On the other hand the third and ninth harmonic emfs, both at the terminals and neutral of the machine, were measured to be essentially unchanged with the alternator synchronised to the infinite-bus but on minimal load. Obviously this is due to the generator transformer presenting an open circuit to these harmonics, but it also proves the validity of neglecting the capacitive components to earth in the simulation model, of the generator transformer and the external transformer.

The degree of match between measured and computed results is close considering the extremely low levels of the harmonics being measured. This is especially true of the ninth harmonic results in figure 4.6b (and further on in figure 4.7b) where measurements were made at the accuracy and resolution limits of the measurement system. Such sensitivity and resolution is characteristic of windowed and interpolated DFT spectrum analysis.

4.3.1.2 The Effect of a Ground Reference at the Alternator Terminals

Figures 4.7a and b illustrate, for $R_G = R_P$ which is the normal British practice [94], the effect of an additional ground (potential transformer) at the terminals of the micro-alternator on the open-circuit third and ninth harmonics at the neutral and terminals.

The results illustrate that the additional ground does not compromise the steady-state values of these harmonics. Specifically two features are of note. They are:

(i) The third and ninth harmonic components of the terminal and neutral emfs are approximately independent of the values of the grounding resistances.

(ii) Their order of magnitude is unchanged.

An alternative connection for the potential transformer is to connect it from the terminals of the machine to the neutral though this is not a recommended procedure [80,81] and is not British practice [94]. Schlake et al. [71] have investigated the effect of this alternative connection, using similar methods, and shown that it does not reduce the neutral third harmonic significantly.

As for the previous section measured and calculated results agree well and the effect of the infinite-bus was measured to be negligible.

4.3.1.3 The Capacitance to Ground

Figure 4.8 shows the variation of the third harmonic component of the neutral and terminal emfs with the capacitance to ground of the armature windings for a grounding resistance of 1k ohm. The equivalent results for the ninth harmonic are very similar.

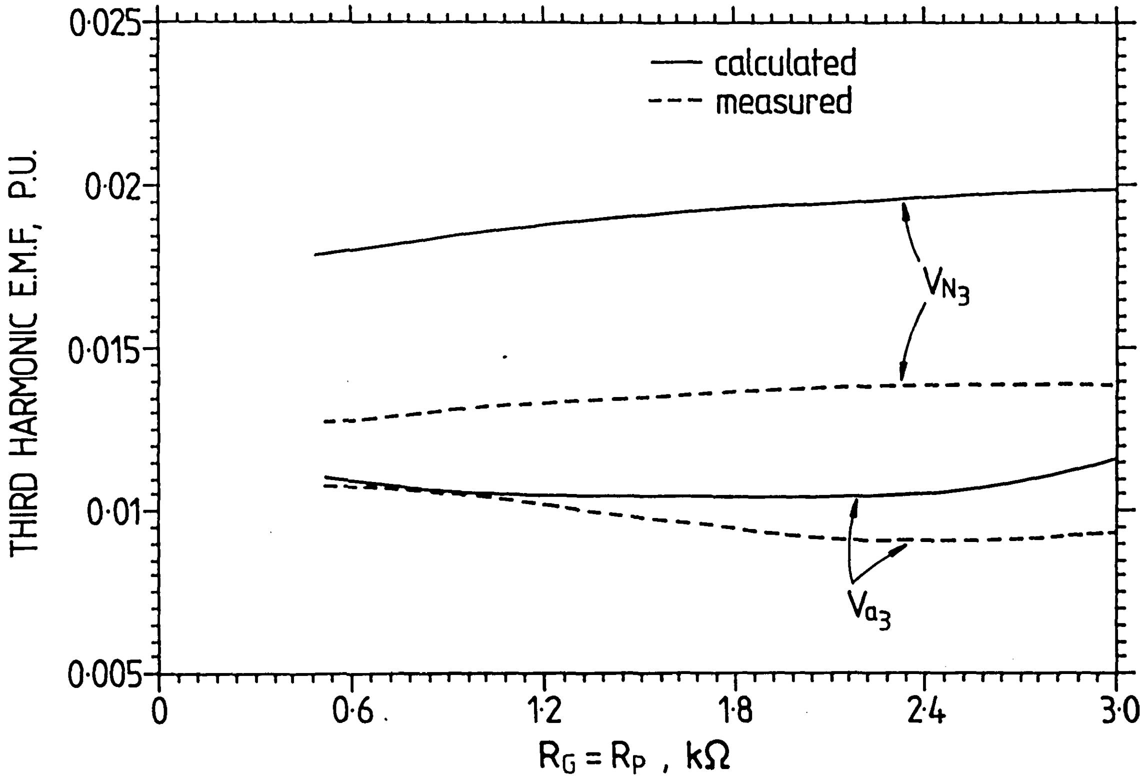

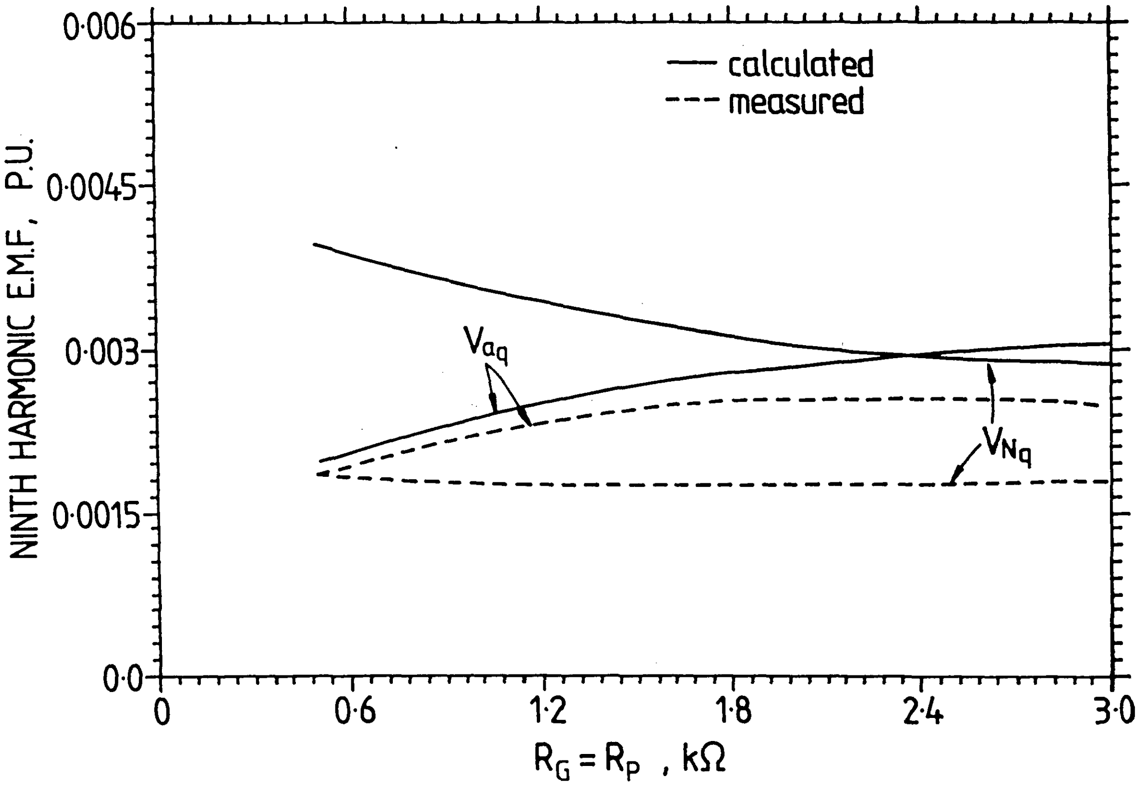

Figure 4.7: Effect of an additional ground at the alternator terminals on the variation of the (a) third and (b) ninth harmonic components versus grounding resistance.

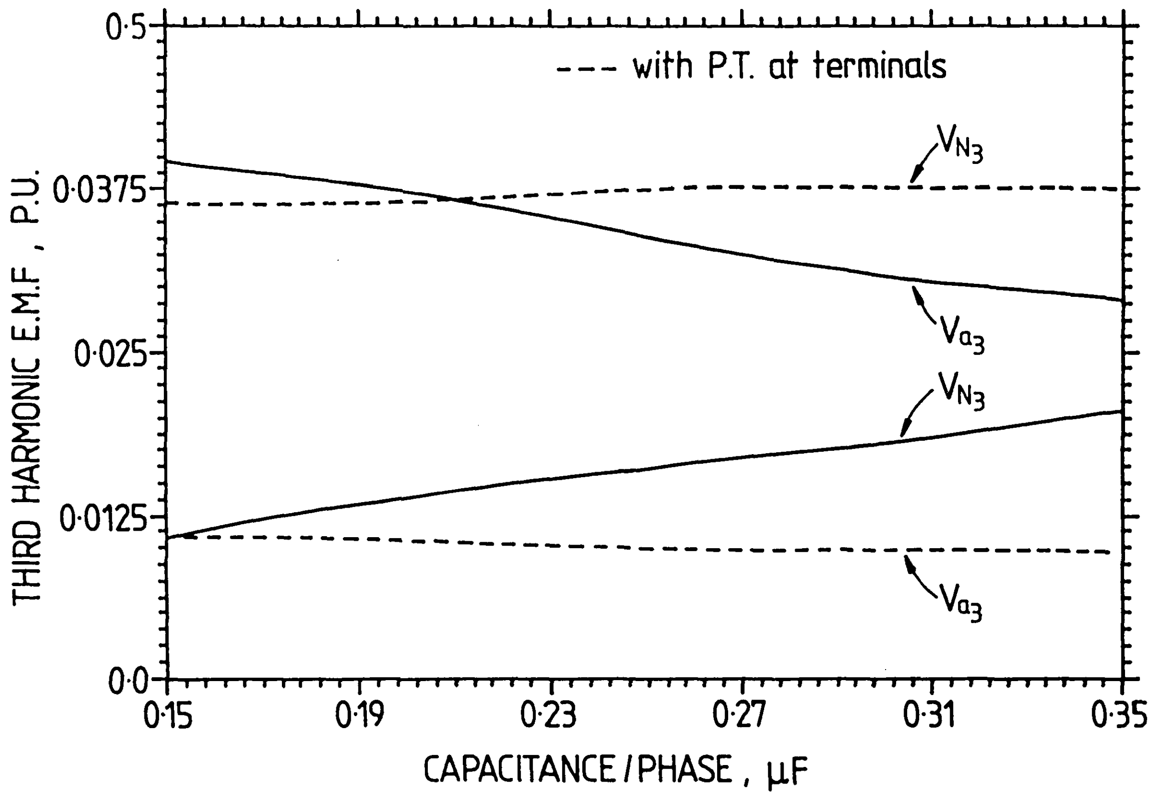

Figure 4.8: Variation of the third harmonic components of the neutral and terminal emfs with the capacitance to ground of the armature windings for R_G=1k ohm.

It illustrates two very important results which are:

(i) A variation in the armature stray capacitance to ground of upto 50% (most large alternators have a measured value in the range 0.2µF - 0.25 µF per phase [28,71,84,88,93], because higher ratings are achieved not by an increase in size but by a higher specific loading) between alternators does not seriously affect the order of magnitude of the neutral third and ninth harmonics.

(ii) The additional ground at the terminals of the machine, by providing an additional path to earth, reduces the importance of the winding capacitances as paths for these two circulating triplen harmonic ground currents.

These results were not verified by experiment because of the practical difficulty of modifying the alternator coil capacitances, but there is no reason to doubt them because of the close match between computed and measured results in figures 4.6 and 4.7.

4.3.2 The Simulation of an Earth Fault

4.3.2.1 Variation of Neutral and Terminal Triplen Harmonics

Figures 4.9a and b illustrate the variation of the terminal and neutral third harmonic emfs for earth faults on one phase of the armature windings and a neutral grounding resistance of 1k ohm. The results were taken at 0.8 p.u. power, 1 p.f. Calculated results were obtained with the value of the coil emfs derived from figure 4.4.

Figures 4.9a and b show that as the fault position moves from the neutral to the terminals of the machine, the neutral third harmonic increases from zero and tends to the prefault terminal value, while the terminal third harmonic emf decreases from it and tends to zero. Obviously, at a certain position (marked by a dashed line in figure 4.9a) the postfault third harmonic neutral emf will be exactly equal to its steady-state prefault level. This point will be called the ´neutral´ third harmonic null point. (The steady-state prefault neutral third harmonic emf can be obtained for any value of R_G and alternator power setting at unity power factor from figures 4.4 and 4.6a).

A similar null point will also exist if both the neutral and terminal third harmonic emfs are used, in a voltage comparison scheme (section 5.1.2), as the principal protection measurands. This null point will be called the ´voltage comparision´ third harmonic null point to distinguish it from the neutral third harmonic null.

Figures 4.9c and d illustrate the equivalent calculated results for the ninth harmonic emfs. Unlike the reasonably smooth variation of the

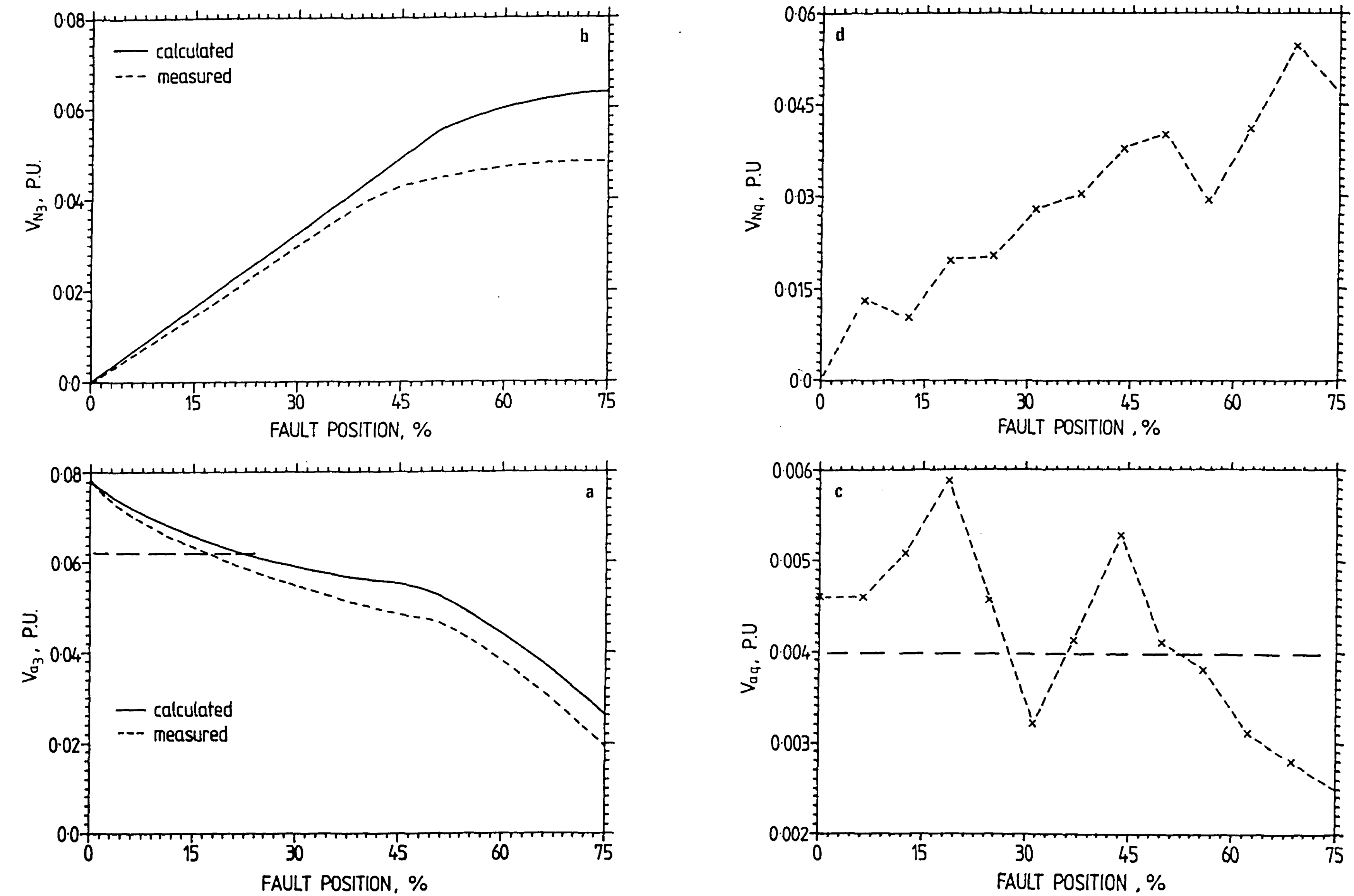

Figure 4.9 : Variation of the terminal and neutral third (a and b) and ninth (c and d) harmonic emfs with fault position.

third harmonic components versus fault position, the variation of the ninth harmonic is piece-wise continuous because of its very large slot angle of 135 degrees compared to the third harmonic value of 45 degrees (see figure 4.5). The practical effect of this uneven voltage variation is to give more than one null point for the ninth harmonic emf component as can be seen by the dashed line, representing its prefault value at the neutral, in figure 4.9c.

From a protection point of view, the position of the nulls is very important as they represent blind spots where the harmonic measurands will not register an earth fault. In the next section, the variation of the third and ninth harmonic null point positions with the system parameters will be investigated.

4.3.2.2 The Position of the Null Points

Figures 4.10a-d illustrate the variation of the third and ninth harmonic null points along the armature winding versus the neutral grounding resistance with and without a ground at the terminals of the machine.

The three most important conclusions are:

(i) The variation of both the neutral and voltage comparision third harmonic null points, and the main ninth harmonic null point (figure 4.10a) are very similar and therefore one measurand cannot be used to cover for the others null point. The presence of an additional terminal ground does apparently make this possible by separating the third and main ninth harmonic null points, (figure 4.9b and d) but this advantage is offset by the presence of the other two ninth harmonic null points.

(ii) The separation of the voltage comparison third harmonic null from the neutral is slightly greater than that of the neutral null point.

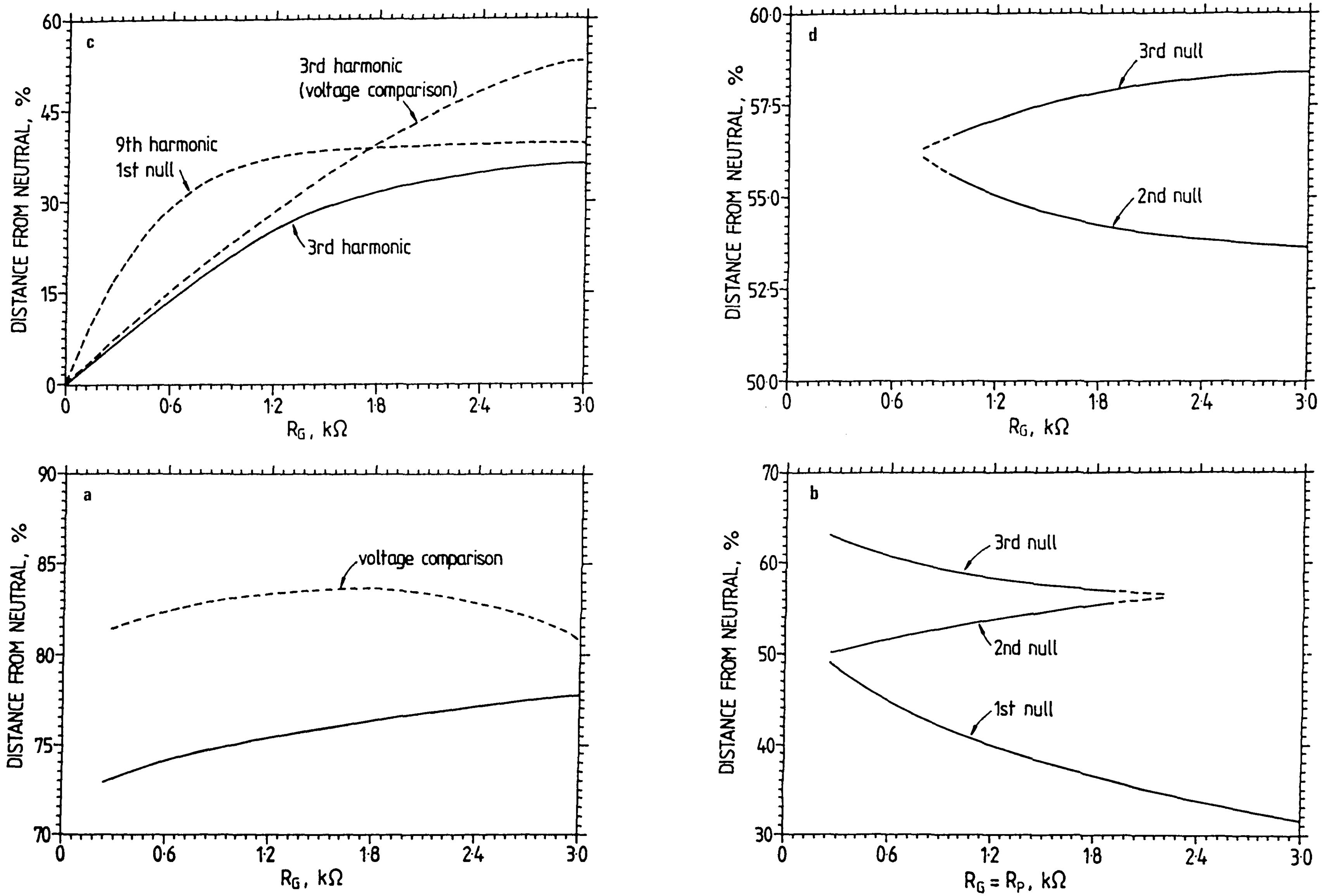

Figure 4.10 : Variation of the 3rd and 9th harmonic null points versus the neutral grounding resistance with (a and b) and without (c and d) a ground at the machine terminals.

(iii) Provided R_G is of the order of 10^3 ohm all the null points are well away from the neutral.

The effect of a variation in capacitance to earth, of the order 0.1 μF about a nominal 0.25 μF, between machines was found not to significantly affect the position of the null points. On the other hand the fault resistance has significant influence as shown in figures 4.11a and b.

Figures 4.11a,b illustrate that a high fault resistance does not compromise the integrity of the third harmonic as a measurand for two reasons:

(i) An increase in the fault resistance increases the separation between the two possible third harmonic nulls and the neutral.

(ii) The presence of a ground reference at the terminals of the machine reduces the sensitivity of the null points to the fault resistance and therefore enhances the integrity of the measurand.

4.4 Conclusions

In summary, the main conclusions of this study are:

(i) The third harmonic emf is the only harmonic present at both the neutral and terminals of the machine which is robust enough to be used as a measurand for a 100% stator earth fault protection. The fifth and seventh harmonics are too unpredictable because of the influence of the infinite-bus and, in any case, will not normally appear at the neutral. The very small amplitude and multiple null points of the ninth harmonic emfs are a very severe disadvantage. Furthermore, in a real alternator system, the

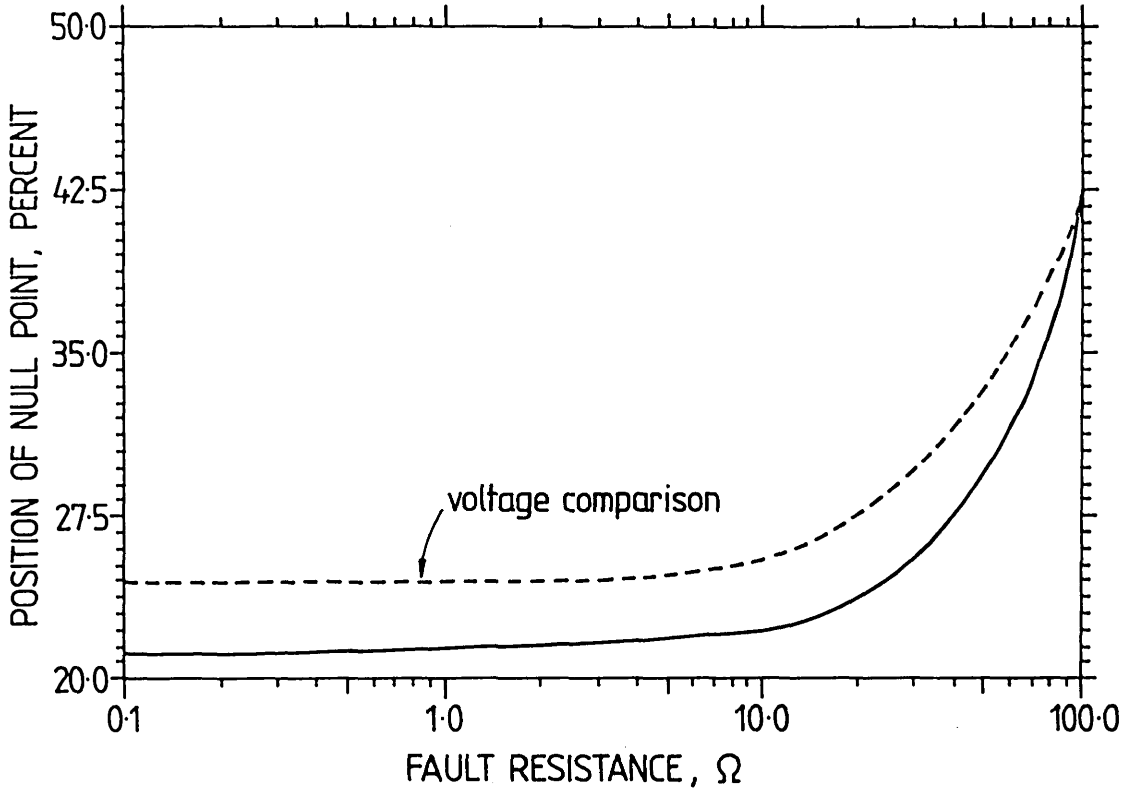

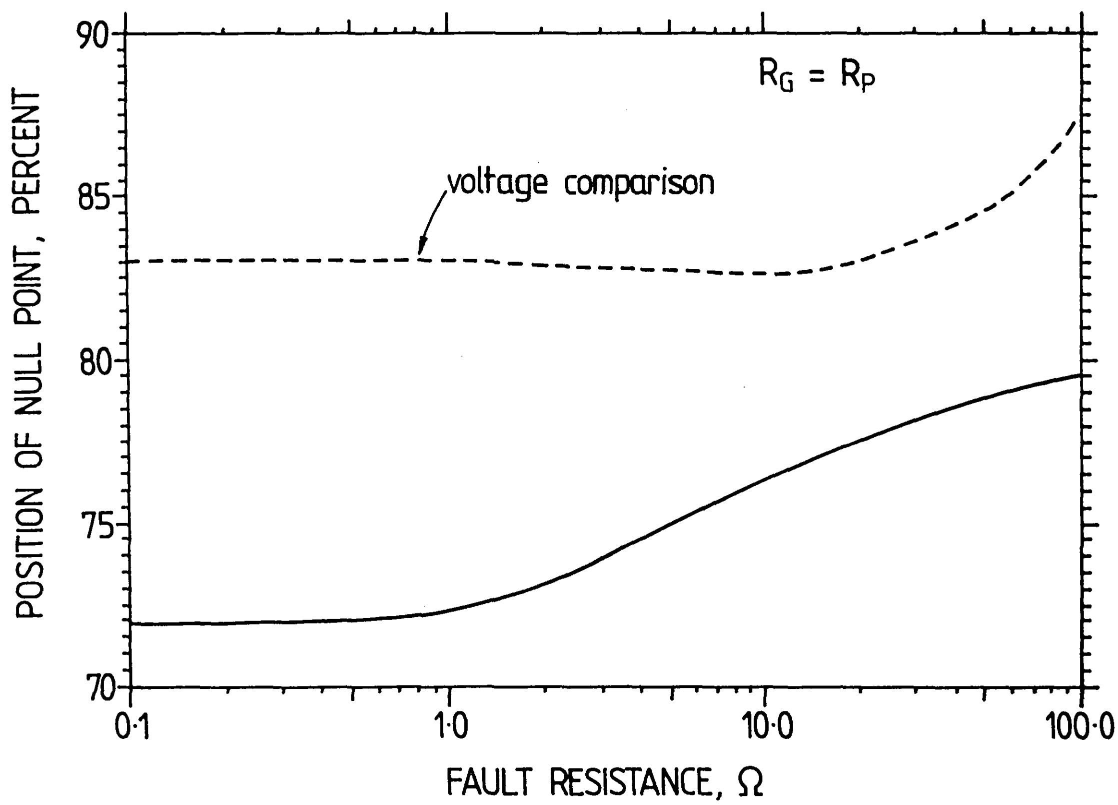

Figure 4.11: Effect of the fault resistance on the position of the third harmonic null points (a) with and (b) without an additional ground reference at the terminals of the machine.

neutral distribution transformer grounding arrangement may very well further attenuate it.

(ii) A ground reference at the terminals of the machine is highly desirable because by providing a well defined path to earth for the circulating ground currents, it increases the robustness of the neutral third harmonic emf The practical effects of this are:

(a) An increase in separation between the third harmonic null point and the neutral (figures 4.9a,b).

(b) A drastically reduced sensitivity to variations between machines in the value of R_G (figure 4.9b), the capacitance to ground (figure 4.7a), and the fault resistance (figure 4.10b).

CHAPTER FIVE

Algorithms For 100% Digital Stator Earth Fault Protection

Two algorithms for the digital protection of the complete armature windings of large generators are described and evaluated in this chapter. They are:

(i) A digital neutral third harmonic algorithm.

(ii) A digital voltage comparison algorithm between the neutral and terminal third harmonic emfs.

Both algorithms are based on the natural third harmonic emf, present in all large generators, this being shown in chapter 4 to be the only harmonic robust enough to be used as a protection measurand. DFT spectral estimation methods described in chapter two are used to filter the third harmonic components from the neutral and terminal emfs. A detailed evaluation of the performance and protection stability of both algorithms is presented to demonstrate that they offer a superior performance to present methods.

5.1 The Relaying Process

In general, the protective relaying process consists of three stages as illustrated in figure 5.1.

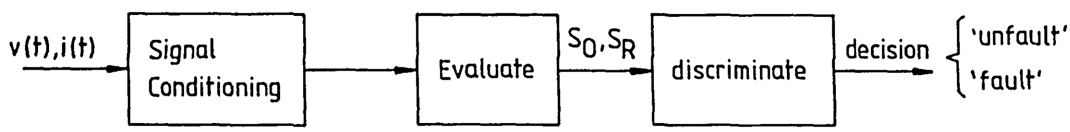

Figure 5.1: The general relaying process.

For a digital relay the first stage consists of the discretization of the protective relaying measurands. The evaluation process uses signal processing methods (see section 2.2) to produce operate and restraint signals, which the discrimination stage uses to evaluate the logical ´fault´ or ´unfault´ decision. The first stage consists of a hardware interface between the analogue measurands and the digital hardware. The evaluation and discrimination stages together constitute the software relaying algorithm.

The essential part of the relaying algorithm consists of the evaluation of the operate and restraint signals. The discrimination process can then be easily and simply formulated as a deterministic logical decision though recent research by Sakaguchi [70] has indicated that it may be possible to formulate probabalistic trip criteria based on a knowledge of the random nature of the operate and restraint signals and the relaying measurands. For the purposes of this research, a deterministic tripping criterion will be used. Research is here concentrated on the formulation of operate and restraint signals to achieve 100% stator earth fault protection based on the third harmonic emf of the alternator.

Two possible protection schemes will be studied. They are:

(i) An undervoltage scheme with the neutral third harmonic emf as the primary relaying measurand.

(ii) A voltage comparison scheme between the neutral and terminal third harmonic emfs.

The main design objectives compared to present schemes based on electromagnetic relays are:

(i) High protection stability against heavy current winding faults, external system faults and abnormal operating conditions.

(ii) Sensitivity independent of the turbine governor load setting.

(iii) Universal application and ease in commissioning.

5.1.1 The Neutral Voltage as the Measurand

5.1.1.1 A Neutral Third Harmonic Undervoltage Scheme

In section 4.3.2.1 it was shown that protection against earth faults close to the neutral could be achieved by looking for undervoltage of the neutral third harmonic emf compared to its steady-state prefault value (see figure 4.9a). Therefore the simplest digital evaluation process is to use the third harmonic component of the neutral emf, obtained as a DFT spectral estimate, as the operate signal and a fixed threshold as the restraint signal. The following equations illustrate the process.

The operate signal at sample n is given by

$$S_{o_3}(n) = E_{N_3}(n) \qquad (5.1)$$

where $E_{N_3}(n)$ is the DFT estimate of the peak magnitude of the third harmonic component of the neutral emf. It is computed as

$$E_{N_3}(n) = 2 \mid E_N(3) \mid$$

$$\text{where} \quad E_N(k) = \sum_{n=0}^{p} e_N(n)\, W^{-nk} \qquad k = 0,1, \ldots, p \tag{5.1a}$$

The restraint signal is given by

$$S_{R_3} = \Delta_3 \tag{5.2}$$

where Δ_3 is a fixed threshold independent of time.

The logical ´fault´ and ´unfault´ decisions can then be made, respectively, as

$$S_{O_3}(n) > S_{R_3} + k_a \tag{5.3a}$$

and

$$S_{R_3} > S_{O_3}(n) + k_b \tag{5.3b}$$

where k_a and k_b are parameters controlling the degree of hysteresis associated with the threshold.

This simple evaluation process will only detect earth faults over a limited part of the armature winding close to the neutral because, as shown in sections 4.3.2.1 and 2, after a certain point (the null point) the change in the postfault neutral third harmonic emf compared to its prefault value reverses direction. Coverage at and past the third harmonic null point can be achieved by formulating a similar evaluation process but based on an overvoltage of the fundamental component of the neutral emf, to give a two zone scheme.

The operate and restraint signals for this zone can be formulated as

$$S_{o_1}(n) = E_{N_1}(n) \tag{5.4}$$

where $E_{N_1}(n) = 2 \mid E_N(1) \mid$

and $$S_{R_1} = \Delta_1 \tag{5.5}$$

The two zones will be referred to as 'zone 1' and 'zone 3', the integer suffices referring to the order of the harmonic component of the neutral voltage contributing to that particular zone. The typical reach of the two zones for an alternator system without a V.T. connection to ground at the generator terminals is illustrated in figure 5.2. Note that the zone 1 reach is shown to extend past the alternator line terminals. In fact, the zone 1 reach will extend right upto the low voltage sides of the generator and unit-auxiliary transformers.

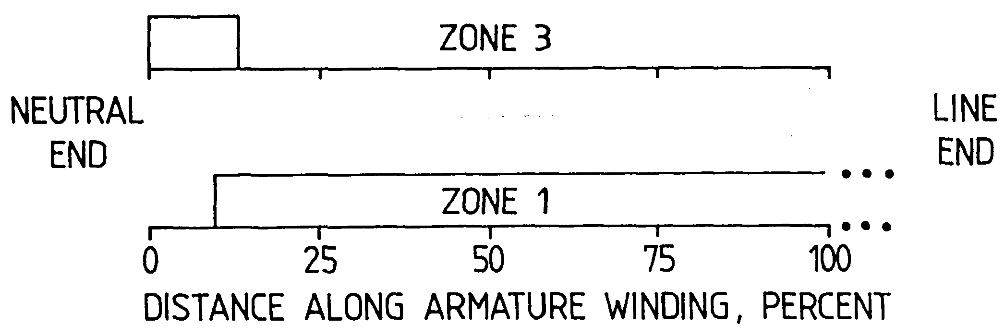

Figure 5.2: Typical zone 1 and 3 reaches for neutral third harmonic undervoltage scheme.

Such a scheme would be essentially identical to the 100% stator earth fault protection scheme implemented using conventional electromagnetic undervoltage and overvoltage relays tuned to the third and fundamental harmonics respectively (figure 1.9), as reported by Griffin, Pope [28,63]. Their field experience has shown the scheme to have significant disadvantages which are:

(i) Calibration of the scheme (the choice of the third harmonic threshold, Δ_3) involves an extensive prior study of the neutral emf harmonic content, and consequently commissioning is difficult.

(ii) The neutral third harmonic emf will vary with power and therefore some sort of supervision is essential to prevent possible maloperations during low power operation.

(iii) Inherent protection stability is poor, especially against power swings, and therefore the trip needs to be time delayed to increase stability resulting in a slow operating time. Griffin, Pope [28,63] report using a time delay of 5 seconds.

(iv) The sensitivity of the relay will vary with the governor load setting.

5.1.1.2 An Enhanced Neutral Third Harmonic Scheme

The major disadvantages of the previous scheme are due to the fact that it operates, because of a time invariant restraint signal, for absolute changes in the neutral third harmonic emf Consequently, the scheme is inherently incapable of distinguishing whether the change in neutral third harmonic emf is due to a genuine earth fault or other reasons such as power swings, load changes or other types of winding faults, and additional supervision is necessary to stabilize it.

In the enhanced scheme proposed in this section the protection operates, in contrast, for relative changes in the neutral third harmonic emf compared to its prefault value, whatever it may be. This difference between the two schemes is extremely significant for the following two reasons:

(i) As the absolute level of the neutral third harmonic emfs is of no importance, calibration will be unnecessary. The only criterion for successful application of the protection is that a useable measurand is present under all normal operating conditions.

(ii) The load setting of the governor and generator power output will not affect either the sensitivity or stability of the protection. The sensitivity is dictated by the third harmonic voltage reduction at the neutral required to give a trip. For the basic scheme this will vary with the governor setting as the restraint signal is fixed but for the enhanced scheme the sensitivity will be constant provided the dynamic range of the measurand is sufficient.

Implicit in the implementation of this scheme is the need for a memory feature to store the prefault third harmonic. Three criteria need to be considered:

(i) How far back in time from the fault instant should the prefault third harmonic emf be taken?

(ii) A secure control is required to prevent the memory being updated during the fault period.

(iii) The stored prefault third harmonic emf must be conditioned to reject noise and interference.

Figure 5.3 illustrates, in block diagram form, the proposed enhanced scheme and shows that its implementation is inherently suited to and exploits more fully than the basic scheme the potential of the micro-computer, because the prefault third harmonic can be stored and updated easily in a first-in first-out (FIFO) memory stack. In contrast the digital neutral third harmonic undervoltage scheme, apart from the use of fourier filtering for the fundamental and neutral third harmonic components, would basically just represent the transfer of an existing scheme to a new hardware medium.

The operate signal is derived as the absolute difference between the instantaneous neutral third harmonic emf and a constantly updated reference derived from a previously computed value. The restraint signal

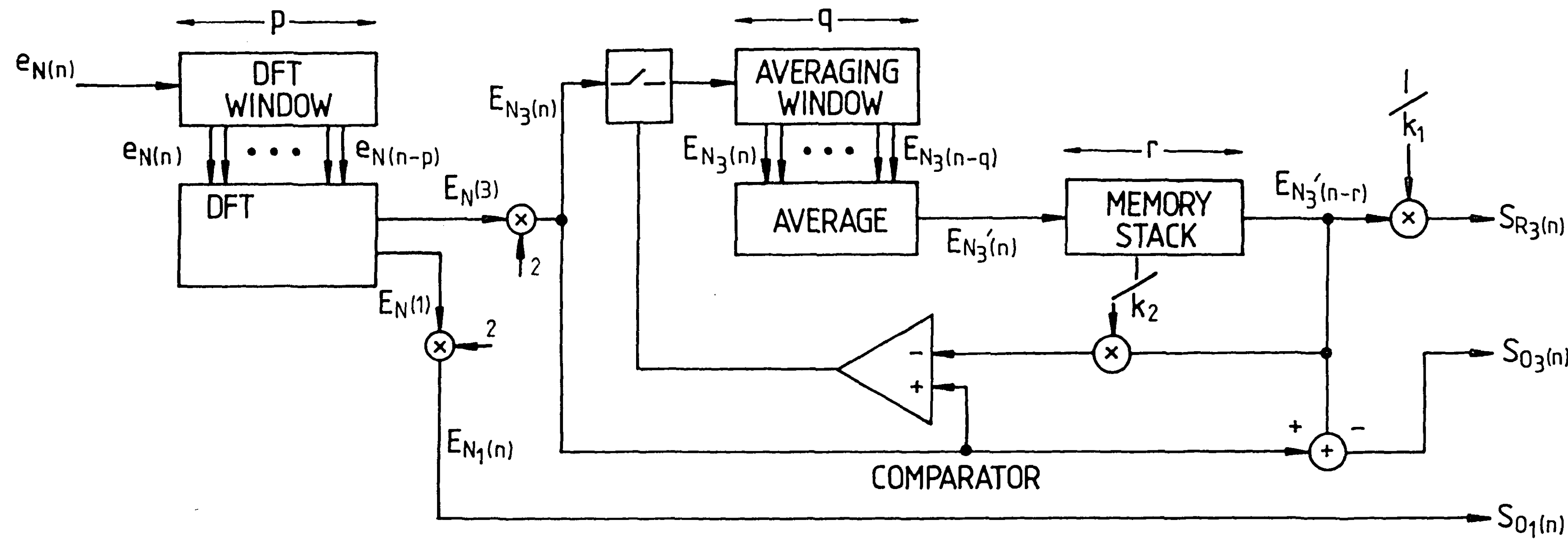

Figure 5.3 : Evaluation process for the enhanced neutral third harmonic scheme.

is derived relative to the reference and, in contrast to the undervoltage scheme, is time variant. The evaluation process is illustrated by the equations,

$$S_{o_3}(n) = | E_{N_3}(n) - \Upsilon(n) | \tag{5.6}$$

and $$S_{R_3}(n) = \Upsilon(n) / k_1 = \Delta_3(n) \tag{5.7}$$

where $\Upsilon(n)$: the reference signal.

k_1 : sensitivity factor.

the 'operate' decision being given by the condition $S_{o_3} > S_{R_3}$.

The reference signal at sample n is derived as the moving average over past values of E_{N_3} starting from the past value at n-r, as shown below:

$$\Upsilon(n) = E_{N_3}'(n-r) = 1/q \sum_{m=0}^{q} E_{N_3}(n-r-m) \tag{5.8}$$

where $E_{N_3}'(n-r)$: the moving average of E_{N_3}.

The derivation of the reference as a moving average is designed to give a very high level of noise immunity and stability to the reference signal as its integrity ultimately governs the integrity of the relaying algorithm.

To prevent the reference signal being corrupted during the fault period, its updating must be inhibited as quickly as possible after the start of a fault. This is accomplished by formulating another threshold at a much higher sensitivity than $S_{R_3}(n)$,

$$\delta(n) = \Upsilon(n) / k_2 \tag{5.9}$$

where $k_2 << k_1$.

$\delta(n)$: 'start' threshold.

The logical ´update´ and ´not update´ conditions are then given respectively as $S_{o_3}(n) < \delta(n)$ and $S_{o_3}(n) > \delta(n)$.

The choice of how far back in time to derive the reference signal, $\gamma(n)$, (i.e. the choice of the parameter ´r´ in equation 5·8) is dictated by the maximum possible rate of change of power possible from a large alternator under abnormal operating conditions such as pole slipping for which the stator earth fault protection must remain stable. This rate of change of power, which is mirrored in the neutral third harmonic emf, is for a large machine mainly a function of its mechanical inertia and will, consequently, be an order of magnitude less than the rate of change of the neutral third harmonic emf under fault conditions. Therefore ´r´ must be chosen so that the reference always tracks the instantaneous neutral third harmonic emf to within the ´start´ threshold. The logical ´update´ condition for the reference signal will then be satisfied and stability assured.

The zone 1 evaluation process can be derived exactly as for the previous scheme as the fundamental is well defined and accurately known. The typical reach of the two zones of protection is illustrated in figure 5.4.

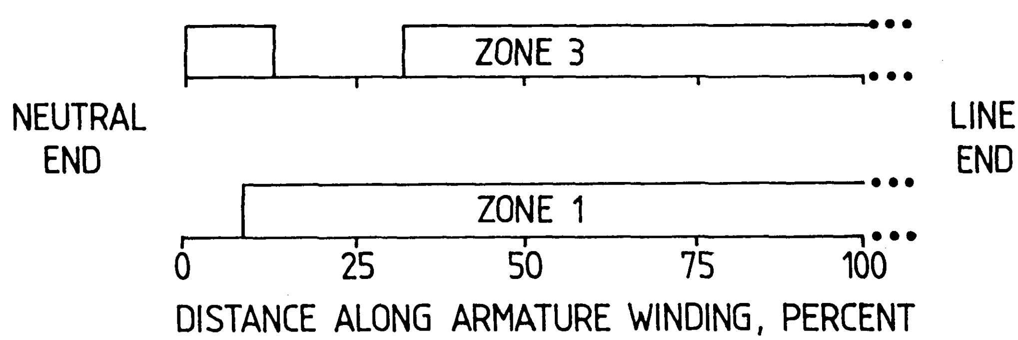

Figure 5.4: Typical zone 1 and zone 3 reaches for enhanced neutral third harmonic scheme.

In contrast to the zone 3 reach of the basic scheme (see figure 5.2), the zone 3 reach for the extended scheme covers both ends of the armature windings giving a much greater degree of backup to zone 1. This difference in zone 3 reach between the two schemes arises because as the enhanced scheme uses the absolute relative change in neutral third harmonic emf from its prefault value for the operate signal, it will operate both for an undervoltage or overvoltage of the neutral third harmonic emf In the basic scheme, the zone 3 reach could be similarly extended by defining an additional threshold to detect overvoltages but, in practice, this is impractical because of the need to retain adequate safety margins against variations in the load setting and during transient power swings.

In summary the enhanced scheme, compared to the neutral third harmonic undervoltage scheme, should possess the following advantages:

(i) Insensitivity to the load setting and therefore off-line supervision is unnecessary.

(ii) Inherently greater protection stability.

(iii) Greater zone 3 reach.

The performance of a software relaying algorithm based on this protection scheme is evaluated in section 5.2.1.

5.1.2 The Neutral and Terminal Emfs as Measurands

5.1.2.1 The Basic Third Harmonic Voltage Comparison Scheme

Figures 4.9a and b demonstrate that the neutral and terminal third harmonic emfs vary in an opposite sense with respect to each other for stator earth faults. As the fault point moves closer to the neutral, the terminal postfault third harmonic emf tends to the full third harmonic emf of the alternator and vice versa. Using this property a simple voltage comparison scheme can be achieved by formulating the operate signal by equating to zero the neutral and terminal third harmonic emfs under steady-state conditions. When an internal stator earth fault occurs, the balance will be upset and the operate signal increases from its prefault zero value.

Using a mechanical analogue, the terminal and neutral third harmonic emfs behave very much as a see-saw. Obviously at some point a null will exist where an earth fault will not register. Section 4.3.2.2, however, shows that the null point is well away from the neutral and therefore it can be covered by a zone 1 protection similar to that used for the previous two schemes.

The zone 3 operate signal can be formulated as

$$S_{o_3}(n) = \mid E_{a_3}(n) - K.E_{N_3}(n) \mid \qquad (5.10)$$

where $E_{a_3}(n) = 2 \mid [E_A(3) + E_B(3) + E_C(3)] /3 \mid$

K : gain factor.

The simplest evaluation process is to use a fixed restrain signal as used in the neutral third harmonic undervoltage scheme (equation 5.2), and similar tripping criteria (equation 5.3). This results in a scheme essentially similar to that reported by Pope [63].

They report it to have three important advantages over the neutral third harmonic undervoltage scheme which are:

(i) Provided the ratio of the neutral and terminal third harmonic emfs is constant for all load settings of the alternator (this may not always be true [28,71]), they will mirror each other for all faults external to the generator. Therefore such a scheme will be inherently stable against load changes, offer greater stability against external system disturbances, and not require off-line supervision.

(ii) Calibration and field commissioning is simpler though still not easy.

(iii) The zone 3 reach is extended to the terminal end of the stator winding in a similar manner to that illustrated in figure 5.4 for the enhanced neutral third harmonic scheme. The null points for the two schemes do not significantly differ (section 4.3.2.2).

However, this scheme still suffers from two of the disadvantages associated with a fixed restraint signal,

(i) the need for extensive field measurements prior to calibration.

(ii) varying sensitivity with the load setting.

5.1.2.2 A High Stability Third Harmonic Voltage Comparison Scheme

Both these disadvantages can be overcome by using a time variant restraint signal dependent on the prefault neutral or terminal third harmonic emfs, in a similar manner to the enhanced neutral third harmonic scheme. The zone 3 restrain signal can then be formulated as,

$$S_{R_3}(n) = K.\gamma(n) \;/\; k_1 \qquad (5.11)$$

where $\gamma(n)$ is given by equation 5.8.

An additional bonus is that the scheme will possess improved protection stability over both the enhanced neutral third harmonic scheme and the basic voltage comparison scheme, as it will exhibit both their stability characteristics. The protection stability, however, can be further improved by using, in addition to equation 5.11, restraint signals based on the mutual phase relationship of the terminal third harmonic emfs.

Under normal operating conditions the third harmonic components of the terminal emfs of an alternator will be identical and equal in phase, the third harmonic components in a three phase system being zero-sequence components. Therefore if the positive and negative-sequence third harmonic symmetrical components are derived they will be very small in magnitude. This will also be true for stator earth faults, as illustrated in figure 5.5a, because they do not produce any significant magnetic imbalance within the machine. However, for high current winding faults and severe abnormal operating conditions this is not true. Figure 5.5b illustrates the variation of the terminal third harmonic symmetrical components with fault position for an inter-phase fault on the B and C phases, the fault position being identical on both phases. Significant negative and positive-phase-sequence components are present.

Two additional restraint signals can, therefore, be derived as the third harmonic negative and positive-phase-sequence components of the terminal emfs of the generator. They are given, respectively, by the equations,

$$S_{R_3}'(n) = | 2[E_A(3) + \lambda E_B(3) + \lambda^2 E_C(3)]/3 | \tag{5.12}$$

and $$S_{R_3}''(n) = | 2[E_A(3) + \lambda^2 E_B(3) + \lambda E_C(3)]/3 | \tag{5.13}$$

where λ : 120 degree phase shift operator.

The logical 'restrain' decision to block the main trip can be formulated as:

$$S_{R_3}'(n) > \delta(n) \quad \text{AND} \quad S_{R_3}''(n) > \delta(n) \tag{5.14}$$

Figure 5.6 illustrates in block diagram form the complete evaluation process.

This algorithm will provide exceptional protection stability and discrimination resulting in a very secure trip decision. However, present protection practice is to treat the stability of earth fault protection to

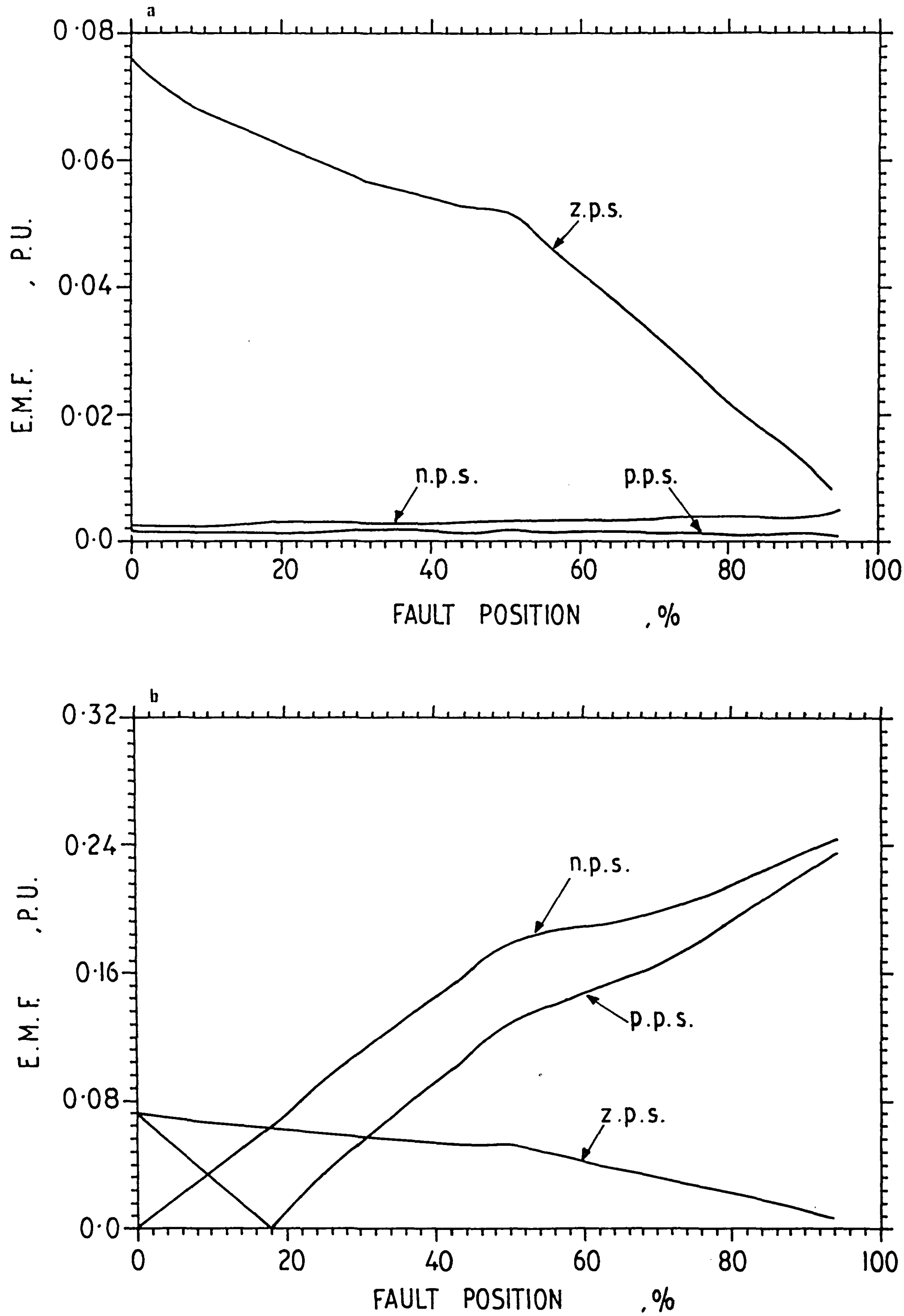

Figure 5.5: Variation of third harmonic symmetrical components with fault position for (a) earth faults and (b) phase faults

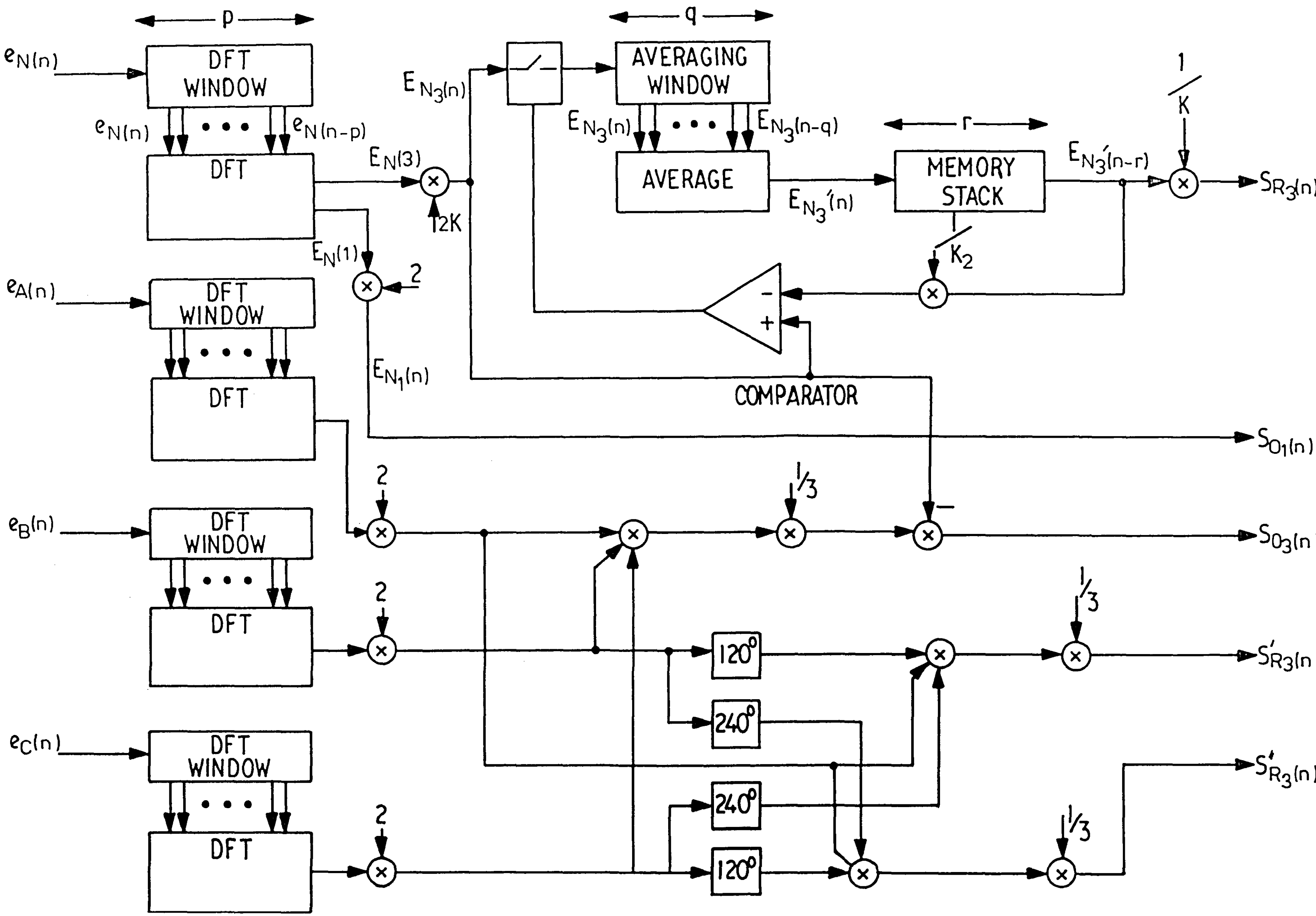

Figure 5.6 : Evaluation process for the high stability third harmonic voltage comparison scheme.

high current winding faults as unimportant, as the differential and backup overcurrent protection will operate in any case. In fact some utilities prefer this lack of discrimination as it gives a measure of backup to the main winding protection.

This philosophy is arguable and the view is taken here that a highly predictable and discriminative protection is preferable for all the protection functions of a generator system so as to obtain a consistent and predictable overall protection system. If a backup to a particular protection function is necessary it should be implemented with a parallel protective scheme based on different operating principles rather than relying on the uncertain performance of a protective relay not dedicated to the particular function.

Zone 1 can be evaluated in a similar fashion to the undervoltage neutral third harmonic scheme. The overall reach is identical to the basic voltage comparison scheme and its performance is evaluated in section 5.3.

5.2 Performance of the Neutral Third Harmonic Scheme

The performance of the neutral third harmonic scheme proposed in section 5.1.1.2 was evaluated using a software algorithm run on the NOVA mini-computer. Data recorded from the micro-alternator via the data acquisition system interface was used as input. The validity of this approach has already been examined in section 3.1.2

5.2.1 The Structure of the Algorithm

The main criterion required for the implementation of the algorithm was versatility. With this objective, all the parameters of the algorithm were made variable and selectable by the user and comprehensive DFT signal processing procedures included. Flowchart 5.1 illustrates the structure of the algorithm.

The algorithm is written as a single loop with the various procedures being executed sequentially every sample. For a practical real time implementation, parallel processing paths addressed using a priority interrupt scheme will yield a more time efficient structure but the logical sequence will be the same.

The first routine, 'INIT', initializes the algorithm. It initializes the DFT data window, W_D; the moving average window, W_A, which is used to compute the reference signal; and the memory stack, W_M (see figure 5.3). If a weighted DFT is chosen, the selected window function is generated in a similar manner to that shown in flowchart 3.1 for the spectrum analysis programs. 'INIT' will contribute a delay of p+q+r samples for a one cycle (of fundamental) data window or p/2+q+r samples for a half cycle window on startup. The variables p, q, and r are the respective lengths of the data, moving average windows and the memory stack as illustrated in figure 5.3. Apart from p which defines the group delay of the DFT (section 2.3.2), q and r will not contribute any delay to the normal operation of the algorithm.

The peak amplitudes of the fundamental and third harmonic components of the digitized neutral emf are estimated by the routine 'DFT' which implements a direct solution of the discrete fourier transform for these two frequencies. The FFT algorithms used in the spectral analysis software (see section 3.2) were not used, because as a class they are computationally inefficient if a spectral estimate at only a limited number of frequencies is required. Halberstein's [29] recursive procedure (section 3.2) could have been used to accelerate the filtering process for the selection of a full length unweighted data window but was omitted for simplicity.

The flag F_H selects a half cycle DFT to evaluate the effect of its improved group delay but reduced spectral accuracy compared to a one cycle DFT, on the relaying algorithm. The half cycle DFT (equation 2.9) is implemented by a negative repetition of the half cycle window to give a synthesized full cycle window [16] (section 2.1.2).

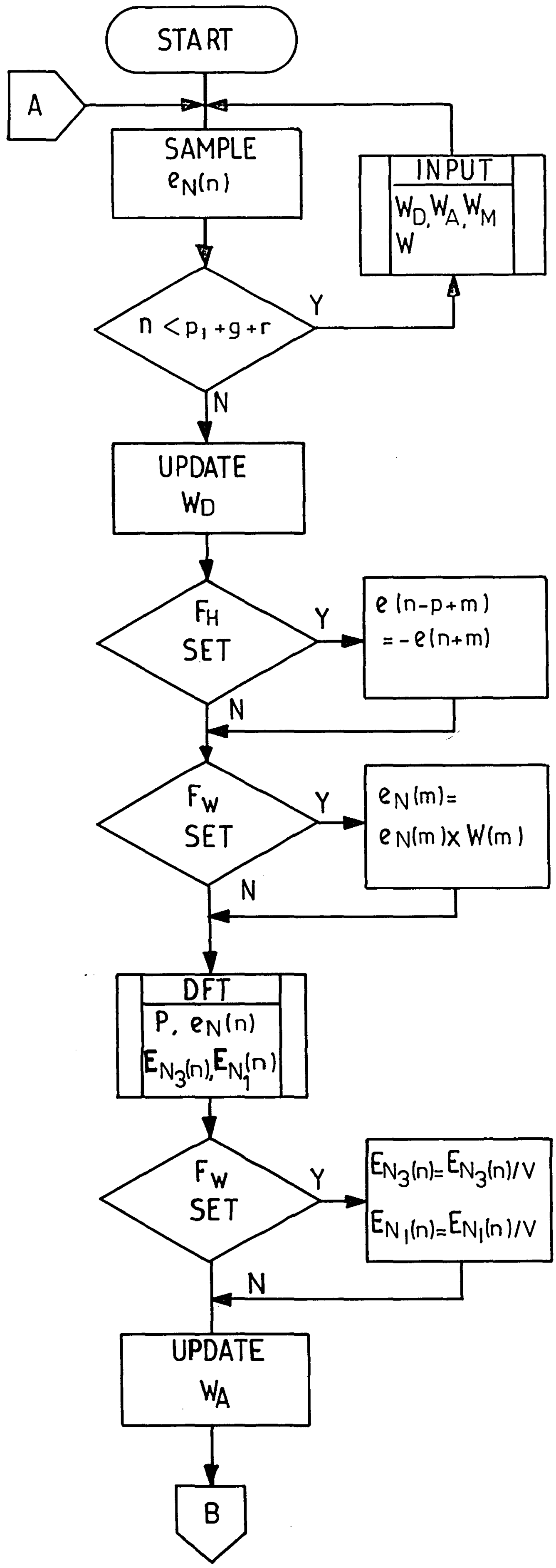

Flowchart 5.1: Structure of the neutral third harmonic algorithm.

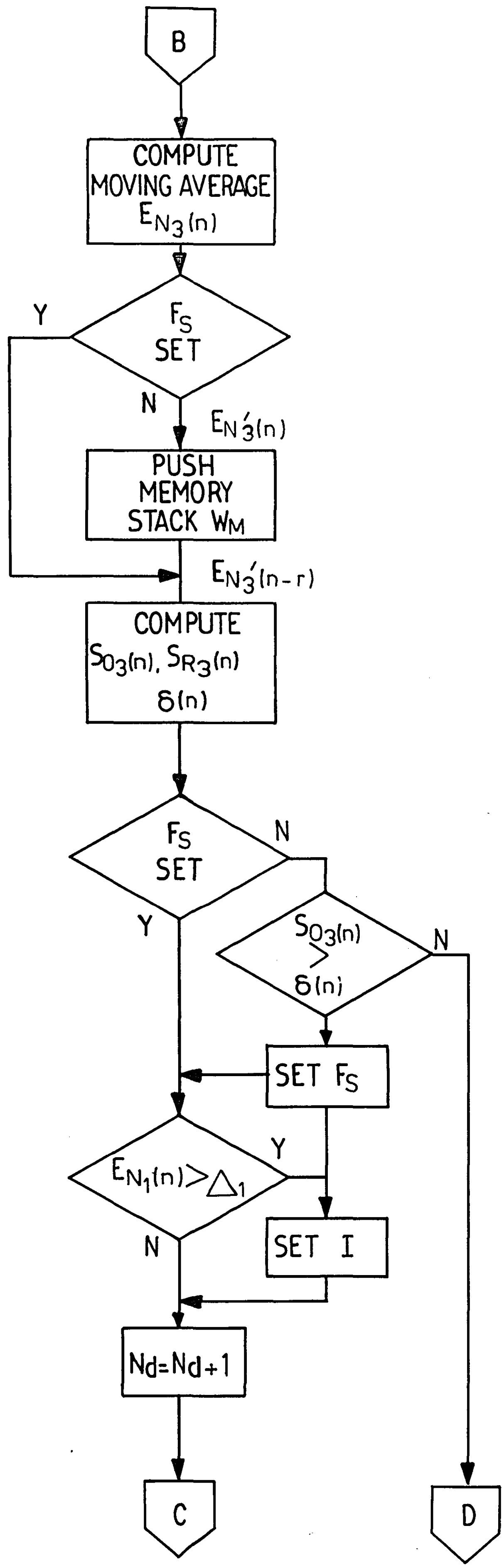

Flowchart 5.1: (continued)

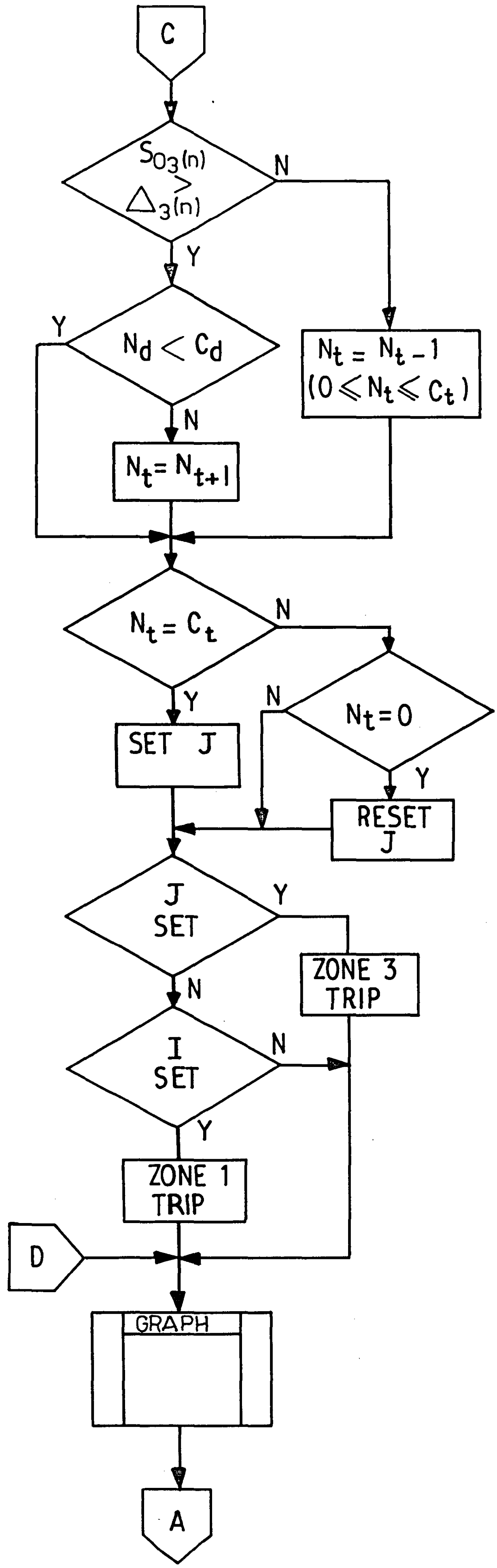

Flowchart 5.1: (continued)

The evaluation process is implemented as given by equations 5.4 to 5.9, the logical structure of the flowchart being identical to that of the block diagram of figure 5.3. The values of p (within constraints imposed by the sampling frequency - section 3.2.1), q and r are user selectable.

The discrimination process is based on the deterministic criterion of the operate signal being greater than the restraint signal representing a logical ´fault´ decision and vice versa. Zone 3 has some additional sophistications to improve the security of the discrimination process. These consist of:

(i) A definite time delay implemented as a delay counter, N_d, initiated by the ´start´ flag, F_S, being set. This inhibits any trips for a period C_d, the delay count, after the fault instant to prevent maloperation during the fault transition period of the DFT filter (section 2.3.2).

(ii) Software hysteresis to prevent ´chatter´ on the trip flag after the fault transition period. The hysteresis is implemented as an up/down counter, N_t, which counts up for a logical ´fault´ decision and down for a logical ´unfault´ decision. A trip count of C_t sets the trip while a count of zero resets it. A count in between 0 and C_t leaves the present state of the trip unchanged.

The zone 1 trip, however, is direct and incorporates no delays or hysteresis. This is possible for two reasons:

(i) The fundamental will be the dominant spectral component of the postfault neutral voltage and therefore during the fault transition period, the fundamental spectral estimate will change smoothly and in a well damped manner (see figure 2.7).

(ii) The overlap between the two zones of protection will be sufficient to prevent any instability on the trip output.

5.2.2 Performance for Earth Faults

The action of the algorithm is illustrated using composite graphs plotted by the routine ´GRAPH´ (flowchart 5.1). Unless otherwise stated, all results have been taken at a governor setting of 0.8 p.u. power at unity p.f. and with a neutral grounding resistance of 1k ohm.

5.2.2.1 The One Cycle DFT Algorithm

Figure 5.7 illustrates the response of the algorithm with a one cycle DFT filter to an earth fault 6.25% from the neutral on the A-phase of the alternator. This fault is sufficiently close to the neutral that a normal earth fault protection based on the fundamental would not give an instantaneous trip.

The first curve, $e_N(t)$, illustrates the faulted neutral voltage waveform. Note how the harmonic content clearly changes at the fault instant from predominantly third harmonic to fundamental. The exact degree of change is illustrated by the estimates of the DFT filter, $E_{N_1}(n)$ and $E_{N_3}(n)$.

Also illustrated on the same scale as $E_{N_3}(n)$ is $\gamma(n)$, the reference signal based on the prefault neutral third harmonic emf. This specifies both the ´start´ threshold, $\delta(n)$, which is set at 10% of the reference k_2=10 in equation 5.9) and the restraint signal, $S_{R_3}(n)$, which is set to 50% of the reference (k_1 = 2 in equation 5.7).

As soon as the fault occurs, the zone 3 operate signal $S_{o_3}(n)$ increases sharply, very rapidly crossing the ´start´ threshold. This sets the ´start´ flag, F_S, which the algorithm checks to stop the updating of the prefault reference (note that from this point onwards $\gamma(n)$ remains fixed at the prefault value) and initiates the delay counter, N_d. The delay count, C_t, is selected as one cycle of the fundamental as this will be equal to the fault transition period. After the delay counter has reset, the relaying decision is made to trip zone 3 as the trip criterion

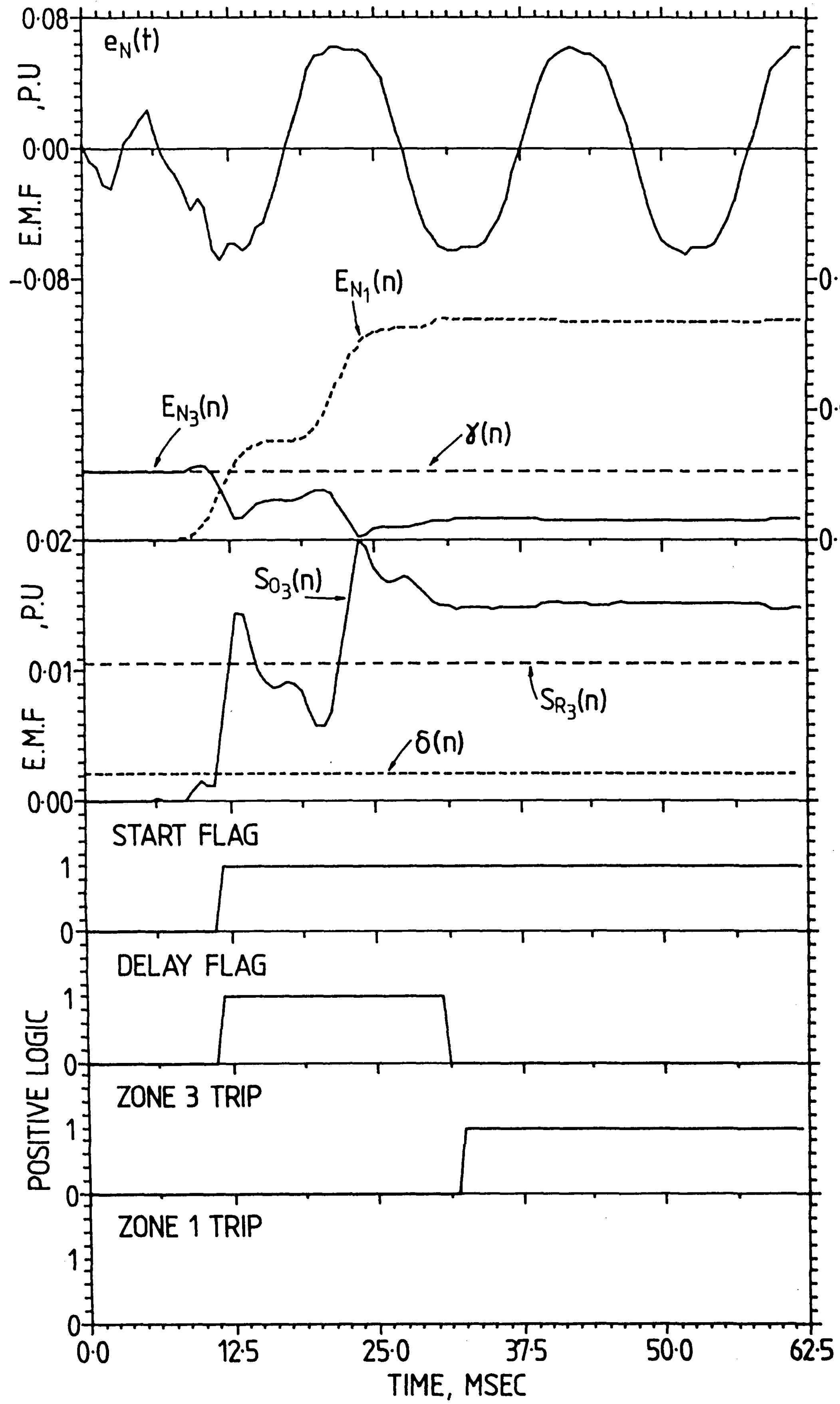

Figure 5.7: Response of the neutral third harmonic algorithm for an earth fault 6.25% from the neutral.

is satisfied. The zone 3 trip occurs three samples later as the trip count, C_t, is selected as three, resulting in a total operating time of 23 ms. Zone 1, however, does not trip because a tripping threshold of 0.10 p.u. was chosen (the postfault value of $E_{N_1}(n)$ is 0.068 p.u.).

Figure 5.8 illustrates the response to a similar fault 12.5% from the neutral. For this case zone 3 does not trip as it is within the null band but the fault is covered by zone 1. As soon as the fundamental neutral voltage component, $E_{N_1}(n)$, exceeds the zone 1 tripping threshold of 0.10 p.u., the zone 1 trip is instantaneously set. The operating time is 15.0 msec.

The value of $k_1 = 0.5$ for the restraint signal was chosen as the optimum sensitivity for both the faults. For the value of grounding resistance chosen this represents an optimum compromise between stability, and the overlap between the two protection zones. Too high a value of k_1 will give increased protection stability but decrease the safety margin in the overlap between the two zones, while too low a value will decrease stability.

Figure 5.9 illustrates the variation of operating time versus fault position for both zones 1 and 3. The zone 3 operating time is fairly constant over most of its reach, but the zone 1 time decreases rapidly from a maximum of one cycle of fundamental to approximately a quarter cycle for faults towards the line end of the machine. The effect of point-on-wave (P.O.W.) on the zone 3 operate times was found to be negligible. This is due to two reasons:

(i) Because of the extremely low level of fault current, low frequency transients do not appear at the neutral.

(ii) Any small variations are engulfed by the delay and tripping counters.

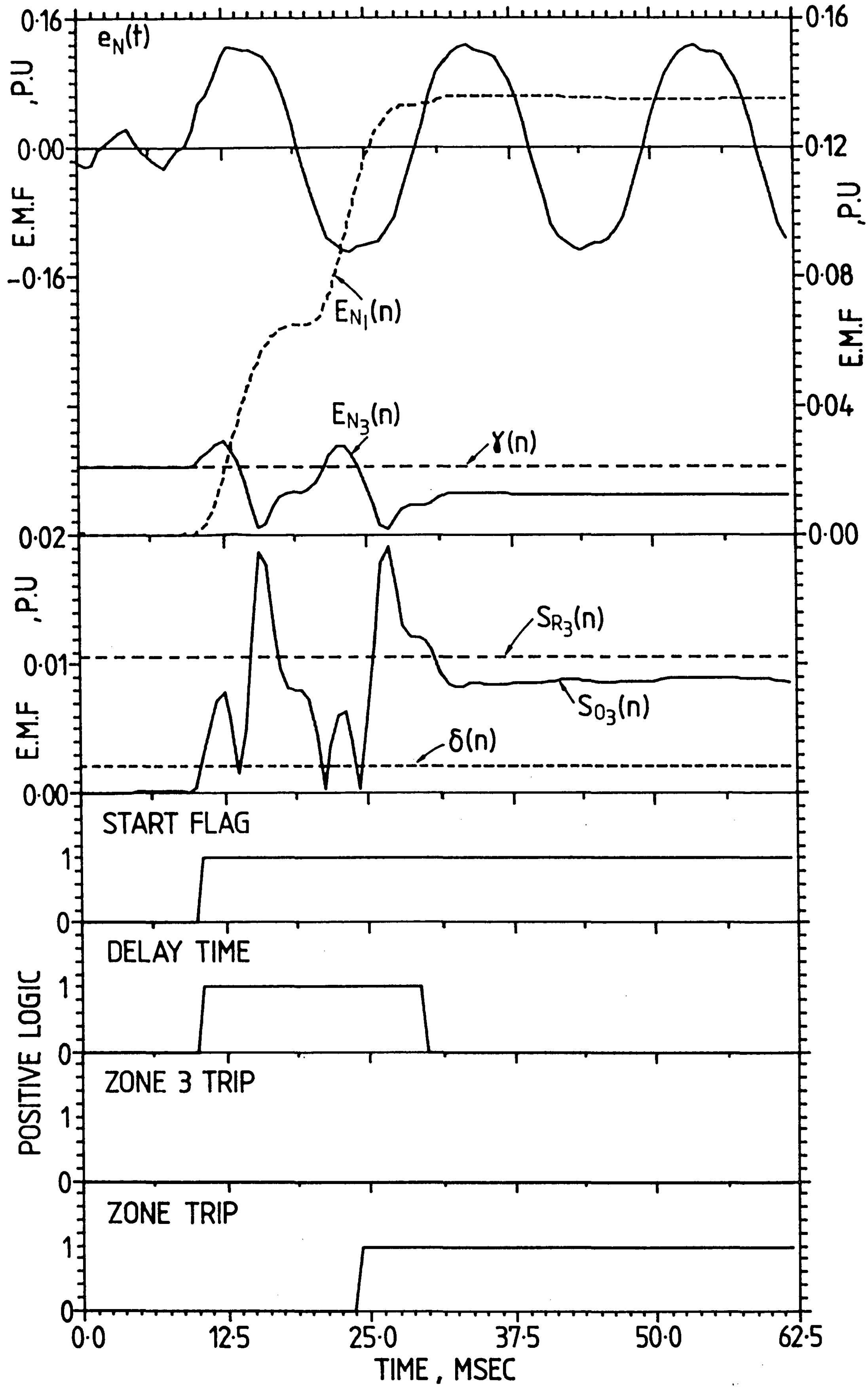

Figure 5.8: Response of the neutral third harmonic algorithm for an earth fault 12.5% from the neutral.

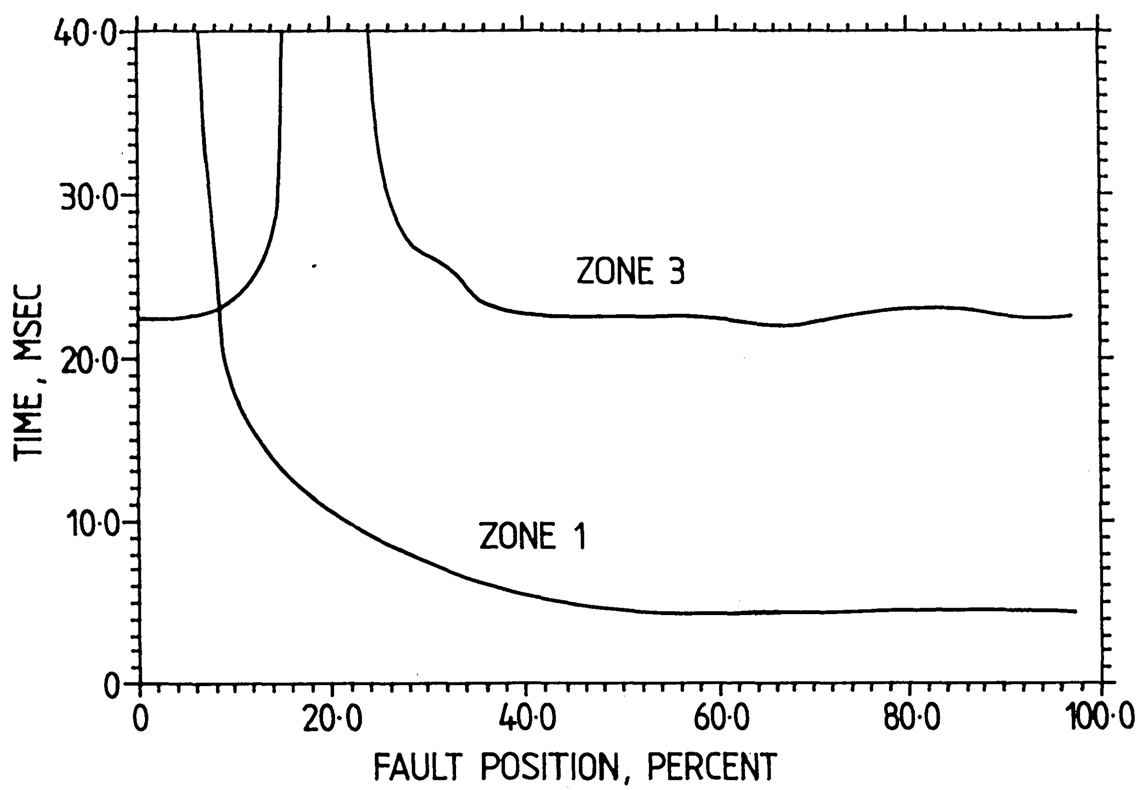

Figure 5.9: Operate time versus fault position characteristic for the neutral third harmonic algorithm.

With the very fast zone 1 times obtained the effect of P.O.W. on the zone 1 times was discernable but not significant. Figures 5.7 and 8 also illustrate the necessity of delaying the zone 3 trip until the fault transition period is past. For both faults the zone 3 operate signal is unstable during this period and a secure 'fault' decision cannot be made. On the other hand, as expected, the fundamental increases very smoothly as it is the dominant postfault spectral component and this limitation does not apply. Note that as the fault position increases from 6.25% to 12.5% the degree of instability in the zone 3 operate signal also increases. This is a consequence of the increased fundamental postfault component in the neutral voltage. As this will increase with the fault position, the degree of instability in $S_{o_3}(n)$ will also get worse with an increased fault position.

It may be argued that an instantaneous zone 1 trip is not good protection practice as under certain conditions the fundamental may not be the dominant spectral component at the neutral. For earth faults on the alternator system, this will certainly not be true, but it could occur for, say, heavy current inter-phase faults. However, for the zone 1 operate signal to become seriously unstable, the amplitude of the third harmonic would have to be at least twice that of the fundamental (compare $E_{N_1}(n)$ and $E_{N_3}(n)$ in the case of figure 5.7). As the zone 1 trip threshold is 0.10 p.u., a third harmonic component of at least 0.20 p.u. would have to be present at the neutral to cause instability; a level which is most unlikely to occur.

Figure 5.10 illustrates the response of the algorithm with a simulated (see section 3.1.1) V.T. connection to ground at the generator terminals to an earth fault 12.5% from the neutral. In contrast to figure 5.8 - the same fault position but without the V.T. connection - a zone 3 trip is obtained as predicted by the simulation results (see figure 4.10b) which indicated that this configuration shifts the zone 3 null point towards the line end of its reach. Two other features are of interest:

(i) Note the increase in the prefault third harmonic component of neutral emf due to the additional path to ground presented by the V.T. at the alternator terminals. The slight fundamental prefault component is a consequence of small imbalances between the three phases of the V.T. simulation and is not significant.

(ii) The response of the zone 3 operate signal during the fault transition period is better with the V.T. connection (compare it with the operate signal in figure 5.8). This is a consequence of the level of the third harmonic component relative to the fundamental being greater.

The overall operate times with the V.T. connection are very similar to those illustrated in figure 5.9 except, of course, that the position of the null point will shift towards the line end of the zone 3 reach.

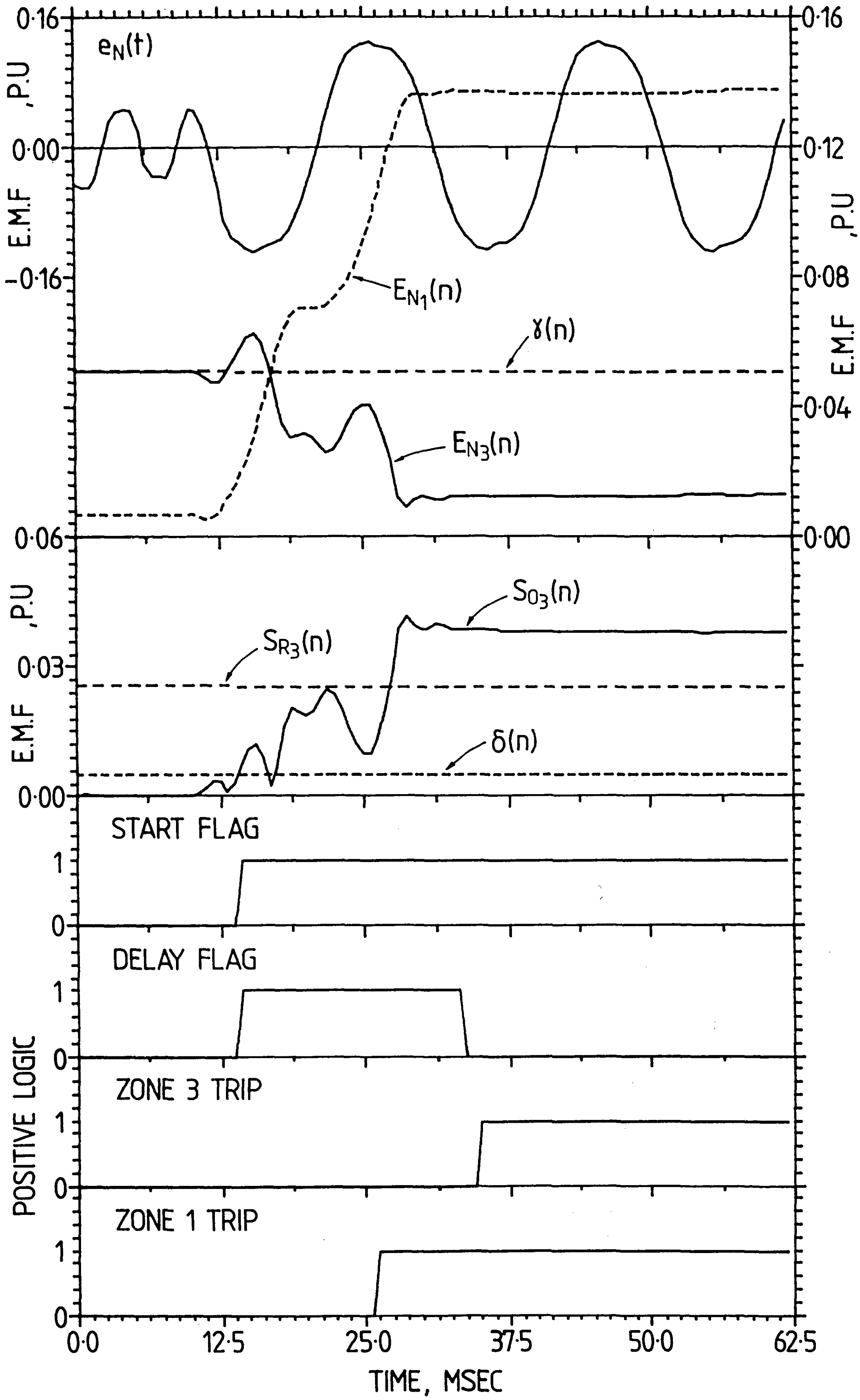

Figure 5.10: Response of the neutral third harmonic algorithm to an earth fault 12.5% from the neutral with a V.T. connection at the alternator terminals.

5.2.2.2 The Half Cycle DFT Algorithm

The operate time of the protection scheme can be considerably decreased, especially close to the neutral where zone 3 contributes most to the trip, by using a half cycle DFT but only at the expense of a decrease in robustness of the filtering process (section 1.2) and therefore in the zone 3 evaluation process. Figures 5.11 and 5.12 illustrate the relaying action of this algorithm for the same fault data used in figures 5.7 and 5.8.

Compared to the one cycle algorithm, the zone 3 trip time is halved to 12.5 msec while the zone 1 trip time is reduced from 14 msec to 8 msec (the fault transition delay is shown selected as half a cycle). This increase in speed is reflected right across the reach of the algorithm as illustrated in figure 5.13. Towards the line end of the armature windings, however, the improvement in the zone 1 operate times is not significantly greater.

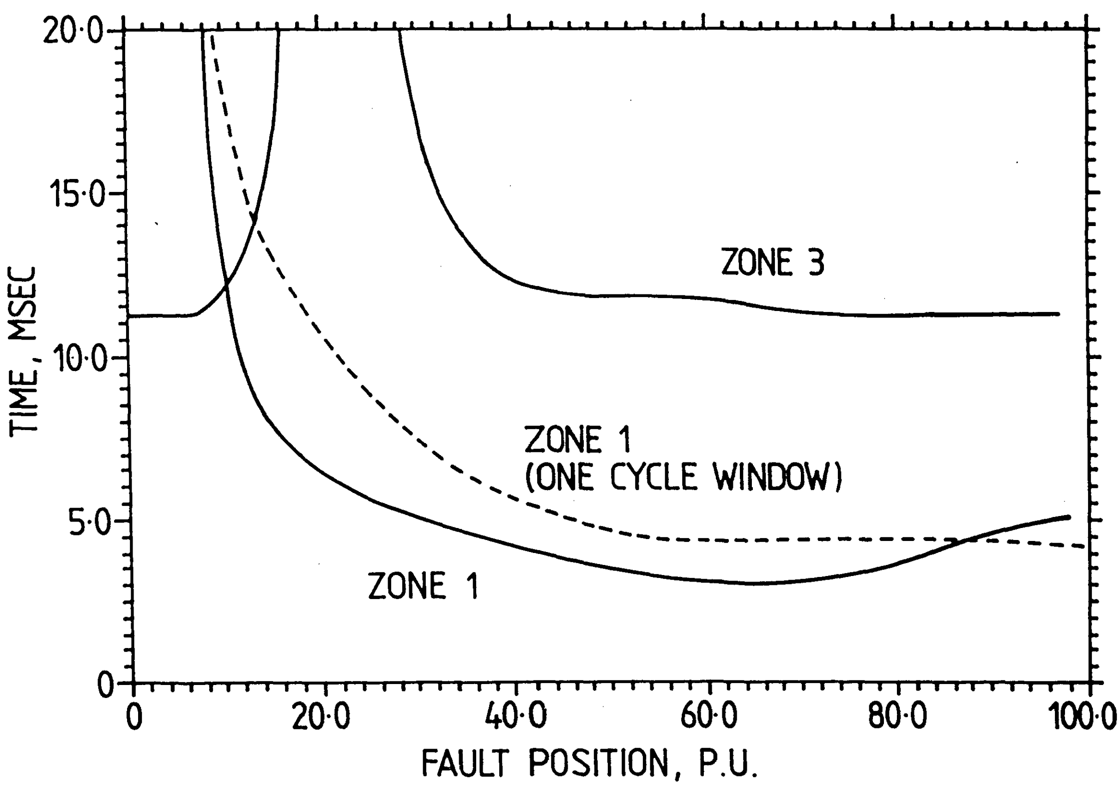

Figure 5.13: Operate time versus fault position characteristic for the neutral third harmonic algorithm with a half cycle DFT filter.

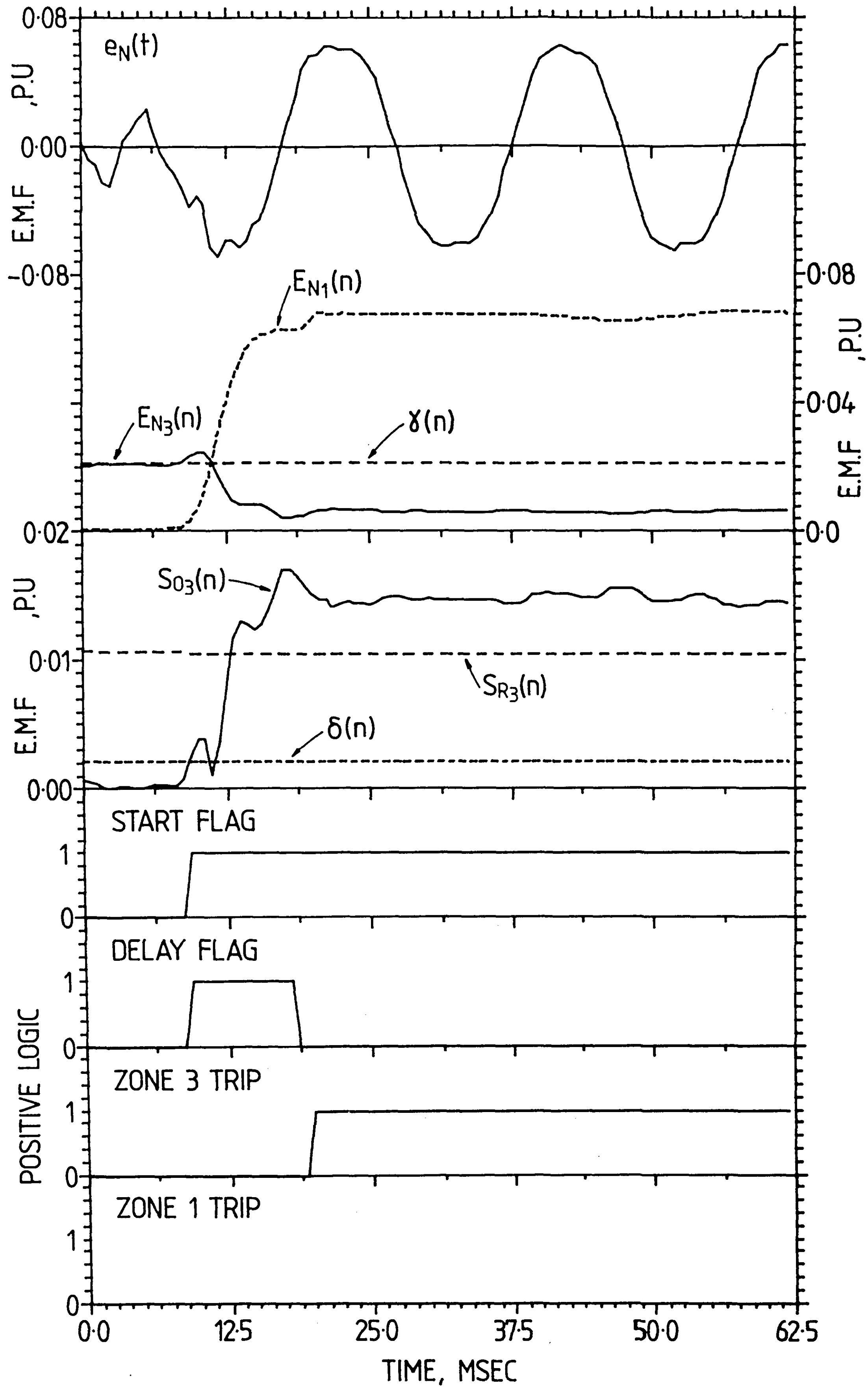

Figure 5.11 Response of the neutral third harmonic algorithm with a half cycle DFT filter to an earth fault 6.25% from the neutral.

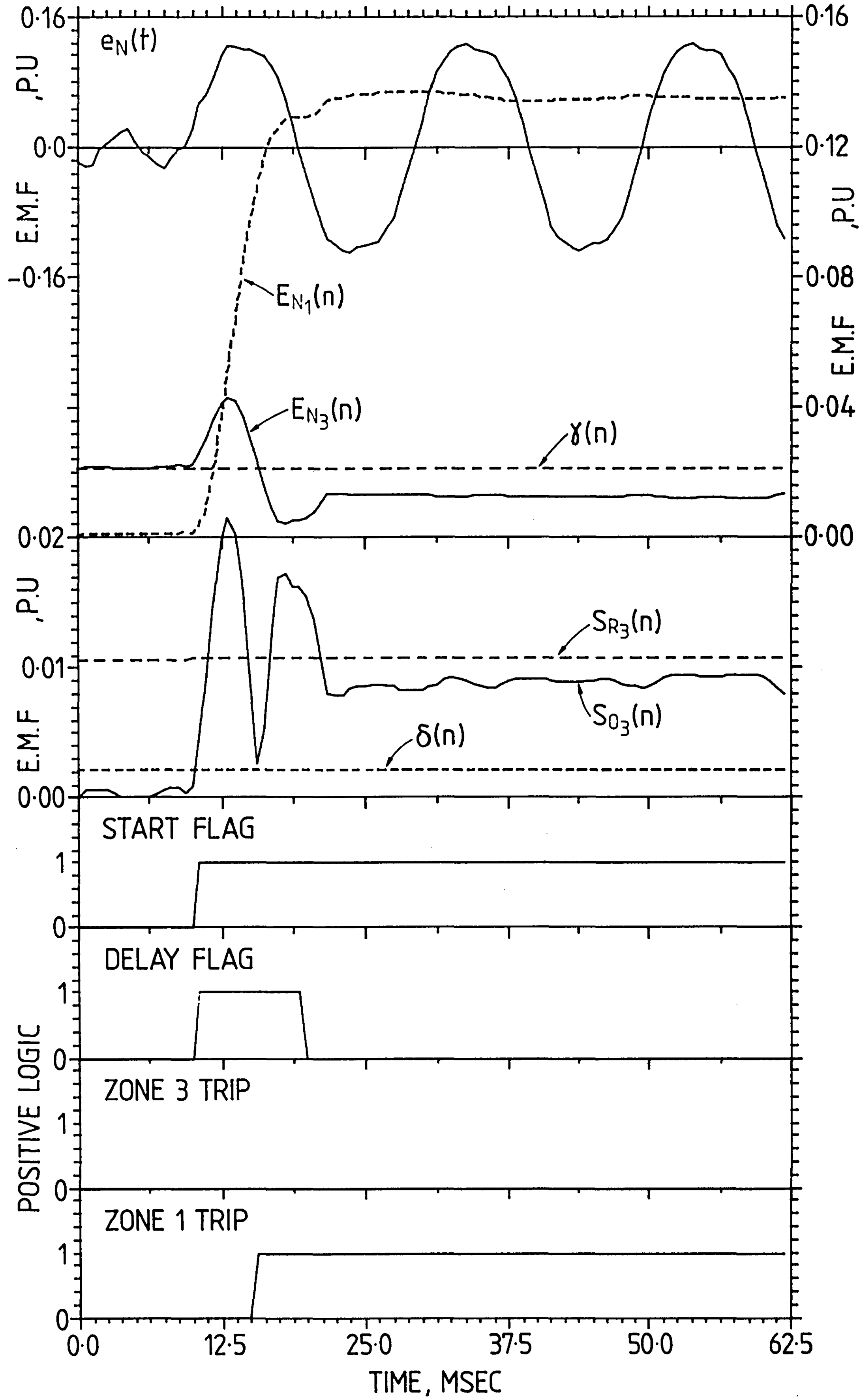

Figure 5.12: Response of the neutral third harmonic algorithm with a half cycle DFT filter to an earth fault 12.5% from the neutral.

The decrease in robustness of the filtering process is apparent in the increased ripple components present in the fundamental and third harmonic spectral estimates and the zone 3 operate signal. In contrast to the case of the one cycle algorithm, a significant ripple component is present in the prefault operate signal as well, indicating that the 10% 'start' threshold may need to be increased.

On the other hand the decrease in accuracy of the filtering process does not appear to compromise the performance of the scheme. As well as for the two cases illustrated, this was verified over the complete reach of the scheme. This is indicative of the extremely mild nature of the fault condition which produces no even harmonics or subtransients at the neutral - almost an ideal input for a half cycle DFT filter.

However, this is unlikely to be the case for severe winding and alternator system faults, and the stability of the algorithm must be evaluated before a judgement can be made.

5.2.2.3 The Two Cycle Weighted DFT Algorithm

The basic limitation to the zone 3 operating time for both the one cycle and half cycle algorithms, is the instability of the third harmonic component during the fault transition period. In contrast, the fundamental component, because it is well damped, can be put to use well before it stabilizes to its postfault steady-state value, resulting in a faster zone 1 operation.

Section 2.3.3.1 demonstrates (see figure 2.10) the action of window functions in controlling spectral errors during the fault transition period, but their use necessarily involves increasing the DFT window length to compensate for the decrease in frequency resolution implicit in their application (see figure 2.9). On the face of it then, the use of window functions is not advisable because of the increased group delay due to the greater window length.

However, if the third harmonic component can be well damped, it might be possible to use it to generate an instantaneous zone 3 trip and therefore obtain fast operation even with an increased window length. This supposition is examined using a DFT with a two cycle window weighted with a mild Hamming weighting (figures B.2b and B.4) in the protection algorithm.

Figure 5.14 illustrates the zone 1 and zone 3 operate times for the two cycle weighted DFT algorithm. The zone 3 trip incorporates no delays other than the software hysteresis (N_t = 3 as for the previous examples but N_d = 0). The other major difference in the evaluation process is a ´start´ threshold of 5% as against 10% for the one cycle and half cycle algorithms. This is necessary as the weighted DFT filter responds more slowly (see figures 2.10 and 5.15). The steady-state stability of the

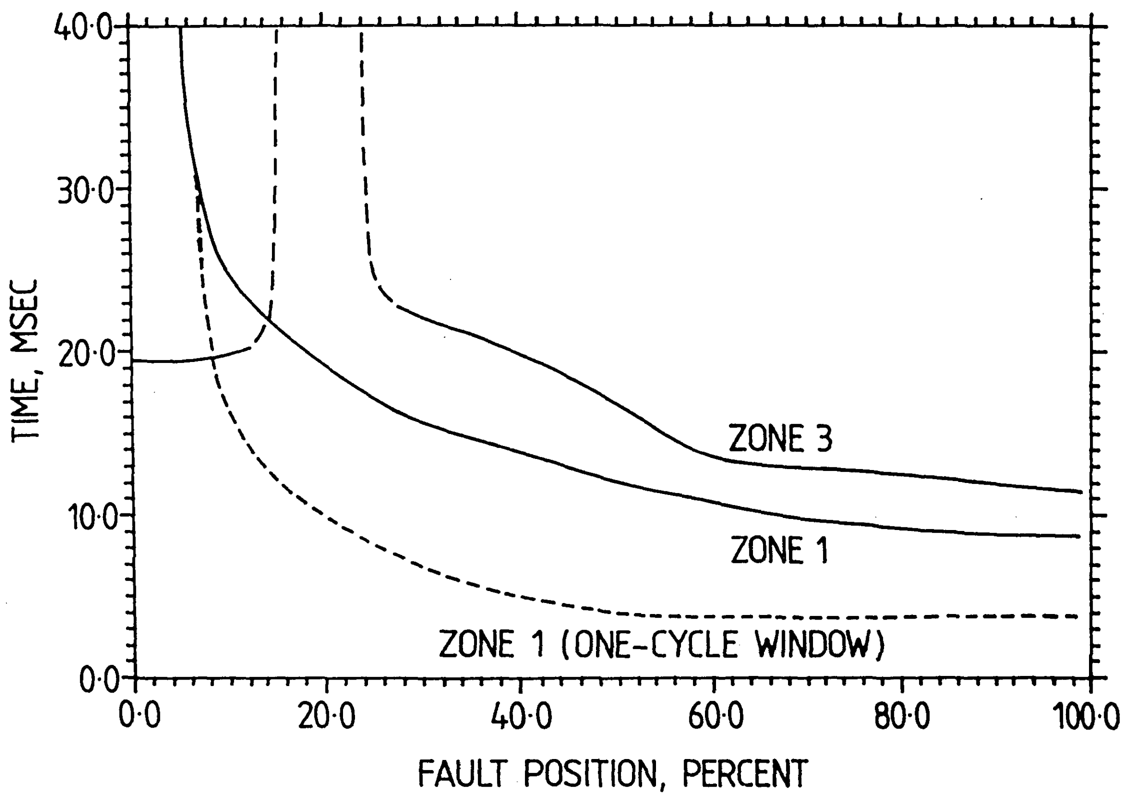

Figure 5.14: Operate time characteristics versus fault position for the neutral third harmonic algorithm with two cycle weighted DFT filter.

´start´ flag is unaffected by this lower threshold because of the damping action of the window function to the filtering process.

Compared to the full cycle window algorithm, the zone 3 operate times are almost identical near the neutral, improving only towards the line end. The zone 1 operate times on the other hand are markedly inferior; half a cycle of fundamental as against a quarter cycle for the full cycle algorithm. Compared to the half cycle algorithm, both the zone 1 and zone 3 operate times are significantly longer.

Note also that near the null zone, the zone 3 operate time curve has been drawn as a dashed line to indicate a transient trip (i.e. the algorithm either trips momentarily and then resets or a sustained chatter of the trip is obtained.) Figures 5.15 and 16 illustrate the causes of this instability for faults at the boundaries of the null zone; specifically at 12.5% and 31.25% from the neutral respectively.

The instability is due to two reasons:

(i) The damping action of the Hamming window, though very considerable (compare the zone 3 operate signals in figures 5.15 and 8 which share exactly the same fault data), is not optimal.

(ii) A ripple component present in the postfault operate signal. In figure 5.16 the ripple causes sustained chatter of the zone 3 trip.

Because the damping is not optimal, the zone 3 trip signal overshoots before settling down to its steady-state postfault value. Figure 5.15 illustrates how this causes the zone 3 operate signal to momentarily exceed the restraint signal causing a transient trip. Stability, however, can be restored by increasing the degree of hysteresis (i.e. increasing the trip count, C_t).

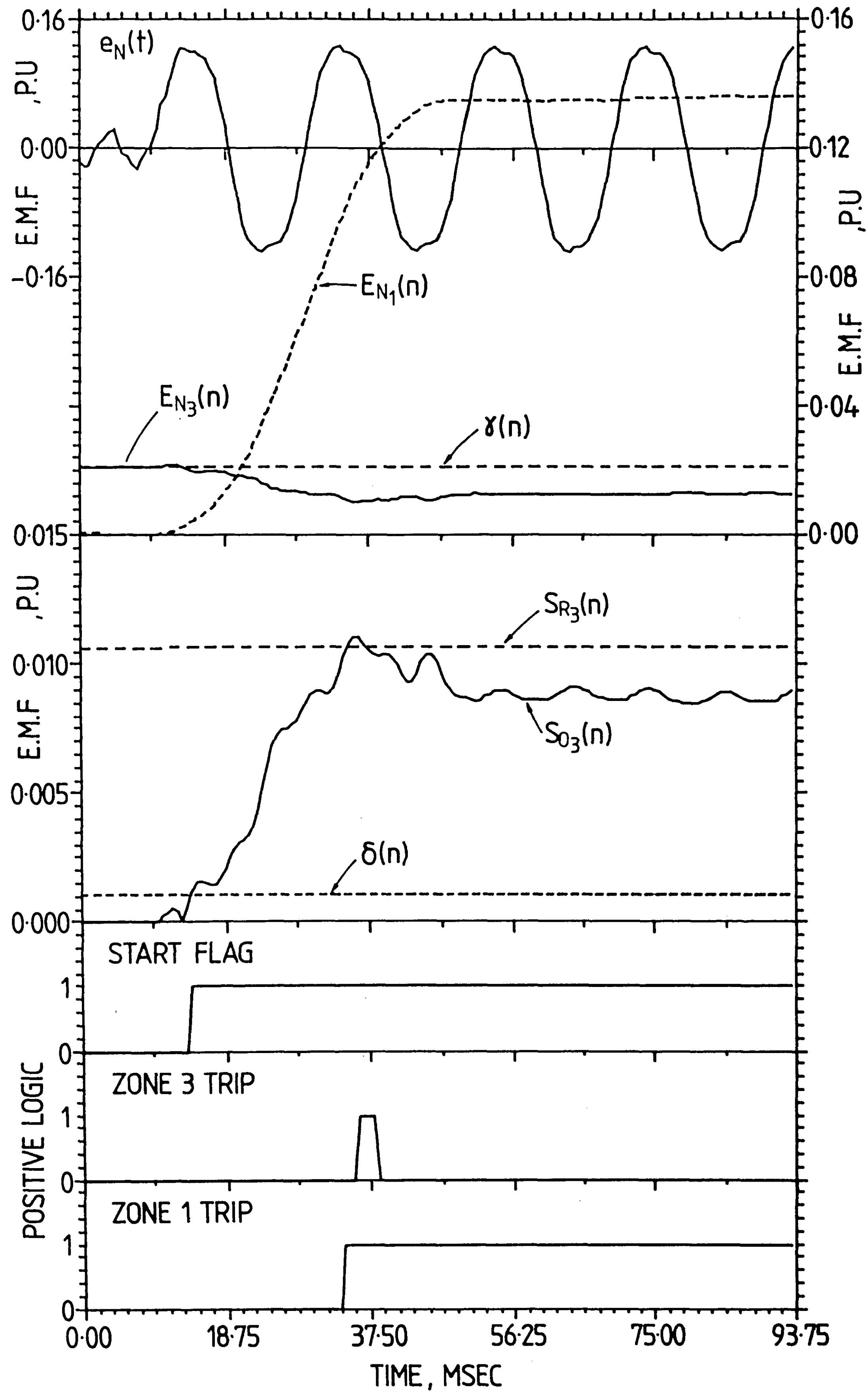

Figure 5.15: Response of the neutral third harmonic algorithm with two cycle DFT filter to an earth fault 12.5% from the neutral.

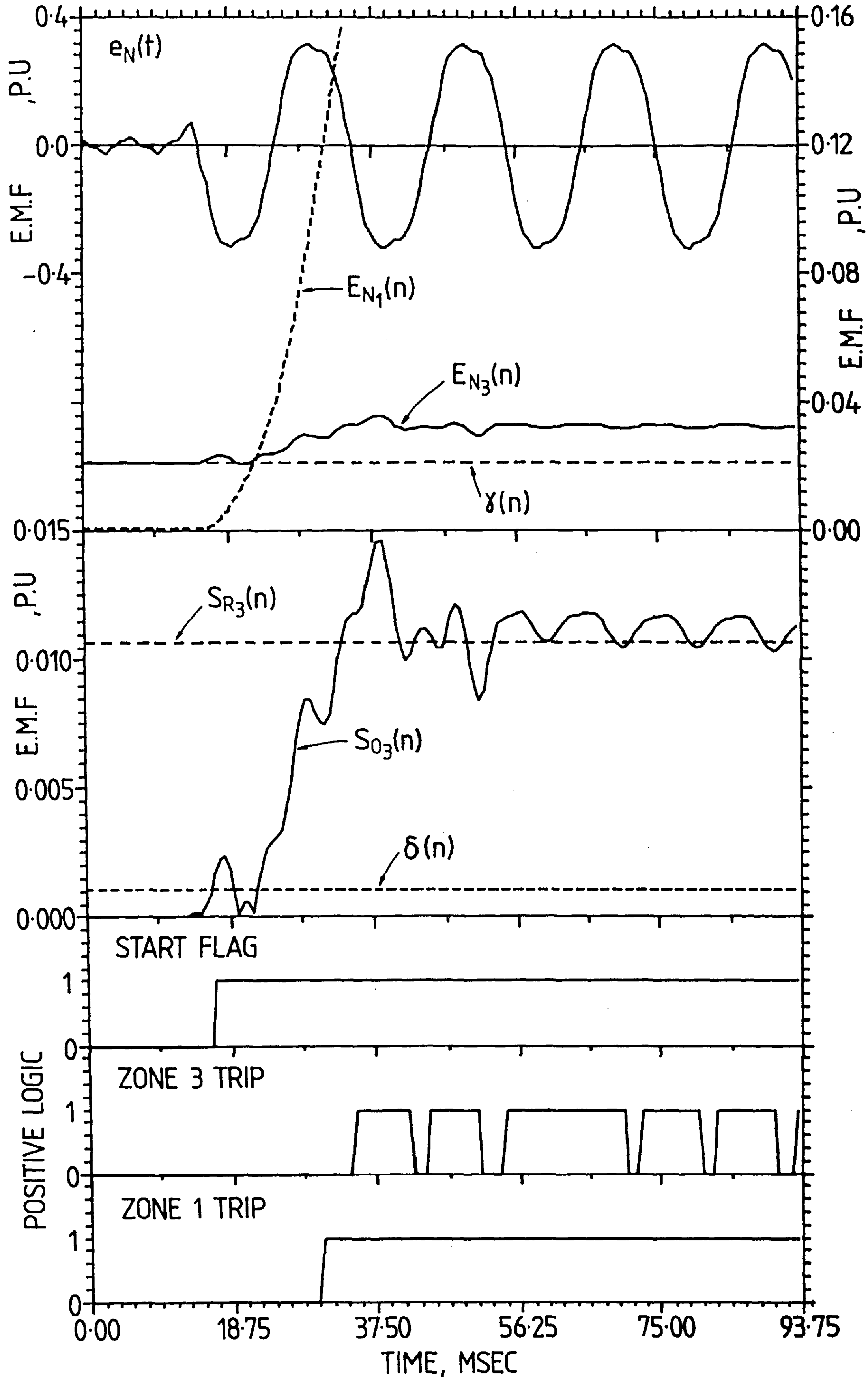

Figure 5.16: Response of the neutral third harmonic algorithm with two cycle DFT filter to an earth fault 31.25% from the neutral.

On the other hand for the example of figure 5.16, though the overshoot is present on the operate signal, the transient trip is due to the ripple component on the zone 3 operate signal. This ripple component is a manifestation of the reduced frequency resolution of the weighted DFT filter, causing leakage errors (see section 2.3.3) between the fundamental and third harmonic spectral estimates. The error is proportional to the amplitude of the fundamental, that being the dominant postfault component in the neutral emf, and will therefore increase with fault position. Note that its magnitude is greater in figure 5.16 (31.25% fault position) than in figure 5.15 (12.5% fault position) and negligible for prefault conditions.

Both the overshoot and ripple component only cause instability near the zone 3 boundaries adjoining the null band and as such do not present a serious problem because of the overlapping zone 1 reach in this region, especially as the results indicate that stability can be restored by increasing the trip count though at the expense of a degradation in operate times. However, the operate times of this algorithm are clearly inferior to the one cycle and half cycle algorithms and it cannot be recommended unless it shows superior protection stability for non-earth fault conditions compared to the other two algorithms.

5.2.3 Protection Stability

5.2.3.1 Load Variations and Power Swings

One of the main strengths of the enhanced neutral third harmonic scheme is its stability and robustness to power swings and changes in the governor load setting. In contrast the basic neutral third harmonic undervoltage scheme, as mentioned earlier in section 5.1.1.1, is inherently unstable to load changes whether transient or due to normal operation.

Figure 5.17 illustrates the response of the algorithm for a change in the governor setting from full load to zero load within the space of less than half a second. The safety margin between the zone 3 operate

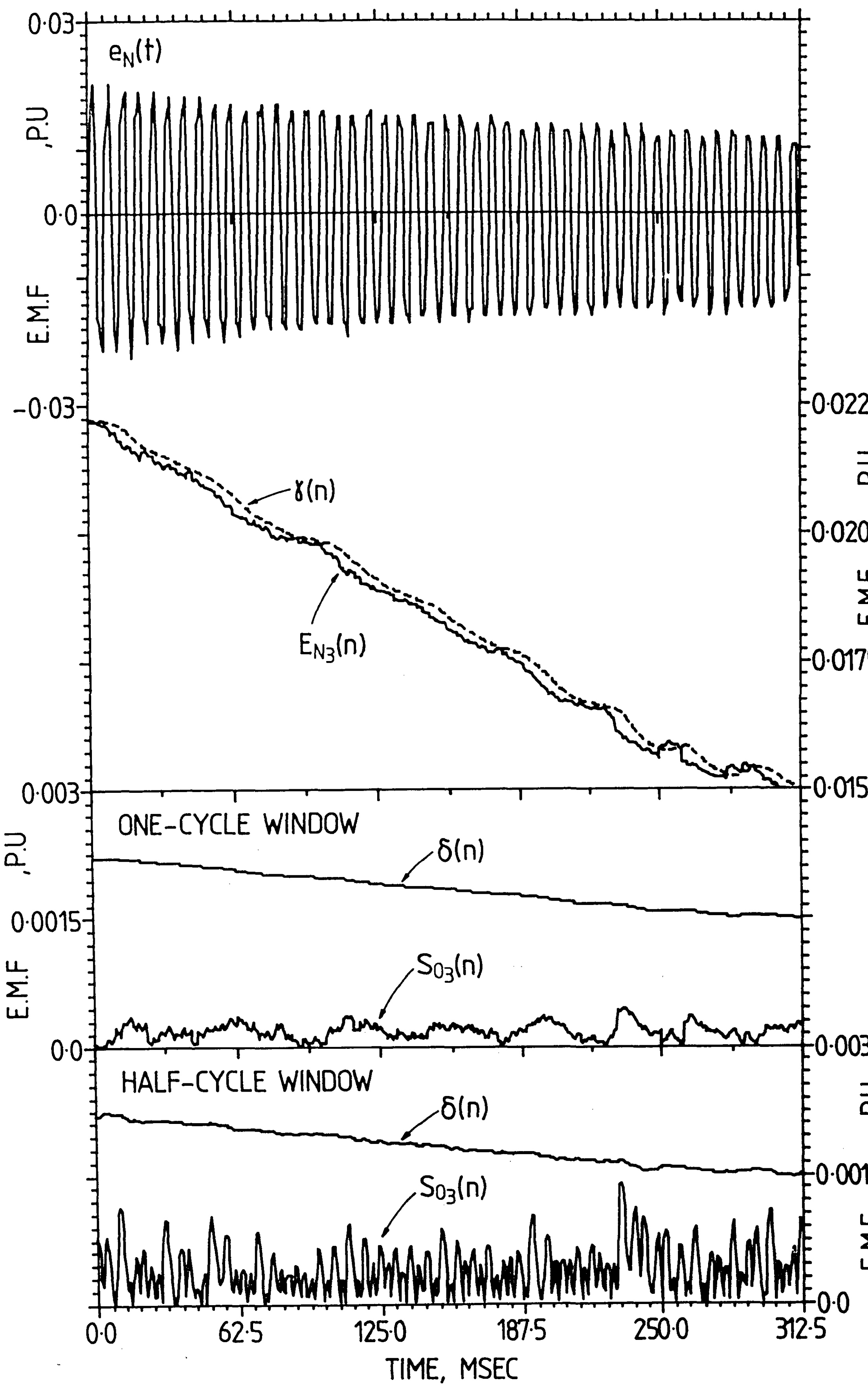

Figure 5.17: Response of the neutral third harmonic algorithm to a power swing.

signal and the start threshold is high over the complete duration of the power change, resulting in the reference accurately tracking the third harmonic component. For the half cycle DFT algorithm, however, the margin of safety is not as high due to its decreased robustness. The weighted DFT algorithm with its lower 5% start threshold is as stable as the full cycle algorithm, though this is not illustrated.

Such a change is unrealistically severe as, in practice, the load setting will be changed very gradually over a matter of minutes rather than seconds. Even under external power system fault conditions, because of the very large mechanical time constants associated with a real machine, it is unlikely to be this severe. However, it does serve to show the very high stability of the protection scheme.

5.2.3.2 Inter-turn Faults

Figure 5.18 illustrates the effect of an inter-turn fault on the stability of the protection scheme. The fault consists of one coil (6.25% of the total winding) shorted on the A-phase at a point 50% from the neutral.

It demonstrates the almost total lack of sensitivity of the protection to such faults. The neutral third harmonic is not significantly affected by the fault to the extent that the operate signal does not exceed the 'start' threshold (k_2=0.1) during the fault transition period. Note that because of this the updating of the reference signal is not inhibited and it tracks the postfault third harmonic component accurately, further desensitizing the algorithm to the fault condition.

Figure 5.18 also illustrates the sensitivity problems inherent in inter-turn protection. A short circuit across 6.25% of the winding of one phase represents a reasonably severe fault and localized circulating currents within the resultant closed coil will be high. Despite this the net total effect on the machine as seen from either the neutral or line terminals is not significant enough to obtain a high sensitivity. A spectral analysis of the neutral emf (see bottom of figure 5.18) reveals an

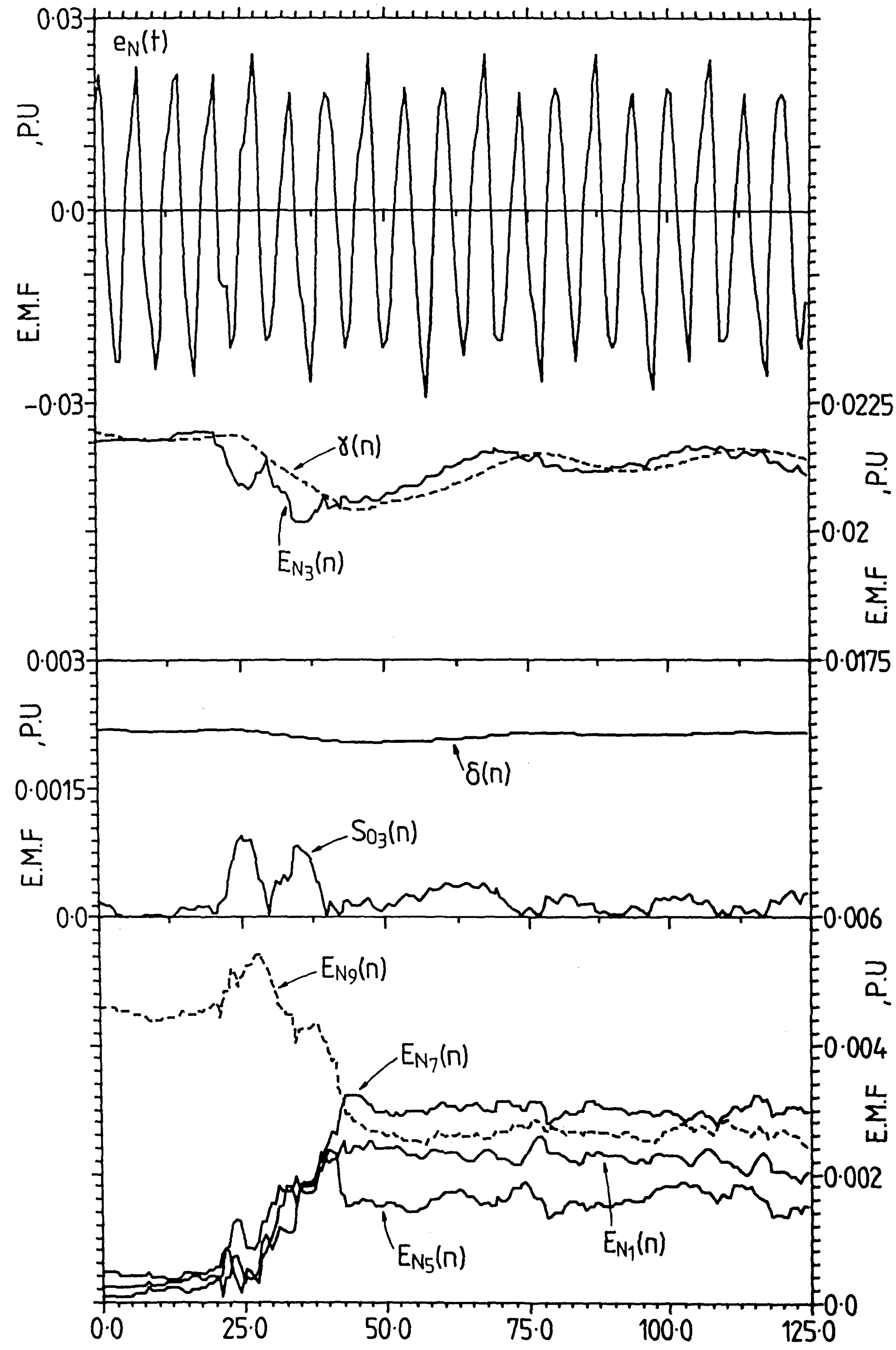

Figure 5.18: Response of the neutral third harmonic algorithm to an inter-turn fault.

increase in the 5th and 7th harmonics due to the increased magnetic imbalance within the machine but it is not significant enough to be used for protection purposes.

5.2.3.3 Inter-phase Faults

The stability of the one cycle DFT algorithm to inter-phase faults is illustrated by figure 5.19. The fault consists of a short circuit between the B and C phases of the alternator, the fault point being 62.5% form the neutral on both phases. To prevent damage to the machine a fault resistance of 1 ohm was also introduced.

The algorithm retains its stability for the fault illustrated, but it is clear that it is not inherently insensitive to it as a large change in the zone 3 operate signal occurs. Zone 1, however, is highly stable as the postfault fundamental spectral component is very low. The severity of the fault is evident from the very large postfault fifth harmonic component, greater even than the third harmonic component, and the third harmonic ripple indicating a high degree of magnetic imbalance within the machine.

Both the half cycle and weighted algorithms returned very similar results with the half cycle algorithm increasing the third harmonic ripple component, though still not enough to cause instability, and the weighted algorithm decreasing it.

5.2.3.4 Three-phase Short Circuits

Figure 5.20 illustrates the performance of the algorithm for an external three-phase short circuit close to the terminals of the machine. Such faults are rare but have been known to occur due to human error [78,93,94] and therefore must be considered. The terminal emfs for this condition are illustrated further on in figure 5.30.

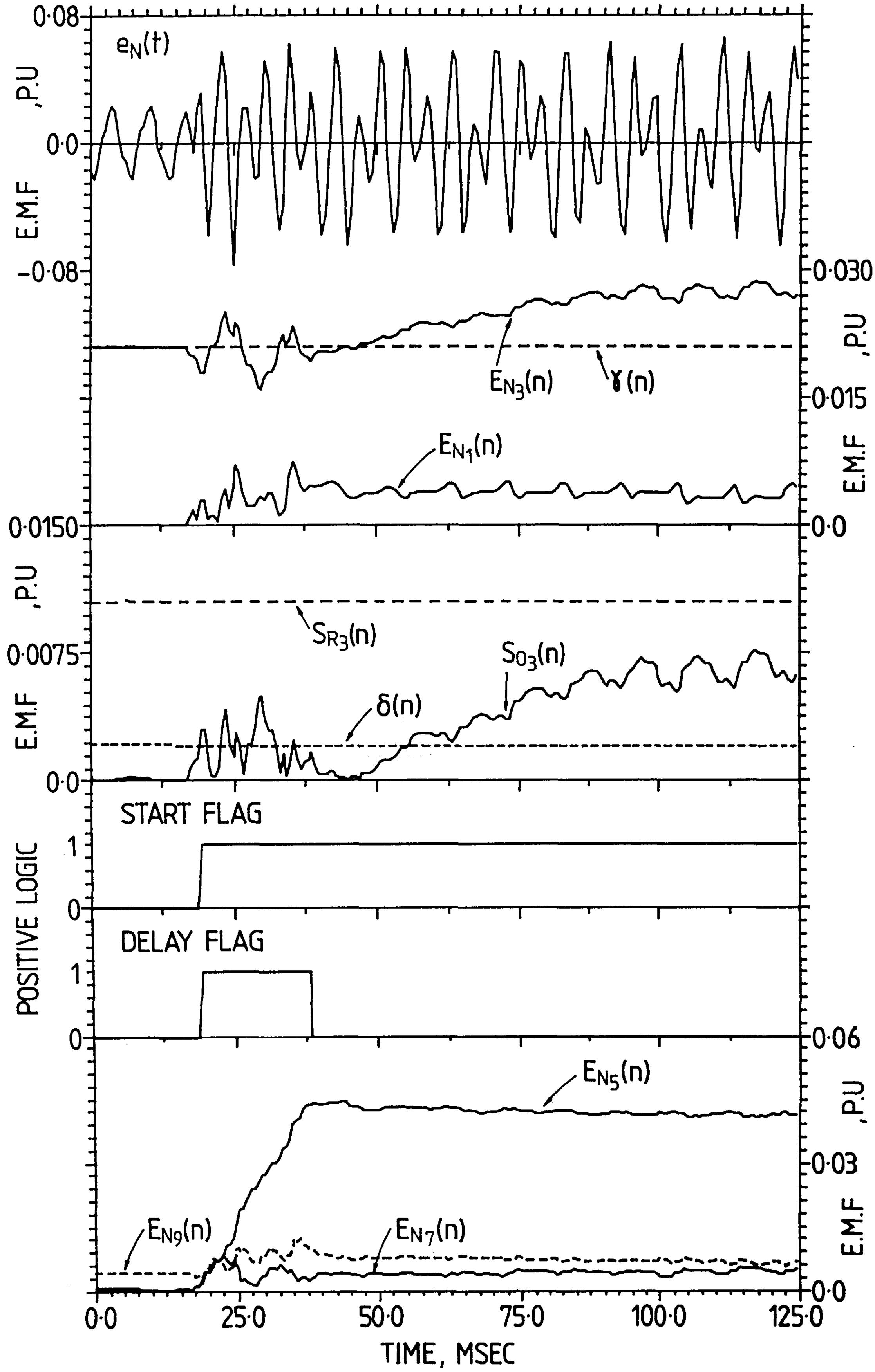

Figure 5.19: Response of the neutral third harmonic algorithm to an inter-phase fault 62.5% from the neutral on the B and C phases.

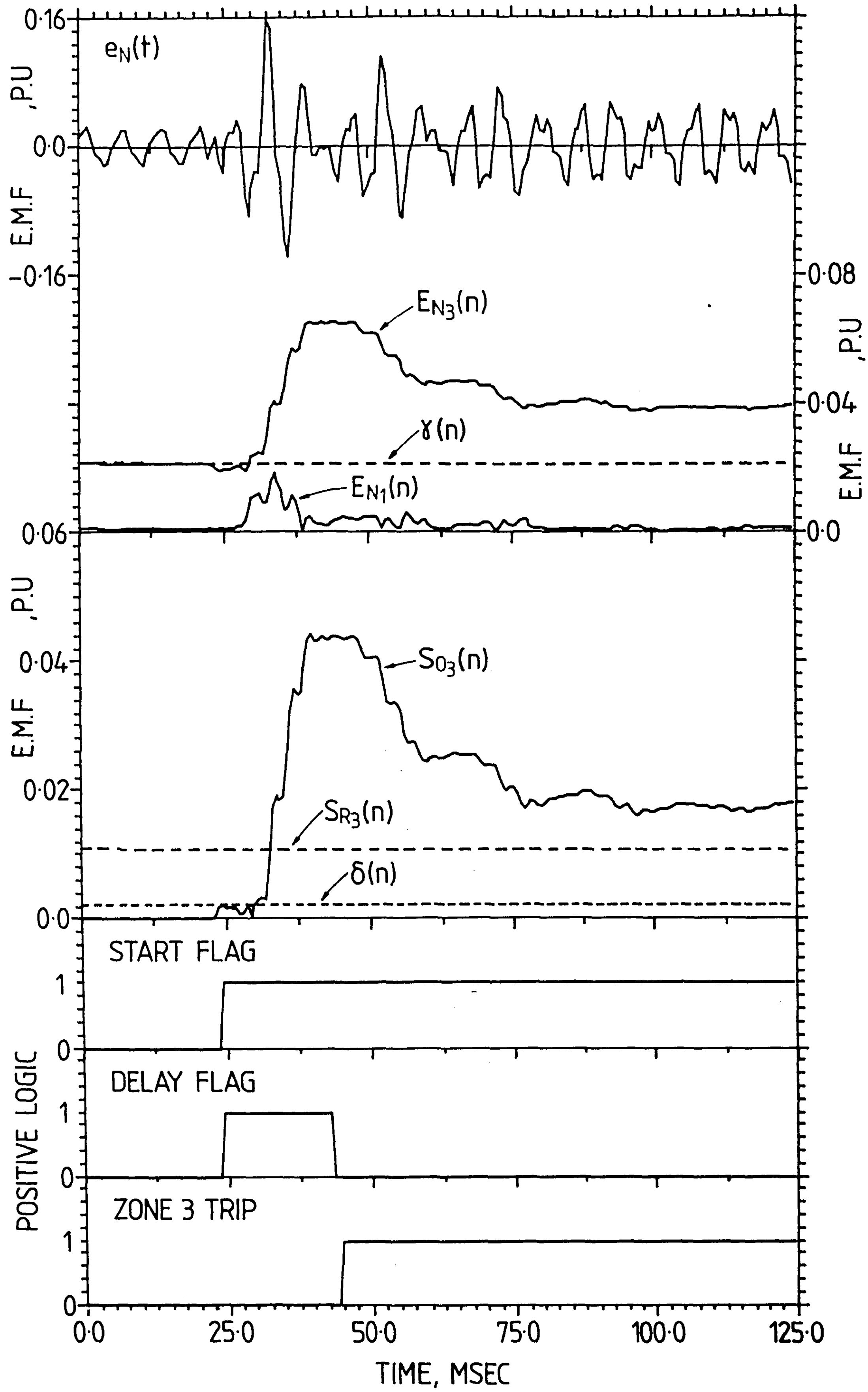

Figure 5.20: Response of the neutral third harmonic algorithm to an external three-phase short circuit close to the alternator terminals.

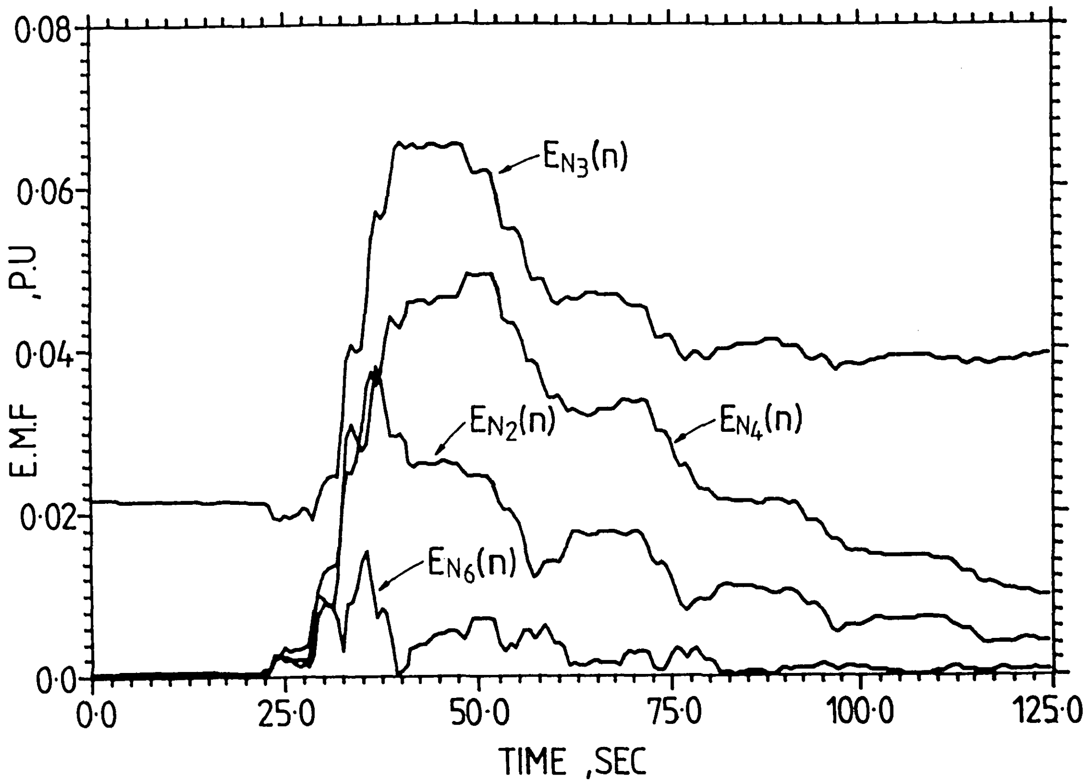

Figure 5.21: Spectral analysis of the neutral emf at the fault instant for the three-phase fault.

The scheme gives a very positive zone 3 trip for this condition because of a very sharp increase in the neutral third harmonic component, but as it is a balanced fault condition zone 1 remains stable. The spectral analysis of the neutral emf in figure 5.21 illustrates the severity of the fault condition with very high levels of both even and odd harmonics present during the initial fault current surge.

Figure 5.22 shows the response of the half cycle algorithm to the same fault condition and illustrates the very poor response of the half cycle DFT filter to signals with a high even harmonic content. The postfault ripple on the third harmonic estimate results in an oscillatory zone 3 operate signal giving a transient trip.

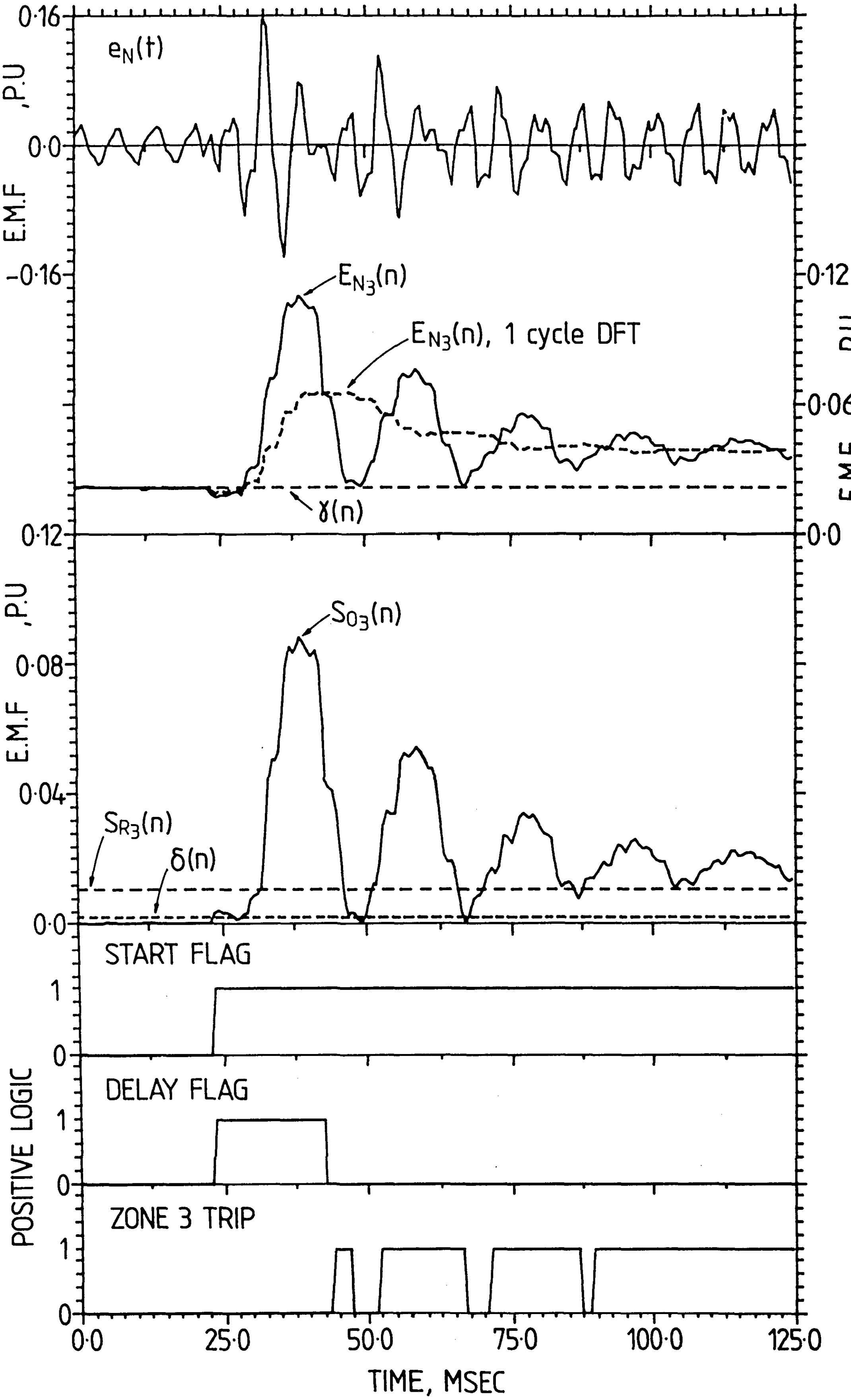

Figure 5.22: Response of the neutral third harmonic algorithm with half cycle DFT filter to an external three-phase short circuit close to the alternator terminals.

5.3 Performance of the Voltage Comparison Scheme

5.3.1 Structure of the Algorithm

The logical structure of the algorithm is very similar to that of the neutral third harmonic algorithm and, therefore, the logical sequence illustrated in flowchart 5.1 is essentially the same for both algorithms.

The initialization and DFT procedures are logically identical, structurally differing only in the number of relaying measurands. 'INIT', therefore, in addition to initializing the neutral data and averaging windows and the memory stack, also initializes data windows for the discretized terminal voltages. The DFT procedure then computes the fundamental and third harmonic spectral components for all four measurands. Additional preprocessing (half cycle or weighted DFT), if selected, is applied to all four relaying measurands.

The evaluation process for the voltage comparison algorithm is implemented as given by equations 5.8-13 and is logically identical to the block diagram of figure 5.6.

The discrimination process for the voltage comparison algorithm, however, differs from the neutral third harmonic algorithm in that two additional restraint signals, the positive and negative-sequence restraint signals (equations 5.12 and 13), influence the tripping criteria as given by equation 5.14. Flowchart 5.2 illustrates the process.

5.3.2 Performance for Earth Faults

Figure 5.23 illustrates the response of the voltage comparison algorithm with a one cycle DFT filter for the same fault data as used in figure 5.7 (i.e. an earth fault 6.25% from the neutral). The values of k_2 and k_1 are also the same as selected in the neutral third harmonic scheme. Note that the zone 1 operate and logic signals are not illustrated as these are identical to those in figure 5.7. The zone 3 delay flag is not shown but this does not imply that it is not present.

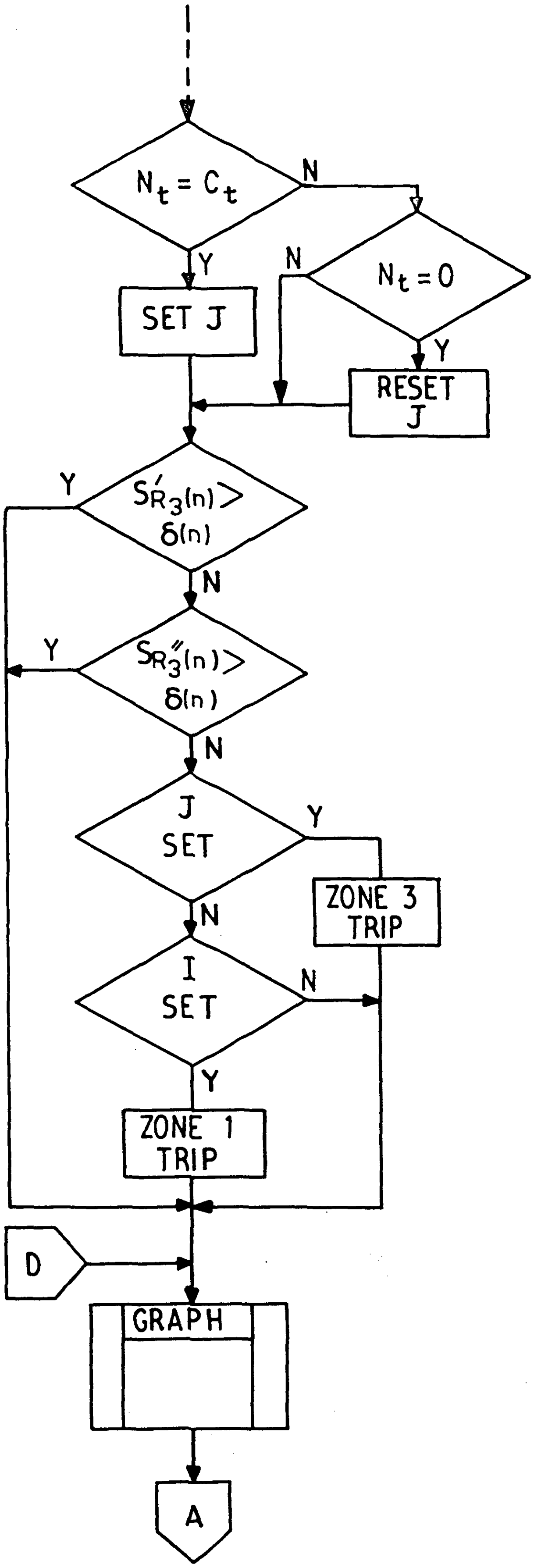

Flowchart 5.2: Discrimination process for the voltage comparison algorithm.

Comparing figures 5.23 and 5.7 demonstrates the similarity in response of the two schemes. The operate signals for both schemes are very similar in form with roughly the same relative postfault trip and start thresholds, indicating that the position of the null points for the two schemes will be similar. This confirms the results of figure 4.10. The zone 3 operate time at 23 msec is identical to that obtained for the neutral third harmonic scheme. The overall zone 3 operating times obtained were also very similar and therefore figure 5.9 is equally valid for both algorithms.

The postfault third harmonic negative and positive-sequence restraint signals are as expected (figure 5.5a) very low. Their amplitude during the fault transition period, however, is also unexpectedly very low with no sign of instability, indicating that the terminal third harmonic vector estimates during the fault transition period are also very similar.

Figure 5.24 illustrates the action of the algorithm for an identical earth fault but with a V.T. connection to ground at the terminals of the micro-alternator. The zone 3 operate time is identical to that obtained in figure 5.23, but note the very wide margin between the operate signal and the tripping threshold indicating that the null band has moved towards the line end as predicted by the computer simulation (see figure 4.10b). As before the third harmonic negative and positive restraint signals are very small.

The overall operate times obtained are very similar to figure 5.9 but with the null band shifted right up against the terminals of the machine and, therefore, zone 3 does not operate for an earth fault close to the terminals. Figure 4.10b shows that this occurs because the null point moves to within 15% of the machine terminals.

The responses of the algorithm with half cycle and two cycle weighted DFT filters were also evaluated but results obtained are very similar to those already illustrated for the neutral third harmonic algorithm. In particular the overall operating times obtained with these

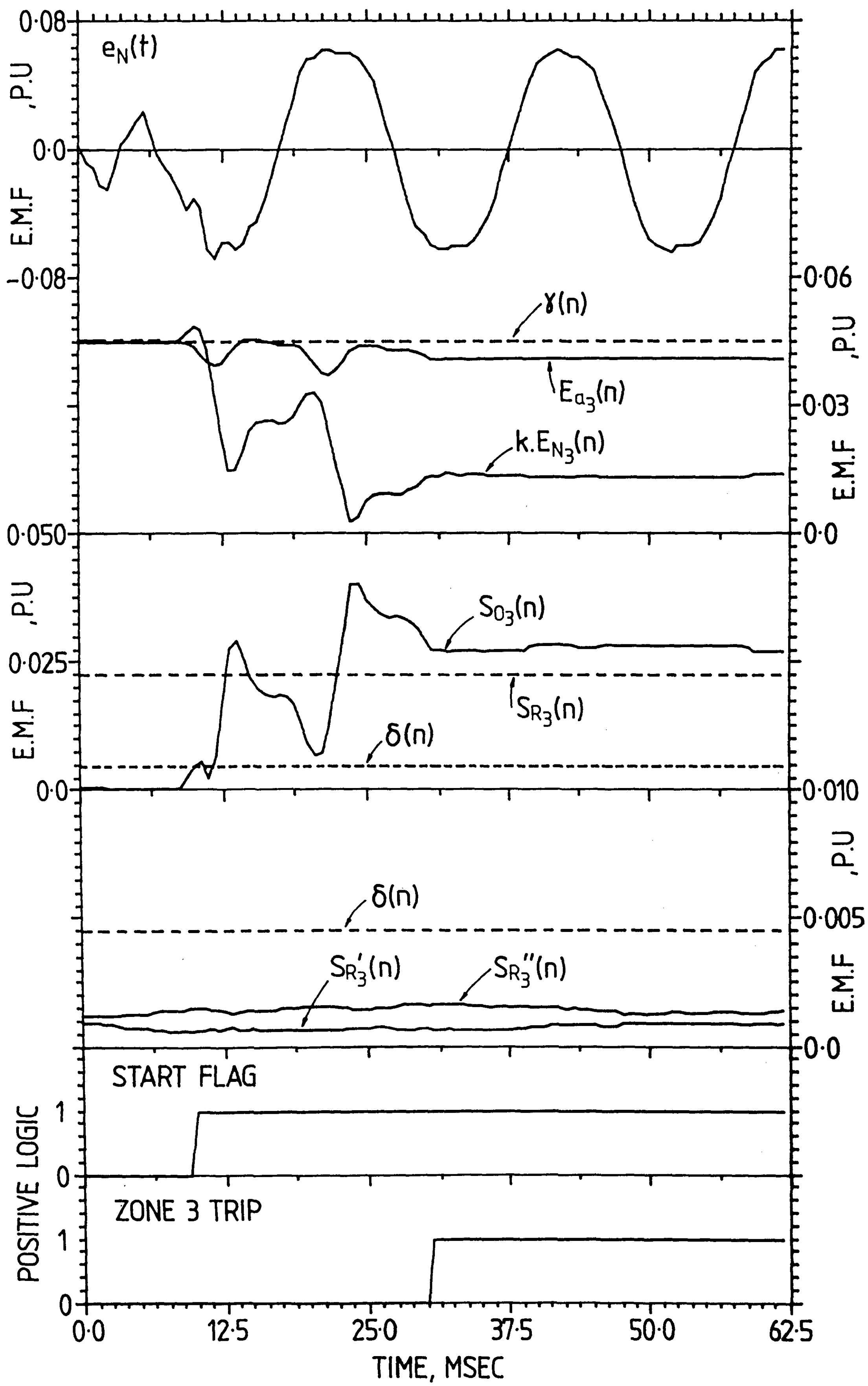

Figure 5.23: Response of the voltage comparison algorithm to an earth fault 6.25% from the neutral.

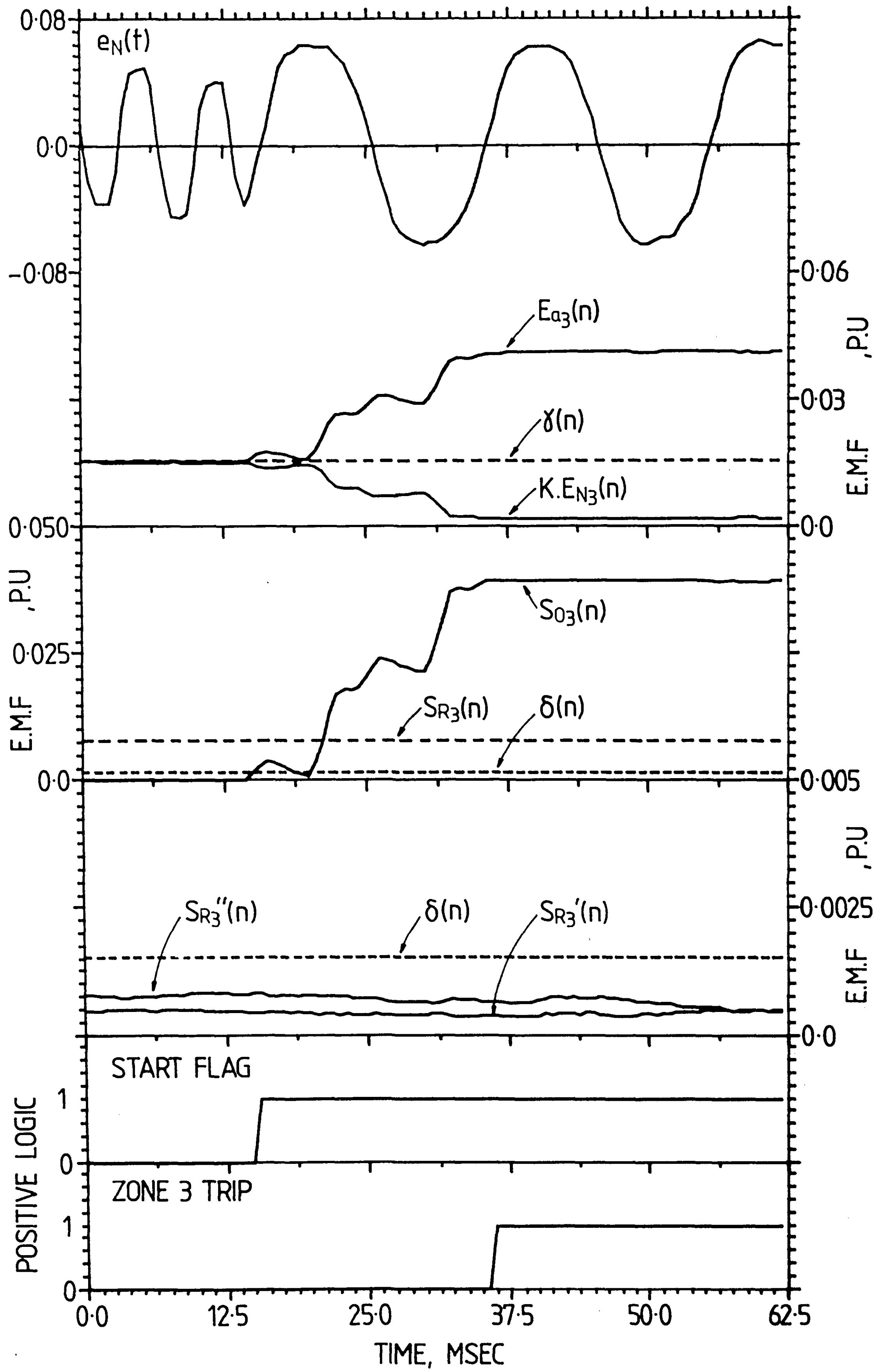

Figure 5.24: Response of the voltage comparison algorithm to an earth fault 6.25% from the neutral with a V.T. connection at the alternator terminals.

windows are identical to results presented in figures 5.13 and 14.

In summary, the voltage comparison algorithm gives a fast and reliable trip decision, the relaying action and performance being almost totally identical to the neutral third harmonic algorithm. For the additional complexity involved, this algorithm would therefore appear to offer no advantages. However, in the next section its superior stabilty over the the neutral third harmonic algorithm will be illustrated.

5.3.3 Protection Stability

The protection stability of the voltage comparison scheme to load variations, power swings and inter-turn faults is very similar to that of the neutral third harmonic scheme. Therefore, the response of the algorithm to these fault conditions will not be illustrated.

5.3.3.1 Inter-phase Faults

Figure 5.25 illustrates the response of the voltage comparison algorithm to the inter-phase fault used to evaluate the stability of the neutral third harmonic algorithm in figure 5.19. The terminal emfs during the fault are illustrated in figure 5.26.

Comparing figures 5.25 and 5.19, the inherent stability of the voltage comparison scheme is immediately apparent in the much reduced zone 3 operate signal which hardly exceeds the starter threshold. In fact, with $k_2=5$ (i.e. a ´start´ threshold of 20%), the algorithm would not have responded at all. Note how the terminal third harmonic component mirrors the behaviour of the neutral component accounting for the increased stability.

The change in the third harmonic negative and positive-sequence restraint signals is very dramatic, increasing past the ´start´ threshold within a millisecond of the fault instant, indicating that even if the algorithm had been unstable a trip would have been restrained. The speed

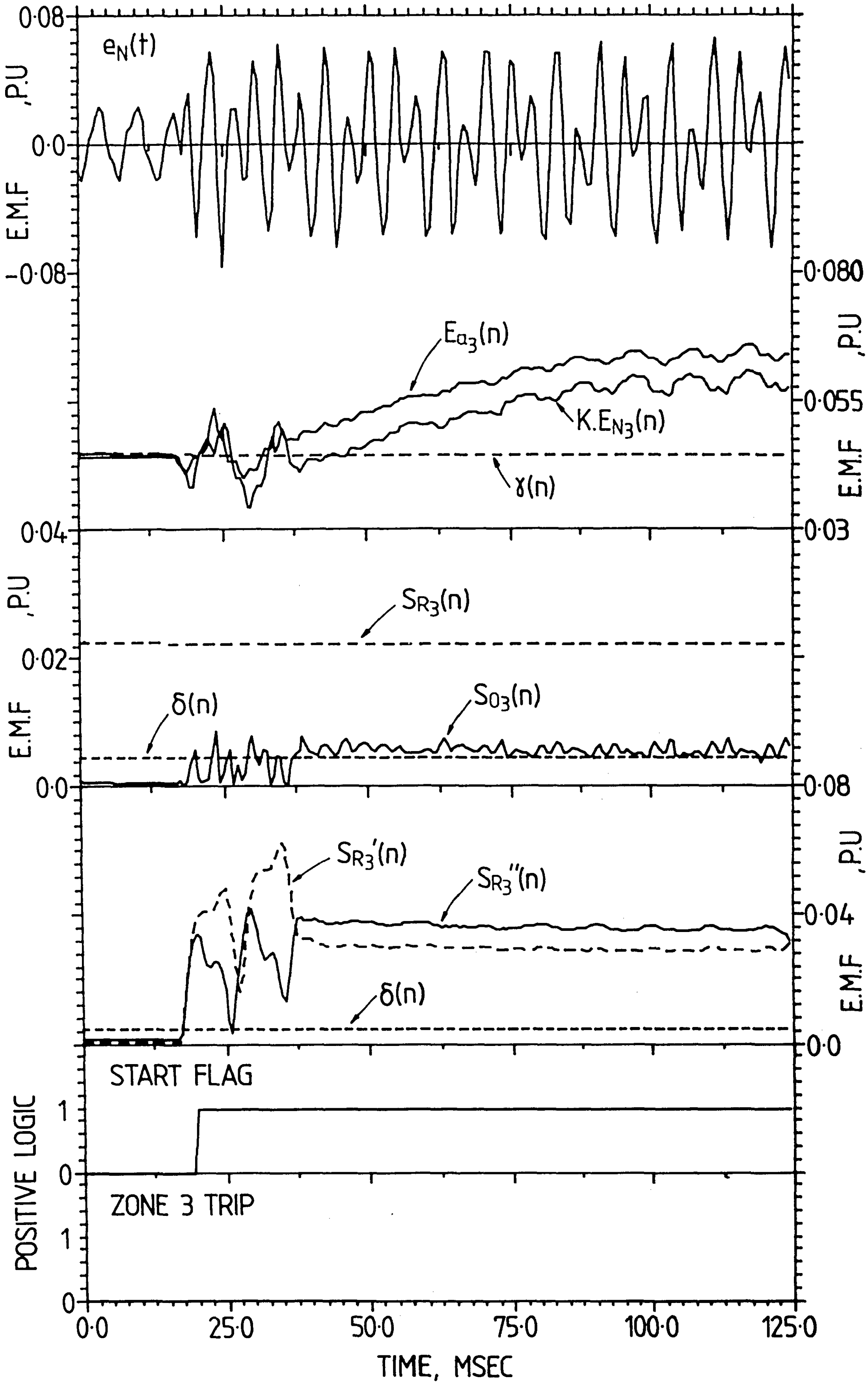

Figure 5.25: Response of the voltage comparison scheme to an interphase fault 62.5% from the neutral on the B and C phases.

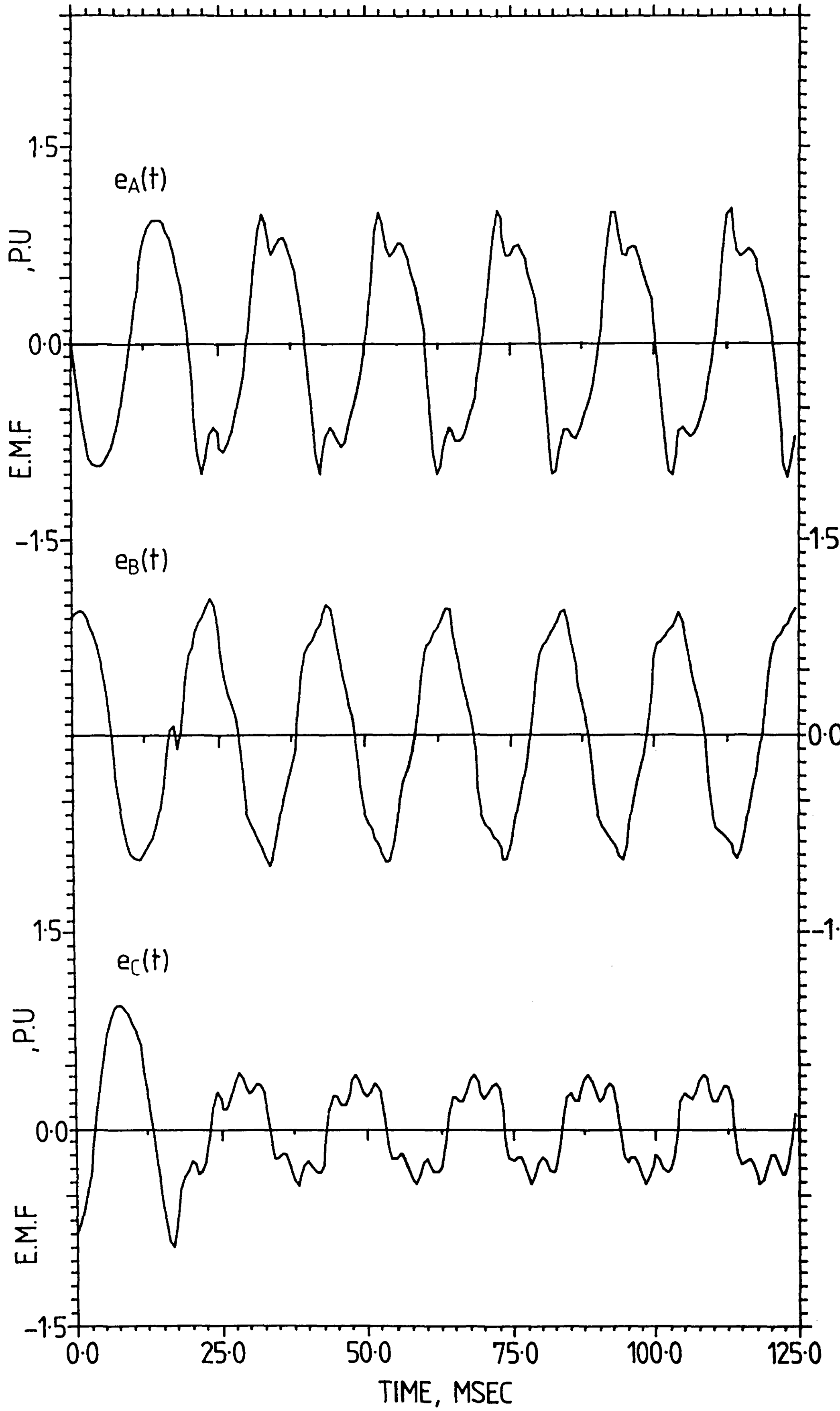

Figure 5.26: Terminal emfs during the inter-phase fault of figure 5.25

of response and magnitude of the two restraint signals is characteristic of the high stability that can be achieved. Figure 5.5b illustrates the variation in the postfault values of the restraint signals with fault position.

The protection stability of the algorithm was tested for a large variety of inter-phase faults, displaying in all cases high stability on both zones 3 and 1. Figure 5.27 illustrates the variation of the zone 3 operate signal with fault position for an inter-phase fault, the fault position being at the same position on both the faulted phases. Note that the operate signal is very low whatever the fault position.

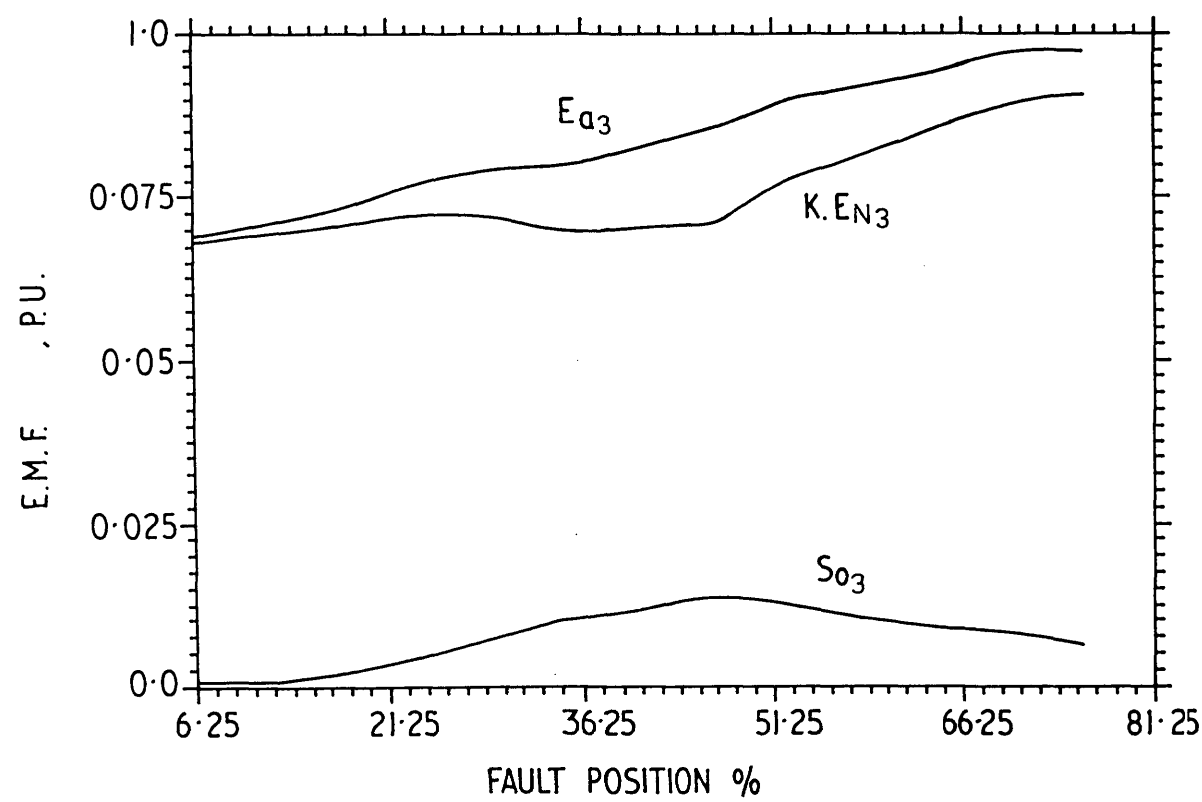

Figure 5.27: Variation of zone 3 operate signal with fault position for an inter-phase fault.

Figure 5.28 demonstrates the response of the half cycle voltage comparison algorithm to exactly the same fault. The reduced robustness of the DFT is evident in the greater ripple component present in the zone 3

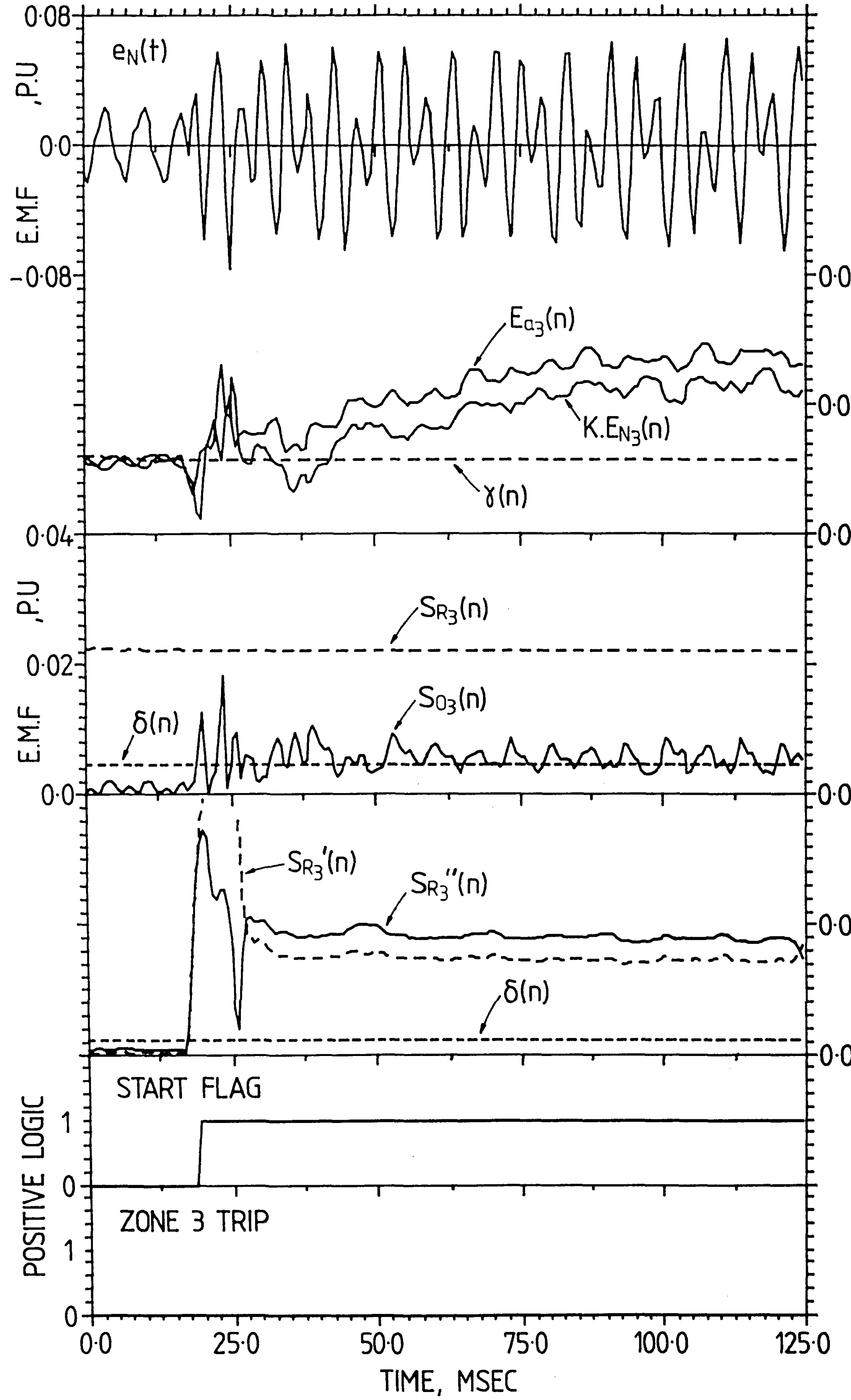

Figure 5.28: Response of the voltage comparison algorithm with half cycle DFT filter to the inter-phase fault of figures 5.25 and 5.26.

operate signal, but the stability of the algorithm is not compromised because of the large amplitude of the third harmonic negative and positive-sequence restraint signals.

5.3.3.2 Faults External to the Generator

One of the characteristics of the voltage comparison scheme is its enhanced zone 3 discrimination against external faults compared to the neutral third harmonic scheme. Figure 5.29 illustrates this characteristic for a very severe external fault; a three-phase short circuit close to the terminals of the machine. The fault data is exactly the same as used in figures 5.20-22. Figure 5.30 shows the terminal emf waveforms during the fault instant.

Because the fault is external to the alternator, both the neutral and third harmonic components accurately mirror each other, resulting in a very low zone 3 operate signal and ensuring stability. Note that if the fault had been at the terminals or internal to the machine this would not be true and zone 3 would have tripped. The additional restraint signals, however, do not contribute to the stability of the algorithm (Note, neglecting the fault transition period, their very low postfault amplitudes), this being a consequence of the balanced nature of the fault. Figure 5.30 illustrates this point; all the postfault terminal emfs are remarkably similar, indicating that their third harmonic components are all in phase. The zone 3 stability to other external faults, including earth faults, was also verified.

For the fault illustrated, zone 1 is also stable as shown in figure 5.20 because of the balanced nature of the fault. However, for other external faults, earth faults due to a blown terminal V.T. fuse for example, zone 1 will operate and the directional characteristic of the zone 3 reach is then of no consequence. A completely directional algorithm to cover only the stator windings may be possible by formulating the zone 1 operate signal as a voltage comparison between the terminal and neutral fundamental components but has not been investigated because of lack of time.

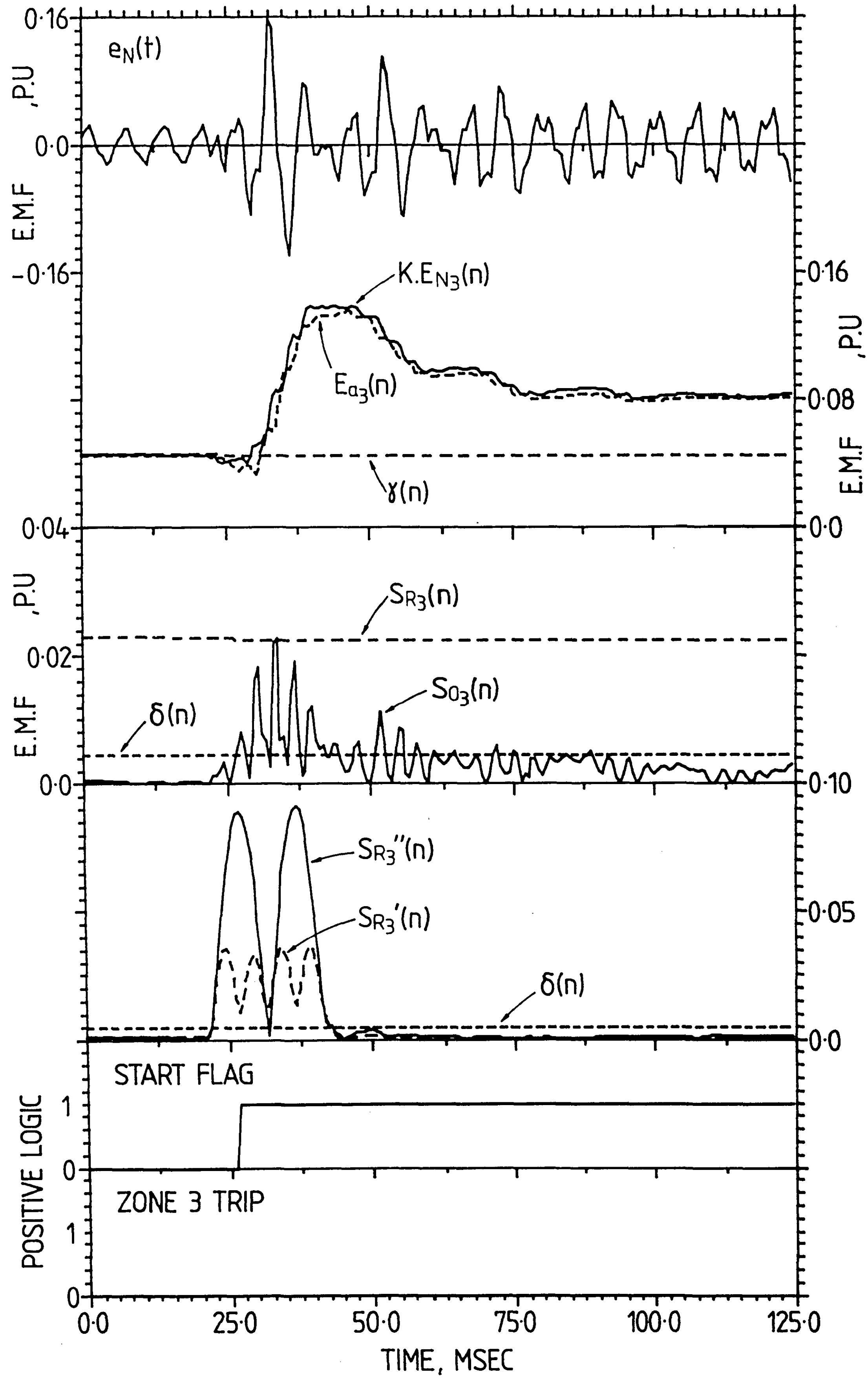

Figure 5.29: Response of the voltage comparison algorithm to an external three-phase short circuit close to the alternator terminals.

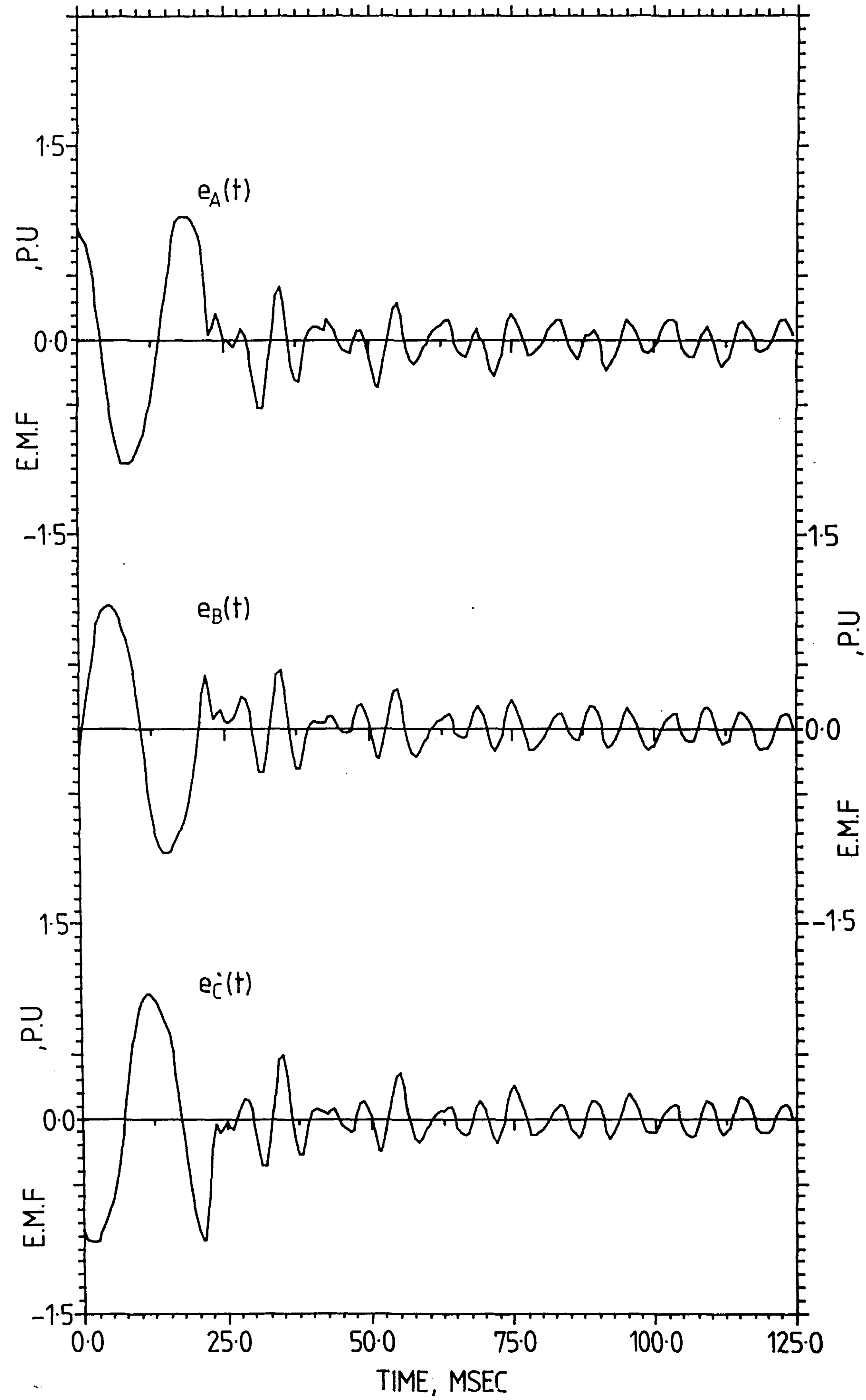

Figure 5.30: Terminal emfs during the three-phase fault.

Figure 5.31 illustrates the zone 3 performance of the half cycle voltage comparison algorithm to the three-phase short circuit. In contrast to the one cycle algorithm, it is unstable. This is a direct consequence of the reduced accuracy of the half cycle DFT in the presence of even harmonics (section 5.2.3.4) resulting in a very unstable zone 3 operate signal.

5.4 Conclusions

5.4.1 General conclusions

The results of this study show that both the neutral third harmonic and the third harmonic voltage comparison algorithms fulfil the main performance objectives set for this research. The general conclusions are listed below.

(i) Both algorithms are capable of fast operation, whatever DFT window is chosen, detecting earth faults well within a maximum of one and a quarter cycles. The zone 3 and 1 operate time characteristics are virtually identical for both algorithms and, therefore figures 5.9, 5.13 and 5.14 apply equally to both.

(ii) Stability to load changes and power swings is high for both algorithms with the voltage comparison algorithm possessing the better stability characteristic. Figure 5.17 illustrates the response of the neutral third harmonic algorithm to a load change and is equally valid for the voltage comparison algorithm. An indication of the very high stability achieved is the fact that the inherently higher stability of the voltage comparison algorithm to power swings could not be verified directly (the result obtained being identical to figure 5.17) but is deduced from its stabilty towards external and heavy current faults (figures 5.25,28,29).

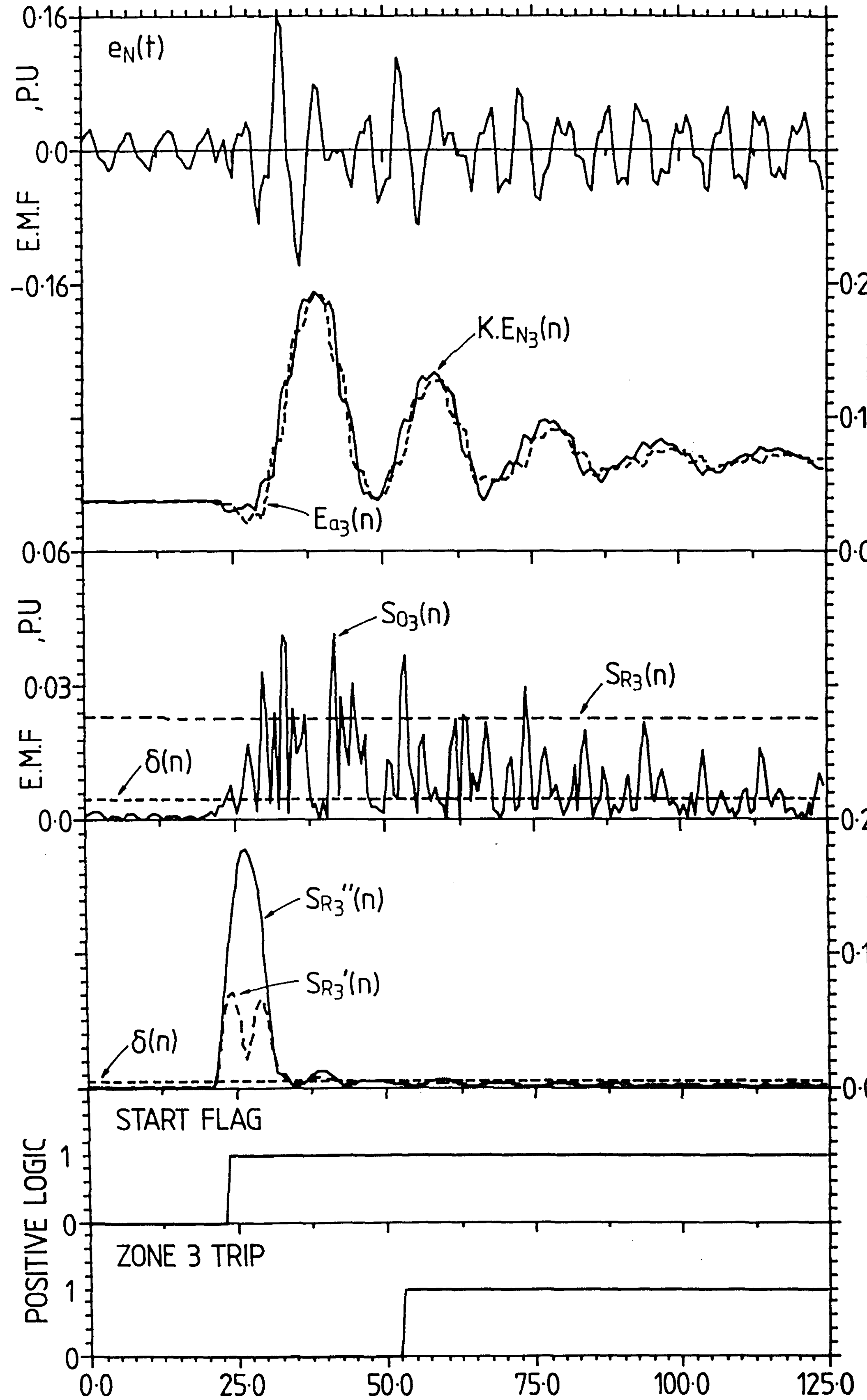

Figure 5.31: Response of the voltage comparison algorithm with half cycle window to an external three-phase short circuit.

(iii) A terminal V.T. connection to ground at the terminals of the generator was found to have no effect on the performance or stability of the scheme apart from shifting the null point further away from the neutral (figures 5.10,24). The overall operating times are unchanged.

(iv) Towards inter-phase winding faults the voltage comparison scheme possesses a superior overall stability than the neutral third harmonic algorithm. The voltage comparison scheme is inherently stable primarily because of the additional third harmonic negative and positive-sequence restraint signals (figures 5.5b,25,28). The neutral third harmonic algorithm on the other hand is not (figures 5.19), even though under laboratory conditions instability could not be observed.

(v) Both algorithms are totally insensitive to inter-turn stator faults.

(vi) Both algorithms will operate for a three phase fault at the terminals or within the stator winding because such faults maximize the neutral third harmonic emf (figures 5.20,21,26).

(vii) Zone 3 of the voltage comparison algorithm is extremely stable to faults external to the generator, remaining stable even for a three-phase short circuit close to the terminals of the machine (figure 5.29). However, this selectivity cannot be put to use because it is not matched by an equivalent zone 1 selectivity.

5.4.2 The Optimum DFT Window For the Algorithms

The evaluation results further reinforce the conclusion reached in chapter two that the one cycle DFT window is the optimum window. The reason for this conclusion is that the it offers the optimum compromise between protection stability and operating speed compared to the half cycle and the two cycle weighted windows.

The half cycle window, though resulting in a faster operate time characteristic (figure 5.13), lacks robustness. For earth faults this does not compromise the stability of the 'fault' decision (figures 5.11,12) because the levels of even harmonics and subtransients are very low due to the small fault current. However, it does affect the protection stability of the algorithms. This is especially pronounced for three-phase faults where very high levels of even harmonics are generated (figure 5.21) resulting in extremely unstable zone 3 operate signals (figures 5.22,31). For power swings (figure 5.17) and inter-phase faults (figures 5.19,25,28) a general decrease in robustness of the zone 3 operate signals is apparent.

The two cycle weighted algorithm possesses very similar stability characteristics to the one cycle window but gives longer operate times (figure 5.14) despite not delaying the zone 3 trip during the fault transition period. The third harmonic spectral estimates obtained from such a window will have a ripple component if it is not the dominant frequency component of the measurand (figure 5.15,16) but this does not seriously compromise stability because it is always of a low order and can be countered by increasing the degree of hysteresis.

CHAPTER SIX

A Stator Earth Fault Location Algorithm For Large Alternators

This chapter describes and evaluates the performance of a digital stator earth fault location algorithm to complement the earth fault protection algorithms described in the previous chapter. The main features of the algorithm are:

(i) A high accuracy.

(ii) It discriminates effectively between internal armature winding faults and external earth faults on the alternator system.

(iii) It is robust. The accuracy of the fault location process is unaffected by the value of the grounding resistance or a ground reference (potential transformer) at the alternator terminals.

6.1 The Nature of the Problem

The fault location process is based on a knowledge of the postfault imbalance of the alternator terminal emfs (ignoring harmonics for the time being) relative to ground and its stator winding factors (sections 4.2.4.1 and 2). Figures 6.1a and b illustrate the typical nature of unbalance for an earth fault on the A-phase of an alternator.

Under steady-state conditions, the terminal emfs relative to ground are balanced and the therefore the neutral will be at earth potential. Note in figures 6.1a and b the terminal voltage of each phase is illustrated to be the resultant of all the coil emfs contributing to it (the coil emf distribution shown is that of the laboratory micro-alternator and is identical to figure 4.5a). However, for an earth fault, the fault point is forced to earth potential (assuming zero fault resistance) and to compensate the neutral potential alters. The terminal emf relative to ground of the faulted phase then takes the value of the vector sum of all the coil emfs from the fault point upto the terminals of the generator. Similarly the neutral potential takes the value of the vector sum of all the coil emfs from the fault point down to the neutral.

The terminal potentials relative to earth of the unfaulted phases are given by the vector sum of their respective phase emfs and the neutral emf. Note, however that the terminal potentials of the alternator relative to its neutral are still perfectly balanced and therefore the power system sees no imbalance whatsoever. This behaviour is characteristic of stator earth faults on machines with high resistance neutral grounds and is one of the reasons why certain utilities do not trip their alternators for such faults.

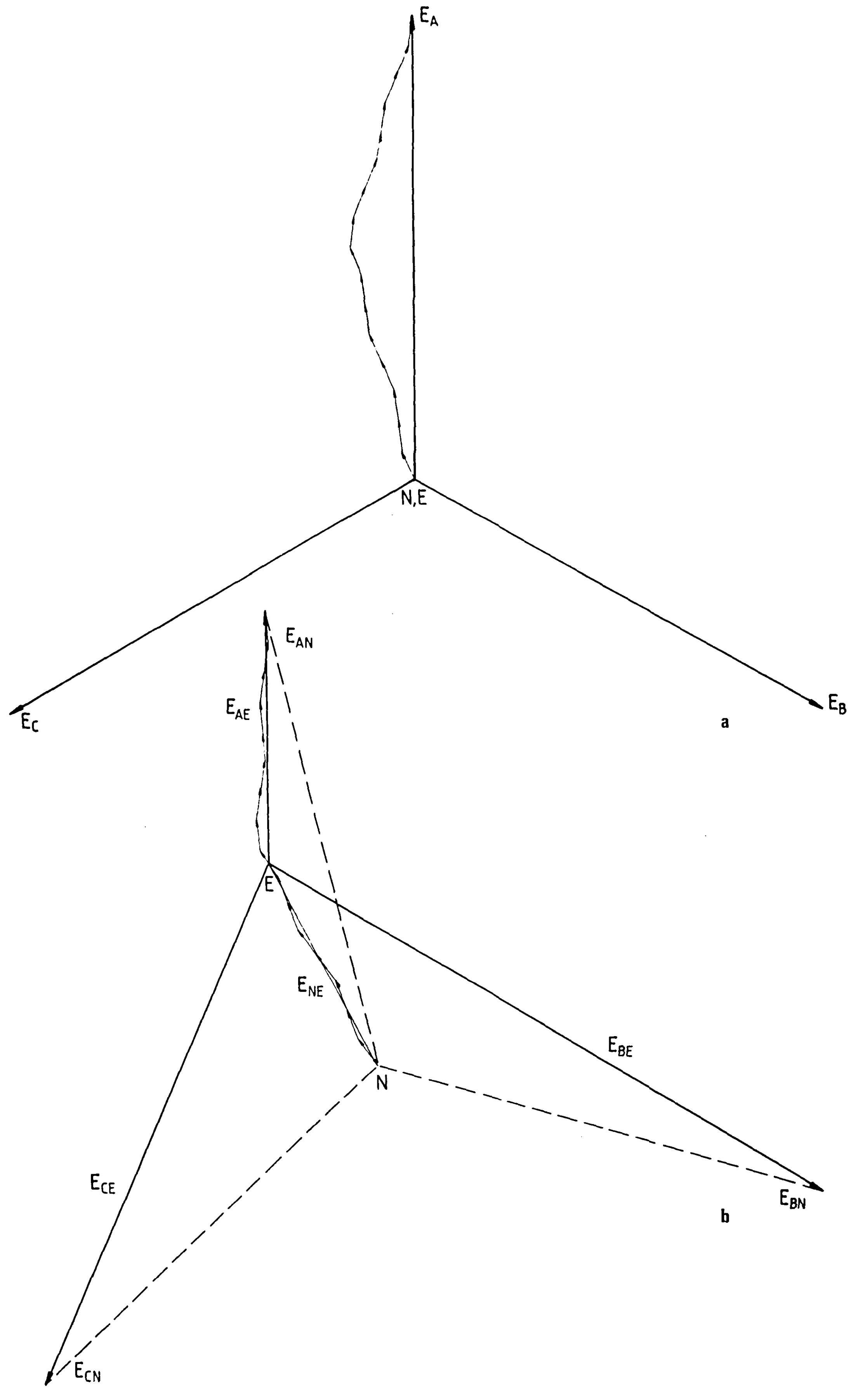

Figure 6.1: The terminals `emfs relative to ground of an alternator for (a) steady-state conditions and (b) for an earth fault on the A-phase.

The vector diagram of figure 6.1b suggests two methods by which fault location could be achieved. They are:

(i) As a ratio of the neutral and terminal emfs relative to earth of the faulted phase, with corrections based on the stator winding factors to compensate for the nonlinear voltage distribution of the phase windings.

(ii) Using iterative methods, to successively match the observed terminal emf imbalance to calculated values, calculated using knowledge of the armature distribution factor and slot configuration, until a match to within a specific tolerance is obtained.

The second method is used to derive a fault location algorithm because it requires only three measurands (the terminal emfs) as opposed to four for the first method (it requires the neutral as well) resulting in one less error input. The comparative complexity of the second method is not a drawback as fault location is not a real-time process.

6.2 The Fault Location Process

The fault location process consists of three distinct stages which are:

(i) The faulted phase is first determined.

(ii) The fault point is located by iteratively building a test vector until a match is obtained with the measured terminal emf of the faulted phase.

(iii) The integrity of the fault location process against earth faults external to the armature windings is verified by calculating the terminal vector emfs of the unfaulted phases, based upon the phase component of the test vector, and comparing them with their measured values.

The faulted phase is determined by the algorithm as the phase which has the lowest postfault terminal emf relative to ground. This is readily apparent from a study of figure 6.1b and was verified by experiment.

The main part of the fault location process is the iterative calculation of the fault point. This is accomplished in two stages. First the position of the faulted coil from the terminal end of the faulted winding is located. This is obtained by iteratively building a vector based on a knowledge of the value of the stator coil emfs and the slot angle distribution of the stator winding. The process is described by the equation

$$(V_{test})_{r+1} = E.e^{j\theta r} + (V_{test})_r \tag{6.1}$$

where V_{test} : test vector.

r : coil number from the terminal end of the machine
= 16-c.

c : coil number from the neutral end of the machine.

E : coil emf (given by equation 4.20 for n=1).

θ_r : slot angle for the rth coil referenced to the slot angle for the first coil which is assumed to be zero (the slot angle is given by equations 4.22a-f for n=1 and c=16-r).

The faulted coil is m when

$$(V_{test})_m > E_A' \quad \text{AND} \quad (V_{test})_{m-1} < E_A' \tag{6.2}$$

where E_A' : measured terminal emf relative to ground of faulted phase assumed to be the A-phase for consistency with figure 6.1b. Note that a dashed value will be used to indicate the measured value of a variable in the following equations.

Flowchart 6.1 illustrates the logical sequence of this process.

The second stage in the iteration process consists of the calculation of the exact fraction of the faulted coil, m, contributing to the terminal voltage of the faulted phase. It is described by the following equations

If $(V_{test})_i < E_A'$ (6.3a)

then $(V_{test})_{i+1} = (V_{test})_i + E_i$ (6.3b)

but if $(V_{test})_i > E_A'$ (6.3c)

then $E_{i+1} = E_i/2$ (6.3d)

where i : iteration step

$E_i = E_i e^{j\theta_m}$

$E_i = E/2$ for i=0

and $(V_{test})_i = (V_{test})_m$ for i=0

The fault position is located at the kth iteration when

$$(V_{test})_k - E_A' \leq \Delta_1 \tag{6.4}$$

where Δ_1: convergence criterion.

Flowchart 6.1 illustrates the iteration process more clearly but essentially it consists of a search pattern based on the successive halving of the magnitude of the faulted coil emf. At each iteration, the halved faulted coil emf, E_i, is added to the test vector, $(V_{test})_i$. If their resultant magnitude is greater than the terminal emf of the faulted phase, the search range is increased by half but, if not, it is decreased by half.

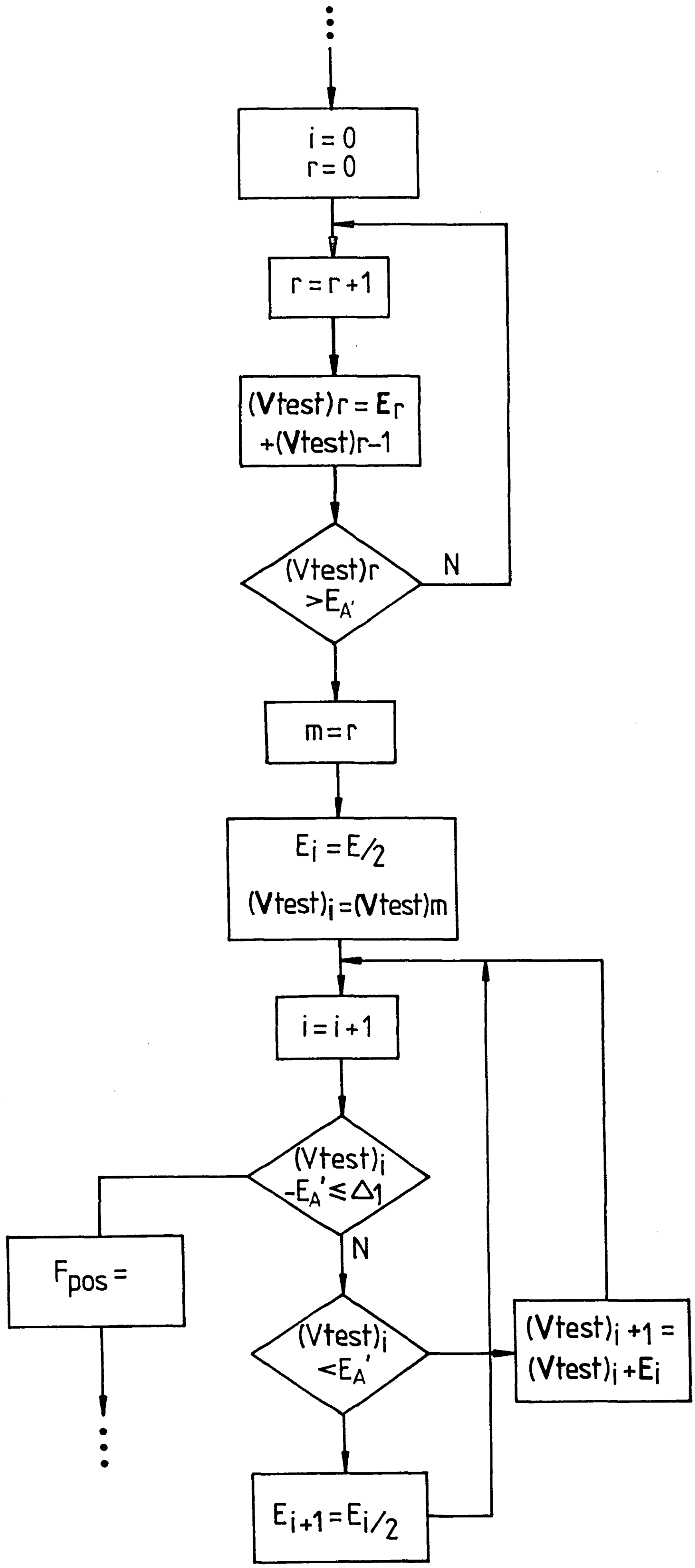

Flowchart 6.1: The fault location process.

The fault position as a percentage of the total winding can then be calculated as

$$F_{pos} = (m/N_{c_a} + E_k/E).100 \tag{6.5}$$

N_{c_a} : number of stator coils per phase.

The final stage in the fault location process is the verification of the solution to ascertain whether the earth fault is within the alternator or external to it. This stage is essential for the fault location process because an earth fault outside the alternator armature windings but within the alternator system (say, at the low voltage side of the generator transformer) will also unbalance the terminal emfs of the alternator relative to earth. Without the verification stage, the algorithm would simply interpret this as due to an internal fault.

This verification is achieved by calculating the terminal emfs relative to earth of the unfaulted phases and comparing them with measured values. In other words, the vectors $\mathbf{E}_{BE}$ and $\mathbf{E}_{CE}$ in figure 6.1b need to be calculated. If calculated and measured values do not match, then the calculated fault position is known to be incorrect and rejected. A directional check at the terminals of the machine based on the fault current is not possible because of its very low level.

To calculate the vectors $\mathbf{E}_{BE}$ and $\mathbf{E}_{CE}$, the values of $\mathbf{E}_{NE}$, $\mathbf{E}_{BN}$, $\mathbf{E}_{CN}$ must first be known. $\mathbf{E}_{NE}$ can be calculated as

$$\mathbf{E}_{NE} = (V_{test} - \mathbf{E}_T).e^{j\phi} \tag{6.6}$$

where $\mathbf{E}_T = \sum_{r=1}^{16} E.e^{j\theta_r}$

and $\phi = \theta_{test} - \theta_{A'}$

$\mathbf{E}_{BN}$ and $\mathbf{E}_{CN}$ can be derived as

$$E_{BN} = \lambda E_T . e^{j\phi} \tag{6.7a}$$

and $$E_{CN} = \lambda^2 E_T . e^{j\phi} \tag{6.7b}$$

where λ : 120 degree phase shift operator.

The fault is verified to be within the armature windings when

$$(E_{BN}' - \Delta_2) < E_{BN} < (E_{BN}' + \Delta_2) \text{ AND } (E_{CN}' - \Delta_2) < E_{CN} < (E_{BN}' + \Delta_2) \tag{6.8a}$$

where Δ_2 : sensitivity factor

and external to the alternator when

$$(E_{BN}' - \Delta_2) > E_{BN} > (E_{BN}' + \Delta_2) \text{ OR } (E_{CN}' - \Delta_2) > E_{CN} > (E_{BN}' + \Delta_2) \tag{6.8b}$$

The verification step is also highly effective at discriminating between stator earth faults and heavy current winding faults such as inter-phase faults. However, this characteristic is not of importance as normal practice would be to trigger the fault location process from the earth fault protection.

6.3 Practical Implementation

Based on this fault location process, a digital algorithm was written on the NOVA mini-computer in FORTRAN and evaluated using recorded data from the micro-machine.

The digital algorithm incorporates three features designed to give a very high accuracy.

(i) The terminal vector emfs are derived as the fundamental frequency estimates from DFT filters.

(ii) Eight cycle Blackman weighted DFT windows are used for the

DFT, each window consisting of the average of four eight cycle blocks of data.

(iii) The terminal emfs are derived as ratio of the postfault to the prefault terminal emfs.

The use of DFT filters greatly reduces the susceptibility of the algorithm to harmonic interference which would otherwise contribute to errors. From the point of view of the fault location process the harmonics, in contrast to the protection algorithms, do not contribute any useful information. The DFT filters by using Blackman weighted eight cycle windows achieve a performance which is an order of magnitude better than that of the one cycle DFT filter. Averaging of data prior to the DFT is a common technique to decrease the noise variance of the spectral estimates [4,64]. The very large group delay involved in using these techniques is not important, as fault location is not a real-time process.

The per unit derivation referenced to their respective prefault values of the terminal emfs relative to ground, desensitizes the algorithm to prefault steady-state load imbalances. The effect of this imbalance on the terminal emfs relative to ground is very similar to that generated by an internal armature earth fault and would otherwise contribute to errors in the fault location process if an earth fault were to occur during a load unbalance.

However, it could be argued that this last sophistication is not really necessary as the sustained load imbalance is never likely to be high. There are two reasons for this thinking,

(i) large alternators cannot withstand a sustained load imbalance of more than a few percent.

(ii) the load imbalance presented by a highly interconnected system is most unlikely to exceed even one percent except for power system fault conditions.

The logical structure of the algorithm is identical to flowchart 6.1 except for one difference. Instead of solving equation 6.1 m times to locate the faulted coil, a process which involves m complex additions, the per unit values of V_{test} are precalulated and stored in a look up table. The faulted coil can then be easily found by searching the look up table, using the criterion defined by equation 6.2. Table 6.1 lists the values of the look up table.

r	V_{test} (p.u.)	θ_{test} (rad.)
1	0.0653	-0.5236
2	0.1294	-0.6545
3	0.1943	-0.6984
4	0.2588	-0.6545
5	0.3236	-0.6282
6	0.3882	-0.6545
7	0.4530	-0.6733
8	0.5176	-0.6545
9	0.5708	-0.5848
10	0.6330	-0.5521
11	0.6958	-0.5253
12	0.7530	-0.4818
13	0.8114	-0.4445
14	0.8756	-0.4310
15	0.9400	-0.4193
16	1.0000	-0.3927

Table 6.1: Look up table for locating the faulted coil.

6.4 Experimental Evaluation

The accuracy of the fault location algorithm was evaluated for earth faults at 6.25% intervals on all phases of the micro-machine, with and without a ground reference at the machine terminals. Table 6.2 illustrates the results.

Fault position from terminals		
Actual (%)	computed (%)	computed with P.T. (%)
100.0	99.95	99.45
93.75	93.57	93.94
87.50	87.59	88.03
81.25	81.69	82.02
75.00	75.12	75.65
68.50	68.63	69.11
62.50	62.76	63.13
56.25	56.90	57.21
50.00	50.24	50.65
43.75	43.95	44.26
37.50	37.65	37.96
31.25	31.37	31.64
25.00	24.99	25.37
18.75	18.90	19.10
12.50	12.62	12.91
6.25	6.21	6.53

Table 6.2: Accuracy of the fault location algorithm (all values are as a percentage of the total winding as seen from the terminals of the machine).

The extremely high accuracy of the fault location process is self-evident with the maximum error being well within 0.5%. The effect of the V.T. connection is to decrease the accuracy slightly but it is still well within 1%. Results were also taken with various values of grounding resistance with negligible effect on accuracy. The algorithm also displays a high degree of robustness to prefault load imbalances with a 10% load imbalance decreasing accuracy slightly to within 2%.

The sensitivity of the algorithm to the fault resistance could, however, not be evaluated because of a serious failure of the data aquisition interface towards the end of the research program. The indications are that the algorithm is sensitive to the fault resistance as it assumes the fault point to be at earth potential. The higher the fault resistance the less this assumption will be valid. However, it may be possible to take into account the fault resistance, as an unconstrained variable, in the iterative fault location process. A proposal for an enhanced algorithm is presented in section 7.1.

The performance of the iterative search process is illustrated in figures 6.2 and 6.3 for the specific case of an earth fault on the A-phase 68.75% from the terminal end of the machine. The measured per unit postfault A-phase terminal emf is 0.6948 which from a search of the look up table indicates a fault very close to the end of coil 11 (which it is) and should, therefore, present the worst possible case for the iteration process as the iteration range is the greatest possible value.

Figure 6.2 illustrates the iterative convergence of the test vector from its initial value of 0.6330 (from the look up table) to its final value of 0.6948. Figures 6.3a and b show the variation in the number of iterations and the accuracy achieved respectively versus the convergence criterion Δ_1. The iteration process is clearly rather inefficient, requiring 20 iterations to achieve a high accuracy. This is a consequence of the use of a fixed criterion, in this case a successive halving of the coil emf, in reducing the search range. If on the other hand the magnitude and direction of the successive differences were used to evaluate the successive search ranges, faster convergence would be obtained.

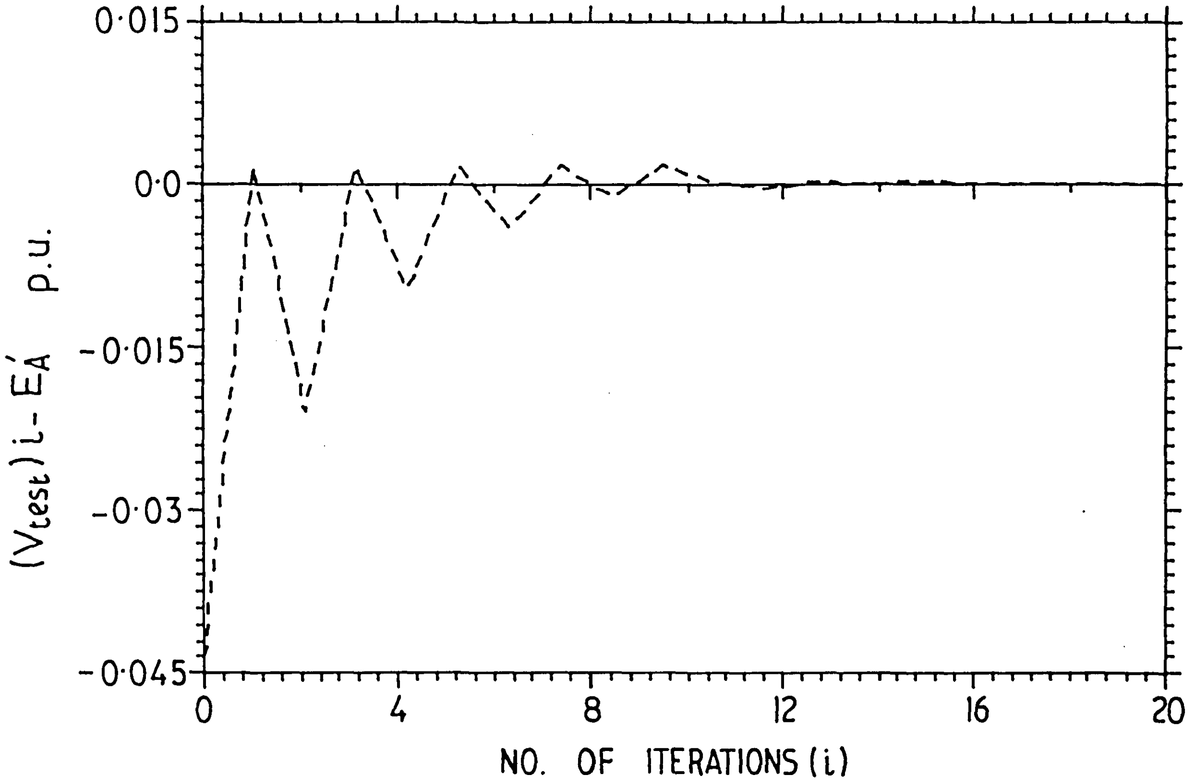

Figure 6.2: Iterative convergence of the test vector.

6.5 Conclusions

The results demonstrate that the proposed method of fault location for stator winding earth faults in large alternators is robust and can be accurate to within ± 0.5%. Its main characteristics are:

(i) The fault location process is unaffected by the specific values of grounding resistance and the exact configuration of the alternator system.

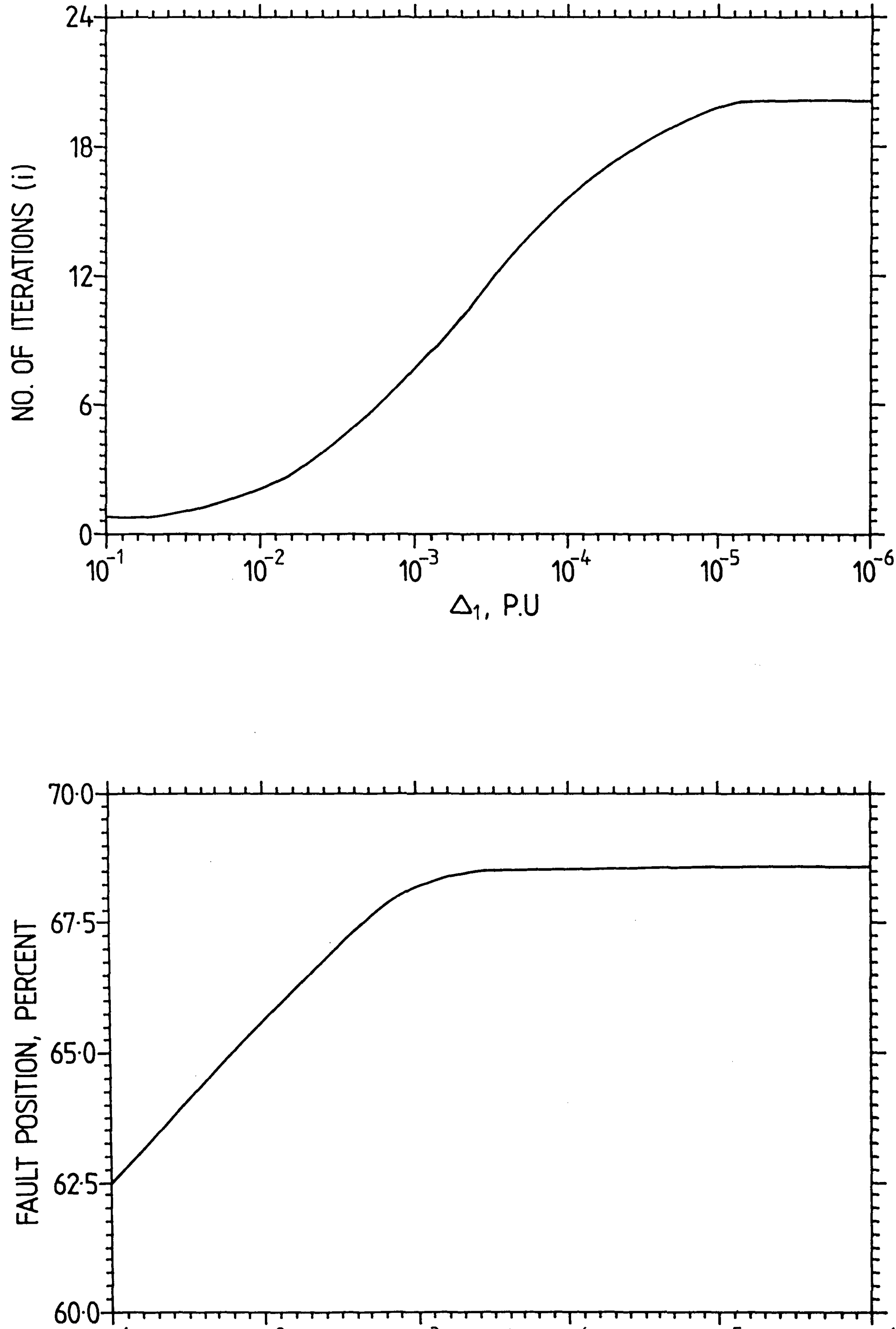

Figure 6.3: The variation in (a) number of iterations and (b) accuracy, versus the convergence criterion.

(ii) The algorithm requires a knowledge of the machine slot and winding distributions, and therefore needs to be customized to each particular type of alternator. However, such information is readily available in generator specification and design documentation.

(iii) The algorithm can distinguish whether an earth fault is within the stator or external to it in the alternator system. However, this does not imply that the fault location process extends past the alternator terminals.

(iv) The iterative procedure used, though accurate, is not very efficient (figures 6.2 and 6.3). However, this is more of a design problem and does not detract in any way from the basic accuracy of the fault location principle.

(v) The accuracy of the fault location process is affected by the fault resistance, though the exact degree of the loss in accuracy was not quantitatively evaluated. An algorithm inherently insensitve to the fault resistance is proposed for further work in section 7.1.

CHAPTER SEVEN

Conclusions

A theoretical and practical study of digital algorithms for 100% stator earth fault protection for large generators has been carried out, using discrete fourier transform spectral estimation methods and based on the third harmonic component of the alternator neutral and terminal emfs. The research is reviewed and the main conclusions, contributions and proposals for further work are discussed.

7.1 Review of the Research

7.1.1 General

Many years of operating experience [18,54,78,88,93,94] has shown that the most common winding fault associated with large generators is an earth fault. Such a fault, unlike an inter-phase fault which generates an extremely large fault current, is not immediately dangerous because of the universal practice of earthing the neutral of the machine via an effective high impedence [84,88]. It is, however, potentially very hazardous because the likelihood of the fault deteriorating into an inter-phase fault is high, and because the current limiting characteristic to earth faults of the neutral grounding scheme is rendered inoperative.

Present protection methods [18,54,78,85,88,91] for earth faults are inadequate because they do not protect the winding completely as they leave a small area close to the neutral without any form of earth fault protection, and their response time is slow. Moreover, even if the protection operates correctly the problem of locating the earth fault remains. This in itself is a major problem because usually very little visual evidence of the fault is apparent due to the extremely low levels of fault current. The main reason for the inadequate protection is that they are based on the fundamental component of the generator emfs. As an earth fault moves closer to the neutral, less and less postfault change occurs in both the terminal and neutral voltages.

Two digital algorithms for 100% stator earth fault protection have been developed and evaluated, which achieve the additional coverage near the neutral based on the third harmonic component of the generator emfs. The first algorithm detects an earth fault by measuring changes, relative to the prefault level, in the neutral third harmonic emf, while the second is based on a comparison of the neutral and terminal third harmonic emfs. Compared to recently reported [28,63,71] electro-mechanical third harmonic protection schemes, the digital algorithms achieve a much higher level of performance and should be much easier to apply. An accurate algorithm for earth fault location has also been developed and evaluated to complement the protection algorithms.

7.1.2 The Experimental System and Computer Simulation

An extensive practical and theoretical study of the harmonic content of a typical generator was first carried out. Practical results were obtained using a micro-machine model [55,83] of a typical large alternator system (section 3.1.1). The theoretical study was conducted using a multiharmonic coil-by-coil computer simulation of the armature windings of the micro-machine model (section 4.1).

The micro-machine model was designed to accurately reflect the capacitance to ground, the neutral grounding impedence, and terminal connections of a typical large CEGB alternator [54,85,88]. The very small capacitance to ground of the micro-alternator was increased to a realistic level by physically distributing small capacitors uniformly throughout the stator winding, an approach which has precedence in work by Abetti [1] on surge phenomena in transformers but has not been applied to machine models before. The need to accurately simulate the capacitance to ground of the stator windings of a real machine is extremely important because they provide a path for capacitive ground currents to flow which, as capacitive impedance is inversely proportional to frequency, will be rich in harmonics. This capacitive ground current will generate a steady-state neutral voltage rich in harmonics, and substantially affect the levels of harmonics at the terminals of the machine

The spectral analysis of the generator terminal and neutral emfs was carried out using a mini-computer based digital spectral analysis system (section 3.1.2) developed using discrete fourier transform (DFT) spectral estimation methods (section 2.3). Conventional spectrum analysers were found to be inadequate because they are not designed to measure rapidly changing spectra, and are not accurate enough in the frequency band of interest. For the measurement of steady-state postfault and prefault spectra, high levels of accuracy were achieved through the use of additional frequency domain interpolation [27,37] and windowing [4,31,64] correction procedures (section 2.3.3). For the measurement of rapidly changing spectral phenomena, however, the DFT estimator is not capable of as high an accuracy because of the need to minimize its group delay which the correction procedures necessarily increase (appendix B).

A review of spectral estimation procedures (section 2.2) indicates that for rapidly changing signals DFT spectral estimation, of which the fourier filter is a derivation, may not be the optimium spectral estimation process for protection as it is based on a signal model of harmonically related sinusoids [64]. This is accurate under steady-state conditions but definitely not at the fault instant. Newer spectral analysis methods [9,48] are based on more robust signal models, and are worthy of further research. Of particular interest is Prony's spectral line decomposition [48] which is based on the more general model of harmonically unrelated sinusoids.

Measured results from the spectral analysis were correlated with data obtained from a computer simulation (chapter 4) of the variation in harmonic content of the neutral and terminal emfs. of the machine for stator earth faults. As stator earth faults result in a very low fault current (typically 10A) and therefore produce negligible magnetic unbalance within the machine, a transient solution was found to be unnecessary. Instead a simpler steady-state mathematical model based on a coil-by-coil representation of the stator windings of the alternator and other components of the alternator system by meshes was used in a similar manner to Schlake et al. [71]; each coil mesh consisting of the coils' nth harmonic emf, leakage and magnetizing reactance, and resistance (in the series arm) and its capacitance to ground (in the parallel arms). However, in contrast to Schlake et al. who only considered the third harmonic, all harmonics, whether originating from the generator or the infinite-bus were accounted for. The solution was accomplished by the use of matrix methods to solve the resultant system of simultaneous complex linear mesh equations for the neutral and terminal emfs.

7.1.3 The Spectral Content of the Alternator Emfs

The study of the spectral content of the generator terminal and neutral emfs conclusively showed that only the third harmonic components are robust enough to be used as the main protection measurands. Both measured and calculated results (section 4.3) demonstrated that the order of magnitude of the third harmonic component was little affected by variations in the capacitance of the windings, the value of the neutral grounding impedence (provided it is of the order of 10^3ohm), the infinite-bus, or an additional ground reference at the terminals of the machine.

A detailed investigation of the influence of these parameters on relaying signals derived from the third harmonic components further confirmed this robustness. A particularly important aspect considered was their influence on the null points (section 4.3.2.2) of the relaying signals (these refer to the fault position for which no change in the relaying operate signals is discernable). Variations in the alternator system parameters were found not to affect substantially the position of the null points which were observed to be well away from the neutral under all conditions. Another very important conclusion was that the fault resistance, provided it is not greater than the order of magnitude of the grounding resistance, does not affect the position of the null points detrimentally (the null point moves away from the neutral). Therefore, earth fault protection schemes based on the third harmonic will operate even for high resistance faults (of the order of 10^3 ohm). However, the sensitivity of the null points to the alternator system parameters is not identical for the two possible protection schemes. Of the two, the voltage comparison scheme null point demonstrates the greater robustness with its position being further from the neutral and less affected by variations in alternator system parameters.

Non-triplen harmonics, as expected, were found to be unsuitable as the main protection measurands because they are not zero-sequence components and therefore do not generate an emf enclosing the neutral. However, their use as subsidiary measurands in formulating restraint criteria to improve the protection stability of the main protection may very well be possible. For example, in the laboratory micro-machine model significant levels of even harmonics were measured for three-phase short circuits at the alternator terminals (section 5.2.3.4) which could be used to discriminate against this condition if it were so required. Similarly significant levels of non-triplen odd harmonics are generated by inter-phase faults (section 5.2.3.3).

Another way of considering these harmonics is to use them not just as subsidiary measurands but as main protection measurands in their own right and protect the alternator against a variety of faults with one protection system. Recent research [6,45] has indicated that not only stator winding faults but rotor winding faults can also be detected this way. This approach, however, implies the application of a measure of pattern recognition to spectral estimates of the generator voltages and the problems are formidable. Not only will the harmonic patterns for each fault condition need to be quantified but so will their consistency between different types of alternators and generator sytems. For non-triplen harmonics the damping influence of the infinite-bus will also need to be considered (the generator transformer represents an open circuit only for zero-sequence triplen harmonics). In addition it is arguable whether such a level of sophistication would be appropriate just to obtain protection functions, when it may very well be possible to achieve condition monitoring functions as well.

The possibility of using the ninth harmonic to achieve the protection function required was also investigated (section 4.3), but was proved, conclusively, to be impractical. The ninth harmonic was found to lack the robustness of the third harmonic because of its much lower amplitude, and because it was shown that a scheme based on the ninth harmonic would possesses multiple null points (section 4.3.2.2) within its reach. In fact the measured level of ninth harmonic components of the terminal and neutral emfs are probably optimistic because no account has been taken of the frequency response characteristics of the measurement transducers of an actual alternator system.

A theoretical study of the spectral content of the generator terminal and neutral voltage harmonics for heavy current stator winding faults was also made. For such faults a transient solution based on the general differential equations of a three-phase synchronous machine [11,67] must be used, the assumption of magnetic imbalance within the machine being no longer valid. Proposals for a possible representation of the faulted windings and a method of solution were formulated (appendix G) but not carried through to completion. This research, however, is very exciting and strongly recommended for further work.

7.1.4 The Protection Algorithms

Based on the results of the practical and theoretical study of the harmonic content of the generator neutral and terminal emfs, the design of two digital algorithms for 100% stator earth fault protection were investigated (chapter 5) using DFT spectral estimation as a filtering process to discriminate between the harmonics from the protection measurands. The first algorithm detects an earth fault by measuring changes in the third harmonic component of the neutral voltage, while the second algorithm achieves the same end by measuring unbalances in a voltage comparison scheme between the third harmonic components of the neutral and terminal voltages. Both algorithms contain two zones of protection, one (zone 3) covering the neutral and terminal ends of the winding with the relaying operate signal based on the third harmonic components of the protection measurands, and the other (zone 1) based on the fundamental component of the neutral emf covering the null band of the previous zone. The voltage comparison algorithm, in addition, derives relaying restraint signals based on the negative and positive-sequence components of the third harmonic terminal emfs.

These algorithms are fundamentally different to present third harmonic 100% stator earth fault protection schemes [28,63,71] in that their respective zone 3 relaying signals are formulated relative to the prefault third harmonic components of the relaying measurands. This characteristic forms the basis of their superior performance (section 5.1), compared to present schemes, because it desensitizes the earth fault protection to absolute changes in the third harmonic measurands. The only criterion for a logical 'fault' decision from these two algorithms is a change in the relaying measurands relative to their prefault values. The high selectivity and accuracy of the DFT spectral estimation process also contributes significantly to the superior performance.

The two algorithms were evaluated (sections 5.2, 5.3) using off-line computer models but using real data gathered from the micro-machine model of the alternator. The performance was assessed using a large number of different fault conditions including heavy current winding faults, power swings, and faults external to the alternator. Both algorithms demonstrated a fast operating time, a maximum of one and a quarter cycles of fundamental, a high protection stability against power swings, insensitivity to load variations, and a high discrimination against other types of winding faults. Of the two, the voltage comparison algorithm was assessed to offer the superior performance because of its better protection stability characteristics.

A one cycle data window was chosen as the optimum window size for the DFT spectral estimator offering the optimum compromise between a fast operate time and protection stability. The performance of both algorithms was also investigated with a half cycle window (section 5.2.2.2) and a weighted two cycle window (section 5.2.2.3). The half cycle DFT was observed to give a faster operate time, with the maximum operate time being reduced to half a cycle of fundamental, but only at the expense of a decrease in protection stability. The weighted two cycle DFT resulted in a slower response with no discernible benefit in terms of protection stability. This study confirms that there really is no benefit in compromising the robustness of the DFT spectral estimator by using windows shorter than one cycle for a nominal increase in operating speeds as shorter windows undermine the mathematical signal model on which the DFT spectral estimation process is based.

The reach characteristic of both zones 1 and 3 for the neutral third harmonic algorithm was found to extend beyond the terminals of the machine upto and including the low voltage windings of the generator and unit-auxiliary transformers. For the voltage comparison algorithm, the zone 3 reach was found to be more discriminative extending upto the terminals of the machine, but this was offset by the open-ended zone 1 reach giving a similar overall reach characteristic to the first algorithm. It may, however, be possible to achieve a zone 1 reach terminating at the terminals by formulating it as a voltage comparison between the fundamental components of the neutral emf and the fundamental zero-sequence component of the terminal emfs. It is strongly recommended that this proposal be verified because then the two algorithms can be combined to give a two zone earth fault protection; one zone covering the stator windings and the other extending to the rest of the alternator system. With such a scheme it will be possible to distinguish conditions such as open-circuit potential transformer fuses for which no protection action is required [94].

The stability of both algorithms to power swings and load changes was assessed to be high with no instability being observed for these two conditions. The performance of the algorithms was found to be unaffected by the prefault governor load setting indicating that off-line supervision for these algorithms is unnecessary. Though the stability towards heavy current winding faults of the neutral third harmonic algorithm was observed to be good, for the voltage comparison scheme it was found to be much greater because of the effectiveness of the third harmonic zero and positive-sequence restraint signals in detecting magnetic unbalance within the machine.

Apart from the high protection stability achieved, another very significant advantage of formulating the relaying signals relative to the prefault values of the third harmonic measurands is that the application of digital protection based on these algorithms should be much simpler than that of present third harmonic schemes. The only criterion for successful application is that the dynamic range (i.e., signal-to-noise ratio) of the third harmonic components present in the relaying measurands be sufficient under all steady-state conditions. In contrast, present third harmonic schemes are difficult to apply [26,63,71] because a detailed knowledge of the absolute levels of the third harmonic components in the relaying measurands is essential. This potential ease of application can, however, only be verified by practical application to a real alternator system and is recommended for further work.

In this context, the whole body of this research must considered as only a first step towards the practical implementation of the proposed protection. The results and proposals presented here must be verified and tested on a practical alternator system before the research can be considered complete. Some of the possible practical restrictions that must be investigated are the frequency response of the neutral grounding transformer, and the nonlinear variation of the neutral and terminal third harmonic emfs reported [28] on some machines which would make a voltage comparison scheme as proposed inapplicable. It is strongly recommended that this research be carried through to its conclusion.

7.1.5 The Fault Location Algorithm

The last part of the research was the design and evaluation of a fault location algorithm (chapter 6) to complement the relaying algorithms developed. The fault location process (section 6.2) consists of the iterative location of the fault point starting from the measured terminal emf (from the point of view of the fault location process the alternator harmonics do not contribute any useful information) of the faulted phase and a knowledge of the armature winding distribution of the machine. The faulted phase is initially chosen as the phase with the lowest postfault terminal emf. A verification stage is also incorporated to distinguish between earth faults external to the windings but within the alternator system, in which the terminal emfs relative to ground of the unfaulted phases are calculated from a knowledge of the calculated fault point and compared with measured values. If the fault is internal to the alternator a match will be obtained, otherwise not. An additional characteristic of this verification stage is that it is also highly effective at discriminating between earth faults and heavy current winding faults, though this is probably not of importance as normal practice [88] would be to trigger the fault location process from the earth fault protection.

The experimental evaluation (section 6.4) of the algorithm achieved promising results with high overall accuracy to within 2% of the actual fault location being obtained. The value of the grounding resistance (provided it is of the order of 10^3 ohm), a ground reference at the machine terminals, the prefault load imbalance, the level of harmonic distortion present at the terminals, and the governor load setting were all found to have negligible effect on the accuracy of the fault location process. However, the major deficiency of the algorithm is its response to high resistance earth faults which, though experimentally not verified due to equipment failure towards the end of the research, will probably degrade accuracy. The reason for this is that the iterative fault location process is based on the assumption of zero fault resistance.

However, it may be possible to include the fault resistance as an unconstrained variable in the iterative fault location process. This could be achieved by starting the iterative process assumming zero fault resistance but if the verification stage is not satisfied, reiterating at progressively higher fault resistances until convergence is obtained between the calculated and measured terminal emfs relative to ground of the unfaulted phases. Further work is recommended in this area. Another area for further work is in optimizing the iterative fault location process used which, though accurate, is not optimum in the number of iterations required for convergence.

In conclusion, the original contributions of this research and recommendations for further work are summarized.

7.2 Original Contributions

Original contributions have been made in the following areas:

(i) A theoretical and practical study of the spectral content of the neutral and terminal voltages of a large alternator for stator winding faults has been carried out using a micro-machine model of a typical large machine.

(ii) The capacitance to ground of large alternators has been simulated in the laboratory by uniformly distributing lumped capacitances in the stator windings of the micro-alternator model.

(iii) A general transient simulation of a synchronous machine for various types of stator winding faults has been proposed.

(iv) The use of the discrete fourier transform as a spectral estimator (previous research has been concentrated on its use as a single frequency 'fourier filter') for power system protection has been evaluated. The applicability and performance of window and frequency domain interpolation correction procedures has been examined.

(v) Two digital algorithms for 100% stator earth fault protection have been developed and evaluated successfully.

(vi) A stator earth fault location algorithm has been developed to complement the protection algorithms. Experimental tests have shown it to be accurate to within 2%.

7.3 Recommendations for Further Work

Further research is recommended in the following areas:

(i) The implementation and evaluation of the proposed transient computer simulation of a synchronous machine with internal armature winding faults.

(ii) The application of Prony spectral line decomposition spectral analysis to protection.

(iii) A practical evaluation of the proposed protection and fault location algorithms on an actual alternator to confirm the laboratory results.

(iv) Methods for achieving a directional zone 1 reach characteristic in the voltage comparison algorithm.

(v) Optimization of the iterative fault location process.

(vi) Methods for improving the accuracy of the fault location algorithm to high resistance earth faults.

APPENDIX A

THE DISCRETE FOURIER TRANSFORM

A.1 The Continuous Fourier Transform as the Limiting Case of the Fourier Series.

A periodic function $x_p(t)$ with time period T_o, expressed as a fourier series [7] is given by the expression

$$x_p(t)=a_o/2 + \sum_{k=1}^{\infty} [a_k\cos(\omega_o kt)+b_k\sin(\omega_o kt)] \tag{A.1}$$

where $\omega_o = 2\pi f_o$
: angular frequency of the fundamental.

k : order of the harmonic.

p : denotes periodicity.

The coefficients, a_k and b_k, of the series are given by the integrals

$$a_k = 2/T_o \int_{-T_o/2}^{T_o/2} x_p(t)\cos(\omega_o kt)dt \tag{A.2}$$

$$b_k = 2/T_o \int_{-T_o/2}^{T_o/2} x_p(t)\sin(\omega_o kt)dt \tag{A.3}$$

where a_o : coefficient of the DC term.

$T_o = 1/f_o$
: period of waveform.

In its most general form the fourier series can be written as an exponential series,

$$x_p(t) = \sum_{k=-\infty}^{\infty} A_k e^{j\omega_o kt} \tag{A.4}$$

$$\text{where } A_k = 1/T_o \int_{-T_o/2}^{T_o/2} x_{p(t)} e^{-j\omega_o kt} dt \tag{A.5}$$

$$= a_k - jb_k$$

The continuous fourier transform (CFT) is the limiting case of the fourier series as T_o tends to infinity,

$$X(\ ) = \underset{T_o \to \infty}{\text{Limit}} [A_k . T_o] = \int_{-\infty}^{\infty} x(t) e^{-j\omega t} dt \tag{A.6}$$

Figure A.1 illustrates the process graphically. As T_o increases, the frequency seperation between the fourier coefficients decreases until for an infinite T_o (i.e., x(t) is no longer periodic and can be any waveform) all frequencies are allowed and a continuous frequency function is obtained.

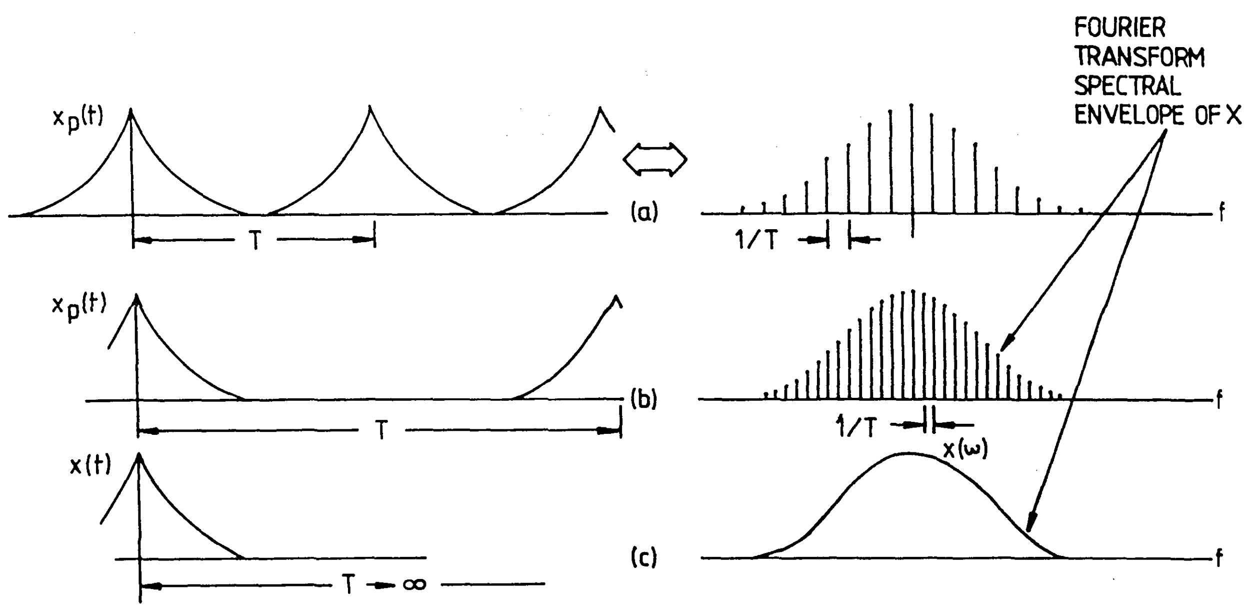

Figure A.1: The CFT as the limiting case of the fourier series.

$X(\omega)$ and $x(t)$, are commonly referred to as the fourier transform pair, with the mathematical process of transformation represented in short form as

$$x(t) \longleftrightarrow X(\omega)$$

Note also that the CFT is commonly referred to as just the 'fourier transform'. Here the name 'CFT' is used to distinguish it from its discrete equivalent (section A.4).

In summary, while the fourier series is only applicable to periodic functions, the CFT is applicable to any waveform. For aperiodic waveforms it gives a continuous spectrum, while for periodic waveforms it gives a sequence of equidistant impulses

$$X_p(\omega) = \sum_{k=-\infty}^{\infty} A_k \delta(\omega - k\omega_o) \tag{A.7}$$

where δ : impulse function.

A.2 The Effect of the Sampling Process on the CFT

A sampled signal $x^*(t)$ can be generated by multiplying a continuous time signal $x(t)$ by an ideal impulse sampler as illustrated in figure A.2. The ideal impulse sampler is given by the equation

$$c(t) = \sum_{n=-\infty}^{\infty} \delta(t - nT_s) \tag{A.8}$$

where $T_s = 2\pi/\omega_s$

: discrete time sample interval.

n : discrete time operator.

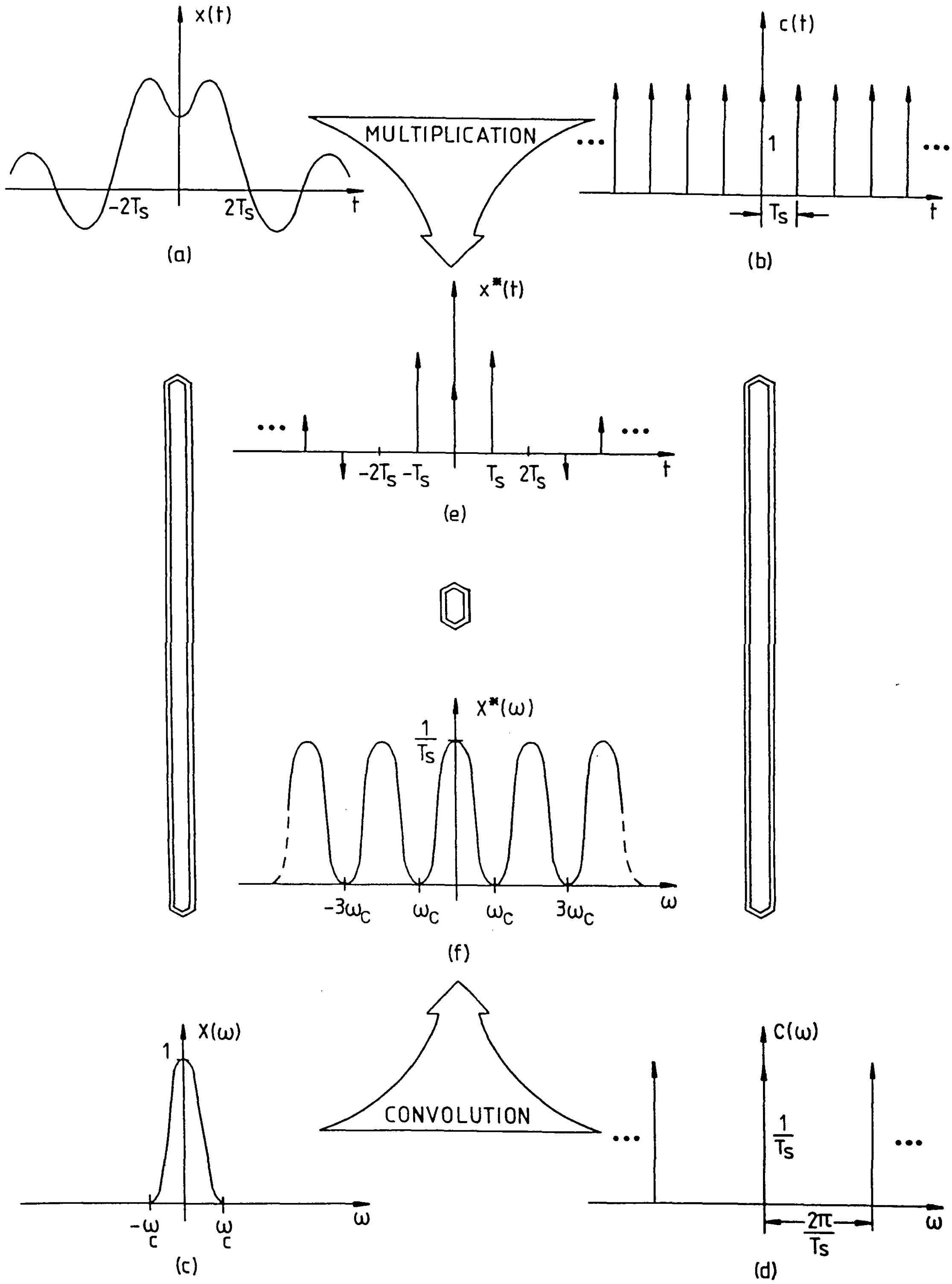

Figure A.2: The Continuous Fourier Transform of a sampled waveform.

Then $x^*(t) = x(t).c(t)$

$$= \sum_{n=-\infty}^{\infty} x(nt)\delta(t-nT_s) \qquad \text{(A.9)}$$

where * : denotes a sampled signal.

The choice of sampling frequency, $_s$, is dictated by the time domain sampling theorem which states that if the CFT of a function is zero for all frequencies greater than a certain frequency, ω_c, such that $\omega_c = \omega_s/2$ than the continuous function x(t) can be uniquely determined from a knowledge of its sampled values (as given by equation A.9).

In particular x(t) is given by

$$x(t) = T_s \sum_{n=-\infty}^{\infty} x(nT_s)\ [\sin \omega_c(t-nT_s)]\ /\ [\pi(t-nT_s)] \qquad \text{(A.10)}$$

where $\omega_c = \omega_s/2$
: foldover (or Nyquist) frequency.

Taking the fourier transform of $x^*(t)$ gives

$$X^*(\omega) = \sum_{n=-\infty}^{\infty} x(nT)e^{-j\omega nt} \qquad \text{(A.11)}$$

From Poisson´s summation formula [7] $X^*(\omega)$ can be written as

$$X_p^*(\omega) = 1/T_s \sum_{n=-\infty}^{\infty} X(\omega+n\omega_s) \qquad \text{(A.12)}$$

The result of equation A.12 is very important because it illustrates that the spectrum (i.e., the CFT) of a sampled waveform is not itself discrete. Time domain sampling simply extends the spectrum of the waveform periodically with a period equal to ω_s. A comparison of figures A.2c and f also demonstrates this point graphically.

For digital computation, therefore, the transform pair $x^*(t)$ and $X_p^*(\omega)$ must be brought into a form suitable for digital computation. This is achieved by truncating $x^*(t)$ and frequency sampling $X_p^*(\omega)$ within bounds defined by the frequency sampling theorem.

A.3 The Frequency Domain Sampling Theorem

The frequency domain sampling theorem states that if a function x(t) is time-limited,that is

$$x(t) = 0 \quad \text{for } |t| > T_c$$

then its fourier transform $X(\omega)$ can be uniquely determined from equidistant samples of $X(\omega)$. In particular, $X(\omega)$ is given by

$$X(\omega) = 1/2T_c \sum_{k=-\infty}^{\infty} X(k/2T_c) \sin[\ 2T_c(\omega - k\omega_c/2)]/(\omega - k\omega_c/2) \qquad (A.13)$$

where $T_c = 2\pi/\omega_c$

A.4 The Discrete Fourier Transform

The following theoretical and graphical development illustrates the frequency sampling of the CFT of a truncated and time sampled version of the periodic waveform $x_p(t)$ to derive a result for the discrete fourier transform (DFT).

Figure A.3 illustrates the complete process starting from the continuous time signal with infinite time bounds. Figures A.3a,b, and c illustrate the sampling process, as described by equations A.8-10.

The truncation of $x_p^*(t)$ (figures A.3d,e) is achieved by multiplying it with a window function chosen to enclose one complete cycle of the sampled waveform.

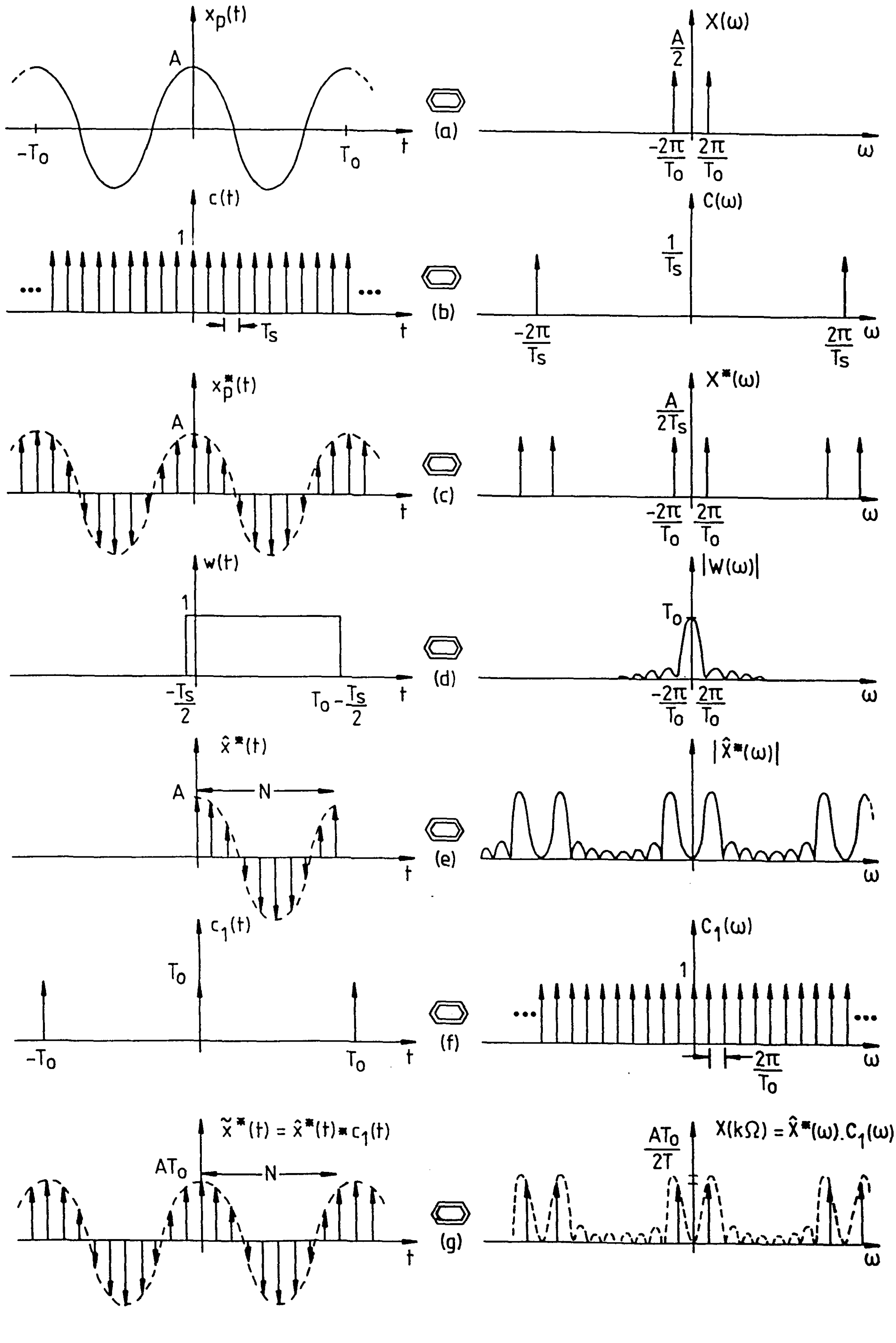

Figure A.3: Discrete Fourier Transform of a band-limited periodic waveform : truncation interval equal to period.

$$\hat{x}^*(t) = w(t)\, x_p^*(t)$$

$$= w(t) \sum_{n=-\infty}^{\infty} x_p(nT_s)\delta(t-nT_s)$$

$$= \sum_{n=0}^{N-1} x_p(nT_s)\delta(t-nT_s) \qquad (A.14)$$

where $w(t) = u(t)-u(t-NT_s)$

: rectangular window function.

$u(t)$: unit step function.

The frequency sampling can be achieved by convolving $\hat{x}^*(t)$ with a time domain impulse sample function

$$c_1(t) = T_o \sum_{r=-\infty}^{\infty} \delta(t-rT_o) \qquad (A.15)$$

The frequency sampled time domain equivalent of $\hat{x}^*(t)$ is then

$$\tilde{x}^*(t) = \hat{x}^*(t) * c_1(t)$$

$$= [\, \sum_{n=0}^{N-1} x_p(nT_s)\delta(t-nT_s)\,] * [T_o \sum_{r=-\infty}^{\infty} \delta(t-rT_o)]$$

$$= T_o \sum_{r=-\infty}^{\infty} \sum_{n=0}^{N-1} x(nT_s)\delta(t-nT_s-rT_o) \qquad (A.16)$$

The CFT of $\tilde{x}^*(t)$, which will give the desired relationship for the DFT, can be developed by substituting for it in the expression for A_k (equation A.5) and then substituting for A_k in equation A.7.

$$A_k = \int_{-T_s/2}^{T_o-T_s/2} \tilde{x}^*(t)e^{-j\omega_o kt}\,dt \tag{A.17}$$

$$= 1/T_o \int_{-T_s/2}^{T_o-T_s/2} T_o \sum_{r=-\infty}^{\infty} \sum_{n=0}^{N-1} x_p(nT_s)\delta(t-nT_s-rT_o)e^{-j\omega_o kt}\,dt$$

$$= \sum_{n=0}^{N-1} x_p(nT_s)\; e^{-j\omega_o kt} \tag{A.18}$$

Since $T_o = NT_s$, equation A.17 can be re-written as

$$A_k = \sum_{n=0}^{N-1} x_p(nT_s)e^{-j2\pi nk/N} \tag{A.19}$$

Substituting for $\mathbf{A}_k$ in equation A.7 gives

$$\mathbf{X}_p(k\Omega) = \sum_{k=-\infty}^{\infty} \sum_{n=0}^{N-1} x_p(nT_s)e^{-j2\pi nk/N} \tag{A.20}$$

where $\Omega = \omega_s/N$

: discrete frequency sample interval.

The infinite summation interval for the summation in k is ambiguous as the vector term $e^{-j2\pi nk/N}$ is periodic in N. Therefore only N distinct values of k will exist and the bounds for k will be identical to that of n. The more usual expression for the DFT leaves out this summation sign,

$$X_p(k\Omega) = \sum_{n=0}^{N-1} x_p(nT_s)e^{-j2\pi nk/N} \qquad k=0,1,\ldots,N-1 \tag{A.21}$$

A shorter expression for the DFT, not explicitly stating its periodic nature, is introduced,

$$X(k) = \sum_{n=0}^{N-1} x(n).W^{-nk} \qquad k=0,1,\ldots,N-1 \qquad (A.22)$$

where $W = e^{j2\pi/N}$

and $\mathbf{X}(k) \equiv \mathbf{X}_p(k\Omega)$, $x(n) \equiv x_p(nT_s)$

A.5 Relationship Between the Discrete and Continuous Fourier Transforms.

The graphical derivation (figure A.3) of the discrete fourier transform process for a periodic signal has illustrated that provided that the truncation interval enloses an integer number of cycles, (i.e., the frequency sampling theorem holds) the sampled spectrum as given by the DFT and the CFT will be identical. The truncation of $x^*(t)$ does significantly distort its spectrum (compare figures A.3c and d), this distortion being produced by the convolution of the CFT of the window function, $\mathbf{W}(\omega)$, and $X_p^*(\omega)$. However, when this function is sampled by the frequency sampling function (figure A.3f), $\mathbf{C}_1(\omega)$, this distortion is eliminated. This follows because the equidistant impulses of the frequency sampling function are seperated by $1/T_o$, which corresponds to the frequency domain impulses of the original CFT, $\mathbf{X}(\omega)$. Note also that the time domain equivalent to the DFT frequency function is a periodic function (figure A.3g).

This example represents the only class of waveforms for which the DFT and CFT are exactly the same (apart from scaling constants). Equivalence between the two transforms requires,

(i) the time function must be periodic and band-limited,

(ii) the time domain sampling theorem must be satisfied,

(iii) the truncation function must exactly enclose an integer number of periodic cycles of the time function.

If a periodic band-limited sampled waveform is truncated to consist of a noninteger multiple of the period, then the CFT and DFT will differ considerably. Figure A.4 illustrates the graphical derivation of the DFT for such a case. Note that the effect of this truncation is to create a periodic function (figure A.4g) with a sharp discontinuity. The introduction of these sharp changes results in additional frequency components in the frequency domain.

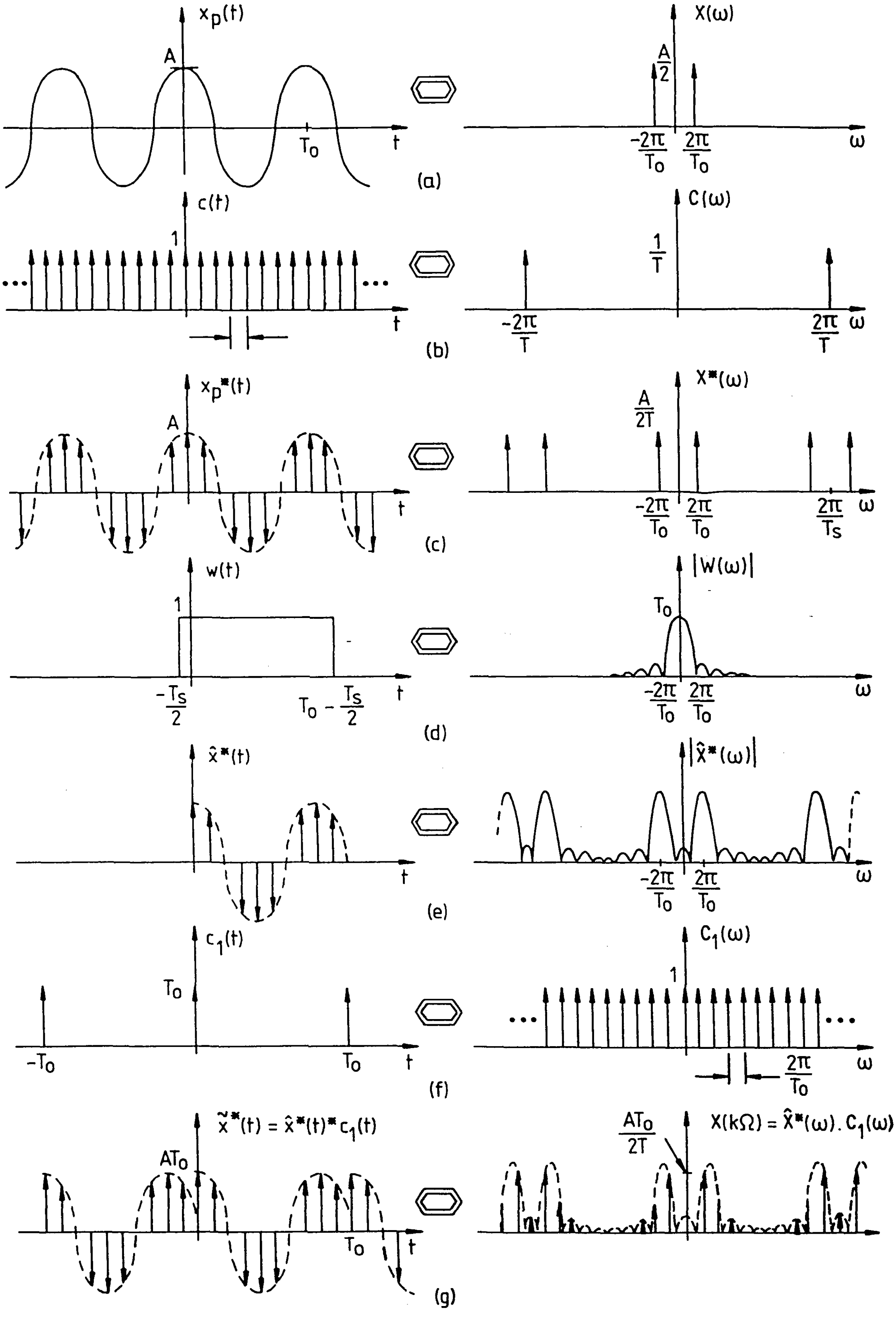

Figure A.4: Discrete Fourier Transform of a band-limited periodic waveform : truncation interval not equal to period.

APPENDIX B

THE USE OF WINDOW FUNCTIONS FOR HARMONIC ANALYSIS

B.1 The Effect of Window Functions in Reducing Leakage Errors

Window functions are a class of discrete time domain weightings which can be multiplicatively applied to a discrete time waveform to reduce leakage errors in its DFT, as illustrated by equation 2.12. However, the action of window functions is best demonstrated by considering the process as the periodic convolution of the fourier transforms of the window function and the discrete waveform,

$$X_W(\omega) = X(\omega) * W(\omega) \tag{B.1}$$

The periodic convolution process is defined [4,7,64] as

$$X_W(\omega) = 1/2\pi \int_0^{2\pi} X(\varepsilon)\, W(\omega-\varepsilon)\, d\varepsilon \tag{B.2}$$

where ε is a frequency operator.

Equation B.2 is best interpreted graphically. Therefore, for the sake of exposition let

$$\begin{aligned} X(\varepsilon) &= 1 \text{ for } 0 < |\varepsilon| < \omega_c \\ &= 0 \text{ for } \omega_c < |\varepsilon| < \omega_s/2 \end{aligned} \tag{B.3}$$

where ω_c: cutoff frequency.

ω_s: sampling frequency.

Let $W(\varepsilon)$ be as illustrated in figure B.1 assuming that its area is unity and

$$W(\varepsilon) = 0 \text{ for } \omega_m<|\varepsilon|<\omega_s/2 \tag{B.4}$$

where ω_m is the extent of its spectrum.

Figure B.1 illustrates the convolution process graphically. Two features are of note:

(i) As ω is varied in the range ω_1 to ω_5 through the discontinuity of $X(\varepsilon)$ the effect of the window function is to increase the transition width of the discontinuity. Clearly, the greater the width of $W(\varepsilon)$ the greater will be the transition width. With reference to the DFT, this will result in an increase in the bandwidth of the DFT filters, reducing its spectral resolution.

(ii) Because $W(\varepsilon)$ as illustrated is band-limited, there is no ripple distortion present in $X_W(\omega)$. However, if it had possessed side lobes it can easily be deduced that before the instant ω_1, as the side lobes are swept past the discontinuity in $X(\varepsilon)$ they will cause oscillations about unity in $X_W(\omega)$, and after the interval ω_4 these will occur about zero. Figures A.3 and 4 illustrate the effect of the poor side lobe response of the default rectangular window (the process of data truncation generates this window by default) in causing ripple errors in the spectrum of the waveform.

In short, window functions reduce errors in the DFT by reducing the side lobe energy of the default rectangular window. However, this can only be achieved at the expense of a reduced spectral resolution as a reduced side lobe level tends to maximize the spectral energy in the main lobe increasing its width.

B.2 An Assessment of Four Window Functions

A large number of window functions are available, but a comparative study by Harris [31] has established that out of all the available types, four windows offer the best performance in their class. These are the Hann, Hamming, Blackman and the optimal Kaiser-Bessel windows.

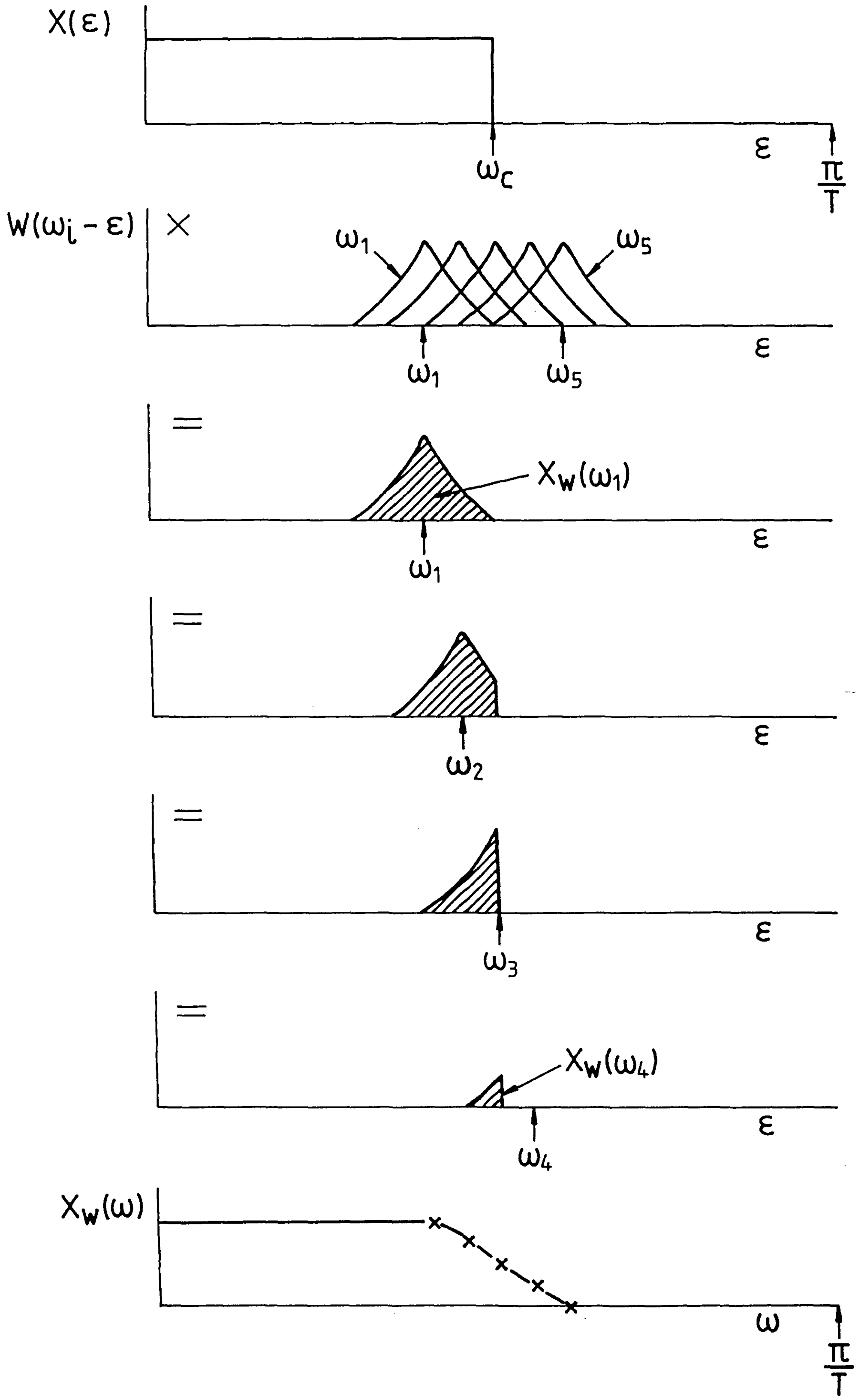

Figure B.1: The effect of a window function.

The Hann and Hamming windows are given by

$$W_H(nT) = \alpha + (1-\alpha)\cos[2\pi n/(N-1)] \quad \text{for } |n| < (N-1)/2 \qquad (B.5)$$
$$= 0 \quad \text{otherwise}$$

where $\alpha = 0.5$ for the Hann window and
$= 0.54$ for the Hamming window.

The Blackman window is given by

$$W_B(nT) = 0.42 + 0.5\cos[2\pi n/(N-1)] + 0.08\cos[4\pi n/(N-1)] \qquad (B.6)$$

and is defined over the same range as equation B5.

The Kaiser-Bessel window is defined by the expression

$$W_K(nT) = I_o(\beta) \,/\, I_o(\pi\alpha) \qquad (B.7a)$$

where $= \pi\alpha[1 - (2n/N-1)^2]^{0.5}$ (B.7b)

and $I_o(x)$ is the zeroth order Bessel function [4,64] of the first kind and can be evaluated as

$$I_o(x) = 1 + \sum_{k=1}^{\infty} [1/k!\,(x/2)^k]^2 \qquad (B.8)$$

Equation B7a is defined over the same range as equations B5 and B6. Unlike the other windows considered, the Kaiser-Bessel window is optimal as any value for the maximum side lobe amplitude can be selected by the appropriate choice of α.

Figures B.2a-d illustrate the time domain shape of the four window functions ($\alpha = 3.5$ for the Kaiser-Bessel window). The shapes are significant in that the sharp truncation boundaries of the rectangular window have been smoothened. However, a comparative assessment can only be made in the frequency domain.

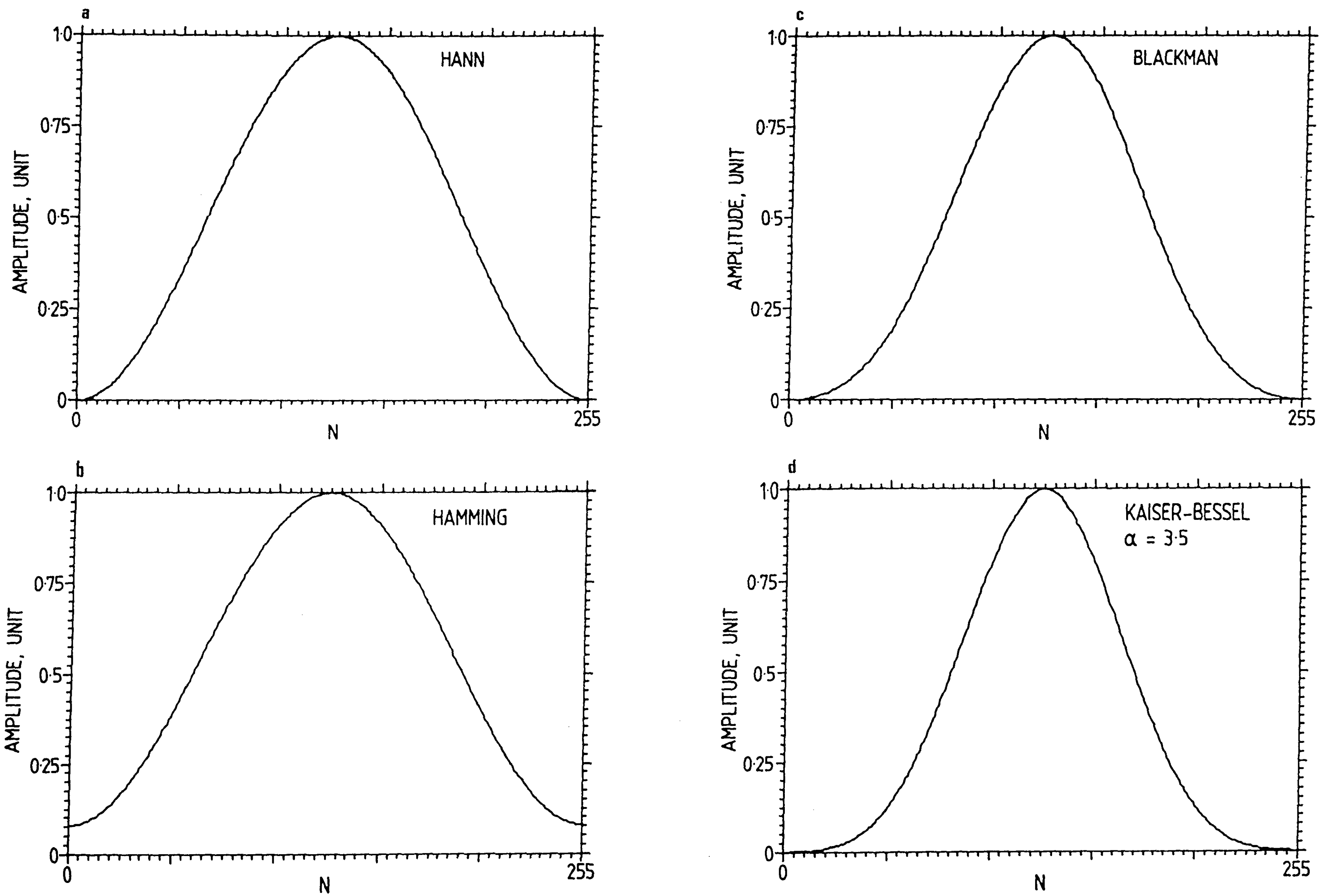

Figure B.2 : The time domain shape of the (a) Hann, (b) Hamming, (c) Blackman and (d) Kaiser windows.

Figure B.3 illustrates, with specific reference to the Hamming window, the frequency domain parameters needed to make a comparative assessment of different windows. The four most important parameters are

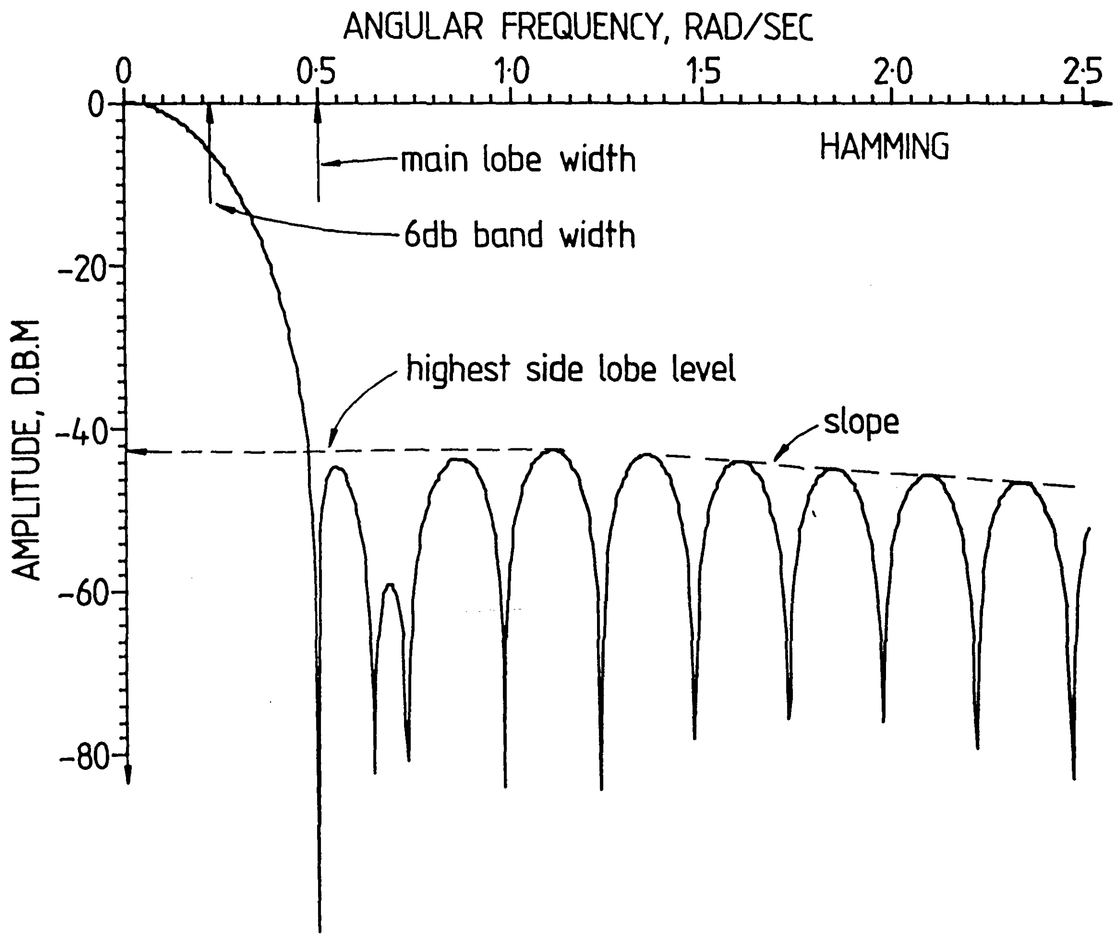

Figure B.3: The frequency domain parameters of window functions.

the 6db and full bandwidths of the main lobe, the highest side lobe level, and the side lobe roll-off slope. These parameters are tabulated in table B.1 for the four windows and the rectangular window, together with their respective insertion losses (section 2.3.3.1). Figures B.4 and B.5 illustrate the frequency response of these windows functions.

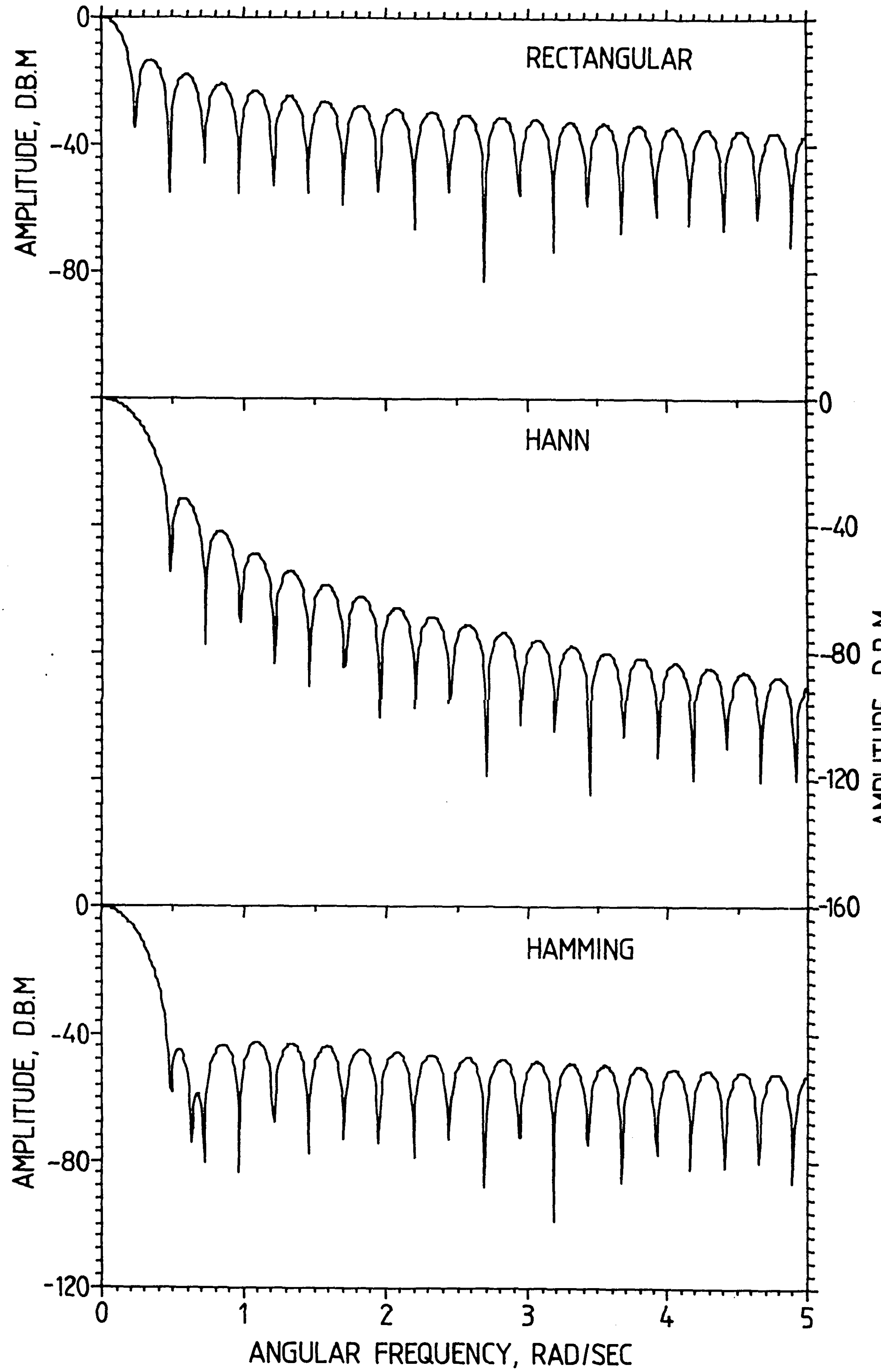

Figure B.4: The frequency response of the rectangular, Hann and Hamming windows (N = 256).

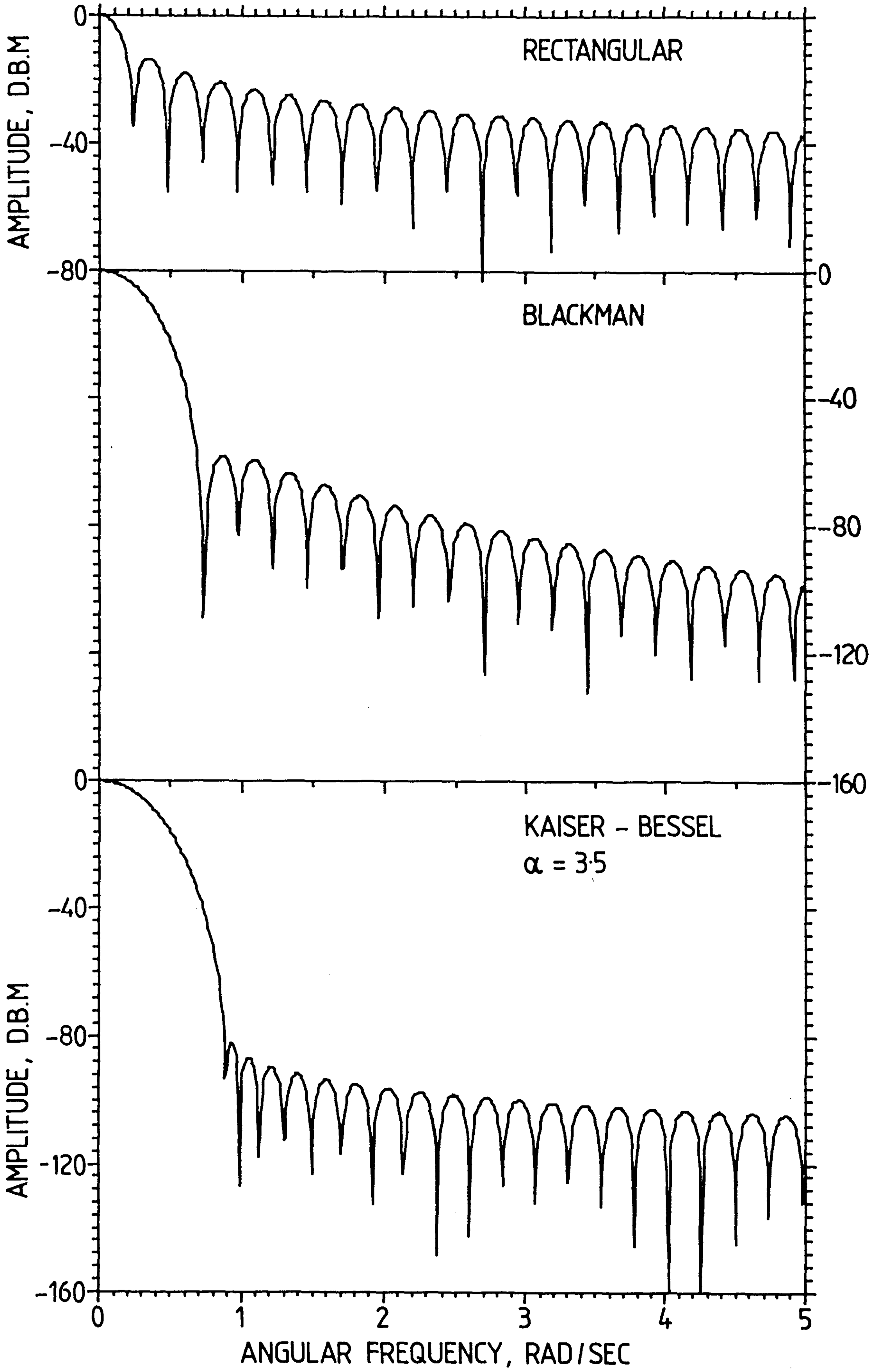

Figure B.5: The frequency response of the rectangular, Blackman and Kaiser (α = 3.5) windows (N = 256).

Window	Highest side lobe level (dbm)	Side lobe roll-off (dbm)	6.0db band-width *	Main lobe width *	G_c (N=1024)
Rectangular	-13	-6	1.0	1.0	1.0
Hann	-32	-18	1.653	1.97	0.4990
Hamming	-43	-6	1.496	2.00	0.5391
Blackman	-58	-18	1.942	2.97	0.4190
Kaiser α=2.0	-46	-6	1.645	2.20	0.4882
α=2.5	-57	-6	1.818	2.74	0.4387
α=3.0	-69	-6	1.975	3.12	0.4016
α=3.5	-82	-6	2.124	3.57	0.3725

* as a ratio of value for the rectangular window

Table B.1: Parameters of the rectangular, Hann, Hamming, Blackman and Kaiser-Bessel windows.

The effectiveness of these window functions can be assessed by comparing their respective side lobe levels. Using this criterion, the most effective windows are the Blackman and Kaiser-Bessel (for $\alpha > 3.0$) windows. However, there is no absolute arbitrary figure of merit between the windows because the reduction in side lobe amplitude must be balanced against the loss in resolution due to the increased main lobe width. For certain conditions, the milder Hamming window may very well give better results than the Blackman window because it inherently produces less frequency aliasing between the DFT filters (its 6db bandwidth is 1.5 compared to 1.9 for the Blackman window). An example of this is the choice of the Hamming weighting for the weighted two cycle DFT algorithm of section 5.2.2.3. The use of a more severe weighting would have resulted in a worse response because of the reduced spectral resolution of the DFT, unless the window size had been increased but this, of course, is unacceptable for real-time applications.

APPENDIX C

THE REDUCTION OF DFT LEAKAGE ERRORS USING FREQUENCY DOMAIN INTERPOLATION

C.1 The Frequency Interpolation Formula

Let $x(nT_s)$ be a discrete sequence with M arbitrarily related spectral components such that

$$x(nT_s) = \sum_{m=1}^{M} A_m \sin(\omega_m nT_s + \Phi_m) \qquad n=0,1,\ldots,N-1 \qquad (C.1)$$

where n : discrete time operator

m : frequency index

A_m : peak amplitude of the mth spectral component

Φ_m : phase of the mth spectral component

$T_s = 2\pi/\omega_s$

: sample period

The DFT of this discrete sequence, assuming the frequency resolution, ω_o, of the DFT ($\omega_o=\omega_s/NT_s$) to be such that no two filters in the DFT filter bank enclose more than one spectral component, is given by the expression [37]

$$X(k) = -0.5j \sum_{m=1}^{M} \mathbf{A}_m\{ e^{ja(\lambda_m-k)} \sin\pi(\lambda_m-k)/[\sin\pi(\lambda_m-k)/N] - e^{ja(\lambda_m+k)} \sin\pi(\lambda_m+k)/[\sin\pi(\lambda_m+k)/N] \} \qquad (C.2)$$

where k : discrete frequency operator

$\mathbf{A}_m = A_m e^{j\Phi_m}$

a : $\pi(N-1)/N$

The parameter λ_m as illustrated by the DFT filter bank model of figure C.1 is given by

$$\lambda_m = L_m + \delta_m \tag{C.3}$$

where L_m : distinct integer such that the DFT filters L_m and L_{m+1} enclose the spectral component of frequency ω_m $(1 < L_m < M)$.

δ_m : a real number, such that $0 < \delta_m < 1$, representing the per unit shift of A_m from the DFT filter centred at $\omega_o L_m$.

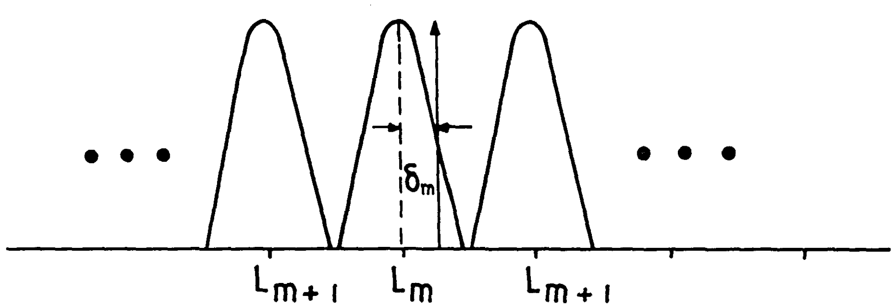

Figure C.1: Parameters of the frequency interpolation formula.

Equation C.2 mathematically describes the response of the DFT filters centred at the frequencies $\omega_o k$, $k=0,1,\ldots,N-1$, to any arbitrary spectral components and as such can be used to precisely calculate the spectral energy leakage. In particular, for a frequency component centred exactly at the filter L_m (i.e. $\delta_m=0$), equation C.2 reduces [37] to the more familiar form of the DFT (equation A.22) for $k=L_m$. In general, however, this will not be so and the spectral energy of the component will contribute to every value of X(k) as has been illustrated in section 2.3 (see table 2.1).

C.2 The Exact Solution

The problem of correcting the DFT spectral estimates is one of finding the true spectral components, A_m, from the DFT estimates, X(k). For a single frequency tone (m=1) only one distinct value of L_m will exist. Therefore, assuming δ_m is known, equation C.2 can be used directly to calculate A_m from its DFT estimate. In practice, single tones are never present and the solution is considerably more complex.

The increase in complexity is due to the fact that each component of the DFT spectral estimate will contain contributions from all the M spectral components - in other words, for each value of L_m in equation C.2 N values of k can be chosen. Thus the computation of the M components A_m must involve the solution of a set of simultaneous linear equations. It can be shown [37] that the solution is given by the M by M matrix equation

$$[\mathbf{F}]\ [\mathbf{Z}] = [\mathbf{W}] \tag{C.4}$$

[W] is a vector such that

$$[\mathbf{W}]^T = [-2V_1, 2U_1, \ldots, -2V_M, 2U_M] \tag{C.5}$$

where $$X(k) = U_k + jV_k \tag{C.6}$$

[Z] is a vector such that

$$[\mathbf{Z}]^T = [X_1, Y_1, \ldots, X_M, Y_M] \tag{C.7}$$

where $$A_m = X_m + jY_m \tag{C.8}$$

[F] is the M by M matrix of form

$$[\mathbf{F}] = \begin{bmatrix} A_{10}, & B_{10}, & \cdots & A_{m0}, & B_{m0} \\ C_{10}, & D_{10}, & \cdots & C_{m0}, & D_{m0} \\ \vdots & & \vdots & & \vdots \\ A_{1m}, & B_{1m}, & \cdots & A_{mm}, & B_{mm} \\ C_{1m}, & D_{1m}, & \cdots & C_{mm}, & D_{mm} \end{bmatrix} \tag{C.9}$$

where $A_{mk} = \text{Csos}\ (\lambda_m-k) \ - \ \text{Csos}\ (\lambda_m+k)$ (C.10)

$B_{mk} = \text{Ssos}\ (\lambda_m-k) \ - \ \text{Ssos}\ (\lambda_m+k)$ (C.11)

$C_{mk} = \text{Ssos}\ (\lambda_m-k) \ + \ \text{Ssos}\ (\lambda_m+k)$ (C.12)

$D_{mk} = \text{Csos}\ (\lambda_m-k) \ + \ \text{Csos}\ (\lambda_m+k)$ (C.13)

The interpolation functions Csos and Ssos are defined as

$$\text{Ssos}(z) = \sin(az)\ \sin(\pi z)/\sin(\pi z/N) \tag{C.14}$$

$$\text{Csos}(z) = \cos(az)\ \sin(\pi z)/\sin(\pi z/N) \tag{C.15}$$

C.3 The Approximate Correction Method

The exact method has two serious drawbacks,

(i) it is computationally complex and unsuited to real-time application,

(ii) the exact frequencies of the spectral components must be known (i.e. λ_m must be known).

An approximate method which is computationally much simpler and includes a frequency identification procedure can be derived from equation C.2 provided the assumption is made that N is large. Jain et al. [37] have shown that for large N (>512) the negative frequency mirror image of the DFT spectral estimate can be ignored with negligible effect on accuracy. Therefore equation C.2 can be re-written as

$$X(k) = -0.5j \sum_{m=1}^{M} A_m\, e^{ja(\lambda_m-k)} \sin\pi(\lambda_m-k)/[\sin\pi(\lambda_m-k)/N] \tag{C.16}$$

Making a further assumption that the sine term in the denominator of equation C.16 can be replaced by its argument, and interpolating between the mth and (m+1)th DFT filters gives the expressions

$$X(m) = 0.5\ A_m|\sin\pi\delta_m|/(\pi\delta_m/N) \tag{C.17}$$

$$X(m+1) = 0.5\ A_m|\sin\ (1-\delta_m)|/[\pi(1-\delta_m)/N] \tag{C.18}$$

If $$\alpha_m = X(m)/X(m+1) \tag{C.19}$$

then from equations C.17 and C.18 it follows that

$$\delta_m = \alpha_m/(1+\alpha_m) \tag{C.20}$$

and the frequency of the mth spectral component can then be found as

$$\omega_m = \lambda_m\omega_o = (m + \delta_m)\omega_o \tag{C.21}$$

Solving equations C.17 and C.18 for A_m gives

$$A_m = 2\pi\delta_m\ X(m)/[N|\sin\ \pi\delta_m|] \tag{C.22}$$

In arriving at equation C.22 the effect of spectral energy leakage from filters other than the mth and (m+1)th has been ignored. Jain et al. [37] have shown that this assumption can lead to serious errors for very low amplitude spectral components due to ´spillover´ from the fundamental and recommend equation C.22 be used only for the dominant spectral components. For low amplitude spectral components they recommend subtracting the ´spillover´ of the fundamental from X(m) and X(m+1) prior to using equations C.20 and C.22. Their modified values, X´(m) and X´(m+1), are given by the expressions

$$X'(m) = X(m) + 0.5jA_1e^{ja(\lambda_1-m)}\sin\pi(\lambda_1-m)/[\sin\pi(\lambda_1-m)/N] \tag{C.23}$$

$$X'(m+1) = X(m+1) + 0.5j\mathbf{A}_1e^{ja(\lambda_1-m-1)} \cdot \sin\pi(\lambda_1-m-1)/[\sin(\lambda_1-m-1)/N] \tag{C.24}$$

APPENDIX D

MICRO-MACHINE PARAMETERS AND MODIFICATIONS

PARAMETER	VALUE
GENERAL	
Phase voltage	115.47 V rms
Full load phase current	8.0 A rms
Full load excitation voltage	23 V
Full load excitation current	4.5 A
Number of poles	4
Frequency	50 Hz
STATOR WINDING	
type: two tier, double-layer	
Number of slots	48
Number of conductors per slot	12
Number of windings per phase	2
Relative phase displacement	30 degrees
Number of turns per winding	48
Conductor size	2 (10mm x 1.25mm)
Coil pitch	1-11
Winding factor	0.92
Length of mean turn	102 cm
Phase resistance, 15 degrees C	0.035 ohm
Slot skew	1 slot pitch
Axial length (gross)	14.0 cm
Axial length (effective)	13.2 cm

DIVIDED EXCITATION WINDING

type: 100% double-layer lap on cylindrical rotor

Number of slots cut	32
Number of slots used	24
Air gap (actual)	0.76 mm (typical)
Air gap (effective)	0.73 mm (d axis)
	0.78 mm (q axis)
Number of conductors per slot	100 (excitation)
	100 (shadow)
Number of turns per winding per pole	285 (effective)
Coil pitch	1-7
Winding factor	0.95
Resistance, 15 degrees C	5.0 ohm (excitation)
	38 ohm (shadow)

D AND Q AXIS DAMPER WINDINGS

type: 100% double-layer lap

Number of conductors per slot	48 (damper)
	48 (shadow)
Number of turns per pole	182 (effective)
Conductor size	4 x 0.50 mm dia. (damper)
	0.50 mm dia. (shadow)
Coil pitch	1-9
Winding factor	0.95
Resistance, 15 degrees C	
damper	0.90 ohm (d and q axis)
shadow	4.38 ohm (d and q axis)

PHASE BELT	COIL NUMBER 1 2	1 2 4 3	4 3 5 6	5 6 8 7	8 7
A	19 20	29 30 31 32	41 42 43 44	5 6 7 8	17 18
B	17 18	27 28 29 30	39 40 41 42	3 4 5 6	15 16
C	11 12	21 22 23 24	33 34 35 36	45 46 47 48	9 10
D	9 10	19 20 21 22	31 32 33 34	43 44 45 46	7 8
E	3 4	13 14 15 16	25 26 27 28	37 38 39 40	1 2
F	1 2	11 12 13 14	23 24 25 26	35 36 37 38	47 48

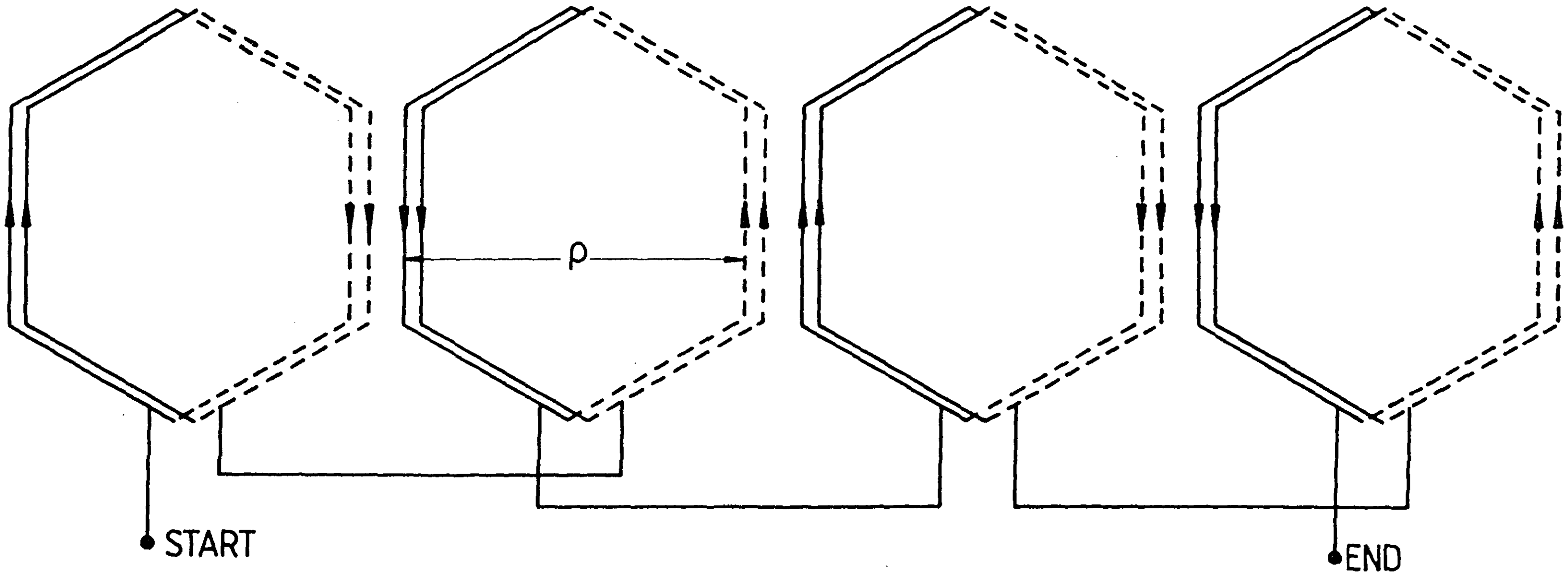

Figure D.1 : Slot distribution of the stator winding coils for the micro-alternator.

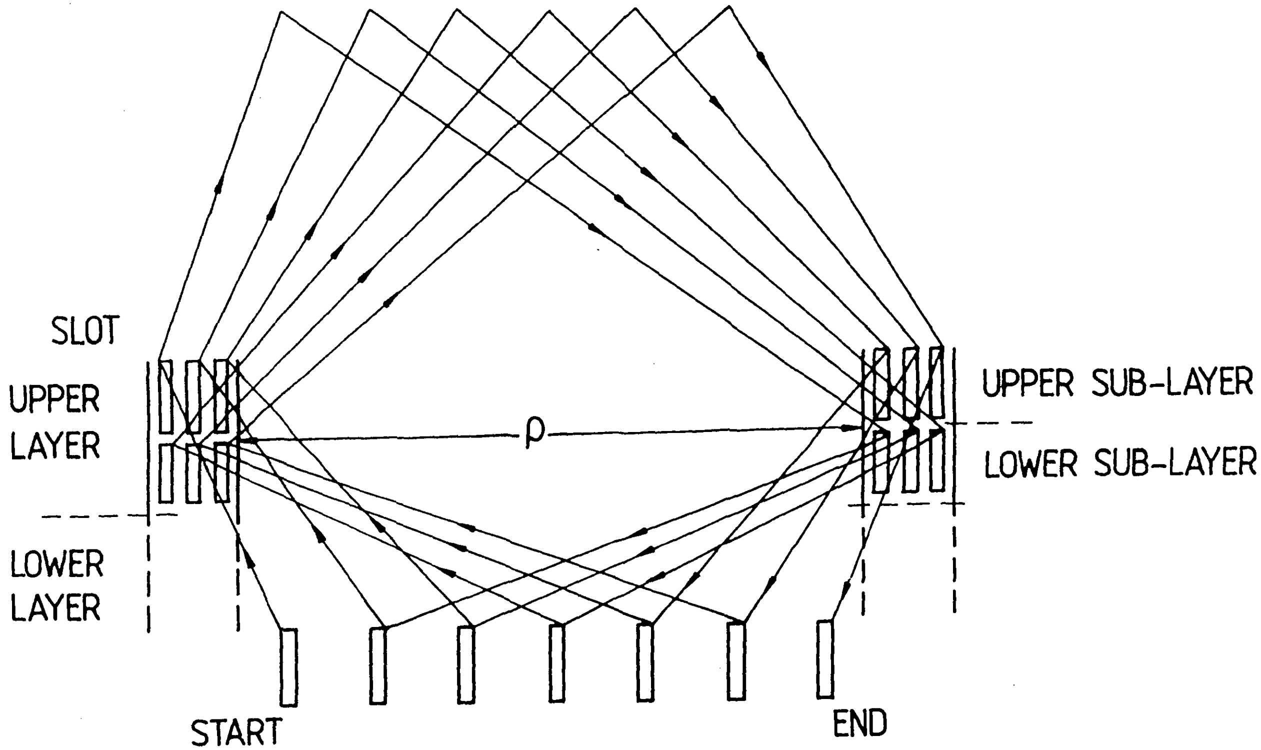

Figure D.2 : Double-layer winding arrangement for each coil of the stator winding.

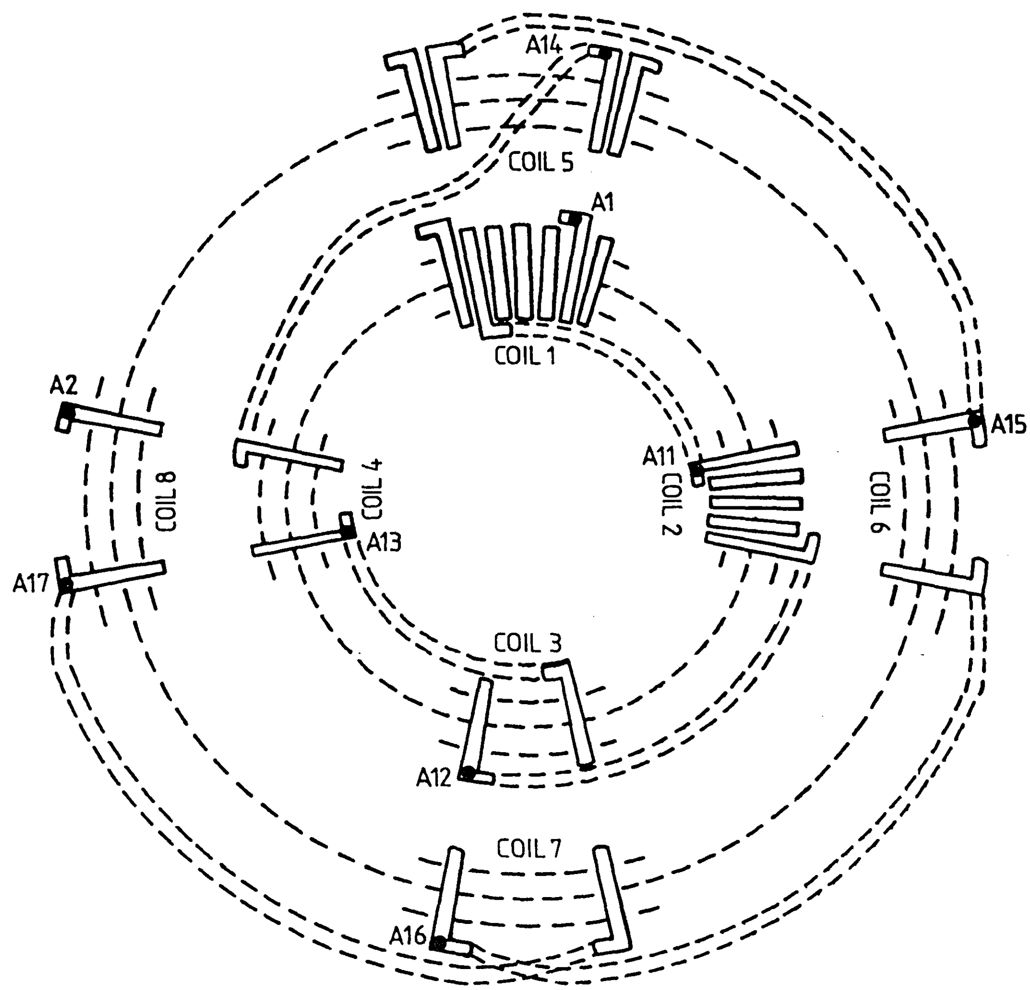

Figure D.3 : Position of tap points for the A-phase at the end windings of the stator.

APPENDIX E

THE FIELD MMF AS THE MAIN SOURCE OF STATOR TIME HARMONICS

Harmonic emfs are induced in the stator because of the presence of space harmonics in synchronism with the fundamental wave in the airgap mmf. The principle source of these synchronous space harmonics is the field winding and is due to it being discontinuous and distributed in coils and groups.

Other factors also contribute to the airgap space harmonics. These are:

(i) Saliency and the effect of slot openings.

(ii) Saturation.

(iii) Time harmonic currents flowing in the armature windings (i.e. the armature reaction).

Some of these space harmonics will be synchronous with the fundamental mmf wave and induce stator time harmonics in a similar manner to the field winding space harmonics (e.g. slot ripple harmonics [3,32,44]). Others will be asynchronous and contribute to the losses. Furthermore, for a complete study, the interaction between the various synchronous and asynchronous space harmonics must also be taken into account. Secondary effects may also contribute additional space harmonics.

For the study presented here, only the space harmonic contributions of the field and armature windings will be examined. A more complete study is unnecessary for this research, but the reader is referred to an excellent book by Heller [32] if desired.

E.1 The Mmf Due to a Coil Group

The mmf due to a coil in a slot carrying the current

$$I = \sum_{n} I_n \cos n(\omega t + \psi) \tag{E.1}$$

is given by the equation [32]

$$F_c = 2/\pi\, N_s \sum_{n} \sum_{v} I_n (1/v) k_{p_v}\, k_{s_v} \cos v\theta \cos n(\omega t + \psi) \tag{E.2}$$

where n : order of time harmonic.

v : order of space harmonic.

N_s : number of series turns in the coil.

θ : angular position of the coil in electrical radians. (2π electrical radians equal one pole pitch)

ψ : arbitrary phase angle (elec. radians) at time t=0.

The factors k_{p_v} and k_{s_v} are the nth harmonic coil pitch and slot pitch factors respectively, and given by

$$k_{p_v} = \sin(v\rho\pi/2) \tag{E.3}$$

where ρ : ratio of coil pitch to pole pitch

and $$k_{s_v} = \sin(v\gamma/2) \,/\, (v\gamma/2) \tag{E.4}$$

where γ : slot pitch in radians.

A typical machine winding will consist of a number of coil groups formed by two or more coils in consecutive slots connected in series. The mmfs of N individual coils will be

$$F_1 = F_c$$

$$F_2 = 2/\pi\ N_s \sum_n \sum_v I_n (1/v) k_{p_v} k_{s_v} \cos n(\omega t+\psi) \cos v(\theta-\alpha)$$

$$\vdots$$

$$F_N = 2/\pi\ N_s \sum_n \sum_v I_n (1/v) k_{p_v} k_{s_v} \cos n(\omega t+\psi) \cos v[\theta-(N-1)\alpha] \qquad (E.5)$$

where α : slot angle in electrical radians.

$$= 2\pi p/Q \qquad (E.6)$$

where p : number of pole pairs.

Q : total number of slots.

The mmf of the coil group will be the sum of these mmfs

$$Fg = 2/\pi\ N\ N_s \sum_n \sum_v I_n (1/v) k_{p_v} k_{s_v} \cos n(\omega t+\psi)$$

$$\cdot \{ \cos v\theta[1+\cos v\alpha+\ldots+\cos v(N-1)\alpha]$$

$$+ \sin v\theta[\sin v\alpha+\sin v2\alpha+\ldots+\sin v(N-1)\alpha] \}$$

$$= 2/\pi\ N\ N_s \sum_n \sum_v I_n (1/v) k_{p_v} k_{s_v} (\sin Nv\alpha/2)/(N \sin v\alpha/2)$$

$$\cdot \cos n(\omega t + \psi) \cos v[\theta - (N-1)\alpha/2] \qquad (E.7)$$

For a two layer winding with q, the slots per pole per winding as an integer, $N = q$ [32,44] and

$$F_g = 2/\pi\ N_s\ q \sum_n \sum_v I_n k_{w_v} \cos n(\omega t+\psi) \cos v[\theta - (q-1)\alpha/2] \qquad (E.8)$$

where $k_{w_v} = k_{p_v}\, k_{s_v}\, k_{d_v}$ (E.9)

: nth harmonic winding factor.

and $k_{d_v} = (\sin qv\alpha/2)\ /\ (q \sin v\alpha/2)$ (E.10)

: nth harmonic distribution factor.

E.2 The Steady-state Field Mmf

From equation E.8 the field mmf can be written, the subscript 'r' representing the field (rotor) variables, as

$$F_r = 2/\pi\ N_r I_r \sum_v (1/v)(k_{d_v})_r \cos v\theta_r \qquad v \text{ is odd} \tag{E.11}$$

where $N_r = (N_s N_g q)_r$

: total number of series turns in the field winding.

N_{g_r} : number of field winding coil groups.

$k_{s_v} = 1$ (see appendix D).

$k_{p_v} = 0$ for v even, 1 for v odd (see section E.5).

$\theta_r = \theta - (q_r - 1)\alpha_r/2.$

: field winding reference angle.

The time harmonic summation term vanishes as under steady-state conditions the field current will be DC.

The rotation of the field can be accounted for by including a time variant angular term in equation E.11 which can then be re-written with some additional simplification as

$$F_r = 2/\pi\ I_r \sum_v (1/v)(T_{w_v})_r \cos v(\theta_r + \omega t) \qquad v \text{ is odd} \tag{E.12}$$

where $(T_{w_v})_r = N_r(k_{d_v})_r$
: effective series turns in the field winding.

The significance of equation E.12 is twofold

(i) It shows that the field mmf consists of a series of odd space harmonics synchronous with respect to the fundamental wave, which will therefore induce armature time harmonics of order n=v and contribute to the synchronous torque.

(ii) The magnitude of the space harmonics is at the most 1/v of the fundamental, though in practice the winding factor k_{w_v} is arranged to drastically attenuate higher order harmonics. The harmonic content of the induced stator time harmonics, as will be seen in section E.4, will be lower still due to the additional influence of the stator winding factors.

The degree of harmonic distortion is best appreciated by substituting for the winding parameters from appendix D in equation E.12. This gives

$$F_r = I_r \, [301.73 \cos(\omega_r + t) - 14.60 \cos 3(\omega_r + t) - 5.85 \cos 5(\omega_r + t) + 8.56 \cos 7(\omega_r + t) - 6.66 \cos 9(\omega_r + t) + \ldots] \quad \text{AT/pole} \qquad (E.13)$$

E.3 The Armature Reaction

The second main component of the airgap mmf is due to time harmonic currents - this includes the fundamental as well - flowing in the armature windings.

The mmf contributions of each of the three-phases of the armature winding when excited by balanced sinusoidal currents such that

$$I_A(\theta) = \sum_n I_{a_n} \cos n(\omega t + \psi_a) \tag{E.14a}$$

$$I_B(\theta) = I_A(\theta - 2\pi/3) \tag{E.14b}$$

$$I_C(\theta) = I_A(\theta - 4\pi/3) \tag{E.14c}$$

can be derived from equation E.8 and are given below.

$$F_A = 2/\pi \sum_n \sum_v I_{a_n}(1/v)(T_{w_v})_a \cos v\theta_a \cos n(\omega t + \psi_a) \tag{E.15}$$

where the subscript 'a' represents the armature variables and

$(T_{w_v})_a = N_a(k_{w_v})_a$
: effective number of series turns per phase in the armature winding.

$$F_B = 2/\pi \sum_n \sum_v I_{a_n}(1/v)(T_{w_v})_a \cos v(\theta_a - 2\pi/3) \cdot \cos n(\omega t + \psi_a - 2\pi/3) \tag{E.16}$$

$$F_C = 2/\pi \sum_n \sum_v I_{a_n}(1/v)(T_{w_v})_a \cos v(\theta_a - 4\pi/3) \cdot \cos n(\omega t + \psi_a - 4\pi/3) \tag{E.17}$$

The total armature contribution to the airgap mmf can be obtained by adding equations E.15, E.16 and E.17. Using the identity

$$\cos X \cos Y = 0.5 \cos (X \pm Y)$$

and rearranging gives

$$F_a = 3/\pi \sum_n \sum_v I_{a_n}(1/v)(T_{w_v})_a \{ \cos [n(\omega t + \psi_a) \pm v\theta_a] + \cos [n(\omega t+\psi_a) \pm v\theta_a - (n\pm v)2\pi/3] + \cos [n(\omega t+\psi_a) \pm v\theta_a - (n\pm v)4\pi/3] \} \tag{E.18}$$

which reduces to

$$F_a = 3/\pi \sum_n \sum_h I_{a_n}(1/h)(T_{w_h})_a \cos [n(\omega t + \psi_a) \pm h\theta_a] \quad (E.19)$$

where $v = 6h \pm n$ (E.19a)

Equation E.19 is the general equation for the armature mmf due to a balanced nth harmonic three-phase current, and can be interpreted as a number of cosine waves travelling either in an anticlockwise or clockwise direction with an angular velocity given by

$$d/dt\ [n(\omega t + \psi_a) \pm v\theta_a] = 0$$

or $$d\theta_a/dt = \pm(n/v)\omega \quad (E.20)$$

Table E.1 lists the relative angular velocities of all the possible space harmonics upto v = 13 for time harmonic armature currents of order n = 1,3, ..., 13.

v	Order of time harmonic n						
	1	3	5	7	9	11	13
1	1		-5	7		-11	13
3		1			3		
5	-1/5		1	-7/5		11/5	-13/5
7	1/7		-5/7	1		-11/7	13/7
9		1/3			1		
11	-1/11		5/11	-7/11		1	-13/11
13	1/13		-5/13	7/13		-11/13	1

Table E.1: Relative angular velocities of space harmonics of v for time harmonics of order n.

In summary table E.1 and equation E.19 demonstrate two very important conclusions regarding the armature reaction. These are:

(i) An nth harmonic current in the armature will generate a synchronous space harmonic of the same order which will interact with the synchronous vth (=n) harmonic field wave to produce torque. This is fact, for a fundamental frequency armature current, forms the fundamental basis of the synchronous machines.

(ii) In addition, a series of asynchronous space harmonics are also generated which will contribute to the losses. In practice, the asynchronous space harmonics due to the fundamental frequency armature currents, will constitute the dominant asynchronous components.

E.4 The Open-circuit Armature Emf

The emf induced in a machine winding by an mmf, F, is given by [32]

$$E = 4\mu_o/\delta_e \; f\tau l \; \sum_v T_{w_v} \; F_{v_{max}} \tag{E.21}$$

where δ_e : effective airgap (metres)

l : effective axial length (metres) of the machine

$\tau = D/2p$: pole pitch (radians)

D : diameter of rotor (metres)

$\mu_o = 4\pi.10^{-7}$ H.m^{-1}

$f = 2\pi/\omega$

Substituting for the mmf term in equation E.21, equation E.11 gives

$$E_a = 8/(\pi\delta_e) \; \mu_o f\tau l \; I_r \; \sum_v (1/v)(T_{w_v})_r \; (T_{w_v})_a \tag{E.22}$$

Substituting for the variables from appendix D, and including a time variant term, the A-phase open-circuit emf can be written as

$$E_A = I_r\,(149.20 \cos \omega t + 3.530 \cos 3\omega t - 0.155 \cos 5\omega t - 0.161 \cos 7\omega t - 0.536 \cos 9\omega t + \dots) \quad V \qquad (E.23)$$

Comparing equations E.23 and E.13 it can be seen that the per unit reduction in harmonic distortion in the open-circuit emf over the field mmf is quite considerable (e.g. $E_{A_3} = 0.0247$ p.u., $F_{r_3} = 0.0483$ p.u.). This is due to the inclusion of the armature winding factors in equation E.22.

Obviously, the winding factors are of fundamental importance in reducing harmonic distortion in the machine and this influence will be examined next.

E.5 The Winding Factors

The winding factors express the per unit reduction in the amplitude of either time or space harmonics - the same winding factors are applicable to both - relative to the fundamental. By suitable winding design, a drastic reduction in time and space harmonic distortion can be achieved at the expense of a slight reduction in the amplitude of the fundamental.

The nth harmonic distribution factor is as can be seen from equations E.7 and E.10 the ratio of the vector sum of either the nth harmonic space or time harmonics to their arithmetic sum. The pitch factor expresses the ratio of the coil pitch to the pole pitch for the winding and the skew factor, the slot skew which is commonly used to smoothen the transition of the mmf wave from slot to slot [32,44]. Figures E.1-3 illustrate for the micro-machine the variation of the stator distribution, coil pitch and slot skew factors respectively versus their primary variables for various values of n.

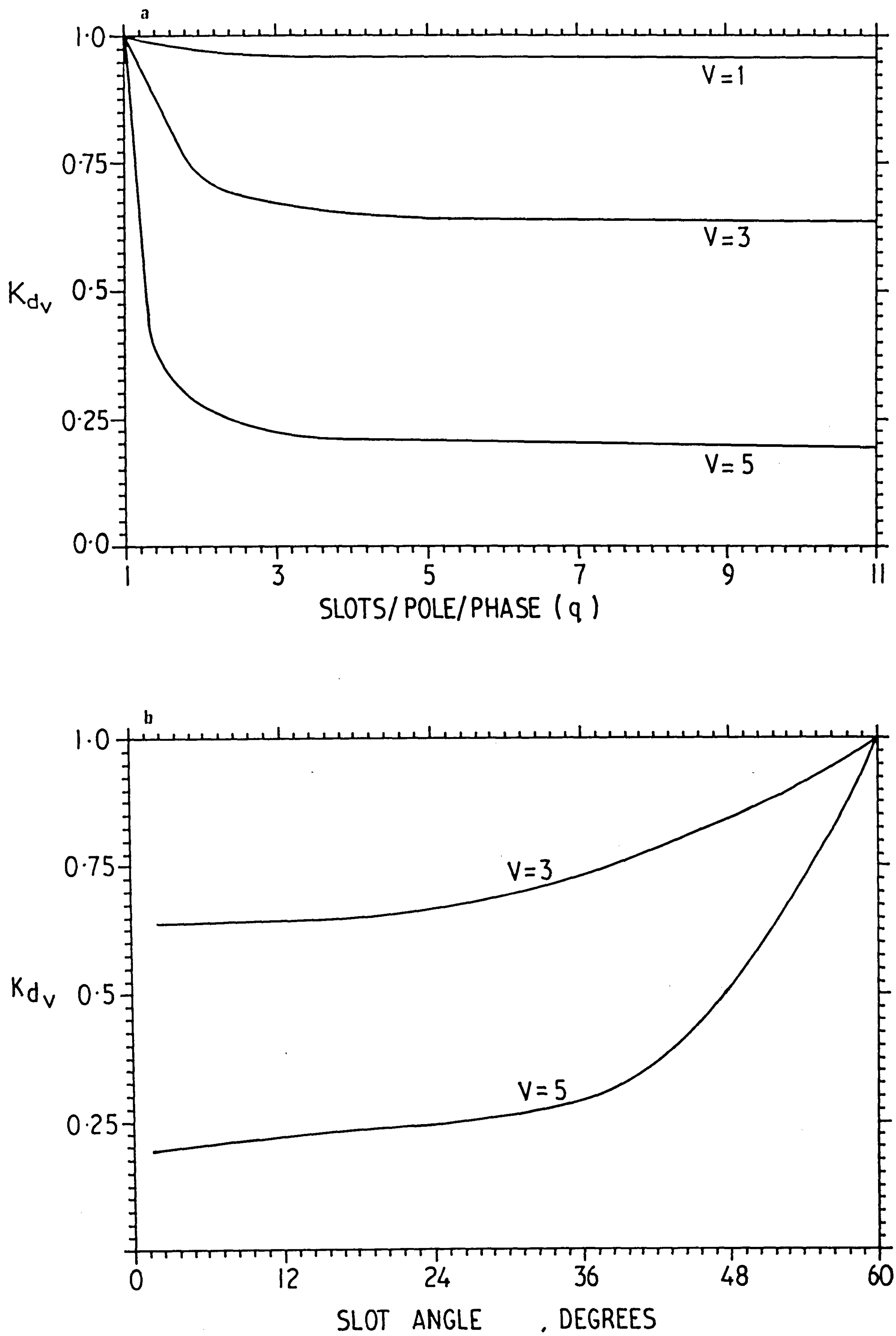

Figure E.1: Variation of the distribution factors versus (a) q (b) the slot angle.

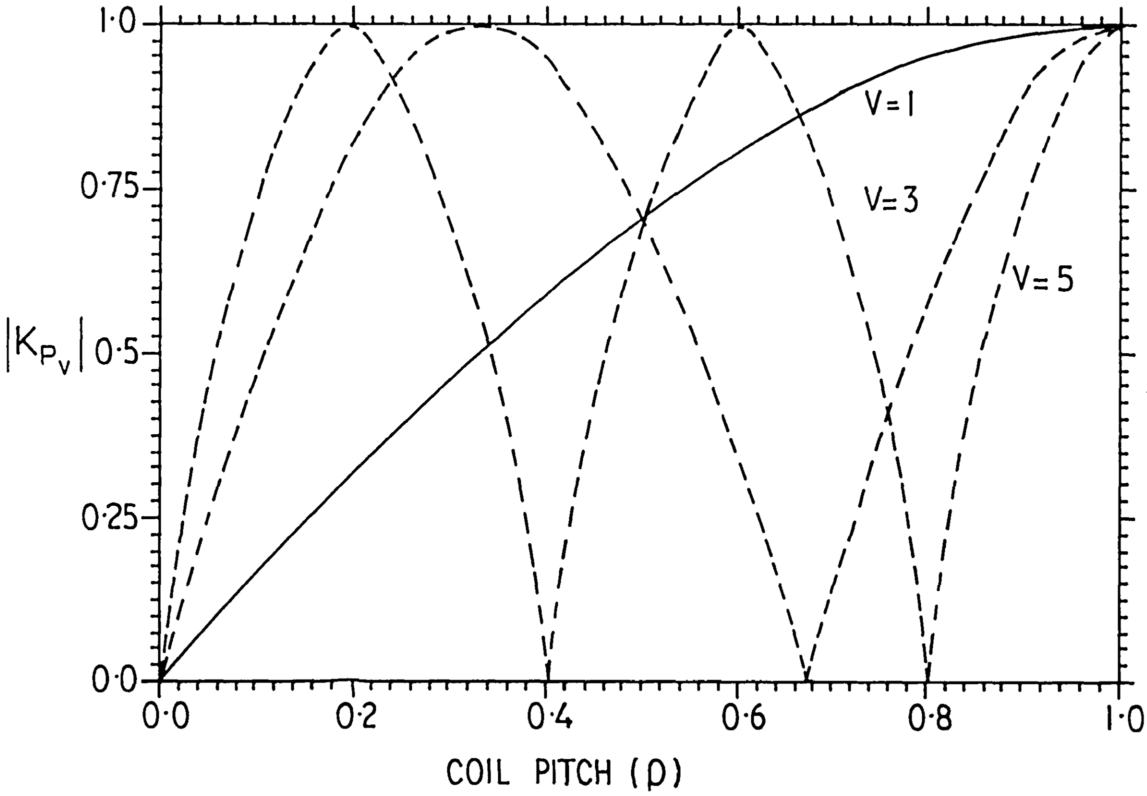

Figure E.2: Variation of the coil pitch factor versus the coil pitch

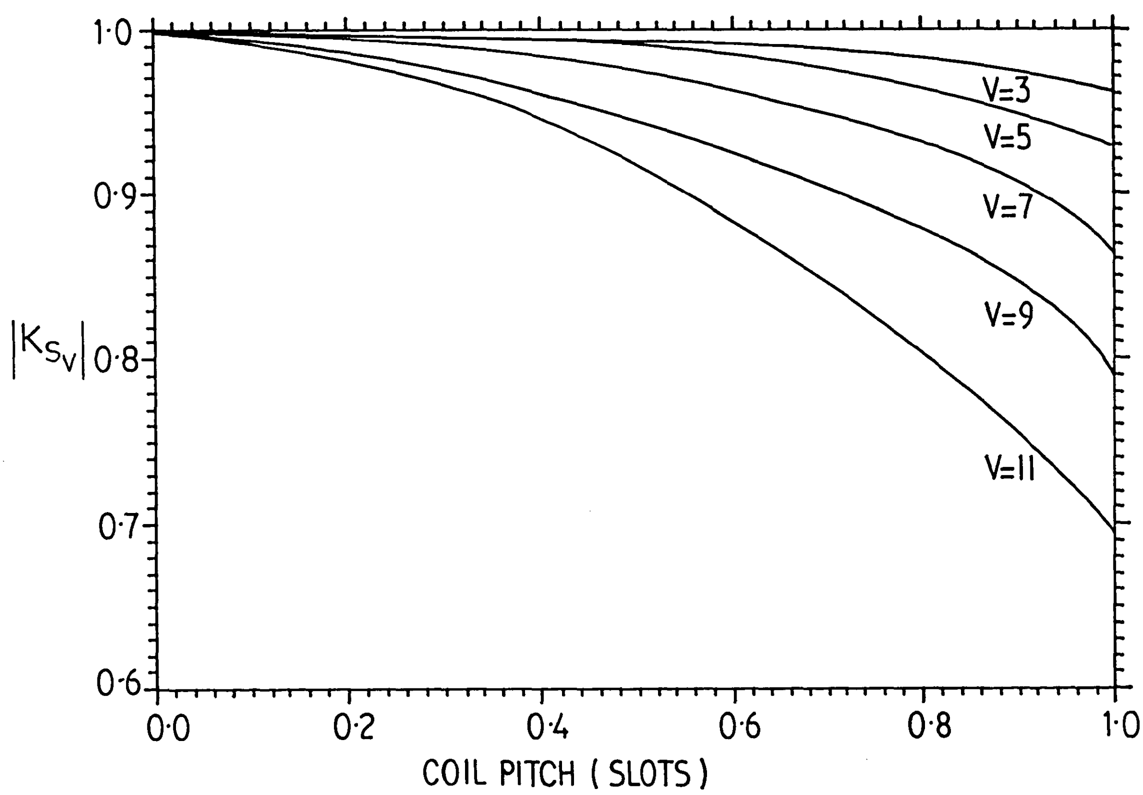

Figure E.3: Variation of the slot skew factor versus the slot skew

A number of important conclusions can be made. They are:

(i) The optimum value of q (α = 15 degrees) is 4 or greater (e.g. for q=4, k_{d_3}= 0.653, k_{d_1}= 0.958, k_{d_5}= 0.205). Note that in figure E.2 not all the values given by the curves are physically realizable. Noninteger values of q are allowed (fractional slot windings [32,44]) but only if q is an integer and divisible by three.

(ii) By suitable selection of the pitch factor any harmonic can be eliminated (or chorded out). For the micro-alternator, the field is fully pitched thereby completely eliminating any induced even time harmonics in the armature. The armature pitch factor is chosen as 0.833 substantially reducing the fifth and seventh harmonics. This is typical of real alternators as well.

(iii) The third harmonic can also be chorded out as illustrated in figure E.3 by choosing a pitch factor of 0.65. In large alternators, however, this is never done; firstly because of the penalty of the 18% reduction in the fundamental; and secondly because the third harmonic currents, being zero-sequence components, will sum to zero in a three phase system.

Tables E.2 lists calculated values for the stator and field winding factors.

v	1	3	5	7	9	11	13
$(k_{p_v})_a$	.966	-.707	.259	.259	-.707	.966	-.966
$(k_{s_v})_a$	.997	.975	.930	.866	.784	.688	.583
$(k_{d_v})_a$	.958	.653	.205	-.158	-.271	-.126	.126
$(k_{w_v})_a$	.922	-.450	.049	-.035	.150	-.084	-.071
$(k_{d_v})_r$	.789	-.115	-.077	.157	-.157	.077	.115

Table E.2: Stator and field winding factors

E.6 Summary

The theory presented in this section illustrates three very important points regarding the nature of the stator time harmonics. They are:

(i) The source of the stator time harmonics is the presence of odd space harmonics, due to the field, in the airgap mmf in synchronism with the fundamental wave (equations E.13 and E.23). The harmonic distortion of the mmf contribution of the field winding is due to it being discontinuous and distributed in coils and groups (equations E.2 and E.8).

(ii) The nature of the stator time harmonics can be controlled by the stator and field winding factors (equations E.3,E.4 and E.10). Figures E.1 and E.3 illustrate the effect of the winding factors on the harmonic distortion of the mmf due to a discontinuous winding.

(iii) Present design practice is to minimize the 5th,7th,11th etc. harmonics at the expense of the triplen harmonics. This is because in a balanced three-phase system triplen harmonic currents cannot flow and, therefore, cannot contribute to the losses.

APPENDIX F

CALCULATION OF THE STEADY-STATE EQUIVALENT CIRCUIT REACTANCES OF A SYNCHRONOUS MACHINE

F.1 The nth Harmonic Steady-state Equivalent Circuit

The classical steady-state equivalent circuit of a synchronous machine is that of a 50Hz emf source behind an impedence consisting of the armature resistance per phase and the magnetizing and leakage reactances of the armature. Equations E.19 and E.22 show that this simple equivalent circuit can also be used to account for the induced armature time harmonics.

A similar nth harmonic equivalent circuit can be formed with an nth harmonic emf source as given by equation E.22. It has been shown in section E.3 that an nth harmonic armature current will generate a synchronous space harmonic of the same order which will contribute to the nth harmonic magnetizing reactance exactly as for the fundamental. Similarly, the asynchronous space harmonics due to the nth harmonic current (see table E.1) in the armature will contribute to an element of the nth harmonic leakage reactance known as the differential leakage reactance. The other two components of nth harmonic leakage reactance, the slot and end-winding leakage reactances, constitute the residual nth harmonic ($n=v$) synchronous flux consumed by the slot and end windings.

A complete multi-harmonic steady-state solution can be obtained by the linear superposition of a number of equivalent circuits, one for each harmonic being considered.

F.2 The nth Harmonic Magnetizing Reactance

The nth harmonic magnetizing reactance constitutes the flux interlinkage with the armature winding due to the vth space harmonic produced by an nth harmonic current flowing in it. In other words, it constitutes the nth harmonic back emf, and therefore it can be calculated from equation E.21.

The maximum value of the vth space harmonic of the armature mmf due to an nth time harmonic, where n=v, is given by equation E.19 as

$$(F_{a_n})_{max} = 3/(\pi v)\ I_{a_n}(T_{w_v})_a \qquad v = n \qquad (F.1)$$

Substituting for F_{max} in equation E.21 gives the magnitude of the nth harmonic back emf as

$$(E_{a_n})_{max} = 12\mu_o f\tau l(T_{w_v})_a^2\, I_{a_n}/(\pi\delta_e v^2) \qquad (F.2)$$

The nth harmonic magnetizing reactance is by definition

$$E_{a_n}/I_{a_n} = 12\mu_o f\tau l(T_{w_v})_a^2/(\pi\delta_e v^2) \qquad \Omega\ /ph \qquad (F.3)$$

F.3 The nth Harmonic Slot-leakage Reactance

The nth harmonic slot leakage reactance for a single coil imbedded in a slot is given by [44]

$$X_{slot_n} = 2\pi f n S_a\, L_{slot} \qquad \Omega\ /ph \qquad (F.4)$$

where $S_a = Q_a/3$

: total number of armature slots per phase, neglecting the irregularity of the flux crossing the slot at its opening.

For a two layer short pitched winding such as that of the laboratory micro-alternator and a real machine, the self and mutual inductances of the layers must also be taken into account. Equation F.4 expands to

$$X_{slot_n} = 2\pi f n S_a \left(L_X + L_Y + k_{s_n} M_{XY}\right) \tag{F.5}$$

where L_X, L_Y : self-inductances of the two layers.

M_{XY} : mutual inductance between them.

k_{s_n} : nth harmonic slot leakage factor.

The slot leakage factor is a correction factor to compensate for the current phase difference between the two layers in the slot due to short-pitching the winding. Hanna [30] has shown that for a three-phase winding with 60 degree phase belts and a coil pitch greater than 0.67, k_{s_n} is given by the equation

$$\begin{aligned} k_{s_n} &= 1.5\rho - 0.5 \qquad n = 6h \pm 1 \qquad h = 0,1,2, \dots \\ &= 6\rho - 5 \qquad\quad\; n = 6h + 3 \end{aligned} \tag{F.6}$$

However, equation F.5 cannot be used directly as it stands because of the additional complication of each of the two layers being further subdivided into two as shown in figures D.2 and F.1, this odd winding arrangement being used to maximize the machine terminal emf relative to its small size. Fortunately each of the sub-tiers comprising one layer belong to the same coil side and additional correction factors are not needed. Therefore the slot inductance can be written as

$$\begin{aligned} L_{slot} = {} & L_{X_1} + L_{X_2} + L_{Y_1} + L_{Y_2} + 2M_{X_1X_2} + 2M_{Y_1}M_{Y_2} \\ & + 2(2k_{s_n}-1)\left(M_{X_1Y_1} + M_{X_1Y_2} + M_{X_2Y_1} + M_{X_2Y_2}\right) \end{aligned} \tag{F.7}$$

The individual self and mutual inductances of the tiers can be calculated using standard formulae [44]. With reference to the slot dimensions of figure F.1 they are

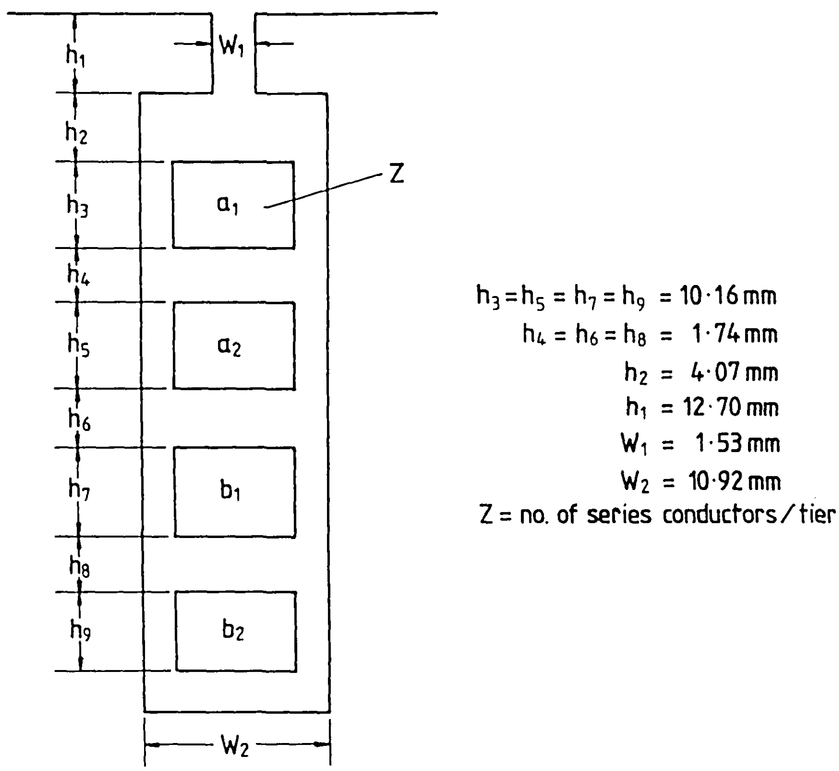

Figure F.1 : Stator slot dimensions for the micro-alternator.

$$L_{X_1} = \mu_o z^2 l \; [h_1/w_1 + h_2/w_2 + h_3/3w_2] \tag{F.8}$$

where $z = N_a/2S_a$

: number of series conductors/tier.

$$L_{X_2} = \mu_o z^2 l \; [h_1/w_1 + (h_2+h_3+h_4)/w_2 + h_5/3w_2] \tag{F.9}$$

$$L_{Y_1} = \mu_o z^2 l \; [h_1/w_1 + (h_2+h_3+h_5+h_6)/w_2 + h_7/3w_2] \tag{F.10}$$

$$L_{Y_2} = \mu_o z^2 l \; [h_1/w_1 + (h_2+h_3+h_4+h_5+h_6+h_7+h_8)/w_2 + h_9/3w_2] \tag{F.11}$$

$$L_{X_1X_2} = L_{X_1Y_2} = L_{X_1Y_2} = \mu_o z^2 l \; [h_1/w_1 + h_2/w_2 + h_3/w_3] \tag{F.12}$$

$$L_{X_2Y_1} = L_{X_2Y_2} = \mu_o z^2 l \; [h_1/w_1 + (h_2+h_3+h_4)/w_2 + h_5/2w_2] \tag{F.13}$$

$$L_{Y_1Y_2} = \mu_o z^2 l \; [h_1/w_1 + (h_2+h_3+h_4+h_5+h_6)/w_2 + h_7/2w_2] \tag{F.14}$$

Inserting these expressions for the inductances into equation F.7, and substituting for the slot inductance in equation F.4 gives, on simplification, the formula

$$X_{slot_n} = 2\pi f n \mu_o l N_a^2 (1.48 + 38.72k_{s_n})/S_a \qquad \Omega\ /ph \qquad (F.15)$$

F.4 The nth Harmonic End-winding Leakage Reactance

The formula used to calculate the end-winding leakage reactance is due to Alger [3] but extended by Hanna [30] to account for harmonics. Alger shows that it is given by the equation

$$X_{e_n} = X_{ea_n} + X_{ep_n} \qquad (F.16)$$

where X_{ea_n} : component due to axial currents.

X_{ep_n} : component due to circumferential surface currents.

The two components are given by the expressions

$$X_{ea_n} = \frac{0.197nf3N_a^2 (k_{d_v})_a^2 D_1 \cdot \tan\lambda[(np - \sin v\rho\pi)/\ ]}{v^2p^2 10^5} \qquad \Omega\ /ph \qquad (F.17)$$

and $$X_{ep_n} = \frac{0.8nf3N_a^2 (k_{d_v})_a^2 D_1 \cdot [\ln(4D_1/r_c)-1.75]}{v^2p^2 10^6} \qquad \Omega\ /ph \qquad (F.18)$$

where λ and D_1 are shown in figure F.2 and r_c is the mean radius of the imaginary circular coil in which the circumferential armature end-winding current flows. Alger [3] suggests that this should be taken as half the depth of the stator slot. λ can be calculated as

$$\tan\lambda = y_e/2y_s \quad \text{for} \quad y_s = \pi D_1 \rho/2p \qquad (F.19)$$

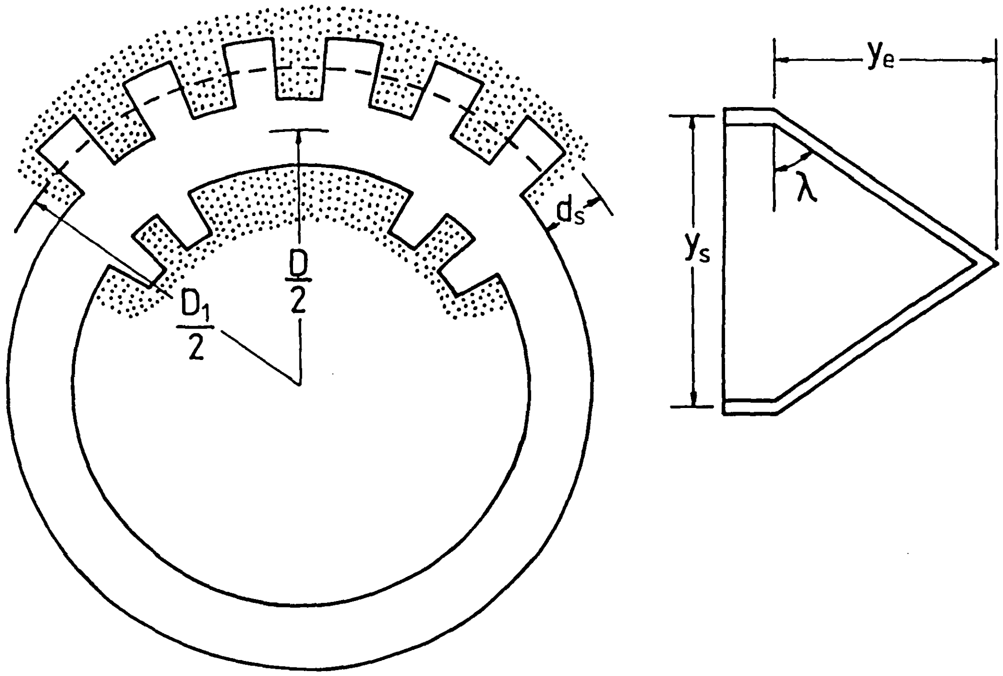

Figure F.2: End-winding dimensions.

F.5 The nth Harmonic Differential Leakage Reactance

The formula for the nth harmonic differential leakage reactance is also due to Alger [3]. He for convenience splits the differential reactance into two components, the zigzag and belt leakage reactances.

He defines the zigzag leakage reactance as constituting the asynchronous space harmonics of order 2hs ± 1, where h is an integer and derives the expression

$$X_{z_n} = \pi^2 X_{m_n}(k_{s_v})_a(6k-1)/[60(k_{w_v})_a^2 s_a^2] \qquad \Omega\ /\mathrm{ph} \qquad \text{(F.20)}$$

where $k = \delta/\delta_e$

: the ratio of the actual and effective airgaps.

$s = Q_a/p$

: armature slots per pole

The nth harmonic belt leakage reactance constitutes the asynchronous space harmonics of order $v = 6h \pm n$ and is given by the expression

$$X_{b_n} = X_{m_1}/(k_{w_1})_a^2 \sum_h [(k_{w_h})_a/h]^2 \qquad \Omega\ /ph \qquad (F.21)$$

This formula is derived without considering the damping effect of the rotor. In the case of the laboratory micro-alternator, due to the presence of damper bars, this effect is severe [30] and the belt leakage reactance neglected.

F.6 Calculated Values

Table F.1 lists calculated values of these reactances for the laboratory micro-alternator. Machine parameters listed in appendix D are used for the calculations.

n	1	3	5	7	9	11	13
X_{m_n}	29.56	2.35	.0167	.0061	.0879	.0223	.0135
X_{slot_n}	1.125	2.00	5.625	7.875	5.971	12.38	14.63
X_{e_n}	.2443	-	.0064	.0040	-	.0027	.0027
X_{z_n}	.1540	-	.0308	.0220	-	.0140	.0118
X_{1_n}	1.52	2.00	5.66	7.90	5.971	12.39	14.63

Table F.1: Calculated reactances for the micro-alternator

APPENDIX G

GENERAL SIMULATION OF CIRCULATING HARMONIC GROUND CURRENTS IN AN ALTERNATOR FOR ARMATURE WINDING FAULTS

G.1 The General Equations for a Three-phase Machine

The general equations for a three-phase alternator, neglecting saliency but including the effects of space harmonics are [11]

$$[e] = [R][i] + p[L][i] \tag{G.1}$$

where p : differentiation operator d/dt.

[e] is the column vector of instantaneous emfs such that

$$[e]^T = [e_A, e_B, e_C, e_F, e_D] \tag{G.2}$$

consisting of the three-phase infinite-bus emfs, and the field and damper winding (usually equal to zero) emfs respectively. Similarly, [i] is the column vector of instantaneous currents such that

$$[i]^T = [i_A, i_B, i_C, i_F, i_D] \tag{G.3}$$

[R] represents the resistances of the windings and is given by

$$[R] = \begin{bmatrix} R_A + R_{Ae} & & & & \\ & R_B + R_{Be} & & & \\ & & R_C + R_{Ce} & & \\ & & & R_F & \\ & & & & R_D \end{bmatrix} \tag{G.3}$$

where R_A, R_B, R_C, R_F, R_D : resistances of the armature, field and damper windings respectively.

R_{Ae}, R_{Be}, R_{Ce} : external resistances of the interposing impedence from the machine terminals to the infinite-bus.

[L] is the matrix of the self and mutual inductances of the windings. Its structure is:

$$[L] = \begin{bmatrix} L_A+L_{Ae} & M_{AB} & M_{AC} & M_{AF}(\theta) & M_{AD}(\theta) \\ M_{AB} & L_B+L_{Be} & M_{BC} & M_{BF}(\theta) & M_{BD}(\theta) \\ M_{AC} & M_{BC} & L_C+L_{Ce} & M_{CF}(\theta) & M_{CD}(\theta) \\ M_{AF}(\theta) & M_{BF}(\theta) & M_{CF}(\theta) & L_F & M_{FD} \\ M_{AD}(\theta) & M_{BD}(\theta) & M_{CD}(\theta) & M_{DF}(\theta) & L_D \end{bmatrix} \tag{G.4}$$

where L_{Ae}, L_{Be}, L_{Ce} : external inductance components of the interposing impedence from the machine terminals to the infinite-bus.

L_A, L_B, L_C : inductance of the armature windings.

M_{AB}, M_{BC}, M_{CA} : mutual inductances between the armature windings.

M_{FD} : mutual inductances between the field and damper windings.

$$M_{AF}(\theta) = \sum_v M_{AF_v} \cos v\theta \qquad v \text{ is odd.}$$

$$M_{BF}(\theta) = M_{AF}(\theta-2\pi/3) \quad \text{and} \quad M_{CF}(\theta) = M_{AF}(\theta-4\pi/3)$$

$$M_{AD}(\theta) = M_{AD}(\theta-2\pi/3) \quad \text{and} \quad M_{CD} = M_{AD}(\theta-4\pi/3).$$

For steady-state conditions all the equivalent parameters for the three phases are equal in magnitude, and the damper winding can be neglected. Therefore, the machine is fully described by two equations; one for the field and one for the armature. They reduce to the synchronous machine equivalent circuit equations. For a transient solution due to external faults, equation G.1 can be solved as it stands using numerical differentiation methods for unbalanced initial conditions.

The general equations can also form the basis for a synchronous machine simulation for internal armature winding faults. This can be done by simulating the effect of an internal winding fault as a change in configuration of the armature windings, and modifying equation G.1 appropriatly. Circulating ground currents can be accounted for by representing each of the armature windings as a series of meshes with the parallel arms representing the stray capacitance to ground of the windings (section 3.1.1).

The proposed method of analysis is illustrated for the example of a stator inter-turn fault, but it is general and can be extended to other types of high current winding faults. In the following description the minimum number of meshes possible per phase to fully describe the fault will be used so as to minimize the size of the matrices in the equations. This is only intended to enhance the clarity of the description as, obviously, for an accurate representation of the distributed armature capacitance to ground, a reasonable number of meshes per phase are essential.

G.2 Example of an Inter-turn Short Circuit

An interturn fault on the armature can be represented as shown in figure G.1. The fault splits the faulted phase, shown as the A-phase, into three parts each represented by a mesh together with its equivalent stray capacitance to ground. The unfaulted phases are represented by a single mesh. The capacitance to ground of the generator transformer and the external impedence are neglected for simplicity.

The parameters of the model, with the A-phase as the faulted phase are listed below:

R_e+pL_e : external resistance and inductance to the infinite-bus (i.e. $R_{Ae} = R_{Be} = R_{Ce}$ and $L_{Ae} = L_{Be} = L_{Ce}$).

e_{AB}, e_{BC}, e_{CA} : instantaneous infinite-bus phase-phase emfs.

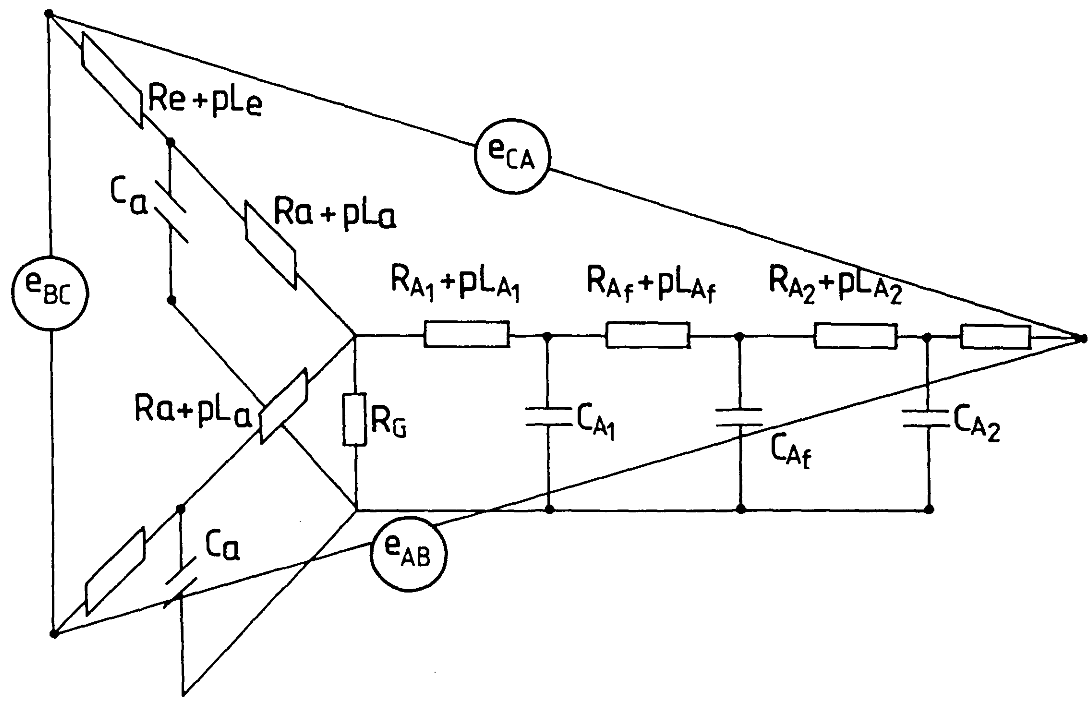

Figure G.1: Mesh model of a stator winding for an inter-turn fault on the A-phase.

R_a+pL_a : resistance and inductance of the unfaulted phases.

C_a : equivalent capacitance to ground of the unfaulted phases.

$R_{A_f}+L_{A_f}$: resistance and inductance of the shorted turns.

R_f : fault resistance.

C_f : equivalent capacitance of shorted terms.

$R_{A_1}+pL_{A_1}$, $R_{A_2}+pL_{A_2}$: resistance and inductance of the remaining parts of the faulted winding.

C_{A_1}, C_{A_2} : their equivalent capacitance to ground.

R_G : neutral grounding resistance.

If i_{A_1}, i_{A_f}, i_{A_2}, i_B, i_C, i_{AB}, i_{BC}, i_{CA} and i_F, i_D are the mesh currents of the model, and the field and damper winding currents respectively, the mesh equation for mesh A_1 can be written as

$$[R_G + (R_{A_1}+pL_{A_1}) + 1/pC_{A_1}]i_{A_1} - R_G(i_B+i_C) - (1/pC_{A_1})i_{A_f}$$

$$- (i_{AB} + i_{CA})(R_{A_1} + pL_{A_1}) + p(M_{A_1B}\cdot i_B + M_{A_1C}\cdot i_C + M_{A_1A_2}\cdot i_{A_2}$$

$$+ M_{A_1A_f}) + p[M_{A_1F}(\theta)\cdot i_F + M_{A_1D}(\theta)\cdot i_D] = 0 \qquad (G.5)$$

where $M_{A_1F}(\theta) = \sum_v (M_{A_1F})_v \cos v\theta$

$M_{A_1D}(\theta) = \sum_v (M_{A_1D})_v \cos v\theta$

The last two terms in equation G.5 can be written as

$$M_{A_1F}(\theta)\cdot pL_F - v\omega\, M_{A_1F}(90-\theta)\cdot i_F + M_{A_1D}(\theta)\cdot pi_D$$

$$- v\omega\, M_{A_1D}(90-\theta)\cdot i_D$$

where ω is substituted for $p\theta$, i.e. the speed is assumed constant. Thus the solution will be valid only over a few cycles, which is perfectly adequate for protection purposes.

Substituting in equation G.5 and rearranging gives

$$\begin{aligned} &[\ (R_G+R_{A_1})i_{A_1} - R_G \cdot i_B - R_G \cdot i_C - R_{A_1} \cdot i_{AB} - R_{A_1} \cdot i_{CA}\ ] \\ &\quad - v\omega\ [M_{A_1F}(90-\theta) + M_{A_1D}(90-\theta)] \\ &\quad + 1/p\ [1/C_{A_1}(i_{A_1}+i_{A_f})] + p[L_{A_1}(i_{A_1} - i_{AB} - i_{CA}) \\ &\quad + M_{A_1B} \cdot i_B + M_{A_1C} \cdot i_C + M_{A_1A_F} \cdot i_F + M_{A_1A_2} \cdot i_{A_2}] = 0 \end{aligned} \tag{G.6}$$

In a similar manner, equations for the other meshes can be formed to give a set of eight linear differential equations given by the matrix equation

$$[R][i] - v\omega[M][i] + 1/p[C][i] + p[L][i] = [e] \tag{G.7}$$

[i] and [e] are the column vectors of instantaneous currents and voltages respectively such that

$$[i]^T = [i_{A_1},\ i_{A_f},\ i_{A_2},\ i_B,\ i_C,\ i_F,\ i_D,\ i_{AB},\ i_{BC},\ i_{CA}]$$

and $$[V]^T = [0,\ \ldots,\ 0,\ e_{AB},\ e_{BC},\ e_{CA}]$$

[R] is the 8 x 8 matrix of resistance terms whose elements are:

$R_{1,1} = R_{A_1} + R_G$
$R_{2,2} = R_{A_f}$, $R_{3,3} = R_{A_2}$
$R_{4,4} = R_{5,5} = R_a$
$R_{6,6} = R_F$, $R_{7,7} = R_D$
$R_{8,8} = R_{10,10} = [R_a+R_e] + [(R_{A_1}+R_{A_f}+R_{A_2})+R_e]$
$R_{9,9} = 2(R_a + R_e)$
$R_{1,4} = R_{1,5} = -R_G$
$R_{1,8} = R_{8,1} = R_{1,10} = R_{10,1} = -R_{A_1}$

$R_{2,8} = R_{8,2} = R_{2,10} = R_{10,2} = -R_{A_f}$
$R_{3,8} = R_{8,3} = R_{3,10} = R_{10,3} = -R_{A_2}$
$R_{4,8} = R_{8,4} = R_{4,9} = R_{9,4} = R_{5,10} = R_{10,5} = -R_a$
$R_{8,9} = R_{9,8} = R_{9,10} = R_{10,9} = -(R_a + R_e)$
$R_{8,10} = R_{10,8} = -[R_e + (R_{A_1}+R_{A_f}+R_{A_2})]$

The elements of matrix [M] are:

$M_{1,6} = M_{A_1F}(90-\theta)$
$M_{1,7} = M_{A_1D}(90-\theta)$
$M_{2,6} = M_{A_fF}(90-\theta)$
$M_{2,7} = M_{A_fD}(90-\theta)$
$M_{3,6} = M_{A_2F}(90-\theta)$
$M_{3,7} = M_{A_2D}(90-\theta)$
$M_{4,6} = M_{BF}(90-\theta) = M_{5,6} = M_{CF}(90-\theta) = M_{aF}(90-\theta)$
$M_{4,7} = M_{BD}(90-\theta) = M_{5,7} = M_{CD}(90-\theta) = M_{aD}(90-\theta)$

The elements of the [C] matrix are:

$C_{1,1} = -C_{1,2} = -C_{2,1} = 1/C_{A_1}$
$C_{2,2} = 1/C_{A_f} + 1/C_{A_1}$
$C_{2,3} = C_{3,2} = -1/C_{A_f}$
$C_{3,3} = 1/C_{A_2}$
$C_{4,4} = C_{5,5} = 1/C_a$

The elements of the [L] matrix are:

$Y_{1,1} = -Y_{1,8} = -Y_{8,1} = -Y_{1,10} = -Y_{10,1} = L_{A_1}$
$Y_{1,2} = Y_{2,1} = M_{A_1A_f}$
$Y_{1,3} = Y_{3,1} = M_{A_1A_2}$
$Y_{1,4} = Y_{4,1} = M_{A_1B}$
$Y_{1,5} = Y_{5,1} = M_{A_1C}$
$Y_{1,6} = Y_{6,1} = M_{A_1F}(\theta)$
$Y_{1,7} = -Y_{7,1} = M_{A_1D}(\theta)$
$Y_{2,2} = -Y_{2,8} = -Y_{8,2} = -Y_{2,10} = -Y_{10,2} = L_{A_f}$
$Y_{2,3} = Y_{3,2} = M_{A_fA_2}$
$Y_{2,4} = Y_{4,2} = M_{A_fB}$

$Y_{2,5} = Y_{5,2} = M_{A_f C}$
$Y_{2,6} = Y_{6,2} = M_{A_f F}(\theta)$
$Y_{2,7} = Y_{7,2} = M_{A_f D}(\theta)$
$Y_{3,3} = -Y_{3,8} = -Y_{8,2} = -Y_{3,10} = -Y_{10,3} = L_{A_2}$
$Y_{3,4} = Y_{4,3} = M_{A_2 B}$
$Y_{3,5} = Y_{5,3} = M_{A_2 C}$
$Y_{3,6} = Y_{6,3} = M_{A_2 F}(\theta)$
$Y_{3,7} = Y_{7,3} = M_{A_2 D}(\theta)$
$Y_{4,4} = Y_{5,5} = L_a$
$Y_{4,5} = Y_{5,4} = M_{BC}$
$Y_{4,6} = Y_{6,4} = M_{BF}(\theta)$
$Y_{4,7} = Y_{7,4} = M_{BD}(\theta)$
$Y_{5,6} = Y_{6,5} = M_{CF}(\theta)$
$Y_{5,7} = Y_{7,5} = M_{CD}(\theta)$
$Y_{6,7} = Y_{7,6} = M_{FD}$

REFERENCES

[1] **Abetti, P.A.** and **Davis, H.F.**, "Surge transfer in three winding transformer", Trans. AMIEE III, 73, No.15, 1954.

[2] **Albright, D.R.**, "Interturn short-circuit detector for turbine generator windings", IEEE Trans. PAS-90, 1971.

[3] **Alger, P.L.**, "Induction Machines", 2nd Edition, Hordon and Breach, 1970.

[4] **Antoniou, A.**, "Digital filters: analysis and design", McGraw-Hill Inc., 1979.

[5] **Aucoin, B.M.** and **Russell, B.D.**, "Distribution high impedance fault detection utilizing high frequency current components", IEEE Trans. PAS-101, No.6, June 1982.

[6] **Buckley, G.W.**, "The effects of rotor inter-turn short-circuits on voltage imbalance and circulating currents in large generator stator windings",

[7] **Brigham, E.O.**, "The Fast Fourier Transform", Prentice Hall Inc., 1974.

[8] **Byars, H.**, "Detection of alternator winding faults using an on-line magnetic field search coil monitoring unit", 17th UPEC Conf., Manchester 1982.

[9] **Capellini, V.**, **Constantinides, A.G.** and **Emiliani, P.**, "Digital filters and their applications", Academic Press Inc., 1978.

[10] **Carr, J.** and **Jackson, R.V.**, "Frequency domain analysis applied to digital transmission line protection", IEEE Trans. PAS-94, No.4, July/August 1975.

[11] **Ching, Y.K.**, "Synchronous machine analysis", Phd Thesis, Imperial College, 1953.

[12] **Cooley, J.W.** and **Tuckey, J.W.**, "An algorithm for machine calculation of complex Fourier Series", Math. Comput., vol 19, April 1965.

[13] **Cooley, J.W.**, **Lewis, P.A.W.** and **Welch, P.D.**, "The Fast Fourier Transform Algorithm: programming considerations in the calculation of Sine, Cosine and Laplace Transforms", J. Sound Vib., vol 12, July 1970.

[14] **Dash, P.K.**, **Malik, O.P.** and **Hope, G.S.**, "Fast generator protection against internal asymmetrical faults", IEEE Trans. PAS-96, No.5, Sept/Oct 1977.

[15] **Einvall, C.H.** and **Linders, J.R.**, "A three-phase differential relay for transformer protection", IEEE Trans. PAS-94, No.6, Nov/Dec 1975.

[16] **Fakhro, Y.A.**, "Discrete Fourier Transform techniques for power transmission line protection", DIC Thesis, Imperial College, 1978.

[17] **Fiorentzis, M.** and **Pencinger, C.J.**, "A new method for the 100% stator and rotor ground fault protection of generators", Paper No. 82SM 443-0, IEEE PES Summer Meeting, July 1982.

[18] **Gantner, J.**, **Schwengeler, A.** and **Warto, P.P.**, "Protection for large turbo-generators", Brown Boveri, Rev. 9-75.

[19] **Gessing, R.**, "Recursive smoothing for discrete time systems as a filtering problem", IEE Proc., vol.131, Pt.D, No.4, July 1984.

[20] **Ghausi, M.S.** and **Laker, K.R.**, "Modern filter design", Prentice-Hall Inc., 1981.

[21] **Gilcrest, G.B.**, **Rockefeller, G.D.**, and **Udren, E.A.**, "High speed distance relaying using a digital computer", IEEE Trans. on PAS-91, No.3, May/June 1972.

[22] **Girgis, A.A.** and **Hamm, F.M.**, "A new FFT based digital frequency relay for load shedding", IEEE Trans. PAS-101, No. 2, Feb 1982.

[23] **Girgis, A.A.**, "A new Kalman filtering based digital distance relay", Paper no. 82WM 166-7, IEEE PES Summer Meeting, Jan/Feb 1982.

[24] **Girgis, A.A.**, "Modelling of fault induced noise signals for computer relaying applications", Paper no. 83WM 100-5, IEEE PES Winter Meeting, Jan/Feb 1983.

[25] **Gonzalez-Urdaneta, G.E.** and **Cory, B.J.**, "Varience and approximate confidence limits for probability and frequency of systems failure", IEEE Trans. on Reliability, vol.27, 1978.

[26] **Graeme, J.G.**, **Toby, G.E.** and **Heulsman, L.P.**, "Operational Amplifiers - design and applications", Mc-Graw Hill Book Company, 1971.

[27] **Grandke, T.**, "Interpolation algorithms for Discrete Fourier Transforms of weighted signals", IEEE Trans. on Inst. and Meas., vol IM-32, No.2, June 1983.

[28] **Griffin, C.H.** and **Pope, J.W.**, "Generator ground fault protection using overcurrent, overvoltage and undervoltage relays", Paper No. 82WN 171-7, IEEE PES Winter Meeting, Jan/Feb 1982.

[29] **Halberstein, J.**, "Recursive implementation of the DFT", Lett. of Proc. IEEE, vol. 54, 1966.

[30] **Hanna, R.A.**, "The 6-phase two-circuit synchronous generator and its associated transformer", Phd Thesis, Imperial College, Jan 1978.

[31] **Harris, H.J.**, "On the use of windows for harmonic analysis with the Discrete Fourier Transform", IEEE Proc., vol.66, No.1, Jan 1978.

[32] **Heller, B.** and **Hamata, V.**, "Harmonic field effects in induction machines", Elsevier Scientific Publishing Co., New York, 1977.

[33] **Hope, G.S., Dash, P.K.** and **Malik, O.P.**, "Digital differential protection of a generating unit: Scheme and real time test results", IEEE Trans. PAS-96, No.2, March/April 1977.

[34] **Hope, G.S.** and **Umamaheswaran, V.S.**, "Sampling for computer protection of transmission lines", IEEE PAS-93, No.5, Sept/Oct 1974.

[35] **Horne, E.**, "The design of micro-processors for digital protection of power systems", Phd Thesis, Imperial College, 1978.

[36] **Horton, J.W.**, "The use of Walsh Functions for high speed digital relaying", Paper No. A-75-582-7, IEEE PES Summer Meeting, July 1975.

[37] **Jain, V.K., Collins Jr., W.L.** and **Davis, D.C.**, "High-accuracy analogue measurements via interpolated FFT", IEEE Trans. on Inst. and Meas., vol. IM-28, No.2, June 1979.

[38] **Johns, A.T.** and **Martin, M.A.**, "New ultra-high-speed distance protection using finite transform techniques", IEE Proc., vol. 130, Pt.C, No.3, May 1983.

[39] **Johns, A.T.** and **Martin, M.A.**, "Fundamental digital approach to the distance protection of e.h.v. transmissions lines", IEE Proc., vol. 125, No.5, May 1978.

[40] **Kwong, W.S., Newbould, A.** and **Lomas, T.H.**, "Overall control systems for EHV substations - a review of system design approaches", CIGRE SC35 WG06 Report, Aug 1983.

[41] **Larson, R.R.** and **Flechsig, A.J., Schweitzer, E.O.**, "The design and test of a digital relay for transformer protection", IEEE Trans. PAS-98, No.3, May/June 1979.

[42] **Last, F.H.** and **Stalewski, A.**, "Protective gear as a part of automatic power system control", IEE Conf. Publ. 16, Part I, March 1966.

[43] **Leondes, C.T.** and **Rivers, D.D.**, "Frequency domain interpolation", IEEE Trans. Aero. and Elect. Sys., May 1977.

[44] **Liwschitz, M.**, "Alternating current machines", 2nd Edition, Von Nostrand, 1961.

[45] **Lodge, I.**, **Mulhaus, J.** and **Ward, D.M.**, "Detection of shorted turns on two-pole alternator rotors by measuring circulating stator currents", 19th UPEC Conf., Univ. of Dundee, April 1984.

[46] **Luckett, R.G.**, **Munday, P.J.** and **Murray, B.E.**, "A sub-station based computer for control and protection", Developments in Power System Protection, IEE Conference Publication No.125, London, March 1975.

[47] **Mann, B.J.** and **Morrison, I.F.**, "Digital calculation of impedance for transmission line protection", IEEE Trans. PAS-90, No.1, Jan/Feb 1971.

[48] **Marple, Jr., L.K.** and **Kay, S.M.**, "Spectrum analysis - a modern perspective", Proc. IEEE, vol.69, No.11, November 1981.

[49] **McCleer, P.J.** and **Mir, M.**, "A new technique of differential relaying: the Delta Differential Delay", Paper no. 82WM 168-3, IEEE PES Winter Meeting, Jan/Feb 1983.

[50] **Mclaren, P.G.** and **Redfern, M.A.**, "Fourier series techniques applied to distance protection", Proc. IEE, vol 122, No.11, Nov 1975.

[51] **Mir, M.** and **McCleer, P.J.**, "Simulation methods for optimum performance estimation of analog and computer impedance relays", IEEE Trans. PAS-103, No.6, June 1984.

[52] **Monro, D.M.**, "Complex discrete Fast Fourier Transform", Applied Statistics, vol 24, No.1, 1975.

[53] **Monro, D.M.**, "Real Discrete Fast Fourier Transform", Applied Statistics, vol 25, No.2, 1976.

[54] **Naylor, J.H.** and **Nunney, H.D.**, "Protection of feeders, busbars, transformers, generators, reactors and other plants", CEGB Transmission Plant Design Branch.

[55] **Noble, A.D.**, "On-line computer control of turbine generators using state estimation and optimal feedback", Phd Thesis, Imperial College, November 1984.

[56] **Nussbaumer, H.J.**, "Fast Fourier Transform and Convolution algorithms", Springer-Verlag, 1981.

[57] **Pavlides, A.S.**, "Implementation of optimal control on a micro-machine", Power system report in preparation, Imperial College.

[58] **Penman, J.**, **Thompson, W.T.**, **Leonard, R.A.** and **Milne, A.J.**, "Failure identification of offshore induction motor systems using on-line condition monitoring", 4th Nat. Reli. Conf., Birmingham, July 1983.

[59] **Penman, J.**, **Hadwick, J.G.** and **Stronach, A.F.**, "Protection strategy against the occurrence of faults in electrical machines", Conf. Developments in Power Systems Protection, IEE Conf. Publ. No.185, 1980

[60] **Penman, J.**, **Dey, M.N.**, **Stronach, A.F.** and **Hadwick, J.G.**, "A micro-computer based machine protection system", 17th UPEC Conf., UMIST 1982.

[61] **Phadke, A.G.**, **Thorp, J.S.** and **Adamiak, M.G.**, "A new measurement technique for tracking voltage phasors, local system frequency, and rate of change of frequency", Paper no. 82SM 444-8, IEEE PES Summer Meeting, July 1982.

[62] **Phadke, Hilbka** and **Ibrahim**, "A digital computer system for EHV substation: analysis and field tests", IEEE Trans. PAS-95, No.1, Jan/Feb 1976.

[63] **Pope, J.W.**, "Comparison of 100% stator ground fault protection schemes for generator stator windings", Paper No. 83SM 416-5, IEEE PES Summer Meeting, July 1983.

[64] **Rabiner, L.R.** and **Gold, B.**, "The theory and application of digital signal processing", Prentice Hall Inc, 1975.

[65] **Ramamoorty, M.**, "Application of digital computers to power system protection", Journal of Inst. Eng. of India, vol 52, No.10, June 1972.

[66] **Ranjbar, A.**, "Computer protection of high voltage transmission lines", Phd Thesis, Imperial College, 1975.

[67] **Reddy, I.G.** and **Jones, C.V.**, "Line-line short circuit of synchronous machine: illustration of computer-aided machine analysis", Proc. IEE, vol 118, No.1, Jan 1971.

[68] **Sachdev, M.S.** and **Wind, D.W.**, "Generator differential protection using a hybrid computer", IEEE Trans. PAS-93, No.5, Nov/Dec 1973.

[69] **Sachdev, M.S.** and **Baribeau, M.A.**, "A new algorithm for digital impedance relays", Paper No. F79-248-6, IEEE PES Winter Meeting, Feb 1979.

[70] **Sakaguchi, T.**, "A statistical decision theoretic approach to digital relaying", IEEE Trans. PAS-99, No.5, Sept/Oct 1980.

[71] **Schlake, R.L.**, **Buckley, B.W.** and **McPherson, G.**, "Performance of third-harmonic ground fault protection schemes for generator stator windings", IEEE Trans. PAS-100, No.7, July 1981.

[72] **Sykes, J.A.** and **Morrison, I.F.**, "A proposed method of harmonic restraint differential protection of transformers by digital computer", IEEE Trans. PAS-91, No.3, May/June 1977.

[73] **Sykes, J.A.**, "A new technique for high speed transformer protection suitable for digital implementation", Paper No. C72 429-9, IEEE PES Summer Meeting, 1972.

[74] **Thorpe, J.S.** and **Phadke, A.G.**, "Microprocessor based three-phase transformer differential relaying", IEEE Trans. PAS-101, No.2, Feb 1982.

[75] **Thorpe, J.S.**, **Phadke, A.G.**, **Horowitz, S.H.** and **Beehler, J.E.**, "Limits to impedance relaying", IEEE Trans. PAS-98, No.1, Jan/Feb 1979.

[76] **Wiszniewski, A.**, "How to reduce errors of fault locating algorithms", IEEE Trans. PAS-100, No.12, Dec 1981.

[77] "Fast Fourier Transformer no.S2814A", Device data sheet, **American Microsystems** Inc.

[78] "Harmonization of protection polices for power stations and generators and of protection polices for H.V. networks", **CIGRE** W.G.34-01 Report, May 1983.

[79] "High frequency disturbance test", Publication no.255-6, Appendix C, IEC Standards, 1978.

[80] IEEE Committee Report, "Generator ground protection guide", IEEE Trans. PAS-103, No.7, 1984.

[81] IEEE Committee Report, "Potential Transformer application on unit-connected generators", Paper 70 TP 18-PWR, IEEE Winter Meeting, New York, Jan 25-30, 1970.

[82] IEEE course "Computer relaying", Course text. IEEE Special Publ. 79EH0148-7-PWR.

[83] "Micro-synchronous generator set specification No.103/R13", **Mawdsley's** Ltd., Dursley, Glos.

[84] "Neutral earthing of main generators in power stations", **CEGB** design memorandum 046/4, Issue 1, Feb. 1976.

[85] "Overall protective arrangements for main generating units", **CEGB** design memorandum 098/4, Issue 2, June 1969.

[86] "Plot-10 terminal control system", Manual no. 070-2241-00, **Tektronix** Inc., 1983.

[87] "Protection of large generators", Publication no. CH-ES 31-02 E, **Brown Boveri** & Company, Ltd.

[88] "Protective relays applications guide", **GEC Measurements,** 1975.

[89] "Real-time disk operating system", Manual 093-000201-03, **Data General** Corporation, 1979.

[90] "The Midos system", Publication no. R6001, **GEC Measurements** Ltd.

[91] "The selection of generator protection systems", Publication no. CH-ES 31-01 E, **Brown Boveri** & Company, Ltd.

[92] "Type MCGG inverse definite time overcurrent and earth fault relay", Publication no. R6002, **GEC Measurements** Ltd.

[93] Correspondence with Mr. **A. Hunt,** GEC Turbines Ltd., Stafford.

[94] Discussions with Mr. **J.G. Hadwick**, CEGB Generation and Transmission Division, Barnwood, Glouc.